STATIONARY FLAMES WITHIN POROUS INERT MEDIA

zur Erlangung des akademischen Grades eines

DOKTORS DER INGENIEURWISSENSCHAFTEN (Dr.-Ing.)

von der Fakultät für Chemieingenieurwesen und Verfahrenstechnik des

Karlsruher Instituts für Technologie (KIT)

genehmigte

DISSERTATION

von

M.Sc. César Bedoya

aus Medellín, Kolumbien

Hauptreferent: Prof. Dr.-Ing. Nikolaos Zarzalis

Korreferentin: Prof. Dr. Bettina Kraushaar-Czarnetzki

Tag der mündlichen Prüfung: 08. Januar 2016

Dedicado a mi esposa Luisa Fernanda Roldán Rojas.

Vorwort

Zusammenfassung

Die vorliegende Dissertation befasst sich mit der grundlegenden Untersuchung der Flammenstabilisierung innerhalb von porösen, inerten Materialien (PIM). Diese Verbrennungsart bietet im Vergleich zu konventionellen Brennern mehrere Vorteile, z.B. niedrigere Schadstoffemissionen, einen hohen IR-Strahlungsanteil und einen breiteren Stabilitätsbereich. In der Literatur existieren bisher nur zwei Studien zu überatmosphärischem Druck, zudem bestehen Widersprüche zwischen den Ergebnissen von Experimenten und numerischen Simulationen der Flammendicke. Die vorliegende Arbeit stellt einen Beitrag dar, um diese Lücke zu schließen.

In Rahmen dieser Arbeit wurden theoretische Betrachtungen sowie experimentelle und numerische Untersuchungen durchgeführt. Untersucht wurden die Einflüsse von Brennerleistung, Luft zu Brennstoff Verhältnis, Druck, Vormischtemperatur und Geometrie des PIM auf Flammendicke und Brenngeschwindigkeit.

Die Durchführung der Experimente fand in einem kegelförmigen Brenner statt. Die Berechnung der Brenngeschwindigkeit wurde durch die Bestimmung der Flammenstelle mit Hilfe von Thermoelementen ermöglicht.

Darüber hinaus wurde ein eindimensionales numerisches Modell erweitert und gegen Experimente validiert. Die effektiven Transportkoeffizienten wurden aus dreidimensionalen numerischen Simulationen in realen Schwammstrukturen gewonnen. Zusätzlich wurde eine neue Methode eingeführt, um Quellterme anhand statischer Wahrscheinlichkeitsdichtefunktionen der Gastemperatur zu berechnen. Diese Erweiterungen des Modells ergaben eine gute übereinstimmung der Aufweitung der Flammendicke.

Als wichtigstes Ergebnis wird das Verhalten der Brenngeschwindigkeit als Funktion des Drucks geschätzt, welches deutlich von dem in laminaren Flammen abweicht. Die Brenngeschwindigkeit in PIM kann mit dem Druck zunehmen, was mit den eindimensionalen Modellen sowohl nummerisch wie analytisch vorhergesagt wurde.

Abstract

The present dissertation contributes to the basic research of stabilization of lean premixed flames in porous inert media (PIM). The presence of PIM in the combustion environment serves to intensify the heat transfer and the mixing of reacting species, this lead to a combustion mode that exhibits considerably different features compared to free premixed combustion, such as considerably reduced emissions of pollutant species, i.e. nitrogen oxides NO_x and carbon monoxide CO. This kind of combustion has been mostly applied commercially to transfer heat by means of thermal radiation, since the solid phase achieves high temperatures and its thermal emissivity is considerably higher than that of gases. Other interesting features such as enlargement of the flame stability range, reduction of thermo-acoustic instabilities, gradual response to operative changes and geometric flexibility of design, open new possibilities of premixed combustion within PIM to be used in applications with ultra lean combustion like piloting the combustion in stationary gas turbines and burning low-heating value gases, which otherwise cannot be burned and must be wasted. With the motivation of studying the potential application of PIM in gas turbine combustion, the flame stability at elevated pressure and temperature must be studied.

During the present work experiments were conducted in order to observe the effect of pressure, air to fuel ratio, temperature and PIM pore size on the flame stability within PIM. Adiabatic condition was intended. A model conical shaped burner was tested. The burner was made of reticulated open pore sponge like solid structures. The material of this kind of PIM was silicon infiltrated silicon carbide (SiSiC). The used flame stabilization technique is based on continuous decrease of flow velocity provided by the change of cross sectional area of the conical shaped burner. The measurements of temperature profiles and flow rates were used to determine the thermal flame thickness and the burning velocity. A definition of the burning velocity was developed in order to allow for comparability with other kind of flame stabilization techniques. As main output of this work it was observed that the pressure influence on the burning velocity can differ considerably from that of laminar free flames, i.e. the burning velocity can increase with the increase

of pressure, which can be explained by the mixing effect on the flow in the solid sponge, which is proportional to the Reynolds number. Thus, for conditions exhibiting different burning velocity, the pressure influence on the burning velocity differs as well.

A semi empirical model was developed that can be used for engineering purposes while dimensioning porous burners for operation at different conditions or with different fuels. This model is based on an analogy of modified Peclet numbers involving the burning velocity of the flame stabilized in PIM related with the laminar burning velocity of a flat free flame. Additionally, a theoretical model based on classical flame theories was derived, which is instructive in understanding and allows also to predict the increase of burning velocity with the increase of pressure and serve as an easy-to-use model for practical purposes.

Additional to the experimental investigation, a numerical one dimensional model was implemented for the simulation of premixed flame stabilization within PIM. The model is based on macroscopically averaged quantities along the porous volume. The effective transport coefficients and correlations, which inform about the pore-level occurring processes, were obtained from results of direct pore level simulations performed on reconstructed real PIM samples from tomographic data. Using these coefficients in the 1D model, premixed flame stability parameters can be fairly well predicted, even the increase of the burning velocity with the increase with pressure and the effect of air to fuel ratio on this dependency. Nevertheless, the results are not exact, especially the flame thickness differs considerably. The reason of the problem was identified as the calculation of the averaged source terms of the species and energy equations. A new method to average the source terms was implemented considering the spatial fluctuations of temperature and mass fractions along the cross sectional area by means of the use of presumed probability density functions. After this modification of the model a well comparison with experiments in terms of burning velocities and profiles of average temperature was achieved.

Contents

Nomenclature

Greek symbols

α convective heat transfer coefficient $[W/m^2K]$

β extinction coefficient $[m^{-1}]$

δ flame thickness $[m]$

$\dot{\omega}$ volume averaged net species production rate $[kg/m^3s]$

λ air factor $(\mathrm{AFR}/\mathrm{AFR}_{stoich})$

λ thermal conductivity $[W/mK]$

ν kinematic viscosity $[m^2/s]$

ν' reactant (ν'' product) stoichiometric coefficient

ρ density $[kg/m^3]$

σ Stefan-Boltzmann constant $[W/m^2K^4]$

σ variance

τ tortuosity

τ_c characteristic time scale of heat release [s]

θ normalized temperature

υ_D diffusion velocity $[m/s]$

ε porosity (V_g/V)

ζ reaction progress variable

Latin symbols

A_g gas phase cross sectional area $(a_g = A_{pim} \cdot \varepsilon)$ $[m^2]$

a thermal diffusivity $[m^2/s]$

a_{dis} coefficient of axial thermal dispersion $[m^2/s]$

b exponent of pressure in its influence on S_l

C effective transport coefficient $[m^2/s]$

c_p specific heat capacity $[J/kgK]$

c constant parameter

D diffusion coefficient $[m^2/s]$

D_{dis} coefficient of axial mass dispersion $[m^2/s]$

d diameter

h specific enthalpy $[J/kg]$

Hg Hagen number $Hg = \frac{\partial p}{\partial x}\frac{d_h^3}{\rho_g \nu_g^2}$

k_f forward (k_b backward) reaction rate coefficient

K Permeability $[K]$

l characteristic length $[m]$

l^0 quenching radius $[m]$

l air to fuel mole ratio $[mol/mol]$

L Markstein length $[m]$

M molecular weight $[kg/kmol]$

m mass $[kg]$

$\dot{m}$ mass flow rate $[kg/s]$

N_i total number of species considered

N_k total number of reactions considered

Nu Nusselt number $(\alpha \cdot d_h/\lambda)$

p probability

Pe Peclet number $(u \cdot l/D)$

$\dot{r}_k$ reaction rate of a kth reaction

R universal gas constant $8.315 \ J/mol \cdot K$

R PDF contribution factor

R thermal resistance $[W/m^2 K]$

Re Reynolds number $(u \cdot l/\nu)$

S burning velocity $[m/s]$

S surface area $[m^2]$

S_v volumetric surface area $(S/V) \ [m^{-1}]$

t struc size $[m]$

SR burning velocity ratio

T volume averaged temperature $[K]$

T^* local temperature $[K]$

T^0 temperature of activation of reactions $[K]$

t time $[s]$

u volume averaged bulk velocity $(u = u_g \cdot \varepsilon) \ [m/s]$

V volume $[m^3]$

$\dot{W}$ power $[J/s]$

X volume averaged mole fraction

x axial coordinate

Y volume averaged mass fraction

Y^* local mass fraction

Subscripts

0 burner inlet plane

$2-ph$ overall two-phase

a air

ad adiabatic combustion

b burned

dis axial dispersion

eff effective

f flame

f fuel

g gas phase

h hydraulic

i i^{th} species

k k^{th} reaction

l laminar

m molecular

p preheating

r radiation

R reaction

s solid phase

st stoichiometric

t turbulent

t transverse

u unburned

Abbreviations

$\mu-$CT micro computer tomography

AFR air-to-fuel ratio

CFD computational fluid dynamics

DCM direct chemistry model

DPLS direct pore level simulations

PDF probability density function

PIM porous inert media

PIM PDF proposed simulation model of PIM combustion

PPI pores per linear inch

RMS root mean square along a cross section

TCM tabulated chemistry model

Chapter 1

Introduction

1.1 Introduction and motivation

Combustion processes of fossil fuels dominate the energy and transport sectors, so environmentally friendly, efficient and novel combustion processes and systems are a major concern of modern technological efforts in this field [1]. As it was observed that solid materials accommodate the widest spectrum of thermal radiation, combustion in/of porous media has became a topic of intensive research in recent decades and has been used in numerous practical applications to great effect [2].

Combustion in porous media can be classified into three types depending on the physical and chemical nature of the porous media: (i) inert, (ii) catalytic and (iii) combustible [3–5]. The shapes of the porous media can also be classified into (i) consolidated and (ii) packed discrete elements. An example of consolidated porous media is regular non-interconnected channels (bundle of tubes or honeycombs), which have been widely used to support catalytic reactions. Another example is highly porous solid sponges (also called open cell foams or reticulated structures), which were used in the present work have been a subject of extensive research in last two decades for a vast number of applications in process engineering owing to their high volumetric surface area, high degree of cross mixing and low pressure drop imposed on the fluid flow, compared with porous media made of packed discrete elements [6, 7]. Fig.1.1 shows photos of some porous inert media (PIM) commonly used to support combustion.

Porous media allow for the premixed and non-premixed combustion of gas fuels or liquid fuels, but the flame stabilization within PIM of premixed gases has been identified as the basic combustion process of applications of burner technology in energy, thermal engineering and processing industries [9–11]. Combustion within PIM offers high

Figure 1.1: Some examples of commonly used porous inert media to support combustion; some pictures taken from [8]

power density, a high power dynamic range and very low NO_x, CO and noise emissions, compared with free laminar combustion [12]. Intensified heat feedback from the burned zone is transferred through the solid matrix by solid-solid radiation and conduction to preheat the unburned mixture; thus, a superadiabatic peak of temperature is achieved in some locations. This mechanism is well known as heat recirculation [13]. Depending on the PIM topology, cross mixing of the fluid flow (hydrodynamic dispersion) can occur, which enhances the transport of heat and intermediate species from the combustion reactions to the incoming unburned gases. The heat recirculation locally increases the gas temperature and reactions take place at a higher temperature; hence, reaction rates are increased with respect to the free combustion mode. Owing to heat recirculation, extension of the lean flammability limit is attained and the combustion of fuels with low energy content is enabled [14]. The dispersion effect enlarges the flame thickness, which also has a positive effect on the burning velocity [15]. Therefore, the firing rate specific to the burner cross section is increased by an order of magnitude in relation to a laminar free flame [15].

The basic experimental study of combustion processes in porous media faces challenges due to the access limitations for both optical and mechanical probes by the presence of a solid matrix. Owing to these limitations in the processes in porous media, fundamen-

tal discussions are still ongoing, such as the debate about the effects of turbulence in porous media, even in the absence of combustion, since the dispersion effects cannot be separated in experiments from turbulence inside the pore [4].

Modeling is also challenging due to the still scarce knowledge of the fundamentals of thermal, radiative and fluid mechanical processes within porous media and how these affect and are affected by combustion, although considerable progress has been made.

Basically, there are three major classes of modeling approach: (i) macroscopic, (ii) microscopic and (iii) direct pore-level simulation (DPLS). The macroscopic approach is rigorously mathematically correct, derived from the averaging over a representative volume (meso-scale), commonly under the assumption that the random spatial deviations depend linearly on the gradient of average quantities. This model contains effective parameters that connect with microscale processes. Commonly, these effective parameters must be experimentally determined for the particular porous medium being used, in order to minimize prediction inaccuracy [16]. A schematic representation of relevant length scales for describing processes taking place in porous media is given in Fig.1.2.
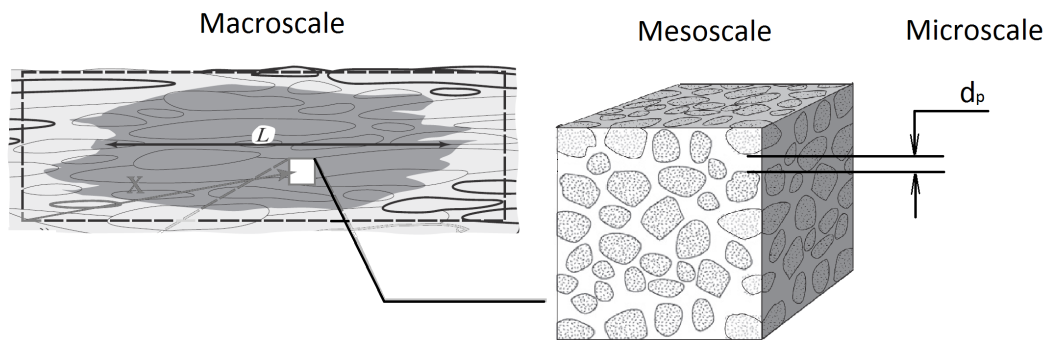
Figure 1.2: Length scales in a porous reactor. (Left) Macroscopic reactor level; (Mid) Representative elementary volume; (Right) Characteristic length of the gas phase d_p [17]

The modeling at the microscale is a recent subject of investigation not performed in earlier times due to the insufficiency of computing resources required to model the detailed geometry of porous media. Nevertheless, the modeling of a few pores is typically insufficient due to the effects of processes taking place at a larger scale, and the assumption of symmetry is commonly inaccurate. Some examples of this kind of modeling are [18, 19]. The demands on computing resources are markedly increased in the third approach, namely, the DPLS, where the complete macro-system is modeled by performing direct numerical simulations of microscale formulations. The performance of DPLS of

combustion within PIM is not yet feasible without simplifications, such as neglecting radiation effects, using global simplified reaction models or simplifying the geometry. Some of the first models of DPLS of combustion were carried out by Bedoya et al. [20] and Yamamoto et al. [21], who showed, as expected by most of the research community, that the flame structure is affected by the porous media, that is, the flame is discontinuous and corrugated. Due to these resource limitations, the numerical study of PIM combustion has been typically carried out using the volume-averaged model with experimentally determined effective parameters. Furthermore, if DPLS were accurately carried out, there is the question of how one would usefully apply such information in macroscopic modeling; a first model to include the effect of spatial temperature variations on the reaction sources is introduced in this dissertation.

Premixed combustion in a PIM is a technology extensively studied in the last two decades, with active development around the world. Numerous papers have been published, but the detailed understanding of all involved transport processes, reaction kinetics and their interactions is still limited and many potential applications have not been deeply studied yet [4, 22].

The combustion processes in PIM are classified as (i) free combustion at the bounding surface (many small free flames), (ii) surface stabilized combustion and (iii) combustion within PIM (also called buried or submerged combustion) [4].

In surface stabilized combustion, the flame is anchored at the outflow porous interface. It occurs when the flow rate is set such that the ignition temperature is reached inside the porous media along most of the cross-sectional area and the mixture burns just under the surface.

Combustion within PIM can occur in a stationary manner or transiently. In the stationary condition, that is, stabilized flame within PIM, the bulk flow velocity equals the burning velocity, which is considerably higher in this mode than in a free-burning flame or a surface stabilized flame. In transient conditions, the flame front travels along the PIM (commonly called seepage or filtration combustion). When the flame front travels in the same direction as the fluid flow, the heat feedback is higher than in the stationary condition, and since the flame front is displaced towards the burned zone, the sensible enthalpy of the solid is transferred to preheat the incoming mixture. This condition is favorable for applications such as in situ combustion for petroleum extraction and burners with reciprocating flow. This condition allows for complete combustion of ultra-lean mixtures up to an air supply that exceeds the stoichiometric air requirement by a factor of seven ($\lambda = 7$) [23, 24].

In the opposite condition, that is, flashback, the flame front travels against the flow

direction and the heat of combustion is being used to warm up the upstream cold porous media; thus, subadiabatic conditions are attained. A commonly used technique to stabilize this kind of condition in which the burning velocity exceeds the flow speed is the use of thermal quenching by inserting a porous layer with finer pores and made of a less conductive base material (called a flame trap or arrestor). In the flame arrestor, the burning velocity is considerably lower, so one could consider that this kind of burner, namely, a two-layer burner, allows for a range of burning velocities between the burning velocity in the flame trap and the burning velocity in the combustion layer. In practice, most researchers state that the burning velocity depends on the mass flow rate in two-phase burners when the flame is located in the layer interface. This technique allows for the highest power modulation or turndown ratio of up to 1:30 [3, 25]. The basic stabilization techniques available to allow for stationary flames within PIM are presented in Fig.1.3.
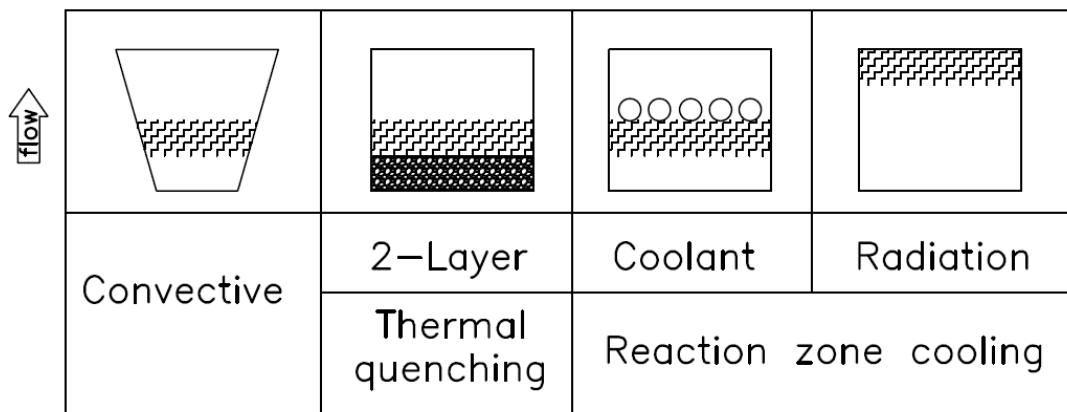
Figure 1.3: Stabilization techniques of stationary flames within PIM

Another possible stabilization technique of flames within PIM is the cooling of the reaction zone, which can be carried out by inserting cooling pipes in the reaction zone or stabilizing the flame near the outflow PIM interface with considerable heat transfer by radiation to a charge (this stabilization technique is called radiation-controlled flame). The cooling of the reaction zone decreases the preheating of the unburned mixture and allows flame stabilization with lower flow speeds than the burning velocity under adiabatic conditions. This compromise between heat transfer to a charge and input power makes this stabilization technique more complicated than that based on thermal quenching in a flame trap (two-layer burner). If a sufficiently long combustion layer is used in a two-layer burner, the reaction zone can be quasi-adiabatic and the power can be varied almost independently of the heat transfer by radiation at the outflow surface. The upper stability limit of power modulation is imposed by the burning velocity of the

porous material in the combustion zone, which is maximal under adiabatic conditions. The lower stability limit is imposed by thermal quenching in the flame arrestor. An accurate definition of the burning velocity in PIM is a cornerstone in the present study in order to validate the possibility of comparing burners with different geometries and flame stabilization techniques. The burning velocity is a measure of the fuel consumption rate, which implies that the specific firing rate ($\dot{W}/A_{pim}$) of a burner can be expressed in terms of the burning velocity S with direct proportionality, thus it has practical relevance for direct use in engineering.

$$\dot{W}/A_{pim} = S \cdot \rho_u \frac{H_l}{1 + AFR} \tag{1.1}$$

Where $\dot{W}$ is the installed power, A_{pim} is the area of the burner channel (solid and gas), H_l is the lower heating value per mass unit of fuel and AFR is the air-to-fuel ratio given in mass.

One of the potential applications of porous burners is the replacement of the diffusion flames used in pilot burners of modern stationary gas turbines. These engines operate with internal combustion at elevated pressure. The replacement of the diffusion pilot flame by a porous burner requires the knowledge about the burning velocity in PIM at elevated pressure, but there is a complete absence in literature of values of this parameter. Additionally, there is not a unified definition of burning velocity in PIM. These two issues mainly motivated the present work, where a test rig was developed to allow combustion up to 20 bar in a conical sponge-like medium and numerical modeling was used to study this process at elevated pressure as well.

The present work focuses exclusively on adiabatic flame stabilization within a homogeneous PIM of lean premixed air-gaseous hydrocarbons. Numerically, adiabatic conditions are easy to impose at the boundaries. In contrast, in experiments, the adiabaticity of the used system has to be validated.

Experimental determination of the burning velocity in the combustion layer of a two-layer burner is excessively time-consuming due to the presence of the solid porous matrix with high heat capacity. Therefore, the flame stabilization technique used in the present work is based on the continuous decrease in the flow speed by the increase of the cross-sectional area of a homogeneous solely PIM layer in the porous burner, with the expectation that the accurate determination of the burning velocity is enabled by acquiring the flame position with thermocouples.

The present work has been accompanied by a parallel work in our institute by Parthasarathy et al. [26–28], who determined effective coefficients of transport in solid sponges by per-

forming different kinds of DPLS on reconstructed real samples of ceramic sponges.

The model used in the present work to simulate the flame stabilization within PIM is based on volume averaging, which is well known in the literature [15]. A limitation of the model has been identified and a possible solution using observations of DPLS has been proposed and validated.

The PIM used in the present work were solid sponge-like structures made of SiSiC with 87% porosity. Two different pore densities were studied at 10 pores per inch (PPI) and 20 PPI. Finally, the obtained experimental results were used to propose a semi-empirical model for burner dimensioning based on modified Peclet numbers. The numerical results have been used to propose a simplified thermal theory based on local thermal equilibrium to determine roughly the burning velocity and the flame thickness. Relevant concluding remarks about the importance of the basic processes are also provided.

1.2 Objectives

The present work has as its main objectives

1. the basic study of processes occurring in premixed flame stabilization of lean air-gaseous hydrocarbon mixtures within PIM under adiabatic conditions and

2. the performing of experiments at elevated pressure.

Specifically, the global parameters such as maximum local temperature, lean flame stability limit, burning velocity and flame thickness are intended to be experimentally determined at different pressure levels, initial temperature and air-to-fuel ratios using porous media with different pore densities, in order to generate a database of crucial importance for achieving the first objective.

The accuracy and further development of a one-dimensional numerical model are to be identified in order to produce more detailed results for the basic understanding of combustion processes within PIM. From both kinds of methods, namely, experimental and numerical, the goals in this work are to establish optimization strategies of porous burners and to generate dimensioning tools of porous burners as practical results for engineering uses.

1.3   Thesis outline

In the foregoing sections, some of the most relevant investigations available are described systematically, ordered by the basic transport processes studied, in order to describe the physics behind each of the processes relevant to the flame stabilization within PIM. In Chapter 3, the used experimental set-up and the employed measuring techniques are described. The experimental results are presented in Chapter 4. In this chapter, a vast database of burning velocity values is presented, where clear tendencies of the effects of mass flow rate, pressure, initial temperature and air-to-fuel ratio are identified. Some relevant results of the macroscopic thermal flame thickness were also produced. The lean blow-off limit of the used flame stabilization technique was observed and the results are discussed and compared with the free combustion mode. A semi-empirical model based on Peclet numbers is proposed to determine the burning velocity in PIM based on the laminar burning velocity of free flames.

The numerical investigation of the flame stabilization within PIM is presented in Chapter 5, where three models are described and their results are presented, namely, the direct chemistry model (DCM), the tabulated chemistry model (TCM) and the so-called PIM-PDF model. The PIM PDF model includes the consideration of temperature deviations along the cross-sectional area as a modification of the first used model, that is, the direct chemistry model, to improve the accuracy of results. Since the PIM PDF model required more efficient use of computer resources, the tabulation of chemistry was used and validated. A parametric study is presented, which indicates the importance of the transport mechanisms in the flame stabilization within PIM, and allows identification of burner optimization strategies.

A simplified theoretical model of flame stabilization within PIM is described and validated in Chapter 6. This model enables rough estimation of the burning velocity and flame thickness based on the laminar burning velocity and using the average ignition temperature observed in the numerical result of the PIM PDF model. At the end of the thesis a discussion of the main results in a kind of summary is presented in Chapter 7.

Chapter 2

Theoretical background and literature review

In order to provide an overview of fundamental concepts related to the processes taking place in premixed-flame stabilization of gaseous hydrocarbons within solid sponges, several areas of knowledge are briefly reviewed, such as premixed laminar free flames and transport processes in solid sponges. The outline of this chapter is as follows. First, some basic definitions for combustion technology are given, with an emphasis on premixed laminar flames, which are one focus of this work, but submerged in a three-dimensional porous structure.

For the topic of flame stabilization within solid sponges, an overview of the processes that occur is briefly given as an introduction to the coming sections. After explaining the most relevant issues of morphological characterization of solid sponges, a brief description of modeling of flow and transport processes in porous media is given as an introduction to the topics of fluid flow (Section 2.5) and transport in sponges itself (Section 2.6). In these sections, emphasis is placed on the effective coefficients of transport processes in solid sponges required in volume-averaged models, such as the one used here in Chapter 5, to simulate the flame stabilization within these structures. In the present overview of the literature, some of the few studies of transport at the pore level are stressed, as a promising research area due to the difficulty of accessibility of experimental probes and optical techniques and the high demand for computing resources in numerical studies. This chapter finishes with an overview of some of the most relevant studies of flame stabilization in PIM of premixed gaseous fuels.

2.1   Combustion-related definitions

In this section, some basic definitions and parameters of combustion processes of premixed hydrocarbons with air excess are reviewed. For more generalized situations and detailed understanding of any of these subjects, refer to any book on combustion, such as [29–31].

Under the assumption that dissociation does not occur during combustion, the global mass balance of combustion of hydrocarbons C_nH_m with air under air excess reads

$$C_mH_n + \lambda \cdot \nu_{O2,st}\left(O_2 + 3.76\ N_2\right) \rightarrow$$
$$m\ CO_2 + \frac{n}{4}H_2O + \underbrace{(\lambda-1)\nu_{O2,st}\ O_2}_{O_2\ excess} + \lambda \cdot \nu_{O2,st} \cdot 3.76\ N_2 \qquad (2.1)$$
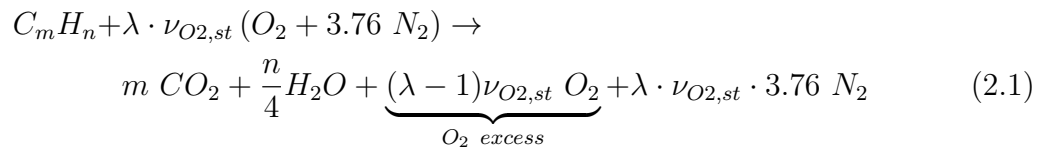
where

$$\nu_{O2,st} = m + \frac{n}{4} \qquad (2.2)$$

is defined as the oxygen mole requirement for stoichiometric combustion of a mole of fuel. Since oxygen is taken from air, the air mole requirement per fuel mole is

$$l_{min} = \nu_{O2,st}\left(1 + 79/21\right) \qquad (2.3)$$

The air factor λ is the ratio between the supplied air l and the required air per fuel unit l_{min} (see Eq.2.4). The air factor is higher than unity for air excess operation, that is, lean conditions.

$$\lambda = \frac{l}{l_{min}} \qquad (2.4)$$

Internationally, the use of the inverse of the air factor is also accepted, which is called the equivalence ratio $\phi = 1/\lambda$.

Consider an isobar reacting system described by Eq.(2.1), where premixed unburned mixture flows in and combustion products flow out. The adiabatic combustion temperature T_{ad} can be determined by performing an energy balance around this reacting system without heat losses, that is, sensible enthalpy fluxes through boundaries and the reaction enthalpy in the system ($\dot{m}_f \cdot \Delta H_R$). Thus, the temperature of unburned reactants has a positive effect on the adiabatic combustion temperature, while the effect of the increase of the air excess is the opposite because the reaction enthalpy is converted to sensible enthalpy in the excess air. In contrast, pressure has an inconsiderable effect on T_{ad} at elevated pressure levels where dissociation of intermediate species is smaller, thus T_{ad} slightly increases [30].

Most combustion systems reach temperatures appreciably higher than 1250 K and dissociation of stable species occurs by several elementary reactions, such as chain-branching reactions of O_2 and H_2 to produce O, H and OH, which are essential steps to sustain the fast reaction mechanism. Since dissociation reactions are quite endothermic, little dissociation considerably lowers the adiabatic combustion temperature [30].

A detailed chemical kinetic mechanism of realistic fuels to describe the chemical reaction processes involves a large number of species and reactions (several hundred). The solution of a chemical kinetic problem requires solution of the species balance equation for each of the species of the mechanism. In order to reduce computational time, simplified mechanisms have been proposed derived by different approaches, which retain only essential features [32].

The rate at which a kth reaction takes place might be expressed in terms of the rate of decrease of concentration of any of the reactants. The mass action law states

$$\dot{r}_k = k_k \prod_{i=1}^{N_{i,k}} [X_i]^{\nu'_i} \tag{2.5}$$

where ν'_i is the stoichiometric coefficient of the ith reactant, $[X]$ is mole density (mol/m^3), $N_{i,k}$ is the number of reactants in the kth reaction, which signifies the overall reaction order, and k_k is the specific reaction rate coefficient, which can be described using a modified form of the Arrhenius equation

$$k_k = A_k \cdot T^\beta \exp\left[\frac{-E_a}{T \cdot R}\right] \tag{2.6}$$

with E_a as the activation energy, A_k the kinetic collision frequency, which limits the reaction rate for reactions with very low activation energy, and T^β accounting for pre-exponential temperature-dependent terms.

The rate of decrease of the concentration of a reactant in a system with a single reaction can be expressed as

$$\dot{\omega}_{i,k} = (\nu''_i - \nu'_i) \cdot \dot{r}_k \tag{2.7}$$

where ν''_i is the stoichiometric coefficient of the ith species in the products.

2.2   Premixed combustion

The case of laminar free flames is used as a relevant basis to define combustion parameters, which could be defined analogously to the flame stabilization within PIM.

2.2.1   Laminar free premixed flames

Consider premixed gases flowing through an adiabatic tube in a laminar regime with a plug flow profile. With an ignition source, a flame front appears as depicted in Fig.2.1 with a planar shape. The flame is undisturbed and without heat loss and buoyancy. The flame can be considered like a wave with propagation velocity S_l, which is called the laminar burning velocity and is defined as $S_l = u_u$, if the wave is fixed with respect to the tube.
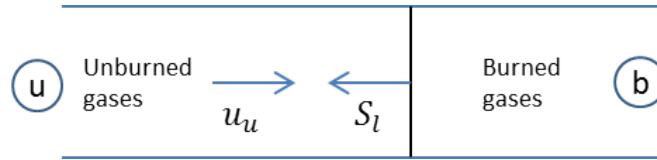
Figure 2.1: A combustion wave fixed with respect to a tube.

The flame front designated in Fig.2.1 represents the premixed gases before they enter the luminous zone where reaction and heat release take place. The luminous zone is less than 1 mm thick and is a portion of the reaction zone. The flame front can be characterized by three zones: a preheating zone, a reaction zone and a recombination zone. In the preheating zone, pyrolysis of fuel could occur, but this is not the case with fuels with stable molecules like methane; thus, this region could be assumed as inert and only diffusion of species and heat conduction from the reaction zone occur. The fast oxidation steps occur in the reaction zone, which begins at an activation temperature T^0 (methane $T^0 \approx 1300\ K$) [33]. Downstream, much slower recombination reactions occur in the recombination zone, which is a more extended region.

Fig.2.2 depicts the temperature profile along the flame front with unburned gases at $T_u = 300$ K. At the reaction zone, the temperature rises exponentially and approaches the adiabatic combustion temperature just past the reaction zone. Performing an enthalpy balance around the preheating zone (with thickness δ_p), it is determined that the enthalpy increase of the unburned gases must be equal to the heat conducted from the reaction zone, which is the basis of the classic thermal theory of Mallard and Le Chatelier [34], assuming a linear temperature profile with slope $(T_b - T^0)/\delta_R$, where δ_R

is the thickness of the reaction zone.

$$\rho_u \cdot S_l \cdot \bar{c}_p (T^0 - T_u) = \lambda(T^0)(T_b - T^0)/\delta_R \tag{2.8}$$

or

$$S_l = \frac{\lambda(T^0)}{\rho_u \cdot \bar{c}_p} \frac{(T_b - T^0)}{(T^0 - T_u)} \cdot \frac{1}{\delta_R} \tag{2.9}$$
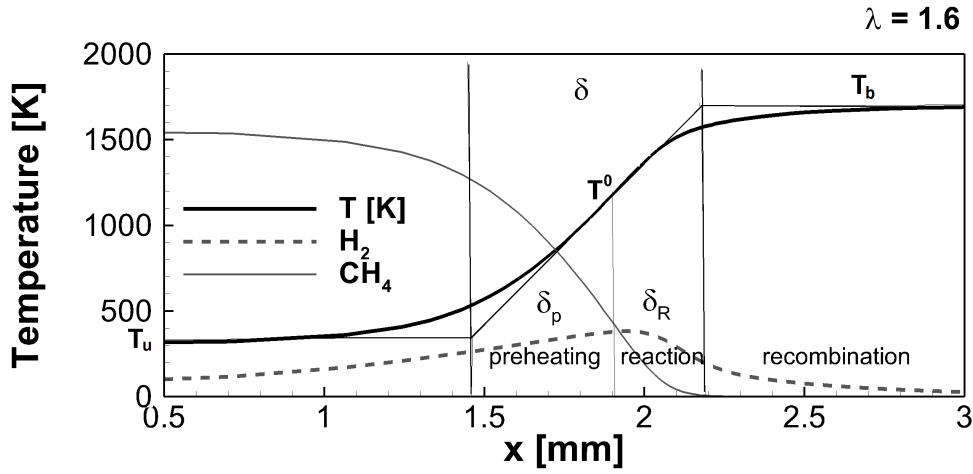
Figure 2.2: Temperature profile of a laminar planar flame of lean air-methane.

The reaction zone thickness is related to the laminar burning velocity

$$\delta_R = S_l \cdot \frac{T^0}{T_u} \cdot \tau_c \tag{2.10}$$

by the heat release time τ_c, which yields the most significant result of the thermal theory

$$S_l \propto \left(\frac{\lambda(T^0)}{\rho_u \cdot \bar{c}_p} \frac{1}{\tau_c} \right)^{0.5} \tag{2.11}$$

and with

$$\delta_R \propto \frac{\lambda(T^0)}{\rho_u \cdot \bar{c}_p} \frac{1}{S_l} \tag{2.12}$$

The heat release time is affected primarily by the reaction rate $\tau_c \propto \dot{r}^{-1}$, which is dominated by the exponential of temperature, Eq.(2.6). Assuming that the heat release occurs close to the maximum temperature, Eq.(2.11) permits establishment of the trend of the burning velocity as the combustion temperature T_{ad} changes (see Eq.(2.13)); that is, an increase of temperature of unburned mixture and a decrease of the air factor will

have a positive effect on the laminar burning velocity.

$$S_l \propto (\exp(-E_a/R \cdot T_{ad}))^{0.5} \tag{2.13}$$

More elaborate theories were subsequently developed, which also include the diffusion of molecules, for example, [35, 36], but all of them coincide in that the laminar flame propagation is a diffusional mechanism, namely, dominated by the conduction of heat and the diffusion of mass, since reaction-activating radicals must diffuse from the reaction zone into the preheating zone to sustain the combustion wave [30]. These theories give a fairly good fit of experimental results. Peters and Williams [37] calculated the values of the activation temperature T^0 at which reactions are initiated as a function of the air factor and pressure, and found that it is independent of the initial temperature.

Modern computational approaches allow calculation of S_l and profiles of temperature and species concentrations, whose accuracy depends on the used database of thermo-chemical and kinetic data. The numerical code PREMIX given by Kee et al. [38] was used to simulate freely propagating, one-dimensional, adiabatic premixed flames. The used data are given in [39, 40]. The used detailed reaction mechanism of methane with air is GRI 3.0 [41]. Results of a simulation with $T_u = 300$ K and $\lambda = 1.6$ are presented in Fig.2.2. Schmid [42] used this numerical set-up to generate a database of laminar burning velocities, which fit in its modified form of Eq.(2.11) as

$$S_l = c \left(\frac{\lambda(T_u)}{\rho_u \cdot c_{p,u}} \frac{1}{\tau_c} \right)^{0.5} \tag{2.14}$$

defining the thermal diffusivity under unburned conditions $a_u = (\lambda/(\rho \cdot c_p))_u$ and the heat release time as the minimum local heat release time:

$$\tau_c = \min(T \cdot (\partial T/\partial t)^{-1}) \tag{2.15}$$

The obtained value of the factor c lies around one. For methane-air premixed flames, c lies between 1.0 and 1.2. For other fuels, it differs by a factor of less than two [42].

The laminar burning velocity of hydrocarbons decreases with pressure. In the case of methane-air mixtures, the relationship is approximately $S_l \propto p^{-0.5}$ [43–45]; therefore, from Eq.(2.11), it might be inferred that τ_c is nearly independent of pressure.

Numerical results of laminar burning velocity of lean methane-air flames are presented in Fig.2.3 as a function of pressure for different air factors. The exponent b of the pressure

dependence of the laminar burning velocity

$$S_l \propto p^b \tag{2.16}$$

was calculated at different pressure levels p_j in [46] as

$$b(p_j) = \frac{\log S_l(p_{j+1}) - \log S_l(p_{j-1})}{\log p_{j+1} - \log p_{j-1}} \tag{2.17}$$

A fit of the obtained results is presented in Fig.2.4. It is observed that the value of the pressure exponent in the dependence of S_l differs from -0.5; in fact, it varies considerably with pressure and with the air factor. Although the used reaction mechanism is sufficiently detailed, it cannot be validated with experimental results for lean mixtures because flames are not stable, due to the decrease of the flame thickness with pressure (which can be deduced from Eq.(2.12)), which makes the flame sensible to any disturbance [43–45, 47]. For example, Rozenchan et al. [47] have validated the GRI 3.0 reaction mechanism at a leanest λ= 1.43 for pressures up to 10 bar.

In contrast to the fairly good demonstration of the capability of the classical theories to predict the laminar burning velocity, for example, [48], in the case of the flame thickness, there is a complication to determine it experimentally. A commonly used definition is based on a linear temperature profile that spans the steepest tangent to the temperature profile between T_u and T_{max} (T_{max} corresponds to T_{ad} for free flames), the so-called thermal flame thickness Eq.(2.18).

$$\delta = (T_{max} - T_u)/\max(\partial T/\partial x) \tag{2.18}$$

From numerical simulations using the above-mentioned set-up, the following link between this definition and the classic thermal theory, see Eq.(2.12), was found as

$$\delta = c \cdot \frac{\lambda(T_{ad})}{\rho_u \cdot c_{p,u}} \frac{1}{S_l} \tag{2.19}$$

with c between 1.10 and 1.23 for methane [49]. A more precise link between this thermal flame thickness δ and the classical definition of the flame thickness was achieved by Goettgens et al. [33] with the following relationship

$$\delta = c \cdot \frac{\lambda(T^0)}{\rho_u \cdot c_p(T^0)} \frac{1}{S_l} \cdot \frac{T_{ad} - T_u}{T^0 - T_u} \tag{2.20}$$
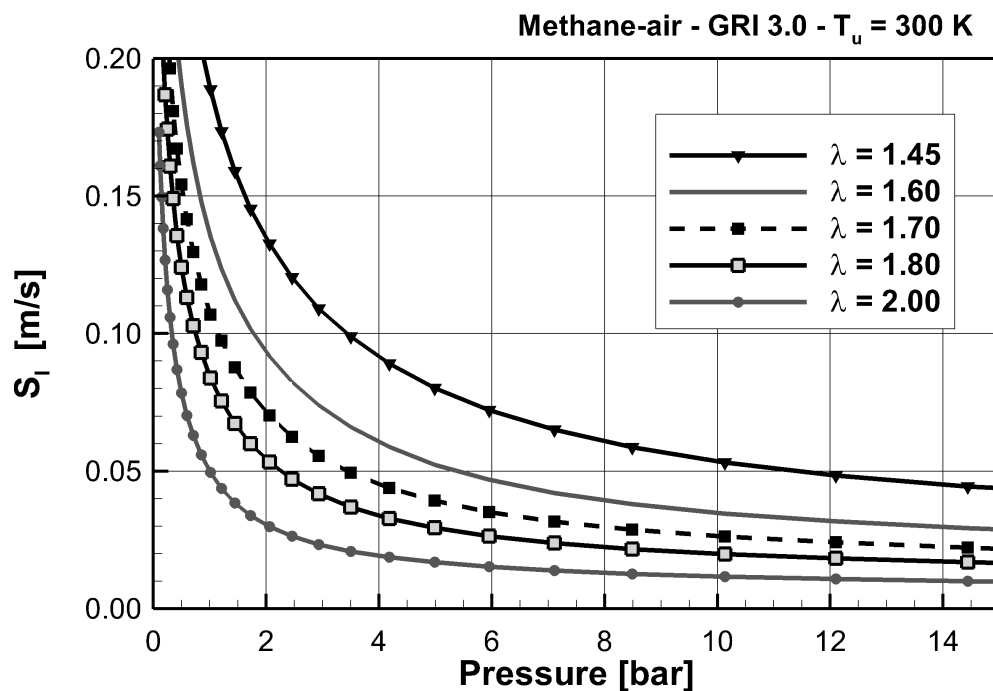
Figure 2.3: Simulated burning velocity of laminar free flames of methane-air mixtures, T_u= 300 K [46].
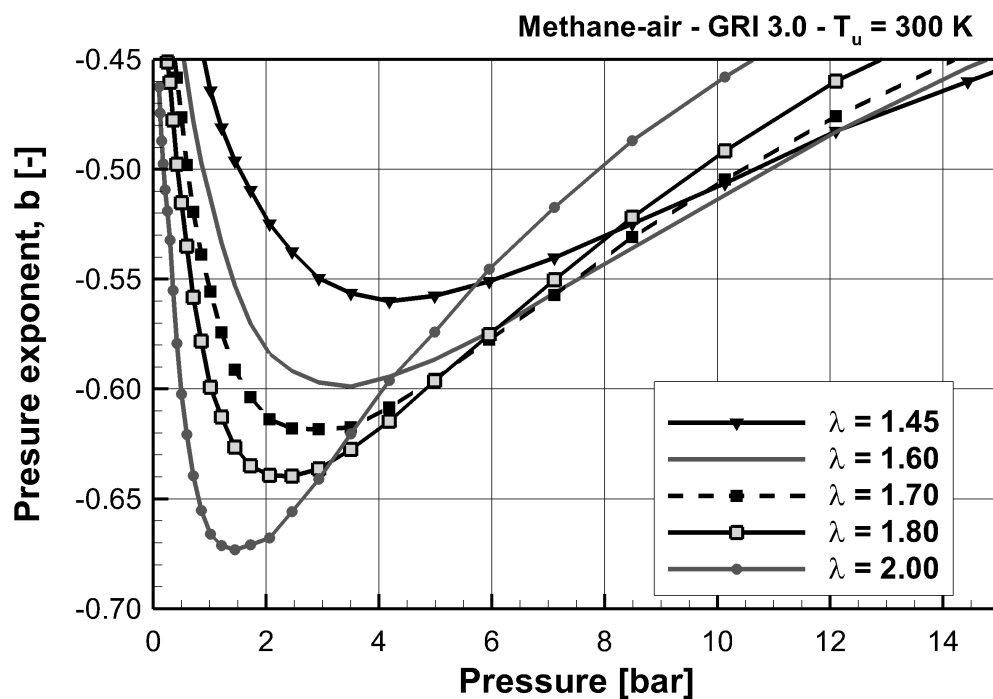

Figure 2.4: Fitted exponent b of pressure influence on the laminar burning velocity, methane-air, T_u= 300 K [46].

where the value of c ranges between 0.994 and 1.179 for hydrocarbons and for methane $c = 0.994$. Note that this model requires knowledge of the activation temperature T^0; thus, the previous definition Eq.(2.19) is simpler but less accurate. In contrast, the link for the burning velocity with the numerically obtained τ_c fits better, defining the thermal conductivity under unburned conditions (Eq.(2.14)).

Other parameters in premixed flames that are important in the present work are related to the stability of the combustion wave: the lean flammability limit, the quenching radius and the flame stability.

Lean flammability limit

The lean flammability limit is defined as the leanest mixture that is capable of sustaining the flame propagation in the absence of adjacent walls. The effect of pressure and temperature on this parameter depends of the fuel kind, but for methane and most of hydrocarbons, it is nearly independent of pressure and is extended with the increase of temperature of unburned mixture. For methane-air mixtures at $T_u = 300\ K$, the lean flammability limit lies at 5%Vol of fuel, that is, at an air factor of $\lambda = 2.0$ [50].

Quenching radius

The quenching radius L^0 is the minimum radius of a tube through which the flame can propagate. The heat loss to a wall and radical quenching at the wall reduce the reaction rate, so that it cannot sustain the flame in a confined situation [30]. As a result, confined spaces can serve as effective flame traps for the safety against flashback. Since the wall material affects the destruction rate of active species, an analytical determination of the quenching radius is not feasible. Thermal theories compare well with experimental data, for example, the proportionality with the flame thickness $L^0 \approx 0.7 \cdot \delta$ [51]; thus, L^0 depends on fuel type ($L^0_{CH4} \approx 0.65mm$), pressure ($\propto 1/p$) and initial temperature ($\propto 1/T_u^{0.9}$) [52, 53]. Recent investigations show that, for a tube radius below $\approx 1\ mm$, the radical quenching dominates above the thermal quenching; hence, the wall temperature, wall thermal conductivity and adsorptivity of species on the wall play important roles [54]. For example, for walls at 1300 K, combustion can take place in channels with a minimum diameter of 0.8 mm for stainless steel, 0.3 mm for alumina and 0.05 mm for cordierite [55].

Flame stability

The flame stability is related to the limitations of stabilizing a flame in an actual experimental situation. A common example is the stability of a laminar premixed flame at a tube exit, that is, the Bunsen burner, where flame stability is attained if the gas velocity at the ignition point $u(L^0)$ (near the burner rim) equals the laminar burning velocity, as a condition to anchore the flame at the burner rim, see Fig.2.5.

$$u(L^0) = S_l \tag{2.21}$$
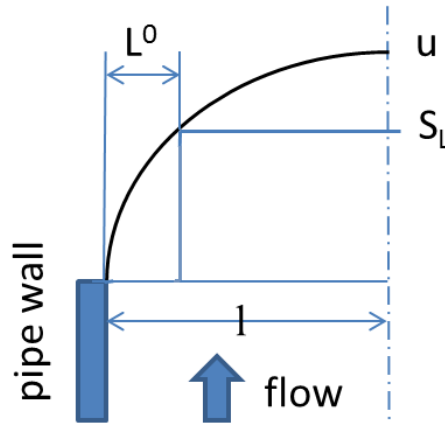
Figure 2.5: Sketch of velocities at burner rim for an attached laminar premixed flame.

The velocity of unburned mixture u is higher than the laminar burning velocity at the other points towards the tube center. At the anchoring point, the value of $u(L^0)$ depends on the ignition location L^0 and the velocity gradient near the burner rim g. The ignition of the mixture does not occur at the burner rim due to the heat losses through the solid material, that is, the flame is quenched near the wall. The quenching radius L^0 is proportional to the flame thickness δ, which in turn can be related to the laminar burning velocity

$$L^0 \propto \delta \propto a_m/S_l \tag{2.22}$$

The velocity gradient g in a laminar stream is linearly proportional to the mean discharge velocity $\bar{u}_0$ and the size of the pipe,

$$g \propto \bar{u}_0/l \tag{2.23}$$

assuming that the velocity gradient is constant near the wall

$$g = u(L^0)/L^0 \tag{2.24}$$

From the last two relationships, it is shown that the velocity at the ignition point can be related to the mean discharge velocity

$$\frac{\bar{u}_0}{l} \propto \frac{u(L^0)}{L^0} \tag{2.25}$$

with Eq.(2.22) and Eq.(2.21), it becomes

$$\bar{u}_0 \propto \frac{S_l^2 \cdot l}{a_m} \tag{2.26}$$

or

$$Pe \propto Pe_{lam}^2 \tag{2.27}$$

where $Pe = \bar{u}_0 \cdot l/a_m$, $Pe_{lam} = S_l \cdot l/a_m$ and d is the burner diameter. This kind of Peclet criterium of flame stabilization has been demonstrated for other burner configurations with the form

$$Pe = C \cdot Pe_{lam}^m \tag{2.28}$$

where C and m depend on the used burner geometry. This model is useful for scaling of burners or for operation with another fuel or changing the air-to-fuel ratio. One of the aims of the present work is to provide a similar tool for porous burners.

2.2.2 Premixed-flame stabilization within PIM: physics overview

Premixed combustion in PIM, in comparison with free laminar flames, features considerably high burning velocities S, low pollutant emissions, high radiant heating rates and increased heat transfer due to dispersion in the gas phase, solid conduction and solid-solid radiation. These features strongly support the use of porous burners as a potential alternative to conventional free flame burners. The process of understanding the physics behind the combustion phenomenon in PIM is challenging due to problems with optical accessibility, the complexity of the phenomena involved and the randomness of PIM. Therefore, continuous research is necessary in the areas of fluid mechanics and heat transfer within PIM and PIM property data [12].

The increased local reaction rate of combustion in PIM leads to extension of the lean stability limit and to higher area-specific loads. Therefore, it is possible to increase
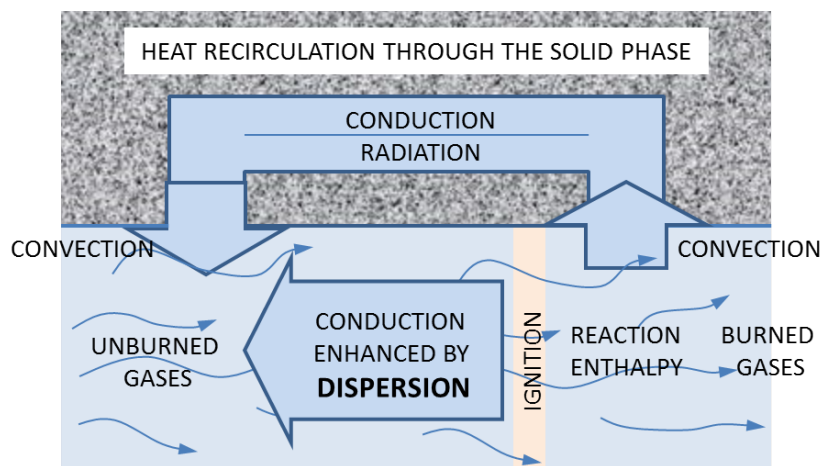
Figure 2.6: Sketch of coupling heat transport mechanisms in combustion within PIM.

the input power, to burn lean mixtures or low-grade fuels and to generate directly
the products at a temperature acceptable to the machinery downstream. Additionally,
owing to the solid material properties, high rates of thermal radiation are emitted, so it
is meaningful to use this kind of burner for industrial processes utilizing radiant heating
[9, 12–14].

State-of-the-art studies on combustion in PIM [56, 57] indicate that the phenomena
occurring in PIM combustion that are responsible for the above-mentioned features are
heat recirculation and hydrodynamic dispersion. A rough coupling scheme of these
transport processes around the macroscopic flame region is proposed in Fig.2.6, which
illustrates in a quite simplified way the strong interactions of reactions with transport
processes.

Since the thermal transport properties of solid matter are several orders of magnitude
higher than those of gas under atmospheric conditions, a considerable amount of sensi-
ble heat from the hot burned gas is transferred upstream by conduction and solid-solid
radiation through the PIM, preheating the incoming unburned gas. The local tempera-
ture in unburned gases increases and the combustion temperature achieved locally may
reach higher values than without this kind of preheating.

The hydrodynamic dispersion enhances both mass and heat transport in the gas phase,
owing to transverse mixing along tortuous flow paths imposed by the random geometry
of porous media. Thus, the effective coefficient of dispersion is around two orders of
magnitude higher than the molecular diffusivity under atmospheric conditions of both
species and heat. This augments the species transport and the macroscopic heating rate
of incoming unburned gas substantially in comparison with an empty pipe flow, which
leads to a flattening of the macroscopic flame thickness and a higher total conversion

rate.

Owing to these two transport paths, namely, heat recirculation and dispersion, the total heat release rate, that is, the burning velocity S, is increased according to the effective transport properties in PIM, which represents at the macroscopic scale the effects of the microscopic interactions.

The use of ceramic sponges as a flame stabilizer has several advantages over the use of other kinds of porous media. While the high void fraction of solid sponges enhances the radiation heat transfer, the continuous strut network allows for enhanced heat conduction [58]. The interface surface area is considerably larger than that of packed beds, so the thermal communication between phases is very effective. Additionally, these structures impose highly tortuous flow paths, which allow for a higher degree of mixing.

2.3   Morphological characterization of solid sponges

The use of solid sponges in process engineering applications that has appeared in the two last decades seems very interesting due to several advantages over the use of packed particles or pebbles because of the higher porosity. Their monolithic construction allows for higher flexibility of reactor design, as well as allowing for higher conduction of heat. In comparison to honeycombs, solid sponges allow for flow in all directions, which offers a high degree of mixing that is beneficial for process intensification [59, 60]. The spectrum of applications of solid sponges is quite broad, including their use as static mixers, filters of liquid metal, filters of flue gases, catalyst carriers, solar receivers, packing in columns, heat exchangers and porous burners [61].

There have been few descriptions of transport phenomena in such commercially available structures owing to the geometrical complexity and random orientation of struts, which cannot be described with nominal macroscopic parameters such as the porosity and pore density. Therefore, their morphology must be statistically characterized, as was carried out by Grosse et al. [7], who modeled and measured the sponges used in the present work, among others, with different materials and structural parameters [7].

Solid sponges are cellular structures with open cells, which consist of a continuous network of solid struts. There are several manufacturing processes available that determine the morphology of a sponge. Direct foaming, void molding and replication are the most frequently applied manufacturing techniques [62]. The sponges used in the present work were produced by the replication technique, which consists of a coating procedure above a polymeric precursor, also called green body, by immersion in a ceramic suspension.

After the excess suspension is removed, the ceramic material is dried and bounded by sintering; thus, the green body is burned and there are hollow channels along the center of the struts left by the green body, which negatively affect the mechanical behavior and heat conduction properties of the sponge.

Several sponge materials have been studied to support combustion in solid sponges, typically cordierite, Al_2O_3, ZrO_2, SiSiC and $FeCrAl$, listed in ascending order of thermal conductivity [63]. Some of the combustion properties of these sponge-shaped materials were experimentally determined and compared by Djordjevic et al. [15] and Gao et al. [64]. An excellent discussion about cellular material assessment for combustion applications based on their mechanical properties and chemical stability at elevated temperature was presented by Fussel et al. [63], where SiSiC appears as the most promising material for this application because of its outstanding resistance to thermal shock, high thermal conductivity and good resistance to chemical attacks at high temperatures [63]. A protective silica layer is formed on this material, which is the reason for the high temperature/corrosion resistance. For temperatures below 1700 K, passive oxidation rates tend to zero in oxidant atmospheres [65] and its mechanical stiffness stays almost unchanged after operation aging [66].

Solid sponge structures are commonly described as follows. The interconnecting **struts** have a triangular or cylindrical cross section (triangular for SiSiC). The struts are connected by **nodes**, where four struts frequently meet (connectivity ≈ 4). **Cells** are polyhedral with 12 to 14 reticulated faces. Two adjacent cells are bounded by a window. **Windows**, more practically called **pores**, are commonly pentagons. The terms marked in bold are the attributes commonly used to describe the sponge morphology, as seen in Fig.2.7.

Since solid sponge morphology is difficult to determine, macroscopic parameters are regularly used to characterize these geometries, such as base material, porosity and pore density (for example pores per linear inch (PPI)). However, in contrast to packed beds, where the particle size is related very precisely to the characteristic sizes in the void using geometrical models, the structure of solid sponges is randomly oriented and cannot be easily modeled [67].

The porosity ε is the void-to-total-volume ratio; it consists of the sum of the open and closed porosity, where the open porosity allows for fluid flow and the closed porosity is the material micro-porosity. In the case of replicated sponges, there are also void channels in struts that counts as closed porosity. The porosity of ceramic sponges ranges between 75 and 90%, while in metal sponges, it ranges from 90% to 98%. Assuming isotropic media, the porosity can be considered the same as the ratio of interstitial cross-sectional
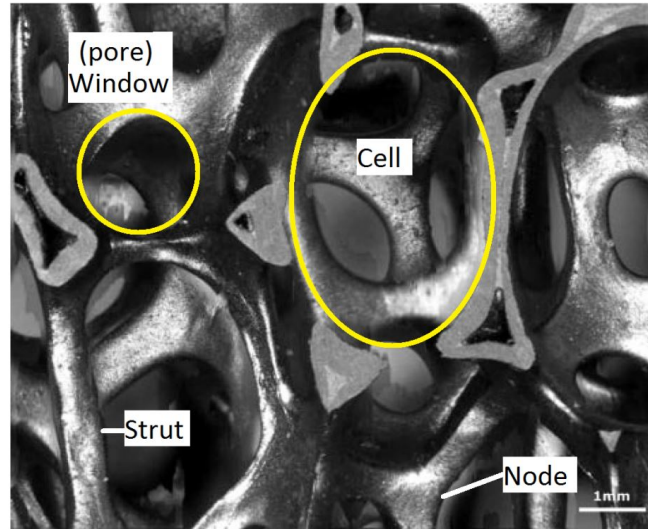
Figure 2.7: Sponge morphological parameters, for example: SiSiC 10 PPI 87% porosity, photo taken from [66]

area A_g to the superficial area A_{pim}.

The pore density is commonly referred to as PPI. However, since the concept of a pore is not well defined in solid sponges, this parameter is insufficient. A more representative size to characterize the sponge could be the window diameter. Grosse et al. [7] found that these kinds of solid sponge exhibit a preferential orientation resulting in cells of ellipsoidal rather than spherical shape and the anisotropy increasing with the pore size. Thus, depending on the direction of the experimental cut, small, medium-sized or large windows can be observed. A statistically averaged window diameter was reported as representative of the characteristic length d_p, which is referred to in this work as the pore diameter. The obtained d_p are approximated to $1/PPI$ with a deviation of 20%.

The manufacture of solid sponges is generally based on foaming processes, which consist of gas cells in a liquid medium separated by thin films with open faces pressed together to form polyhedra with curved faces. These structures tend to form the ideal model of the Kelvin structure, which has the most energetically favorable shape of a single cell in a network. However, depending on the manufacturing process, they are subjected to forces due to viscosity and hydrodynamic pressure gradients, and in the case of replicated structures, they are squeezed with rollers to remove excess base material. This leads to anisotropy, numerous closed windows and connected solid areas and differences of strut shapes [7].

The strut diameter t is defined as the thickness at the middle of the strut, which is usually the thinnest part between nodes. For sponges with the same nominal porosity and pore density and different base material, the strut shape can differ considerably (see

Fig.2.8).The strut shape for Al_2O_3 is cylindrical and $t = 0.81$ mm, while for SiSiC it is triangular and considerably thinner at the middle ($t = 0.69$ mm) than near the nodes.
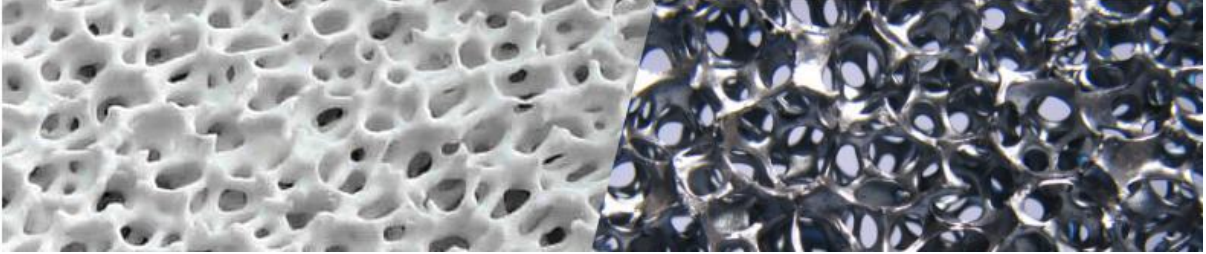

Figure 2.8: Photograph of (Left) Al_2O_3 and (Right) SiSiC sponges ($\varepsilon = 0.87$, 10 PPI)[68].

The volumetric surface area S_v is the interface surface area per unit volume. It is not easy to determine and the manufacturers do not usually provide it. A correlation of S_v as a function of porosity and d_p, which can be more easily measured, was found by [7] for reproduced 3D images of micro-computer tomography μ-CT of real sponge samples and modeled structures. The correlation based on tomographic data is presented in Eq.(2.29), which presents the same form as found for the structure model given by Phelan and Weaire [69] with adapted coefficients.

$$S_v = (4.84 \cdot (1 - \varepsilon)^{0.5} - 2.64(1 - \varepsilon))/(d_p + t) \tag{2.29}$$

Numerous models have been used to analyze sponge properties, such as mechanical, fluid dynamic and heat transfer properties. Nevertheless, they appear either complicated or inaccurate when comparing them with experimental results or results from reproduced sponge samples obtained by tomography. Some of those models are given in [67, 70–74]. These issues have been attributed to randomly driven parameters, such as anisotropy [7].

To avoid inaccuracy in the investigation of commercially available solid sponges due to the random nature of their geometry imposed by the manufacturing process, von Rohr and coworkers have developed designed sponges manufactured by selective laser sintering in order to study more precisely the effect of morphological parameters on flow and heat transfer processes [75–77]. The designed sponges consist of periodic tetrahedral overlapping spherical cells, as shown in Fig.2.9. Fig.2.9 presents, from left to right, 30-PPI and 20-PPI solid sponges and a designed sponge with cells of 2.9 mm diameter. The designed sponge exhibits larger strut sections, lower flow channeling and negligible deviations of properties from sample to sample compared with the solid sponges [78].
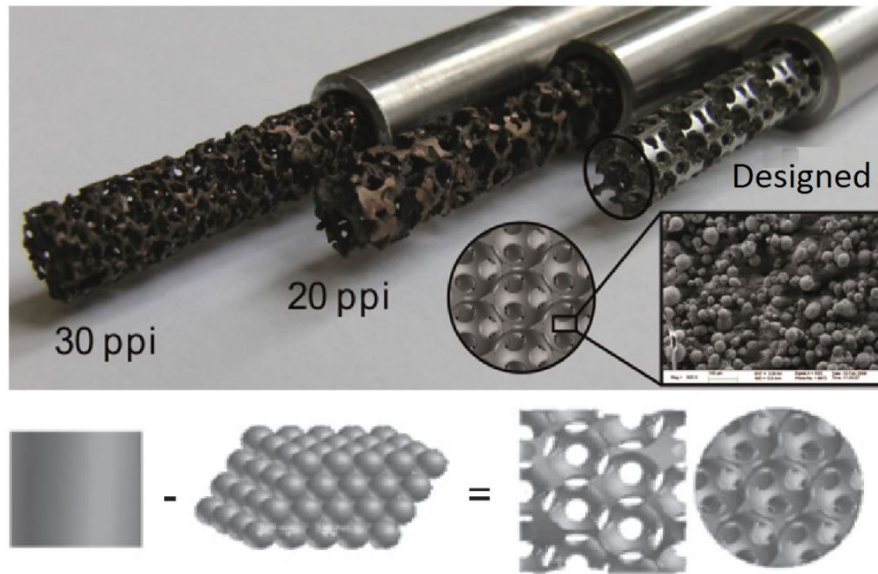
Figure 2.9: Sponges inserted in 7-mm-diameter pipe (Left) 30-PPI sponge (Mid) 20-PPI sponge (Right) Designed sponge, cell diameter 2.9 mm, [78]

2.4 Modeling of flow and transport processes in porous media

The transport phenomena in porous media have recently been modeled directly at the pore level over a large volume including numerous cells of the porous matrix, thanks to the development of enormous modern computing resources. Even the geometry of solid sponges has been taken from tomographic data of scanned structures for this kind of simulation; some examples are [20, 27, 79, 80]. These methods are still rare and very resource-demanding; therefore, the traditional volume-averaged models will remain in wide use for a long time, but the information obtained from direct pore-level simulations (DPLS) is valuable to clarify the phenomena occurring at the micro-scale level and to develop further modeling on the averaged approach.

The porous media can be considered to be hierarchical in nature or characterized by more than one length scale. Owing to these scales being disparate, the hierarchical structure can be analyzed using the volume-averaged approach, which allows for the transport of information over several length scales. That is, the integrated (averaged) quantities

$\epsilon = \frac{1}{V} \int \epsilon^* dV$

coupled with a set of proper constitutive equations representing the effects of microscopic interactions on the integrated quantities, provide an accurate and effective basis for

studying transport phenomena with and without reaction in porous media.

The volume-averaged method allows macroscopic study to be performed even for 1D domains, as the model described in Chapter 5, more simply. The volume-averaged method is derived from classical continuum physics and uses finite volumes to approach the whole reactor's behavior.

The volume-averaged models have been derived by rigorous mathematics in works such as [17, 81, 82]. In order to obtain the governing balance equations, a change in scale must be performed, as illustrated in Fig.1.2, from the meso-scale to the macro-scale, where the meso-scale is defined as a characteristic length associated with the averaging operator used to sample the micro-scale. This supporting scale should be compact in the case of the conventional volume-averaging method, where the size of the supporting volume is large enough to provide uniform distribution of parameters such as porosity. In solid sponges, the size of the edge of a representative elementary cube corresponds to at least two times the pore diameter [28].

The volume-averaged method allows the spatially smoothed balance equations to be obtained and the identification of the constraints that must be satisfied for the equations to be valid, as well as derivation of the closure problems necessary to predict the effective transport coefficients and, finally, performance of comparison between theoretical and experimental values.

The relevant mechanisms in combustion within PIM are: solid-to-solid conduction, convection between solid and gas, solid-to-solid radiation and dispersion [68]. These mechanisms are the basis for the numerical model explained in Chapter 5 and they are further explained in Section 2.5 and Section 2.6.

2.5   Fluid flow in solid sponges

2.5.1   Fluid flow at the pore level

Although there have been only few studies on fluid flow in solid sponges at the micro-scale, there have been some numerical and experimental works that provide representative observations for qualitative generalizations and specific quantitative trends.

Consider a flow which carries mass-less particles. Two adjacent particles, which diverge after impinging a solid strut, will trace random deflections in their flow paths downstream due to interactions with the solid sponge, and in turn, the stream paths diverge more. As a result, a considerable amount of momentum is transferred in the transverse

direction. The average value of the velocity component in the transverse direction is approximately 30% of the bulk superficial velocity [83]. The flow paths are longer than the straight flow field dimension by a factor of 1.3 on average (this ratio is referred to as flow tortuosity τ), but this value exhibits large fluctuations from one particle to another, that is, the standard deviation of the tortuosity and of the particle residence time reaches a value of 0.3 [67]. In general, porous media with lower porosity exhibit higher tortuosity, namely, larger dimensions of the solid struts. However, organized structures such as the one given by Kelvin exhibit a very low tortuosity value; thus, the strut arrangement plays a crucial role and, as is depicted in Fig.2.10, the pattern of particle trajectories in a flow through a solid sponge Fig.2.10.c. differs considerably from that in an organized structure (Kelvin) Fig.2.10.a. The numerical solutions of the Navier-Stokes equations of laminar flow in a randomized model structure with a proportion of closed windows of 40% Fig.2.10.b were comparable to the numerical flow results of the reproduced commercially available sponge Fig.2.10.c, that is, in terms of pressure drop, statistical distributions of tortuosity and residence time [67].
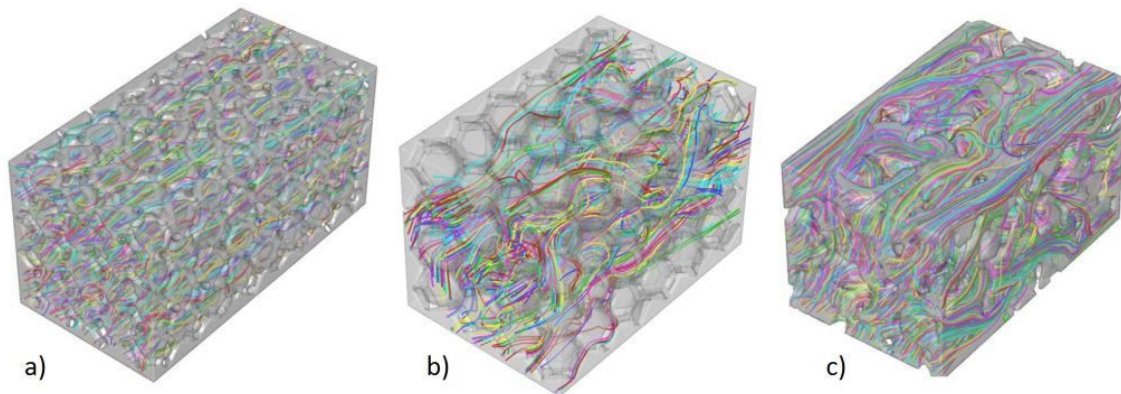
Figure 2.10: Particle trajectories of air flow through a) Kelvin structure, b) randomized Kelvin structure plus 40% closed pores and c) reconstructed sponge sample [67].

The flow in a cell being contracted by passing through a window (pore) produces a jet structure in the downstream cell, which interacts with other jets coming from adjacent pores in this cell (see Fig.2.11). The jet with the smallest angle to the bulk flow direction has the highest total momentum rate and the maximum local velocity in this jet exceeds the bulk superficial velocity[1] by a factor ranging between 2.0 and 2.5 (see Fig.2.12), depending on the dimension of the pore with respect to the cell diameter; that is, again, the strut dimension characterizes this quality [83, 84]. The jet coherence length is limited by the interaction with the solid sponge downstream; hence, the jet coherence length

---

[1]The bulk superficial velocity u is the velocity of the flow in the empty channel where the sponge is fitted. This parameter is used in the present study to characterize the flow instead of the interstitial velocity u_g, which from the Dupuit-Forchheimer relationship $u = \varepsilon \cdot u_g$.

is approximately 80% of the cell diameter [83, 85]. But the existence of preferential streams (channeling) in commercial sponges allows jets to have coherence lengths up to 2.0 the cell diameter, depending on the arrangement of the structure and the strut dimension.

The magnitude of each of the velocity components fluctuates considerably along the space. Independent of the porosity and pore size, the root mean square of the axial velocity along any channel cross section is 69.2% of the bulk superficial velocity in sponges with rounded struts $(u_{r,RMS}/u)$, while for structures with triangular struts, this value increases up to 74.0% [27][2] owing to the shape of the struts of the sponges with triangular ligaments, which show very thin dimensions at the middle and very large sizes close to the nodes. Additionally, the sharper the edges of the triangle ligaments, the higher the mixing amount and the pressure drop [76].

These random recombination processes, characterized by tortuous flow paths and adjacent fast and slow regions with considerable velocity difference, are responsible for the high degree of the macroscopically observed phenomenon of mixing, which is dominated by the strut dimension and shape and the structure arrangement, while for arrangement in a solid sponge, the key points are the avoidance of preferential streams, the existence of partly closed pores and the random orientation of struts. One has to bear in mind that, when the mixing degree is increased, the pressure drop also increases, so an optimum operation point or sponge shape could be found for each application. Although normally, pressure drop is not an important issue for most practical applications due to the low restrictions of flow in sponges, it could be an easy way to estimate mixing parameters indirectly from simple experimental measurement of the pressure drop of flow in the sponge sample [86].

It is recommended that the Reynolds number used to characterize fluid flows in solid sponges be referred to the strut dimension, as it is in the case of fluid flow in packed particle beds, which is based on the particle size [87, 88]. Nevertheless, commonly, it is reported in terms of the pore diameter, which is highly related and thus valid.

Fig.2.12 presents the normalized velocity fields measured by Onstad et al. [83] (with the sponge overlay) using a magnetic resonance velocimetry technique, which allows for the acquisition of time-averaged velocity components in the three coordinates with a resolution of 0.6 mm. Thus, the sponge was a four-factor up-scaled sample made by rapid prototyping based on tomography data of a real sample. The sponge was inserted

---

[2]Obtained by Pathasarathy et al. [27] from direct pore level numerical simulations of laminar flow through a considerably large number of reconstructed sponge samples with rounded struts Al_2O_3 and several samples with triangular ligaments SiSiC with different pore density (the set-up of [67] was used)
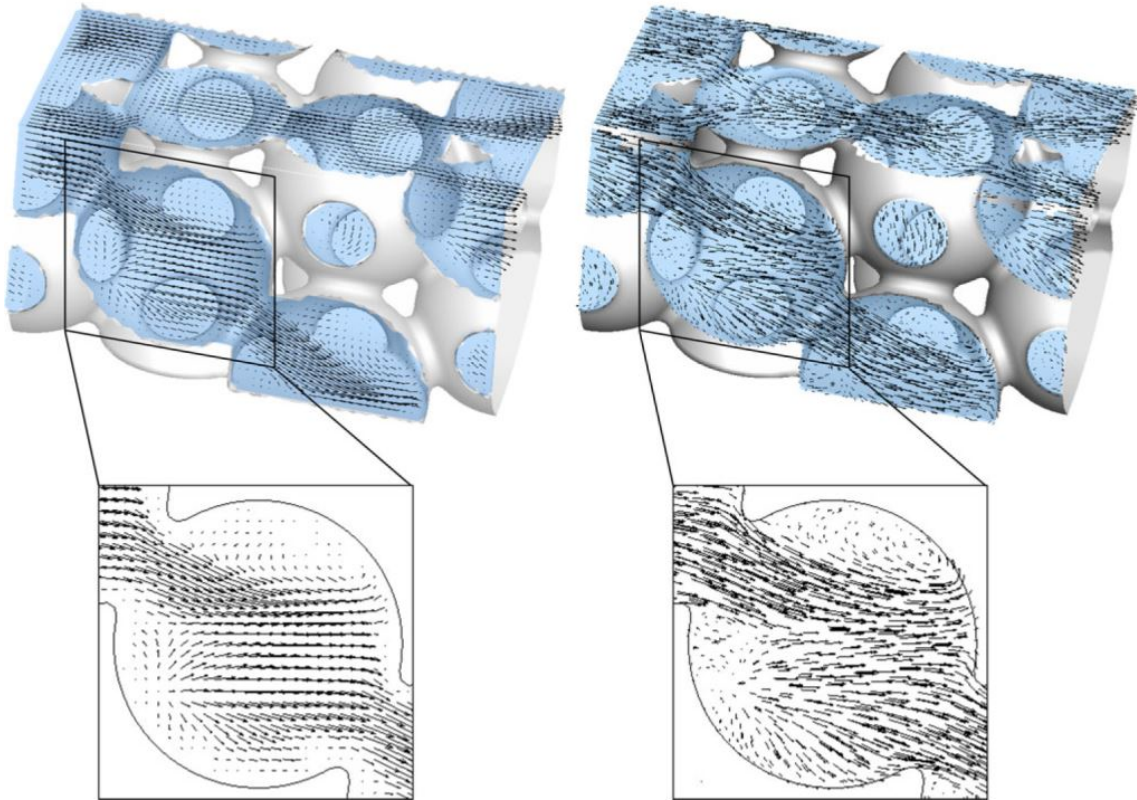
Figure 2.11: Normalized fluid flow in designed sponges $Re_p = 435$ (Left) PIV measurements [85], (Right) large eddy simulations [76].
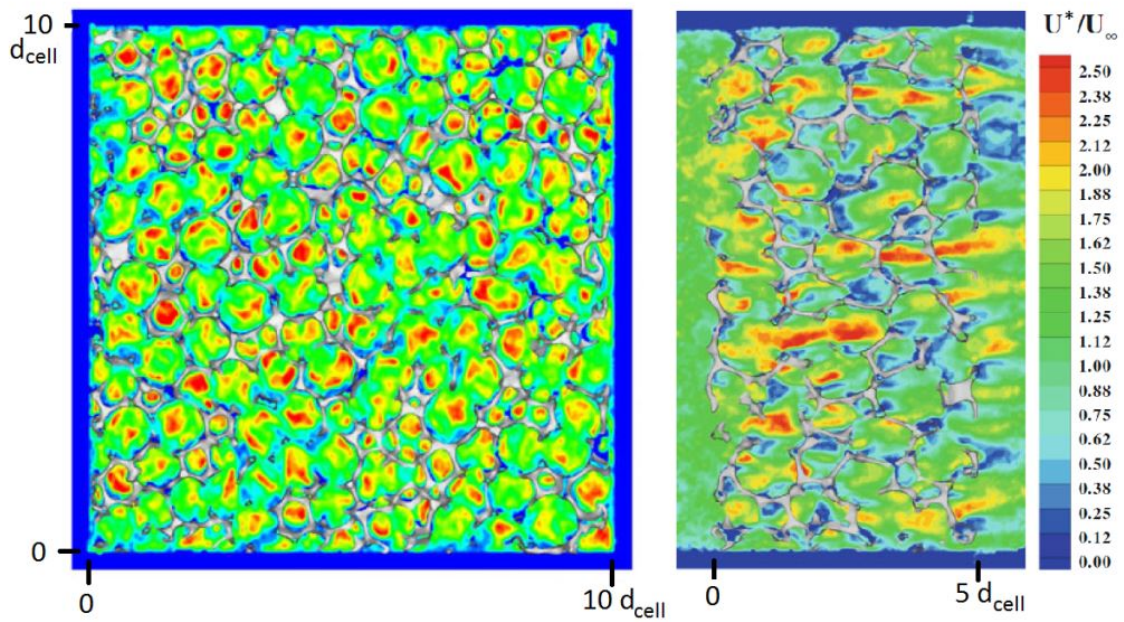

Figure 2.12: Measured normalized velocity magnitude in fluid flow in (Left) flow cross section (Right) Plane parallel to bulk flow direction [83].

in a channel with water flow and the Reynolds number based on the pore diameter was 840 and $\varepsilon = 0.92$.

Fig.2.11 shows normalized velocity vectors in two planes parallel to the bulk stream direction in a designed sponge with a pore-based Reynolds number of 435. The left side shows experimental results obtained by particle image velocimetry in a transparent polymeric up-scaled designed sponge sample using an index matching technique to avoid optical distortion of the porous matrix [85]. The right side of the figure shows numerical results from large-eddy simulations [76].

Although at the micro-scale the flow in solid sponges exhibits large spatial deviations, the strong transverse motion is the reason that the flow averaged at a representative volumetric scale shows high homogenization and flattening of the velocity profile along the channel cross section (see the cross section at the left side of Fig.2.12); that is, a very flat plug profile of volume-averaged velocity is obtained with the insertion of a solid sponge in a channel flow.

The tendency to form a flat profile of volume-averaged velocity is so strong that it can be sustained even in a diverging geometry like the one used in the experimental work for the present thesis. Fig.2.13 shows the numerical results of laminar flow at the micro-scale through a reconstructed sponge of 10-PPI SiSiC obtained by Mendes [89] in a conical channel with a diffuser angle of 20° (larger than that used in the present work, 16°). Considering the average axial velocity along a cross-sectional area at position x, the variation of this volume-averaged velocity along this conical geometry obeys a one-dimensional flow: $u(x) \propto x^{-2}$.
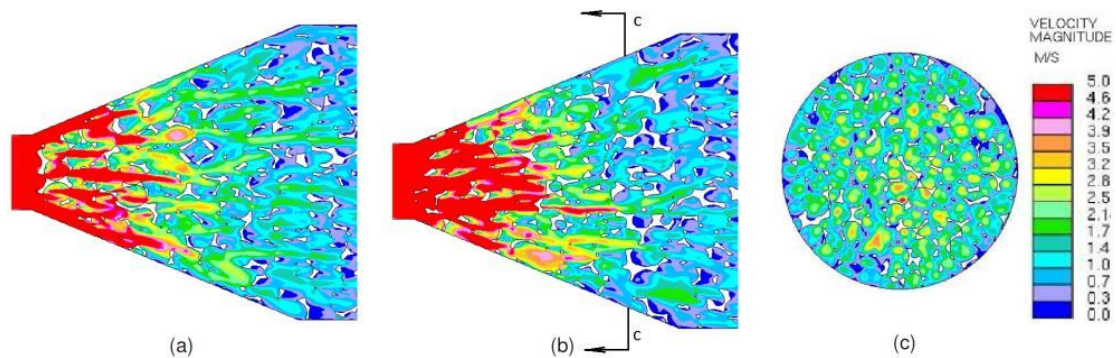
Figure 2.13: Numerical velocity magnitude in fluid flow in a reconstructed sponge of 10-PPI SiSiC, in a channel of 18-mm inlet diameter and 20° diffuser angle: (a) central plane parallel to bulk flow direction, (b) central plane perpendicular to (a)-plane and (c) flow cross section [89].

The complete discussion presented in this manuscript so far refers to time-averaged quantities. However, temporal fluctuations appear in every point of the micro-scale

flow. The turbulence intensity in fluid flow in solid sponges increases monotonically with the Reynolds number. When the Reynolds number based on the pore diameter approaches a value of 150 ($Re = d_p \cdot u / \nu$), the normalized turbulent fluctuations become asymptotically independent of the Reynolds number. In 10-PPI sponges, the constant value of turbulent fluctuations is 90% with respect to the superficial bulk velocity. For smaller pore sizes, the turbulence intensity becomes lower, and the asymptotic behavior is not experienced even at higher Reynolds numbers ($Re_p < 230$). These statements are concluding remarks on the measurements of exiting flow from sponges by Hall and Hiatt [84] and Hutter et al. [90] and measurements in the structure by Seguin et al. [91] and Ferrouillat et al. [88].

Fig.2.14 presents the normalized turbulence intensity in a designed sponge measured by PIV at the pore level. The left side of the figure presents the temporal fluctuations of the axial velocity component and the right side of the figure those of the component perpendicular to the respective shown plane. Note that the levels of normalized turbulence intensities are considerably higher than in commercially available sponges. The reasons for this are basically the avoidance of preferable streams and the larger strut dimension in this designed sponge in comparison to solid sponges.
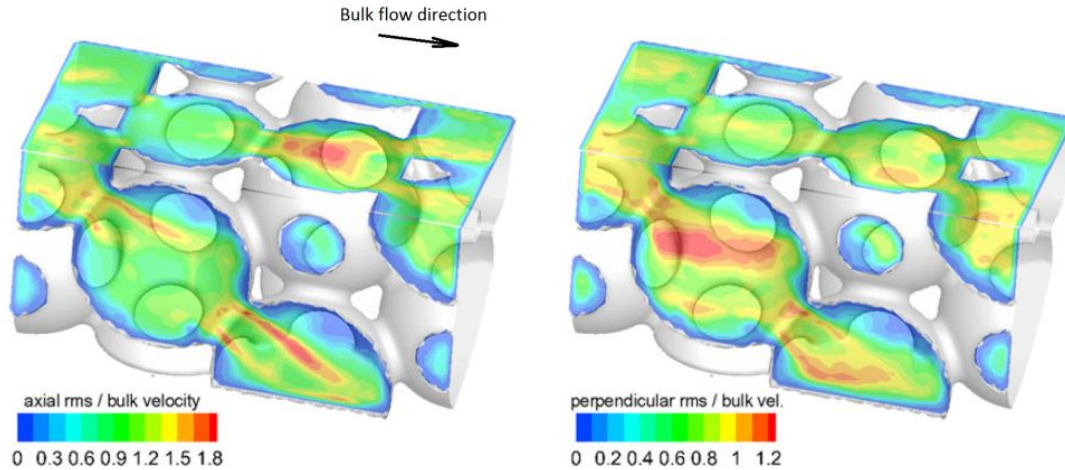
Figure 2.14: Normalized turbulence intensity in a designed sponge measured by PIV. (Left) RMS of axial velocity component. (Right) RMS of component perpendicular to the respective shown plane [85].

Indeed, the discussion on quantification of the effects of turbulence on the macroscopic phenomena of transport is still open due to the strong effects of spatial deviations imposed by the static porous matrix and the fact that the size of turbulent eddies is limited to the pore level [3, 87, 92]. De Lemos and coworkers have proposed models to consider the spatial and temporal fluctuations in the macroscopic calculation of flow and the heat transport in porous media by the introduction of turbulent dispersion coefficients [92–

94]; however, the determination of effective coefficients needs to be further developed, so this is not covered in the scope of the present dissertation.

In addition to the methods used in the literature referenced so far, there is a newly developed numerical method to study the fluid flow at the pore level in reproduced sponges accurately, which allows for more efficient use of the computing resources because the Navier Stokes equations are not solved; it is called the Lattice Boltzmann method. Some studies of flow in reconstructed solid sponges using this method are [95–97].

2.5.2   Fluid flow at the macroscopic level

The following models have been experimentally and mathematically obtained to handle volume-averaged quantities including effective coefficients and correlations.

Pressure drop

Darcy [98] was the first to carry out recorded experiments and to formulate a relationship pertaining to the pressure drop of a flow through a porous medium. He discovered that the area-averaged velocity in a porous medium confined in a channel is proportional to the pressure gradient and inversely proportional to the viscosity of the fluid μ, where the proportionality constant is called permeability K with dimensions $[L^2]$, which represents the Darcy flow law. For higher velocity regimes, the contribution of an inertial term to the flow resistance along with the viscous term must be included, as Forchheimer stated [99]:

$$\frac{\mathrm{d}p}{\mathrm{d}x} = -\frac{\mu}{K}u - c_F K^{-0.5}\rho u^2 \tag{2.30}$$

where c_F is the form drag coefficient. A very extensive review of pressure drop correlations in solid sponges is given by Dietrich [100], in which the following model based on the Ergun approach was obtained from 2,500 data values from the literature for the dimensionless pressure drop, referred to as the Hagen number Hg:

$$Hg = \frac{dp}{dx}\frac{d_h^3}{\rho_g \cdot \nu_g^2} = 110 \cdot Re + 1.45 \cdot Re^2 \;\; with \;\; Re = \frac{u_g \cdot d_h}{\nu_g} \tag{2.31}$$

and $d_h = 4 \cdot \varepsilon/S_v$, for $0.1 < Re < 10^5$.

Hydrodynamic dispersion of gas flow

Hydrodynamic dispersion occurs when one substance (e.g. a tracer) is mixed in another (e.g. a solvent) and variations in the local fluid velocity spread the tracer over a larger

volume than expected by diffusion alone [101]. The dispersion of gas through a porous medium is a consequence of the combination of molecular diffusion and convection (mechanical dispersion) in the free space [102]. Cross mixing and heterogeneous flow fields enhance the transport of molecules and heat by kinetics, through splitting and rejoining events, and by dynamics, through differences in particle velocities along the streamlines and the possible temporal fluctuations due to turbulence [103, 104].

The quantitative treatment of dispersion at the macroscopic level is based on the assumption of following an analogy to Fick's law of molecular or turbulent species transport, with the use of an appropriate dispersion tensor $\mathbf{D}$ (see Eq.(2.32)). A mathematical derivation is given by Carbonell and Whitaker [105] using the tracer pulse example. In other words, dispersion is analogous to the turbulent diffusion phenomenon, where the porous matrix plays the role of turbulent eddies in dispersing the flow [27, 106].

$$\partial c/\partial t + u_g \cdot \nabla c = \nabla(\mathbf{D} \cdot \nabla c) \tag{2.32}$$

$$\mathbf{D} = \begin{pmatrix} D_{eff} & 0 & 0 \\ 0 & D_{t,eff} & 0 \\ 0 & 0 & D_{t,eff} \end{pmatrix} \tag{2.33}$$

where the axial dispersion coefficient D_{eff} (also called longitudinal) describes the streamwise dispersion and the transverse one $D_{t,eff}$ describes the cross-stream dispersion. Generally, D_{eff} is superior to $D_{t,eff}$ by a factor of five, for pore-based Reynolds numbers larger than ten [107].

Vast experimental results of dispersion coefficients are available for packed beds and numerous theories have been proposed for the same kind of porous medium. Since the use of solid sponges in process engineering applications is relatively new, the dispersion effects in solid sponges have been approached as a manner of validation of the use of existing formulations for flow in packed beds. The experimentally obtained dispersion coefficients cannot be separated from those of turbulence contribution, so dispersion in porous media is not fully understood, but it is generally recognized that it depends on the Reynolds (Peclet) number [4].

Extensive experimental data for packed beds have been reviewed by Delgado [107], who found a consistent agreement for gas dispersion in beds of mono-sized particles of constant voidage with considerable column length for molecular Peclet numbers varying up to seven orders of magnitude. The molecular Peclet number describes the relative

importance between convection[3] and diffusion transport as $Pe_m = u_g \cdot d_p / D_m$; for this reason, experimental data are frequently presented in logarithmic plots of D_{eff}/D_m (or $D_{t,eff}/D_m$) versus Pe_m. Here, the relative dispersion coefficients of gaseous flow in packed beds increase monotonically with the Pe_m number. To achieve better resolution of the data, the modified Peclet number based on the dispersion coefficient is defined as $Pe_{dis} = u_g \cdot d_p / D_{eff}$ (or $Pe_{t,dis} = u_g \cdot d_p / D_{t,eff}$). For gas flow in packed particles, asymptotic values of

$$Pe_{eff}(\infty) = 2 \tag{2.34}$$

and

$$Pe_{t,eff}(\infty) = 10 \tag{2.35}$$

can accurately represent the data of packed beds, as the simplified models of Wakao and Kaguei [108] present:

$$D_{eff} = D_m / \tau + u_g \cdot d_p / Pe_{eff}(\infty) \tag{2.36}$$

$$D_{t,eff} = D_m / \tau + u_g \cdot d_p / Pe_{t,eff}(\infty) \tag{2.37}$$

where τ is flow tortuosity. The terms in the equations represent the contribution of molecular diffusion and mechanical dispersion $D_{dis} = u_g \cdot d_p / Pe_{eff}(\infty)$, respectively. At high velocity regimes, $Pe_m > 10$, the contribution of the molecular diffusion is negligible [102].

A good comparison with experimental data was provided by the theory of Koch and Brady [102], one of the most cited works among those on a large number of theories, namely, based on the probabilistic approach.

In terms of fluid flow in solid sponges, experimental results of dispersion coefficients are scarce. The coefficients of transverse dispersion were quantified by experiments of tracer injection in air flow at different regimes in [109–111], which match well together and were also fairly well predicted by the Koch and Brady theory.

Hutter et al. [75] obtained the axial dispersion coefficients by tracer injection measurements of liquid flow in solid sponges. They did not observe any curvature of the trend of dispersion coefficients with increase of the Reynolds number in the turbulent regime.

The axial dispersion coefficients of laminar gas flow have been numerically quantified by Djordjevic et al. [15] and Parthasarathy et al. [27] in many different reconstructed ceramic sponges by direct pore simulations. Again, good agreement with the theory

---

[3]u_g is the spatially averaged interstitial velocity, d_p is the pore characteristic length and D_m is the molecular diffusion coefficient

of Koch and Brady was observed with an appropriate definition of the characteristic pore length, providing sufficient accuracy. Djordjevic et al. [15] proposed defining a dispersion characteristic length d_{dis} that could exactly fulfill the value of $Pe_{eff}(\infty) = 2$. Although d_{dis} depends on the pore size d_p as frequently used, this length scale d_{dis} varies considerably less than d_p and it depends more on the shape of sponge struts and the porosity.

In contrast, Parthasarathy et al. [27] proposed the use of transverse mixing lengths d_t as [112] and tortuosity lengths d_τ:

$$d_t = D_{eff}/u_{x,RMS} \tag{2.38}$$

$$d_\tau = d_p(4.5 \cdot \tau - 4.4) \tag{2.39}$$

which yield constant values of Pe_{eff}, also nearly two. $u_{x,RMS}$ is the mean root square of axial velocity along the cross section. The values of $u_{x,RMS}/u$ were found to be the same as written in Section 2.5.1. For a brief description of the used method, please see the Appendix A and the work of Maier et al. [113]. Fig.2.15 presents the numerically obtained results of [27] for the Pe_{eff} based on the transverse mixing length d_t of gas flow in reconstructed solid sponges compared with Eq.(2.36).

The asymptotic analysis of Koch and Brady [102] for randomly organized particles introduced the following correlations for the axial and the transverse dispersion coefficients, respectively:

$$D_{eff}/D'_m = 1 + \frac{3}{4}\frac{Pe'_m}{2} + \frac{\pi^2}{6}(1 - \varepsilon)\frac{Pe'_m}{2}ln(Pe'_m/2) \tag{2.40}$$

$$D_{t,eff}/D'_m = 1 + \frac{63\sqrt{2}}{320}\sqrt{1 - \varepsilon}Pe'_m/2 \tag{2.41}$$

where $D'_m = D_m/\tau$ and $Pe'_m = u_g \cdot d_p/D'_m$.

2.5.3 Flow instabilities in porous media

Research about processes taking place in gas flow through a porous medium at temperatures above 1300 K have been developed in recent decades motivated on applications for solar receivers [114]. Pitz-Paal et al. [115] showed theoretically the existence of flow instabilities that had been observed in experiments for some conditions. Consider that, for any reason, the flow through a pore is reduced in the presence of a source of
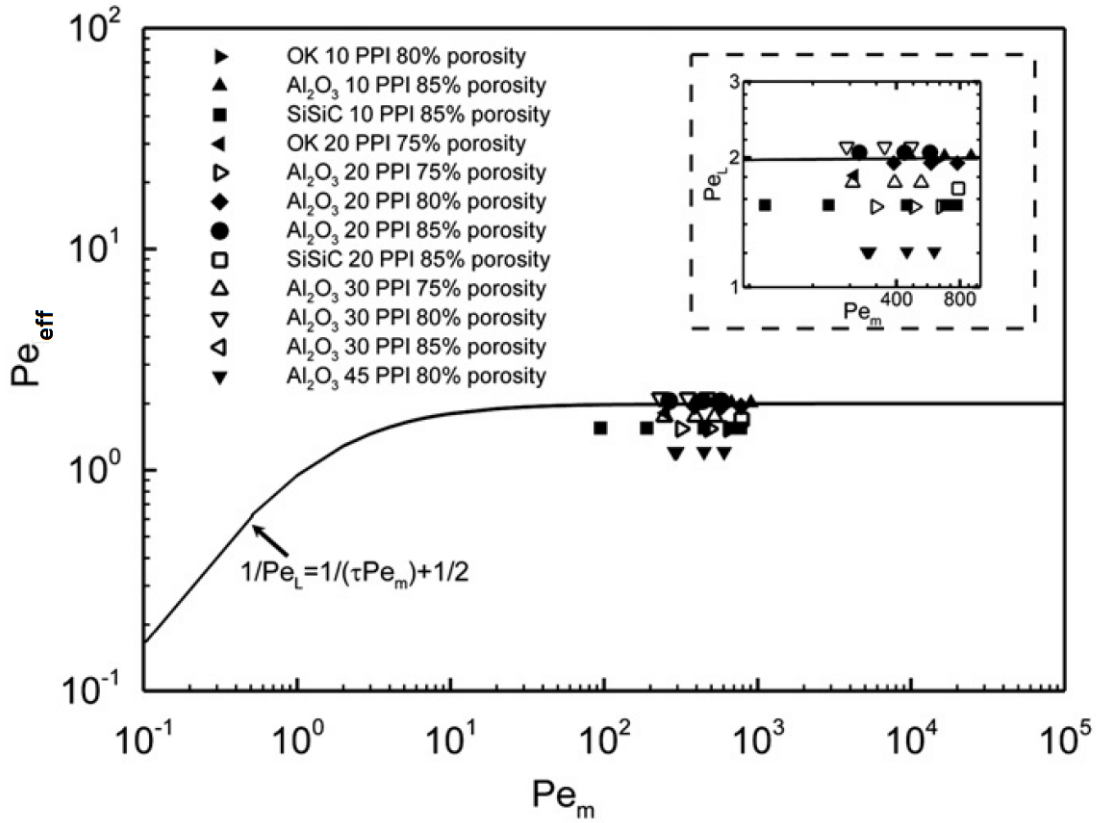
Figure 2.15: Modified Peclet number versus molecular Peclet number, both based on the transverse mixing length d_t compared with Eq.(2.36). A magnified view is shown in dashed box [27].

heat; the temperature around this pore increases, which also increases the flow resistance. Depending on the effect of temperature on the flow resistance, the flow might be disturbed. Fortunately there is a large range of parameters which can lead for a save operation of solar receivers [114]. As influencing factors, the radial heat losses and the type of effect of velocity on the pressure drop in the porous medium, that is, either a linear or a quadratic dominated relationship, were identified.

The thermo-acoustic instabilities in combustion within PIM has been not else published than by Vroemen et al. [116].

2.6   Heat transport in solid sponges

Although extensive studies have been carried out on heat transfer in porous media, most of them mainly focused on packed beds and granular materials with porosities in the range of $0.4 - 0.6$. However, solid sponges have very particular features, such as high

porosity ($\varepsilon > 0.7$) and unique open-celled stiff cellular structure. Consequently, most previous studies on packed beds are not applicable to solid sponges [117]. The most comprehensive discussion of transport and radiation characteristics of cellular materials was probably reported by Kamiuto in 2008 [118], who reviewed previous experimental and theoretical work and suggested correlations for all the model input data [4]. Some other very comprehensive works and reviews of transport phenomena in solid sponges are [117, 119, 120]. Typically, studies of heat transport are accomplished with the combination of conduction, radiation and convection between phases and wall convection because they all occur in some applications, such as heat exchangers. In the following review, the discriminative basic analysis of interface convection, conduction and radiation are presented separately, in relation to the application of the volume-averaged model used in Chapter 5 for the study of flame stabilization within solid sponges. Studies carried out at the pore level in solid sponges have been stressed, since they are few in number and are proceeding to extensive study. Wall convection has been excluded from the focus of this work since the use of adiabatic walls has been attempted. The article of Bianchi et al. [80] refers to that topic.

2.6.1 Interface heat transport

For some applications of flow within a porous medium, such as porous burners, local thermal equilibrium between phases (the same temperature on both phases) cannot be assumed due to significantly different thermal properties of both phases and/or due to a high temperature increase in the reactor.

To describe the interface heat transfer due to convection accurately, the control volume-averaged energy equations are derived separately for the fluid and solid phases. The two equations are coupled by introducing the interface heat transport term. The corresponding heat transport coefficient α in solid sponges has been determined by experiments and theoretical modeling in several works for a wide range of velocities, sponge structures and materials. The results have been commonly correlated for the Nusselt number Nu as function of the Reynolds number based on the pore-level characteristic length, which has not been defined in a unique way. The pore diameter, strut diameter and hydraulic diameter, among others, have been used as characteristic lengths.

The experiments can be classified in terms of a transient or steady state. A recent review of correlations obtained by experiments is included in the work of Dietrich [121], who measured time-dependent temperature profiles of air and solid, with air at 373 K flowing into a cold sponge in an insulated channel. Assuming negligible heat conduction effects compared with convective effects and knowing property data like S_v from Grosse

et al. [7], the heat exchange coefficient α was obtained from the energy equations of gas (Eq.(2.42)) and solid (Eq.(2.43)).

$$\frac{\partial T_g}{\partial t} = -u_g \frac{\partial T_g}{\partial x} - \frac{\alpha}{\rho_g c_{p,g}} \frac{S_v}{\varepsilon}(T_g - T_s) \tag{2.42}$$

$$\frac{\partial T_s}{\partial t} = \frac{\alpha \cdot S_v}{\rho_s c_{p,s}(1-\varepsilon)}(T_s - T_g) \tag{2.43}$$

Note that the convective term is directly influenced by the volumetric surface area S_v, which increases with the reduction of the pore diameter d_p. The results have been correlated in this form:

$$Nu = \alpha \cdot d_h/\lambda_g = c_1 \cdot Re^{c_2} \cdot Pr^{c_3} \quad with \quad Re = \frac{u_g \cdot d_h}{\nu_g} \tag{2.44}$$

with $d_h = 4 \cdot \varepsilon/S_v$ [122]. This factor c_1 is directly related to the porosity and corrected by the Re number, while the pore size does not have a considerable effect on α.

$c_1 \approx 0.59 \cdot c_{corr}$ with $c_{corr} = \frac{\varepsilon^{1.5}}{(1-\varepsilon)^{5/8}} \cdot \left(\frac{Re-1}{Re-1000}\right)^{0,25}$

$c_2 = 2/3$ and $c_3 = 1/3$.

A variation of this correlation was presented by Martin [123] with the analogy between heat and momentum transfer similar to the Léfêque equation for packed beds. This correlation allows the prediction of α from measurements of pressure drop. Dietrich [121] found the following correlation for his data:

$$Nu = \frac{\alpha \cdot d_h}{\lambda_g} = 0.344 \cdot c_{corr} \cdot Hg^{1/3} \cdot Pr^{1/3} \tag{2.45}$$

where Hg is the Hagen number $Hg = \frac{dp}{dx} \frac{d_h^3}{\rho_g \cdot \nu_g^2}$.

Other experimental works of convection in solid sponges have also stated correlations of the form of Eq.(2.44), such as [124–129].

Zarzalis et al. [28] performed direct numerical simulations detailed at the pore level in reconstructed ceramic sponges with different pore diameters, porosities and materials. The method is described in the Appendix A. The results have also been correlated with the form of Eq.(2.44), with $Re = u_g \cdot d_h/\nu_g$. The coefficients in this correlation were determined for each of the samples simulated, as shown in Tab.2.1. Note that the increase of porosity has a direct effect on the correlating constant c_1.

Since determination of the volumetric surface area S_v is not easy, the utilization of a volumetric heat transfer coefficient

Table 2.1: Nusselt number correlation for flow within solid sponges [28]

Pore density PPI	Porosity(%)	c_1	c_2	c_3
10 (Al_2O_3)	80	3.86	0.33	0.18
	75	2.9	0.35	0.20
20 (Al_2O_3)	80	5.0	0.22	0.08
	85	5.5	0.23	0.06
	75	4.8	0.17	0.12
30 (Al_2O_3)	80	6.17	0.22	0.08
	85	6.23	0.22	0.08
45 (Al_2O_3)	80	3.10	0.36	0.25
20 (SiSiC)	85	5.14	0.30	0.24
10 (SiSiC)	85	3.7	0.38	0.25

$$\alpha_v = \alpha \cdot S_v$$

has been preferred in other studies [130–134]. Nakayama et al. [135] developed the following correlation based on the volume-averaged theory, which was validated by comparison with all the empirical results of this kind.

$$Nu_v = \alpha_v \cdot d_m^2/\lambda_g = 0.007 \left(\frac{\varepsilon}{1-\varepsilon}\right)^{2/3} \cdot Re \cdot Pr \quad with \quad Re = \frac{u \cdot d_m}{\nu_g} \tag{2.46}$$

where $d_m = \sqrt{\varepsilon \cdot \pi}/PPI$ is the mid-average pore diameter.

It should be noted that the volumetric heat transfer coefficient α_v is sensitive to the porosity of the solid sponge, but is fairly insensitive to other factors [135].

2.6.2 Thermal conduction in solid sponges

Conduction heat transfer occurs within the solid phase as energy quantum released or absorbed from elementary vibration of atoms in the lattice. Fouriers law of heat conduction describes the relationship of one-dimensionally conducted heat flux:

$$\dot{q}_{cond} = \lambda \cdot \partial T/\partial x \tag{2.47}$$

where λ is the thermal conductivity. Solids in general have a thermal conductivity that is several orders of magnitude higher than that of gases.

In the macroscopic analysis of the heat transfer in PIM, effective coefficients of transport are included in the closure equations (see Chapter 5) obtained by the volume-averaged method. Therefore, Eq.(2.47) must refer to average heat flux and average temperature

along the cross-sectional area of the domain, either solid or gas, or both, depending on the used approach. In the case of the solid separately (in the so-called two-energy equation model), the effective thermal conductivity of PIM $\lambda_{s,eff}$ is lower than the one proper of the material due to the longer tortuous heat flux paths through the interconnected struts of the sponge. For the quantification of these paths, the tortuosity τ_s of the heat flow through the porous matrix describes the ratio between the path length of heat flow and the straight path length, that is, the sponge thickness in the direction of bulk heat flow. Accordingly, the effective thermal conductivity is decreased by this factor:

$$\lambda_{s,eff} = \lambda_s / \tau_s \tag{2.48}$$

The theory of Lemlich [136] of limiting electrical conductivity of a polyhedral structure of high porosity yields a value of $\tau_s = 3.0$ for the ratio of the bulk (volumetric) density to the bulk electrical conductivity. This result was compared with extrapolations of published experiments.

The tortuosity of conductive heat flow in solid phase of sponges was quantified by Zarzalis et al. [28] by DPLS of heat conduction in reconstructed sponges. The results are shown in Tab.2.2. The effective thermal conductivity is found to be quasi-insensitive to the porosity or the pore size; in contrast, it is very sensitive to the shape of the sponges, namely, the base material. While the SiSiC sponges exhibit very thin struts at the middle, the struts of the Al_2O_3 sponges are more uniform and the strut diameter is greater in the middle (see Fig.2.8). Accordingly, the reduction of the thermal conductivity in SiSiC sponges is considerably higher than in Al_2O_3 sponges; the average τ_s among the examined sponge samples of each material are 3.8 and 2.6, respectively.

Table 2.2: Solid phase tortuosity of conductive heat flow for ceramic solid sponges [28]

PIM	Porosity(%)	$\tau_s = \lambda_s/\lambda_{s,eff}$
10 PPI Al_2O_3	80	2.77
	75	2.20
20 PPI Al_2O_3	80	1.87
	85	2.96
	75	2.86
30 PPI Al_2O_3	80	2.57
	85	2.57
10 PPI SiSiC	85	3.76
20 PPI SiSiC	85	3.94

Since determination of the effective solid conductivity with DPLS has been carried out very recently and that an insufficient number of sponge samples were studied, the

two-phase or overall thermal conductivity $\lambda_{eff,2-ph}$ has been quantified in the past by experiments, for example by Calmidi and Mahajan [137], and theoretical models, for example Boomsma and Poulikakos [71]. This parameter is directly used in the volume-averaged model with only one energy equation, where gas and solid phases are considered in local thermal equilibrium as a sole continuum, that is, their temperature is the same. The overall conductivity can be related to $\lambda_{s,eff}$. If the heat conduction in the solid and fluid phases occurs in parallel, then the overall conductivity is the weighted arithmetic mean of the conductivities $(\lambda_{s,eff} + \lambda_r)$ and $\lambda_{g,eff}$ (where λ_r represents the contribution of radiative heat transfer between solid surfaces given by the Rosseland approximation):

$$\lambda_{eff,2-ph} = (1 - \varepsilon)(\lambda_{s,eff} + \lambda_r) + \varepsilon \cdot \lambda_{g,eff} \tag{2.49}$$

In addition, for the gas,

$$\lambda_{g,eff} = \lambda_g + \lambda_{dis} \tag{2.50}$$

the contribution of thermal dispersion due to convective mixing in the gas phase is considered,

$$\lambda_{dis} = a_{dis} \cdot \rho_g \cdot c_{p,g} \tag{2.51}$$

which can be obtained in relation to the velocity Eq.(2.36) assuming that there is no preference of mass dispersion over thermal dispersion $a_{dis} = D_{dis}$; that is, in analogy to the micro-scale problem, the dispersion Lewis number is unity.

For still gas, there is no contribution of dispersion in the ideal stagnant case. For low temperatures, highly conductive materials, like aluminum, and/or low porosities, the contribution of radiation can be neglected [120]. If the conductive effects are analyzed separated from dispersion and radiative effects, it is observed that the $\lambda_{s,eff}$ and $\lambda_{g,eff}$ commonly differ by several orders of magnitude, but in high-porosity structures, the contribution of λ_g is not negligible (see Eq.(2.49)).

The overall thermal conductivity of still fluids in tetrahedral structures with cubical nodes has been modeled by Boomsma and Poulikakos [71], who validated the model with the measurements of Calmidi and Mahajan [137]. This model states that the overall thermal conductivity considerably depends on the porosity, while the increase of the pore diameter slightly reduces it. The results of this model $\lambda_{eff,2-ph}$ compare well with the DPLS results of $\lambda_{s,eff}$ in Tab.2.2, while using Eq.(2.49) to relate the two parameters.

Some of the studies of stagnant overall effective conductivity of solid sponges include [70, 119, 120, 138–140]. The results of the model of Bhattacharya et al. [119] show

that the overall conductivity depends strongly on the porosity and the ratio of cross sections of the strut to the node. However, no systematic dependence was found on PPI effects. Experimentally, the conduction phenomenon cannot be separated from other heat transport effects. For example, Zhao et al. measured the overall effective conductivity of FeCrAlY sponges at 500-800 K at atmospheric and reduced pressure and found that the contribution of natural convection is very significant.

The effect of thermal dispersion, due to forced flow, on the overall thermal conductivity of sponges has been experimentally studied by [118, 125, 141, 142]. Dietrich et al. [142] recently measured the overall effective conductivity of ceramic sponges with and without forced flow of air. The results correlate well, with a correlation similar to Eq.(2.49), although the contribution of radiation was not analyzed, similarly to what Calmidi and Bahajan did [125], to correlate the experimental data of Hunt and Tien [143] of thermal dispersion in fibrous media. The correlation coefficients of [125] fitted well in the theoretical and experimental work of Edouard et al. [141], who studied sponges of SiC and polyurethane.

Since the combination of different heat transport mechanisms cannot be insulated from conduction in experiments, reliable models are needed, such as the DPLS presented by Zarzalis et al. [28] and Bianchi et al. [120], for reconstructed real sponge samples, and Wang and Pan [144] for randomly generated structures. Wang and Pan [144] used the Lattice Boltzmann method to obtain the stagnant overall thermal conductivity of polyurethane open cell foams. To model an approximately realistic porous structure, a random generation-growth method by computer algorithms was developed. After consideration of radiation, the numerical predictions of effective thermal conductivities agree well with their experimental data. The importance of the contribution of radiation decreases as the porosity increases.

2.6.3   Thermal radiation

Because of the high temperatures reached at combustion, the emission and absorption of electromagnetic waves in the form of radiation play an important role in heat transfer between solid surfaces that are at different temperatures. The scope of the present work is not to discuss radiative heat transfer and/or characteristics needed to study it in PIM. The reader is instead referred to reviews on this topic [117, 118, 145, 146]. The spectrum of methods to quantify thermal radiation effects is wide. An outline of methods used most widely in modeling combustion in porous media from 1991 to 2003 is given by Hayashi [147]. The Rosseland equation, for example Glicksman et al. [148], the

Monte Carlo method, for example Hackert et al. [149], and the P-3 spheric harmonics approximation, for example Diamantis et al. [150], are some of the best known methods.

The continuum approach is discussed here briefly, which is consistent with the volume-averaged model used in Chapter 5 to simulate the flame stabilization within sponges.

The Rosseland equation is the simplest method to quantify the solid radiation in porous media under the continuum approach, since an analogy with the heat conduction equation is enabled, which avoids the necessity of solving a radiation transfer equation.

$$\dot{q}_{rad} = \lambda_r \cdot \partial T / \partial x \tag{2.52}$$

where λ_r is called the radiation conductivity:

$$\lambda_r = (16 \cdot \sigma \cdot T_s^3)/(3 \cdot \beta) \tag{2.53}$$

The Rosseland approximation is valid for optically thick media $L \cdot \beta > 3$ [151], where β is the extinction coefficient, L the medium thickness and σ the Stefan-Boltzmann constant.

The extinction coefficient, which is the sum of absorption and scattering coefficients, is the inverse of the penetration thickness of radiation [152]. Experimentally, this coefficient could be estimated by spectrophotometric measurements, integrating the monochromatic extinction coefficient over the whole spectrum [120]. However, this approach is quite complex and therefore empirical correlations were carried out in the literature based on geometrical assumptions of the sponge structure, for example, [138, 153–155]. These works propose the following correlation to calculate extinction coefficients of sponges

$$\beta = 2.656\sqrt{1 - \varepsilon}/d_p \tag{2.54}$$

where the correlating constant and the exponent of the solid fraction $(1 - \varepsilon)$ have been taken from Loretz et al. [155].

These models are commonly based on the geometrical optics theory. In comparison with the experimental results, this theory predicts the extinction coefficients; thus, corrections due to structural topology and material surface conditions are required.

The most accurate way of quantifying these coefficients is the use of the tomography data of sponge samples to be used in ray tracing methods, as done by Parthasarathy et al. [26], Petrasch et al. [79] and Loretz et al. [155]. A database of optical parameters of numerous ceramic sponges generated by this method can be found in [26].

In summary, smaller pore diameters lead to higher extinction coefficients because, in porous media, the void structure is responsible for the pronounced heat transfer through radiation and, with smaller pore diameters, the emitted rays are more easily obstructed by the solid.

To close this section on heat transfer in solid sponges, one can conclude that the stiffness of the geometry of these structures and the random orientations and shape of their struts make determination of heat transfer coefficients in solid sponges difficult, for which considerable uncertainties cannot be completely avoided. The most accurate method is direct pore-level simulation in reproduced sponges using tomography data; nevertheless, this is complicated. The simulation of numerous samples and/or larger-sized samples is encouraged by the author as a possible way to develop more accurate database and correlations for transport parameters.

2.7   State of the art of combustion within PIM

The purpose of this section is not a detailed review of the literature related to the present topic, so it only includes references to relevant reviews and some of the most cited works during the history of the development of our understanding of the processes behind flame stabilization within PIM combustion.

The first reported experimental observations about the manifold acceleration of combustion within interstices and pores were performed in the early 20th century by Bone et al.[156, 157]. Such observations were not reported again for almost half a century until Shaulov [158] and De Soete [159]. De Soete [159] has established a semi-empirical model to predict the filtration flame front velocity accounting for solid conduction, convection and radiation heat transfer. Theoretically, the physical effect was described as heat recirculation through a solid to preheat the unburned mixture, which was referred to as an excess enthalpy flame [13, 160]. Then, the combustion within PIM was modeled as a planar flame using the volume-averaged method by Takeno and Sato [161]. The effects of dispersion in porous media on the flame structure was not taken into account as a relevant process for two decades, until it was included in the model by Henneke and Ellzey [24]. Other kinds of model have recently been proposed, such as direct pore-level simulations; nevertheless, this is a newly developing field that can be predicted to be a major focus of research in the near future. The work of Viskanta [4] and Mujeebu et al. [16] present reviews of only modeling of combustion in PIM, which are actualized at recent time.

The general study of combustion in PIM, that is not only modeling, began to be reviewed

in the decade of 1990. Some of the first reviews were done by Trimis and Durst [9], Howell et al. [12] and Viskanta [162]. Subsequently, the frequency of publication of articles and book contributions on related topics has increased considerably, although to date no book on combustion technology has dealt with this topic. Some excellent newer reviews are [2, 5, 10, 11, 14, 22].

One of the motivations of this study is the scarcity of studies performed at elevated pressures. At atmospheric pressure, there is an abundance of experimental and numerical (mostly volume-averaged models) data in the literature, including on pollutant emissions and temperature distributions along PIM. However, the estimation of burning velocity S has not been reported in many studies [15]. In contrast to the extensive studies performed under atmospheric conditions, at elevated pressure, the flame stabilization in PIM has been studied only in [163, 164].

Noordally et al. [163] studied ignition and steady characteristics of combustion of methane-air mixtures at lean conditions up to 11 bar in reticulated PIM made of partially stabilized zirconia or yttria-stabilized alumina. For the study of flame stabilization at elevated pressure, the velocity of unburned gases u_u was kept constant at 0.49 m/s, as well as the air-to-fuel ratio (λ=2.2) and the inlet temperature ($T_0 = 520\ K$). The temperature along the burner axis was measured using thermocouples. The flame was stabilized at the interface between a flame arrestor and the PIM at 5 bar. It was observed that, at a pressure of 10 bar, the flame was stabilized within the flame arrestor, which was interpreted as an increase of S with pressure. It was reported that the existence of super-adiabatic conditions in PIM compensated for the negative effect of pressure on the burning velocity in premixed methane-air laminar free flames.

Bakry et al. [164] studied the effect of mixture composition (air factor λ), initial temperature and pressure on the flame stabilization in a conical PIM made of Al_2O_3 lamellae, burning also methane-air mixtures at lean conditions up to 9 bar, using the same methodology as [163]. The flame was stabilized in the conical PIM, but for the study of the pressure effect, the flame was stabilized at the inlet of the PIM. The axial temperature profiles along PIM for $T_0 = 300K$ showed that the flame position was shifted upstream at 3 bar for $\lambda = 1.4$ and $\lambda = 1.6$, while for $\lambda = 1.8$ and $\lambda = 2.0$, it stayed fixed for all pressures analyzed. The results are interpreted as an increase of S with pressure, which is less pronounced for leaner mixtures.

The study of combustion processes in PIM has rarely been conducted at the pore scale. Kiefer et al. [165] developed a non-intrusive technique to measure the temperature of the gas phase with high resolution. Chen [166] reported the use of electrical capacitance tomography to depict the meso-scale structure of the flame, which showed different modes

of combustion, such as unsteady combustion. The study of thermoacoustic instabilities of combustion in PIM has been developed by Vroemen et al. [116], who used a OH^* visualization technique to indicate the heat release rate and to generate the acoustic transfer function of the porous burner. As any process that is accompanied by gas expansion, combustion in porous media may become acoustically unstable when a burner is inbuilt into the acoustic system of a combustor.

Owing to such experimental difficulties, besides the restrictions imposed by PIM on the accessibility of measuring appliances and the complexity of the physics behind the combustion process in PIM, the development of porous burner technology must be accompanied by numerical models that can explain the involved relevant phenomena [12].

The majority of the models applied so far are based on 1D volume-averaged methods, while just a few have been applied upon 2D and 3D domains [16]. Especially at the 3D pore level, few studies about combustion have been reported [20, 167, 168].

In the 1D simulations, detailed chemical mechanisms have generally been employed and have included examinations of thermal transport [149], material properties [56, 169, 170] and the complexity of combustion chemistry [171, 172].

1D models assume a 1D flame front condition without radial heat losses, flame stretching and spatial temperature variations. These assumptions may become inaccurate in porous burners with a complex geometry. In such a situation, 1D relations will no longer be valid and multidimensional models are inevitable [16].

Computational fluid dynamics CFD software based on the volume-averaged approach has been used to study hydrocarbon partial oxidation by Al-Hamamrea et al. [173] and the influence of ceramic foam structures upon dispersion by Steven et al. [174]. A volume-averaged method (2D) for the calculation of premixed methane combustion and heat transfer in porous burners with built-in heat exchangers is presented by Malico and Pereira [175, 176]. They also investigated the influence of the radiative properties on some flame characteristics. Other versions of CFD software have been used by Xie et al. [177] and Liu et al. [178] to study the pressure loss and temperature distributions in two different systems.

2D DPLS were carried out in 2D arrays [149, 179]. Hackert et al. [149] developed a model to analyze the influence of multidimensionality on flames within two simple porous structures: honeycomb (no dispersion) and cross plates (solid-solid radiant heat recirculation). Sahraoui and Kaviany [179] studied combustion within discrete or connected square cylinders and found that multiple local burning velocities exist within a pore imposed by the hydrodynamics and the solid thermal conductivity. Compared with the volume-averaged method, the DPLS predicted lower bulk burning velocity and

higher super-adiabatic temperature. Although 2D geometries are simpler to model than 3D complex structures, the DPLS of combustion in 2D geometries has not been further studied. Combustion in micro-channels is a research field with high similarity to the case of combustion within PIM, whose study has increasingly been carried out with direct numerical simulation and detailed reaction mechanisms [19].

3D DPLS of flame stabilization within PIM has rarely been performed. Some researchers used non-conventional modeling techniques, such as flamelet-generated manifolds by Oijen et al. [180, 181], which is a combination of two approaches to simplify flame calculations, namely, a flamelet and a manifold approach, to construct simplified kinetic models that account for the pore-level processes. Others introduced the Lattice Boltzmann method for the simulation of processes of combustion of soot by Yamamoto et al. [21, 167] and non-reacting flow by Zeiser et al. [182], within complex geometries, due to the common belief that such geometries have to be simplified through various approximations in order to be applicable in finite-volume calculations. Furthermore, a 3D mesh-based microstructure representation algorithm for the random generation of PIM geometries under some nominal structural parameters has been developed by Liou et al. [168] in order to provide efficient cost-effective use of computing time. To the best of our knowledge, the real structure of a sponge like PIM has not been used for DPLS of combustion within PIM, as presented by Bedoya et al. [20] and in the Appendix B.

A brief review of the history of modeling flame stabilization within PIM, where researchers attempted to quantify the different heat transport mechanisms, is presented in Tab.2.3. The importance and sensitivity of different physical processes of combustion in PIM is indicated with ++, + and - for very important, important and less important, respectively.

Table 2.3: Importance of heat transport mechanisms in PIM combustion modeling

Rad. solid	Rad. gas	Heat cond. solid	Heat cond. gas	Dispersion	Heat convec.
+	-	++	-	++	+
[169, 183, 184]	[161, 185]	[161, 185–187]	[15, 56, 57]	[15, 56]	[161, 187, 188]
[58, 150, 186]		[188, 189]			

In conclusion, it can be postulated that flow dispersion, solid conduction and solid-to-solid radiation are the controlling heat transfer mechanisms during combustion within PIM.

Many researchers achieved good agreement with experiments, regarding emissions and spatially averaged temperatures. However, three-dimensionality of the flow and flame

front in porous media has not been considered. These considerations, including the radial and axial spatial variations of the flame front (temperature distribution) can be predicted using DPLS, which can be applied under conditions where the capability of prediction of models based on the volume-averaged method is limited. All of the publications about the combustion in PIM lead to the conclusion that there is a wide scope for future works, especially experimental and numerical studies at the pore level.

Chapter 3

Description of experimental methodology

A conical PIM was used to stabilize the flame of lean premixed air-natural gas. Fixed thermocouples were placed inside the PIM at the mid-radii. A closed ceramic pipe was located through the PIM axis to allow for the displacement of a movable thermocouple along it. The hardware involved and the procedure used are presented in this section.

3.1   Experimental set-up

The used test rig consisted of an air-flow-homogenizing segment, a mixing system, a flame arrestor, an insulated porous burner, water-cooled housing, a gas analysis system, a gas cooling system, a throttling valve and a silencer, see Fig.3.1.

The air was discharged perpendicularly in the bulk flow direction through four holes of 2 mm in diameter (see Fig.3.2). The air flow was homogenized using two perforated plates with holes of 2 mm in diameter separated by 4 mm in a rhombus array. The air and the gas were mixed through a pipe with an inner diameter of 27 mm.

The fuel injection was carried out through eight equally spaced ports in cross flow to the air flow. The port diameter was 0.8 mm. It was dimensioned to allow for the velocity of fuel to be greater than the air velocity by at least a factor of two, in order to penetrate effectively in the air cross flow [190]. Downstream, a static mixer was mounted. It had two sets of counter swirl blades, as shown in Fig.3.2, fixed in the pipe with an inner diameter of 27 mm. The mixer was constructed by the company Lewa Hov Pumps and Systems, Germany. For a pressure drop in the mixer of 0.5 mbar, the used static mixer
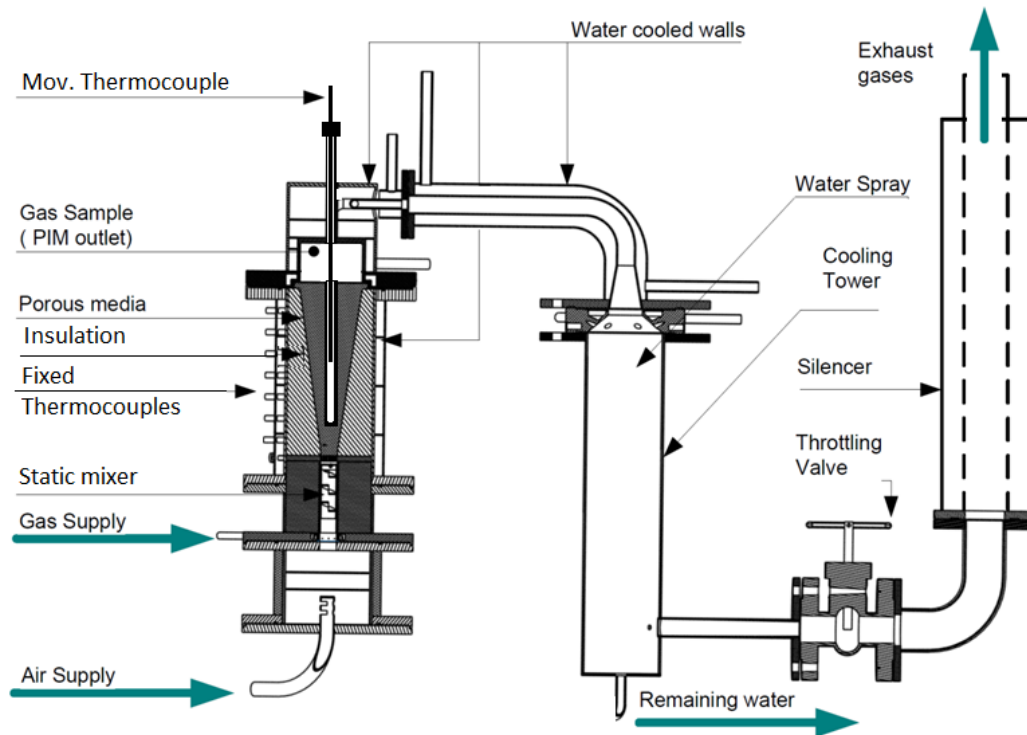
Figure 3.1: Construction drawings of the used test rig

allows for a mixing quality of 95%, as reported by the manufacturer, while in the present experiments, the pressure drop in the mixer ranges between 5 and 60 mbar.

The mixing quality was tested by analyzing a gas sample taken at the downstream end of the conical burner at different radial locations using flowing mixtures of 2% gas in air without combustion. This was carried out at 1.0 and 4.0 bar for a mixer pressure drop of 5 mbar. The obtained radial profile of the methane molar fraction was flat, without any deviation above the measuring error (2%).

The flow-homogenizing segment and the mixing module were insulated with high-temperature-insulating material to reduce heat loss from the preheated unburned gas to the environment.

After the unburned gases were mixed, they flowed through the flame arrestor and then through the conical porous burner. The flame arrestor was an additional safety feature to avoid flame propagation towards the mixing system in the case that the flow rates drop, so that the flame wave could displace the conical burner upstream (flashback). The flame arrestor was a perforated plate with holes placed in a rhombus array with a diameter of 0.75 mm, which is smaller than the flame quenching distance. A gap of 2 mm was kept between the flame arrestor and the porous media to avoid conductive heat transfer from the porous matrix to the flame arrestor in the case of flashback.
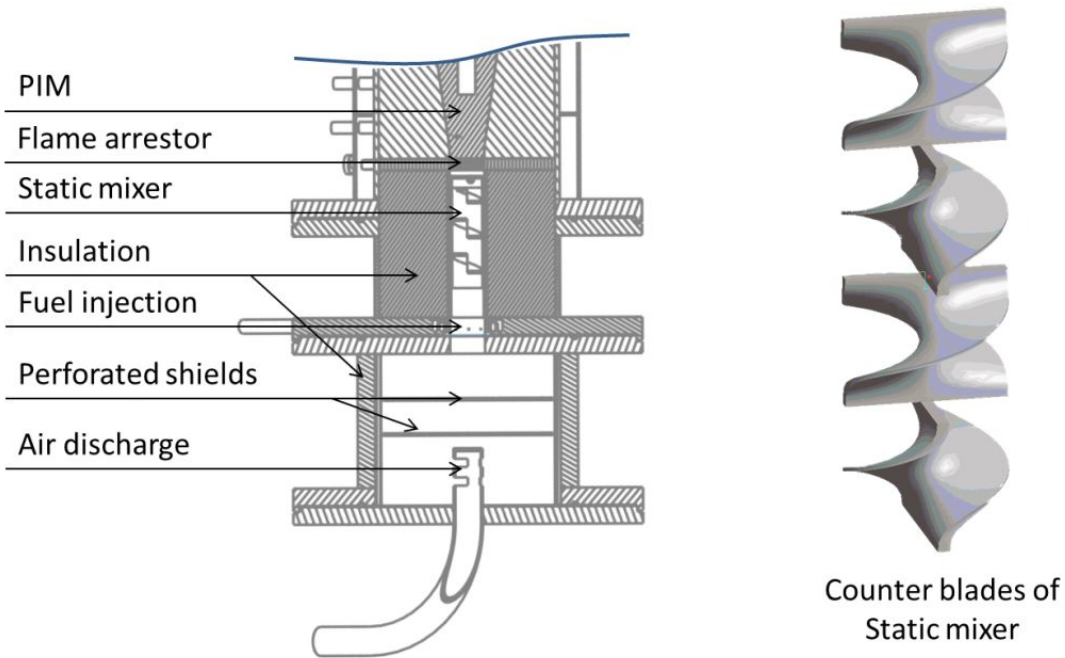
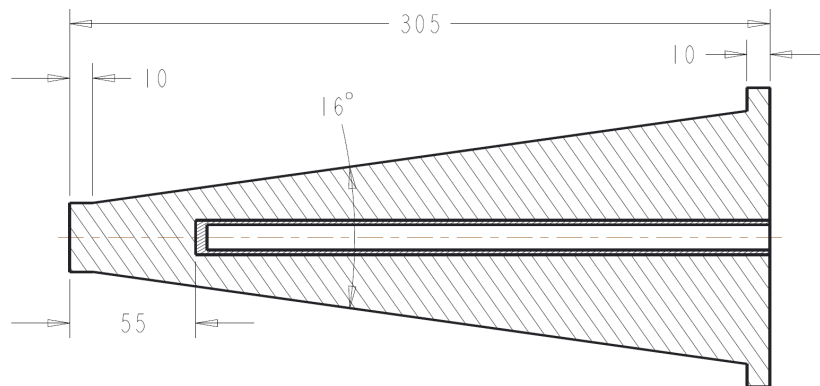Figure 3.2: Construction drawings of the used discharge and mixing system

Figure 3.3: Construction drawing of the used porous burner, dimensions in mm

The convective flame stabilization technique was used, based on the continuous increase of the cross-sectional area. The flame is stabilized in the PIM at an axial position where the burning velocity and the fresh gas flow velocity are equal. The PIM has a conical shape, as shown in Fig.3.3 and Fig.3.4. The flame was stabilized at locations further than 100 mm from the PIM inlet face; hence, this PIM segment contributes to pre-mixing of the air with the natural gas.

The dimensions of the burner in mm are presented in a scaled drawing in Fig.3.3. Basically, it has a conical shape with a vertex angle of 16°, with 10-mm-long cylindrical segments at the extremes to enable its fixation in the combustor. The porous matrix has a central hole along the axis with a diameter of 16 mm. A closed ceramic pipe was inserted in this hole for temperature measurements. The ceramic pipe was made of 99% alumina, with outer and inner diameters of 15 and 12 mm, respectively. The pipe was closed with a metal lid at its bottom in order to avoid any flow of unburned mixture through the pipe.

Fig.3.4 shows a photo of the used porous burners. They were commercially available reticulated sponge-like structures made of SiSiC with 87% porosity. The matrix with linear pore density of 20 pores per inch (PPI) appears on the left side of the picture, while the 10-PPI matrix is on the right side.

The end shapes of the used porous burners were supplied by the manufacturer Erbicol S.A. following the presented drawing. The porous medium was produced by the replication technique. The end monolithic shape was obtained by cutting machining with high precision. Nevertheless, the dimensions of diameters and lengths of the delivered models differed by ± 1 mm.

Fig.3.5 shows a photo of PIM samples with the same material and structural parameters as used in the porous burners in the present work. The 20-PPI sample is on the left side and the 10-PPI sample on the right side. The morphological parameters measured by [7] are presented in Tab.3.1.

Table 3.1: Morphological parameters of used sponges (87% nominal ε) measured by [7]

Pores per inch PPI [1/inch]	Porosity ε [%]	Closed p. ε_{closed} [%]	Pore dia. d_p [mm]	Strut dia. t [mm]	Vol. Area S_v [1/m]
10	87.2	5.6	2.181	0.695	477
20	87.1	2.6	1.603	0.470	683

The porous burner was held by a high-temperature-insulating material made of machined alumina firebrick to reduce the heat loss from the reaction zone to the water-cooled

Figure 3.4: Photo of the used porous burners: left side 20 PPI, right side 10 PPI.

combustor housing.

The combustor module was connected with the water-cooled plenum with water-cooled flanges. An O-ring made of brass was placed between the flanges to seal the connection.

The reactor pressure was artificially increased using a throttling valve downstream. Since this valve can withstand temperatures up to 800 K, cooling of flue gases was required. For that, six sprays nozzles were used to inject atomized water into a cooling tower.

Remaining liquid water from the cooling tower was disposed regularly into the sewage system using a low/high-level signal-controlled valve. The flue gases were disposed into a gas extraction system through a silencer.
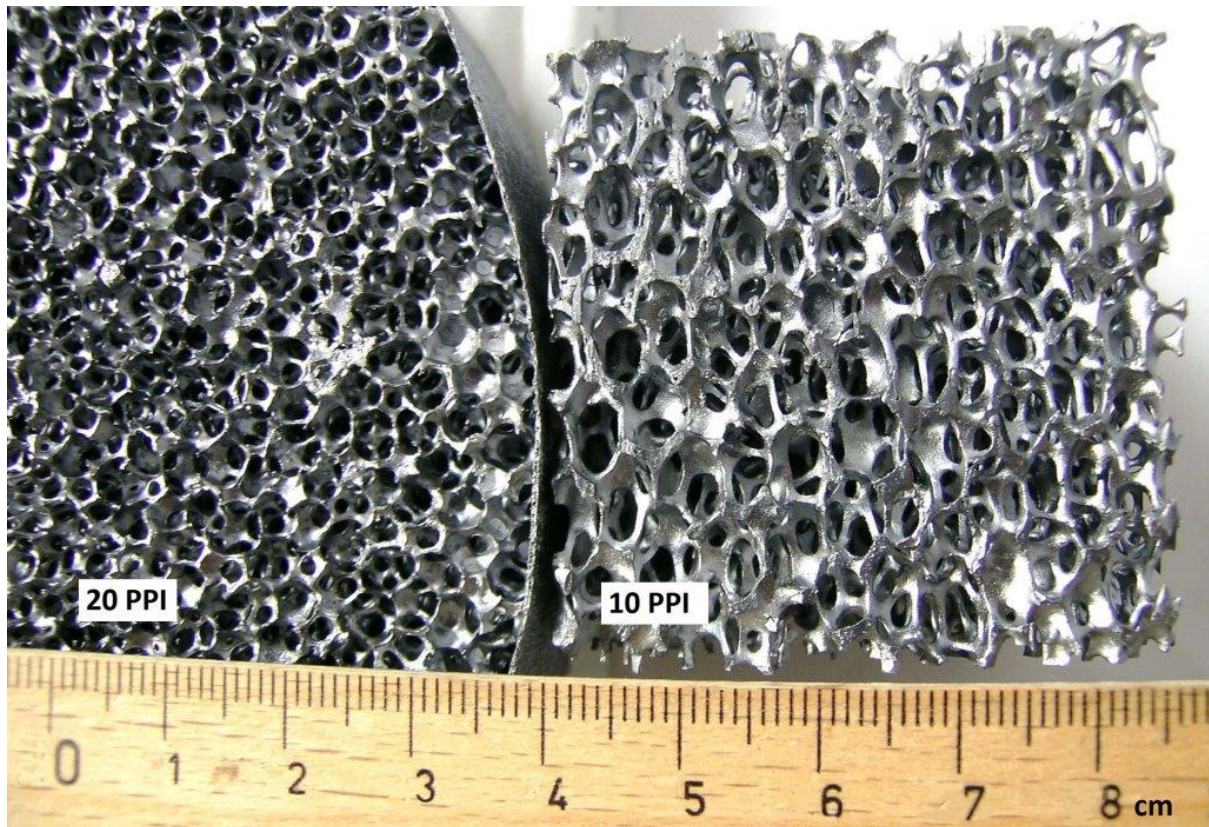
Figure 3.5: Photo of samples of the used porous structures SiSiC $\varepsilon = 87\%$: left side 20 PPI, right side 10 PPI.

3.2 Measurement techniques

To measure the natural gas mass flow rate, two different digital mass flow meters were used in series with different measuring ranges in order to provide sufficient accuracy for a wide range of power. The instruments were from the company Brooks, model S8, with accuracy of $\pm 1\%$ mass. The maximum measuring range limits were 3 and 5 kg/h. They were specially calibrated by the supplier for the chemical composition of the natural gas used.

The composition of the natural gas used is continuously adjusted by the public utility company of Karlsruhe to keep a constant Wobbe Index. We regularly monitored the composition, which is almost constant and has the following components in %Vol: 90 CH_4, 4.4 C_2H_6, 1.0 C_3H_8, 3.0 N_2, 1.6 CO_2. For this gas the lower heating value and stoichiometric air-to-fuel ratio are respectively $H_l = 45.6$ kW, $AFR_{st} = 15.65\ kg_{air}/kg_f$.

To measure the air flow rate, two flow meters in series were also used. One had the maximum range limit of 120 kg/h, with the same model and accuracy as that for natural gas. The other mass flow meter was from the company Bronkhorst, model In-Flow, with

accuracy of ± 7 kg/h and maximum limit of 1000 kg/h. All of the used flow meters were based on the calorific working principle. The temperature of unburned mixture was measured with K-type thermocouples. Piezoelectric transducers were used to measure pressure in the porous burner (measuring limits 0-20 bar).

To detect the flame position and the flame thickness, two temperature measurement configurations were used, namely, fixed thermocouples inside the PIM and a movable thermocouple inside a central closed pipe along the PIM axis. S-type thermocouples were used. The platinum and platinum-rhodium wires were 0.3 mm in diameter. The thermo wires were directed and protected against catalytic reactions by a two-hole ceramic pipe made of 99% alumina with an inner diameter of 0.6 mm and an outer diameter of 1.6 mm for the fixed thermocouples and 3 mm for the movable one. The wires were bound together at the tip by a welding pearl of approximately 0.7 mm in diameter. This type of thermo wire can withstand up to 1900 K.

A total of 32 S-type thermocouples were inserted into the PIM at fixed positions along it, for which holes of 2 mm in diameter was drilled in the PIM using a special water-cooled grip system. The location of the thermocouple pearls in the conical burner was at the mid-radii of the local cross section. Due to restrictions of space, it was not possible to align all the thermo wires in a unified angle, as can be seen in Fig.3.6. For the same reason, the axial spacing between thermocouples in the zone for flame stabilization could not have a constant value; it ranged between 4 and 9 mm at the mid-region (100-200 mm from the inlet) and up to 20 mm at the extremes. The axial, angular and radial locations of the inserted thermocouples are presented in Tab.3.2, where the axial location is referenced to the burner inlet (beginning of SiSiC), see Fig.3.7.

The configuration for measurement of temperature inside the ceramic pipe is shown in Fig.3.8. A photo from the top view of the 10-PPI sponge with the ceramic pipe is displayed in the figure, as well as a detailed view of the thermocouple inside the pipe, with the assumption that good centering was provided. The thermocouple can be displaced as desired along the burner to enable higher resolution of the temperature profile, which could not be attained with the other configuration (temperature measurement in PIM). A water-cooled system to hold and displace the temperature sensor was employed at the top of the combustor plenum.

The gas analysis system for the measurement of dried molar fractions of O_2, CO, CO_2 and NO_x consisted of a stationary gas probe, a pressure reducer, a heated hose (electric coil), a water condenser, a pump and commercial gas analyzers with their respective flow control system.

A flue gas sample was taken from the downstream end of the PIM. The probe was
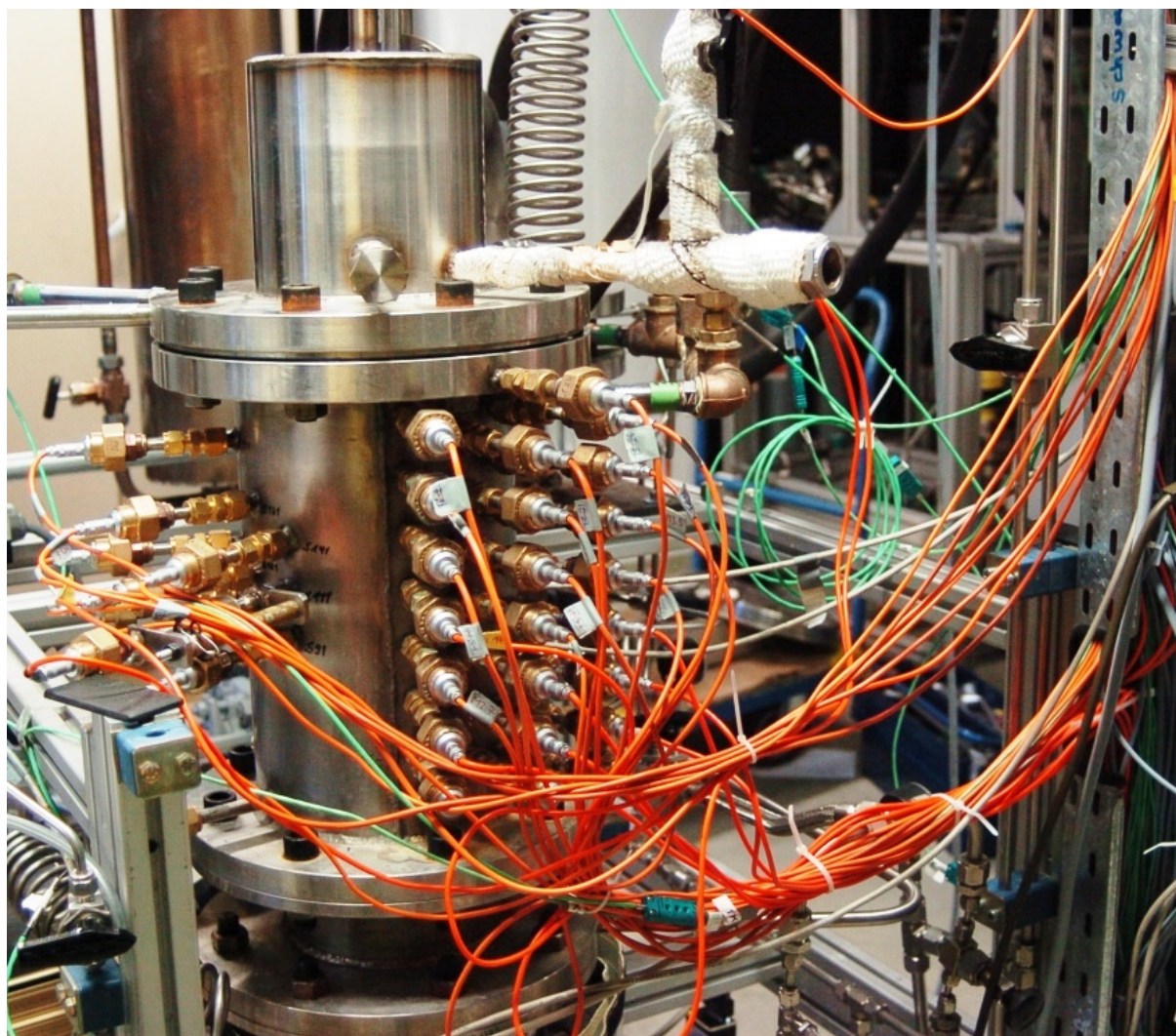
Figure 3.6: Photo of the combustor, note the ports of thermocouples in PIM.

oil-cooled and maintained at 430 K in order to avoid it melting and to prevent the condensation of water at elevated pressure in the probe. After the pressure was reduced down to 1.1 bar, the transport line to the condenser was maintained at 400 K. The dried sample was split in two branches: one for the analysis of NO_x and the other for the analysis of the other species.

The NO_x analyzer was from the company Eco Physics, model CLD 700 EL h, based on chemiluminescence. Its accuracy is ± 0.1 ppm. It measures NO and NO_x and has its own flow control system. The range 0-100 ppm was used.

CO_2 and CO were measured with commercial gas analyzers (Leybold-Heraeus Binos) working on the basis of infrared absorption with accuracies of $\pm 0.2\%$ and ± 7 ppm, respectively. O_2 was measured with a Leybold-Heraeus Oxinos gas analyzer on the basis of paramagnetism ($\pm 0.25\%$). The measuring ranges used were 0-15% CO_2, 0-300
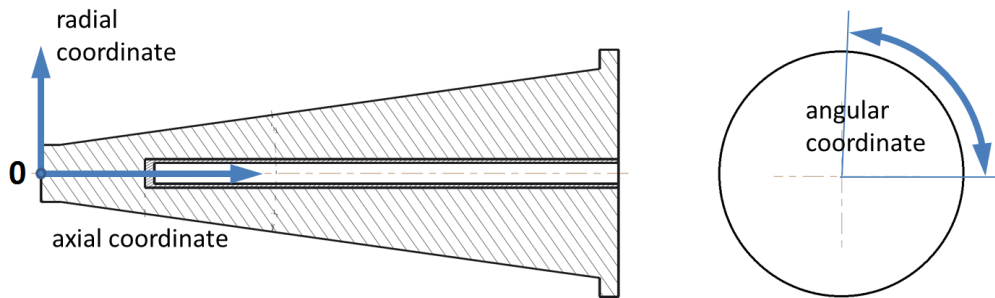
Figure 3.7: Schema of coordinated reference system used for dimensions in Tab.3.2.
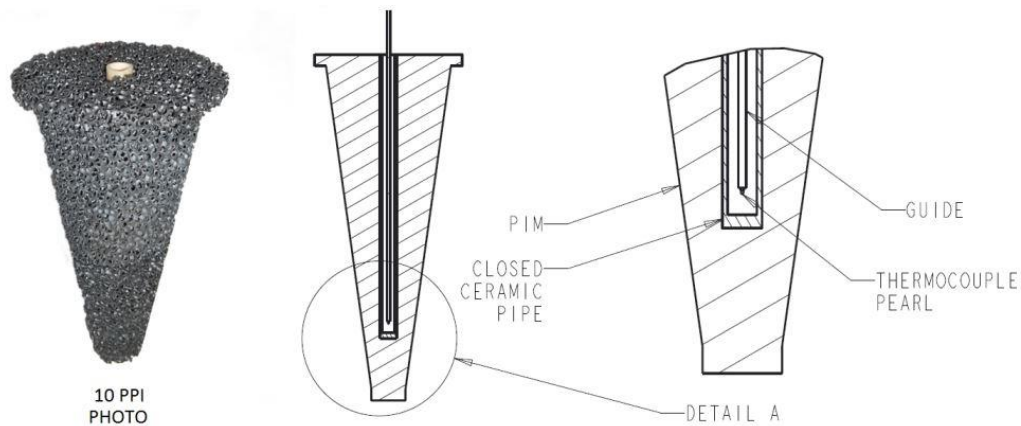

Figure 3.8: Detail of temperature measurement in the ceramic pipe

ppm CO and 0-25% O_2.

The flow was set to 10 liters/min at 1.1 bar using a regulating valve and a rotamer. A pump needed to be mounted upstream for the experiments driven at atmospheric pressure. The analyzers were calibrated every day before measurements using special manufactured gases. Nitrogen at 99.999% was used for calibration of the zero value and, for the end value, mixtures of 15.02% CO_2 and 398 ppm CO in nitrogen, 20.5% O_2 in nitrogen and 99 ppm NO_2 in nitrogen with a relative deviation of 0.5% were separately used.

Experimental procedure: The flame was ignited at atmospheric pressure from the PIM exit with a hydrogen diffusion flame. After ignition, the flame propagates upstream and stabilizes within the conical PIM. For a given operating condition, the flame was considered stable, if the axial temperature distribution was constant for more than five minutes, that is, the maximum variation in the temperature at each location of the flame was less than 2.0% during that time. The sample of flue gases flowed continuously and was continuously analyzed.
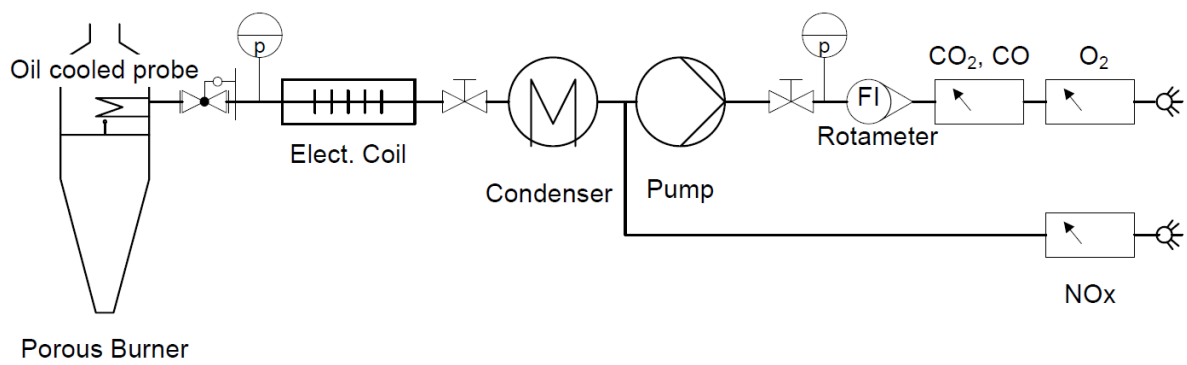
Figure 3.9: Flow diagram of the used gas analysis system

Table 3.2: Locations of the temperature measurement in PIM, reference system shown in Fig.3.7, error ± 0.7 mm

Nr.	Axial location [mm]	Angle [°]	Radial location [mm]	PIM outer diameter [mm]
1	11	0	7.6	30.3
2	19	20	8.1	32.6
3	27	40	8.7	34.8
4	46	0	10.0	40.1
5	56	20	10.7	42.9
6	65	40	11.4	45.5
7	80	0	12.4	49.7
8	93	20	13.3	53.3
9	103	40	14.0	56.1
10	107	90	14.3	57.3
11	111	110	14.6	58.4
12	116	0	14.9	59.8
13	120	130	15.2	60.9
14	130	20	15.9	63.7
15	137	90	16.4	65.7
16	141	40	16.7	66.8
17	146	110	17.1	68.2
18	151	0	17.4	69.6
19	159	130	18.0	71.9
20	167	20	18.5	74.1
21	173	90	19.0	75.8
22	179	40	19.4	77.5
23	186	0	19.9	79.5
24	194	110	20.4	81.7
25	203	20	21.1	84.2
26	217	40	22.0	88.2
27	221	0	22.3	89.3
28	231	110	23.0	92.1
29	241	20	23.7	94.9
30	255	40	24.7	98.9
31	256	0	24.8	99.1
32	284	20	26.8	107.0

Chapter 4

Experimental results and evaluation

The experiments were performed with premixed natural gas-air mixtures at lean conditions ($\lambda > 1.4$) using two burner pore densities, namely, 10 and 20 PPI. The operating pressure was varied in the range of $1 - 14$ bar. Pressure is reported in absolute values. Measured data are reported as the time average of data recorded at 3 Hz over three minutes after the steady state of the flame was ensured. Only results of flames stabilized at the mid-region of the PIM ($60 - 200$ mm axial distance from PIM inlet) under steady conditions are reported. ft The quality of the experimental work was evaluated by comparing the air factor obtained from flow rate measurements of air and fuel against that obtained from a calculation based on the flue gas analysis (CO_2, CO and O_2), the results for inlet temperature of $T_u = 300$ K are shown in Fig.4.1, where the lines represent differences of 10% with respect to the equality. Results outside this range were dismissed. The air factor calculated from the analysis of sample gases taken downstream of the porous burner allowed for a slightly higher accuracy that obtained from the mass flow meters, so the air-to-fuel ratio calculated from gas analysis was reported here and used to calculate the burning velocity.

The main reported results are burning velocity values at elevated pressure for different air-to-fuel ratios and preheating temperatures obtained from the acquisition of the flame location using thermocouples located at the mid-radii of the PIM (named measurements of PIM temperature). Using these temperature measurements, some representative results of the thermal flame thickness were also obtained.

The results obtained from the flame stabilization within the 10-PPI burner are presented first. The results obtained with the 20-PPI burner are presented only in Section 4.5, in which the effect of the pore density on the burning velocity is presented.
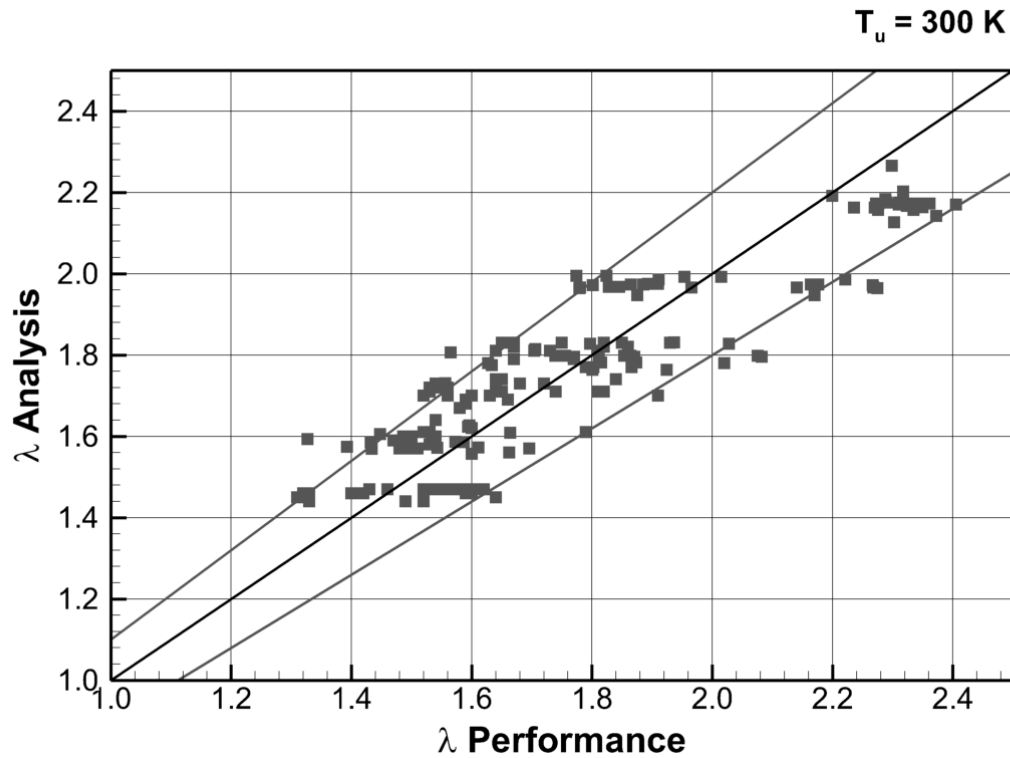
Figure 4.1: Quality of measurements: comparison of air factor obtained from mass flow measurements against that from flue gas analysis.

4.1 Temperature measurements in PIM

In this section, temperature measurements obtained from fixed thermocouples inserted at the mid-radii in the PIM are presented. Fig.4.2 shows an example of a measured temperature profile along the spatial coordinate perpendicular to the idealized planar flame surface under steady conditions and $\lambda = 1.6$, $T_0 = 300\ K$ and $p = 1.0\ bar$. The zero position of the spatial coordinate represents the beginning of the PIM (SiSiC). For comparison, the temperature profile of a laminar free flame of air-methane mixture under the same conditions is also displayed, which was calculated for a planar laminar premixed flame with the PREMIX code of the CHEMKIN package [39] using GRI mech 3.0 [41].

In all experiments, a considerably smoother temperature profile was observed in flames stabilized within PIM with respect to the laminar free flame. Additionally, the maximum temperature achieved was higher than the adiabatic flame temperature. From this, it can be concluded that the heat loss from the used burner does not have a considerable influence on the flame front, owing to the lateral isolation and that the flame location was in the mid-region of PIM. The maximum measured temperature slightly exceeds

the adiabatic combustion temperature due to heat recirculating through the solid porous matrix. Since the measuring thermocouple is surrounded by the porous medium, this measurement is influenced by the heat exchange by radiation between the thermocouple pearl and the surrounding PIM; as a consequence, the gas temperature should locally be slightly higher.
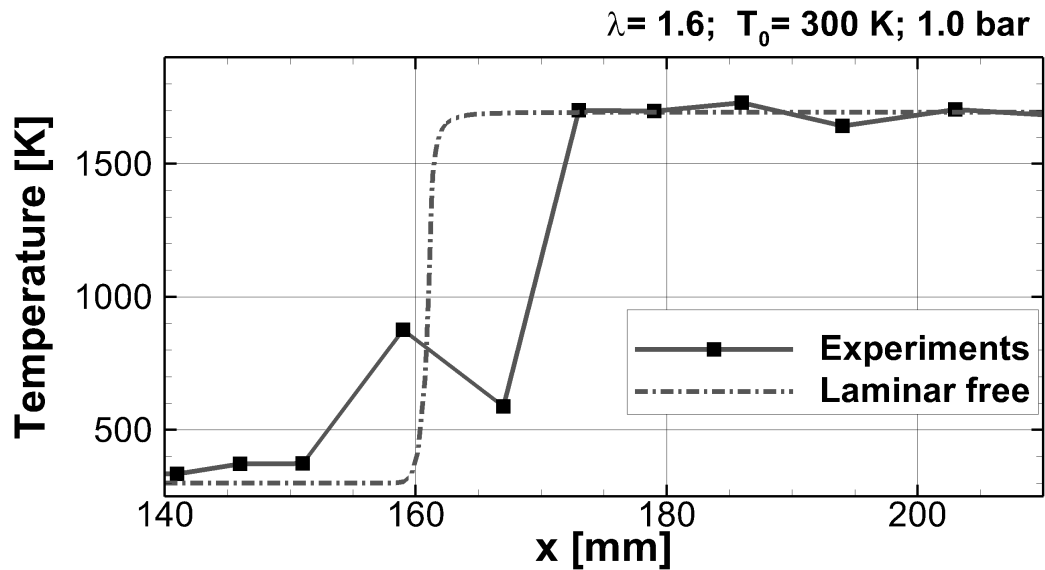

Figure 4.2: Axial PIM temperature profile along 10-PPI PIM, λ=1.6, 1.0 bar, T_0= 300 K, $u_0 = 5.4 \ m/s$.

The temperature profile shown in Fig.4.2 is an exemplary case of a commonly observed situation where the temperature profile was not continuously increasing. One should bear in mind that temperature was measured at few points in the reaction zone and the locations did not correspond to the same streamline, since the location angles differed, although the radii were nearly the same. These temperature measurements demonstrate that both temperature distributions and the flame structure are discontinuous, as was suggested by Viskanta [3, 4] and predicted by Bedoya et al. [20].

Measured PIM temperature profiles for different air factors are presented in Fig.4.3 at 1.0 bar and 300 K. At a higher air factor, the location of the flame front was shifted downstream in the conical burner, which implies a decrease in the burning velocity. In Fig.4.3, it is observed that an increase of the air factor also leads to flattening of the temperature profiles. These effects of varying air factor on the temperature profiles and on the burning velocity occur similarly to those known from laminar free flames.

The flame stability limit of the used 10-PPI burner was investigated at 1.0 *bar* and 300 *K*. In order to acquire the stability limit, the air factor was increased in steps of

≈ 0.2 until the measured CO concentration began to rise or the flame was not stable. Up to an air factor of $\lambda= 2.2$, the flame was stable and the CO molar fraction was lower than 30 ppm. At these conditions, the adiabatic flame temperature of methane/air mixtures is 1390 K, while the measured peak temperature was 20 K higher, owing to heat recirculation through the porous solid matrix by conduction and radiation.

When increasing the air factor beyond the flame stability limit, the CO emissions progressively increased and the flame front displaced downstream with a very low flame front velocity below 1 mm/s. For this condition (i.e. $\lambda= 2.35$), the CO molar fraction acquired was increased up to 120 ppm.
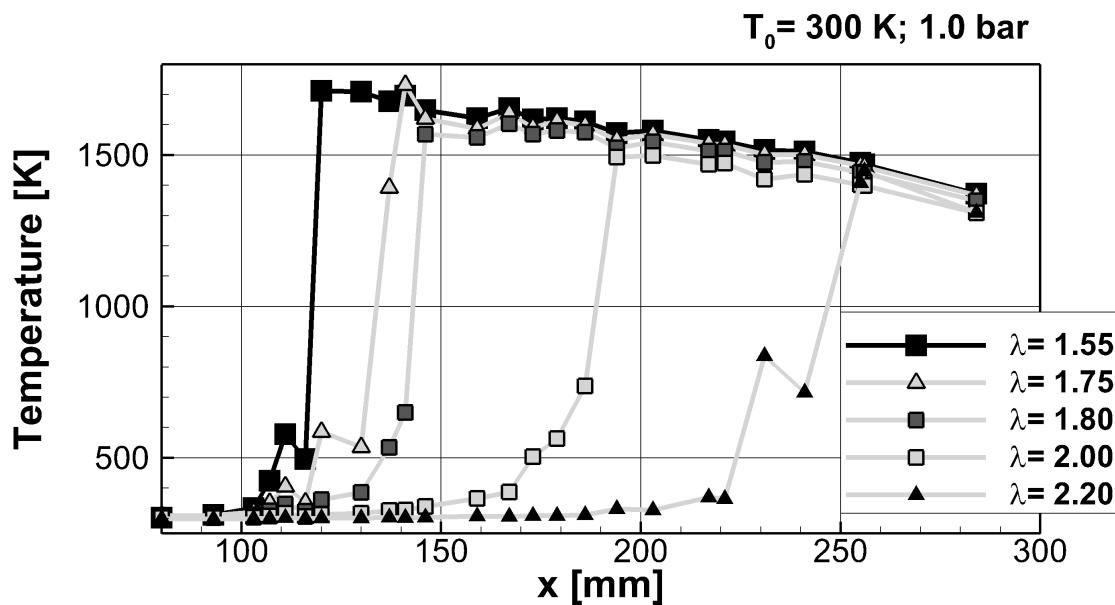

Figure 4.3: Axial PIM temperature profile along 10-PPI PIM, 1.0 bar, $T_0 = 300 K$.

Fig.4.4 presents the PIM temperature profiles for different pressure levels at $\lambda= 1.60$, $T_0 = 300K$ and nearly constant inlet velocity $u_0 = 5.25 m/s$. A substantial flame displacement in the downstream direction was observed with the increase in pressure from 5 to 8 bar; which indicates that the burning velocity should be lower at higher pressure, as occurs in the laminar free combustion mode. Nevertheless, the flame location did not varied significantly at lower pressure ranges, even the flame location was shifted in opposite direction while increasing pressure from 3.0 to 4.0 bar, thus it can be inferred that the burning velocity did not varied considerably at pressure levels below 5.0 bar, which is different from the effect of pressure on the laminar burning velocity of free flames S_l, where the pressure effect is more notorious at smaller pressure values.
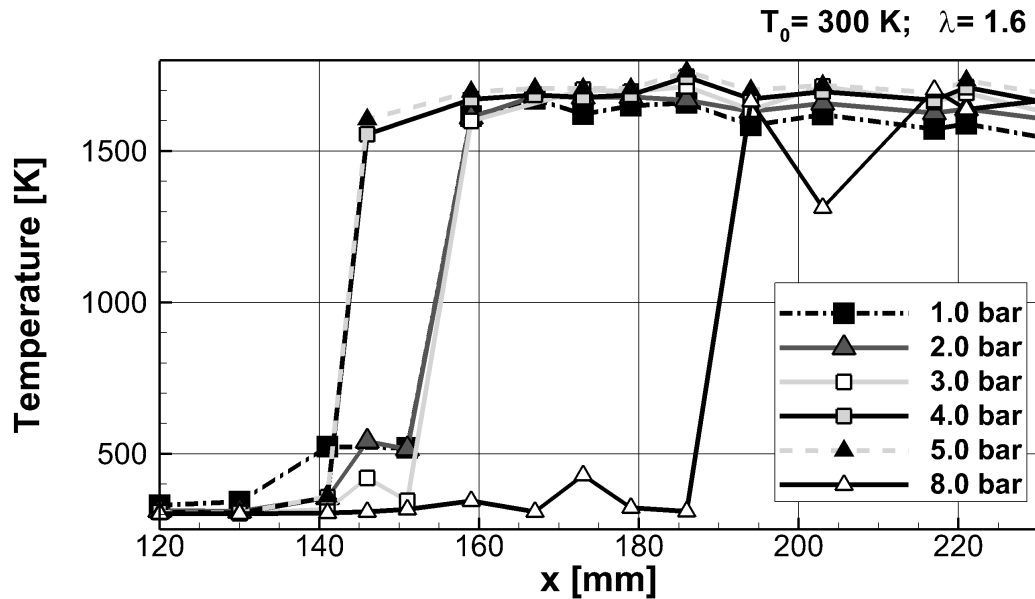
Figure 4.4: Axial PIM temperature profile along 10-PPI PIM at different pressure levels $u_0 = 5.25 \ m/s$, $\lambda= 1.60$, T_0=300 K.

4.2 Thermal flame thickness

Most of the measured temperature profiles exhibit non-continuous increase of tempera-ture. It was expected that the reaction could occur homogeneously and the flame was nearly flat, but this was not the case. The observed temperature heterogeneity indicates that the structure of flames stabilized within PIM is corrugated at the pore level, con-forming to the PIM structure, and the complex flow patterns imposed by considerable temperature deviations in space are presented.

Owing to this heterogeneity and the fact that it was not possible to place a larger number of thermocouples in the reaction zone, the evaluation of the flame thickness is complicated. A possible definition of the flame thickness is the region where the temperature increased from $(1.05 \cdot T_0)$ to $(0.95 \cdot T_{max})$. For example, in Fig.4.2, it corresponded to the x locations of 150 and 173 mm, respectively, so the flame thickness was 23 mm. However, this definition is too arbitrary owing to the low measurement resolution and it neglects the observed measurements inside the flame region. The definition of flame thickness based on the maximum temperature gradient Eq.(2.18), that is, thermal flame thickness, yields a value of 7 mm.

A more accurate determination procedure is to perform extensive repetitions of experi-ments and average the resulting thermal flame thicknesses.

In the present work, the flow rate was varied in order to stabilize the flame at different

locations, while the other properties were maintained nearly constant. The thermal flame thickness was obtained as an average of those results with the expectation that the flow rate was not a factor influencing the flame thickness. The thermal flame thickness was calculated using Eq.(2.18):

$$\delta = (T_{max} - T_u)/\max(\partial T/\partial x)$$

The results show that the maximum measured temperature did not differ considerably with the change of mass flow rate (less than 40 K). Neither the differences in the maximum temperature nor in the maximum acquired temperature gradient were correlated with the variation of the flow rate, as expected, since the burner is well insulated and the differences are in the range of error of the used measuring technique. An example of the results of this kind of experiments, where the inlet velocity is varied and all other parameters are kept constant is shown in Fig.4.5, which shows the temperature inside the PIM along the axis for different inlet velocities at $\lambda = 1.60$, $T_u = 300\ K$ and $1.1\ bar$. The calculated adiabatic temperature of combustion is also shown in this figure. Notice that for all experiments the maximum temperature is considerably near the adiabatic one.
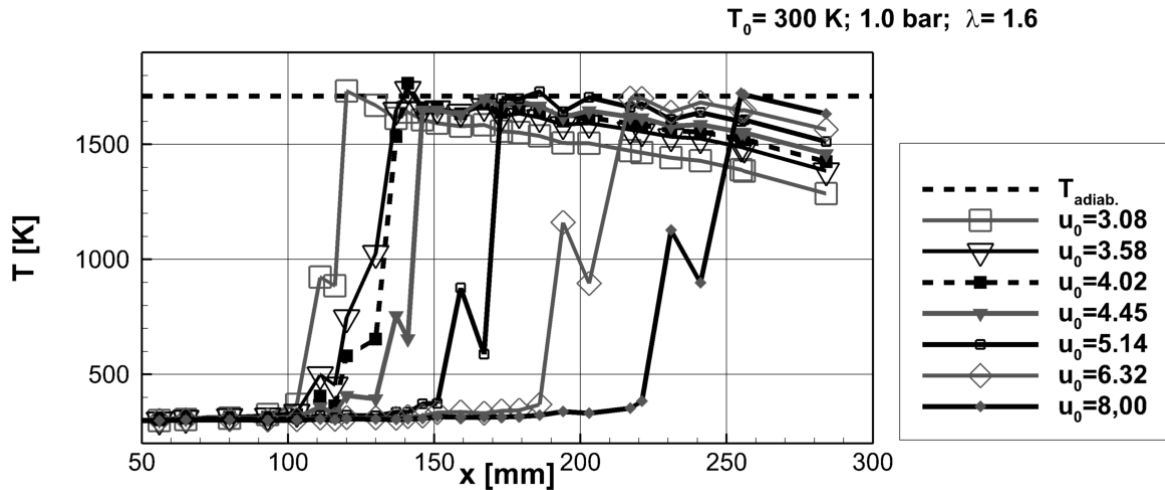

Figure 4.5: Temperature profiles for different inlet velocities u_0 in m/s 10-PPI PIM at $\lambda = 1.6$ $1.1\ bar$ and $T_0 = 300\ K$.

Fig.4.6 shows the thermal flame thickness of different tested air factors at 1.0 bar and $T_0 = 300$ K for several repetitions, varying the mixture flow rate. As reference, the figure shows comparison to the thermal flame thickness of free laminar flames too (based on the same definition of Eq.(2.18)).

The obtained averaged thickness of stable flames within PIM was considerably higher
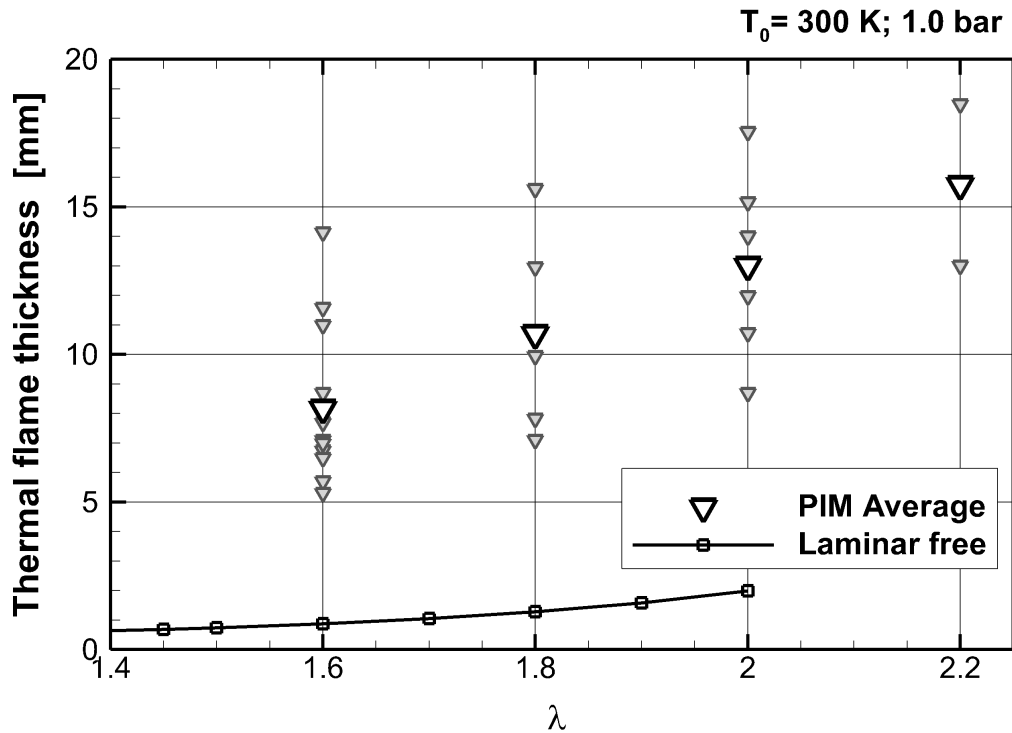
Figure 4.6: Thermal flame thickness 10-PPI PIM at 1.0 bar and T_0= 300 K.

than in the free laminar combustion mode. It increased by a factor of seven, approximately, which is also the ratio of burning velocity increase from experimental results reported in the literature under the same conditions [15].

4.3 Temperature measurements in central pipe

The identification of the effects of pressure on the characteristics of flame stabilization within PIM is the novelty of the present work. Measurements of temperature in PIM did not produce representative results to draw a conclusion on the influence of pressure on the flame thickness.

Compared with the complications encountered when determining the flame thickness from the temperature measurements in PIM, the measurement of temperature in a closed ceramic pipe along the PIM axis appears to have two main advantages. First, the measurement is in the axis and is radially encapsulated; thus, it is influenced by the whole circumference of the surrounding pipe. Second, the axial displacement enables the desired profile resolution to obtain a clean profile of the temperature gradient in the pipe.

The pipe temperature was measured with a resolution of 4 mm. Two minutes had to elapse from every sensor displacement to achieve a nearly steady record.
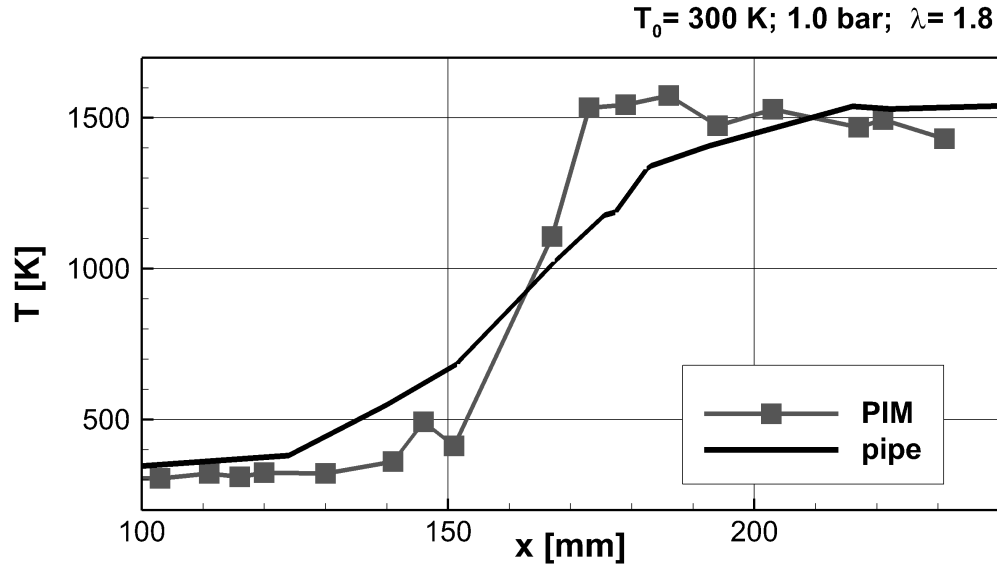

Figure 4.7: Axial profile of pipe temperature along 10-PPI PIM compared with the temperature in PIM at $\lambda= 1.6$, 1.0 bar and $T_0=300$K.

The obtained temperature profile is compared in Fig.4.7 with the temperature measurements in PIM taken with the fixed sensors. The profile of pipe temperature is clearly more homogeneous than the measured temperature in PIM; a Gaussian shape of the temperature gradient profile could be clearly observed. Nevertheless, it is flatter. The reason is that the sensor is influenced by heat exchange by radiation with a region inside the ceramic pipe that is considerably bigger than the region affecting the measurement inside the porous media, as shown in Fig.4.8.

4.3.1   Gradient of temperature in central pipe

The maximum gradient of the pipe temperature was used as an indication of the inverse of the flame thickness analogously to the flame thickness definition in Eq.(2.18). Although the measurements of temperature in pipe differ considerably from measurements in PIM, the obtained results enabled the formulation of qualitative statements about the effects on the flame thickness of physical parameters such as pressure.

The gradient profiles of pipe temperature at different air factors are depicted in Fig.4.9. In agreement with the measurements of temperature in PIM, this figure indicates that the maximum temperature gradient decreases with increasing air-to-fuel ratio, that is, the flame thickness is enlarged.
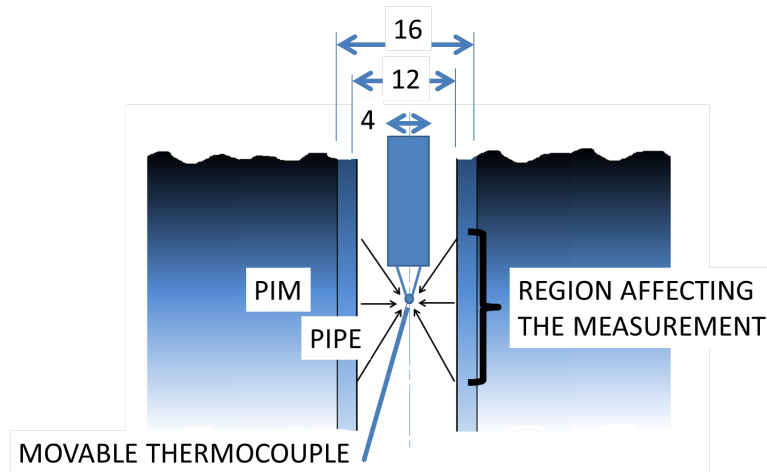
Figure 4.8: Sketch of the temperature measurement with the movable thermocouple. Dimension: mm.
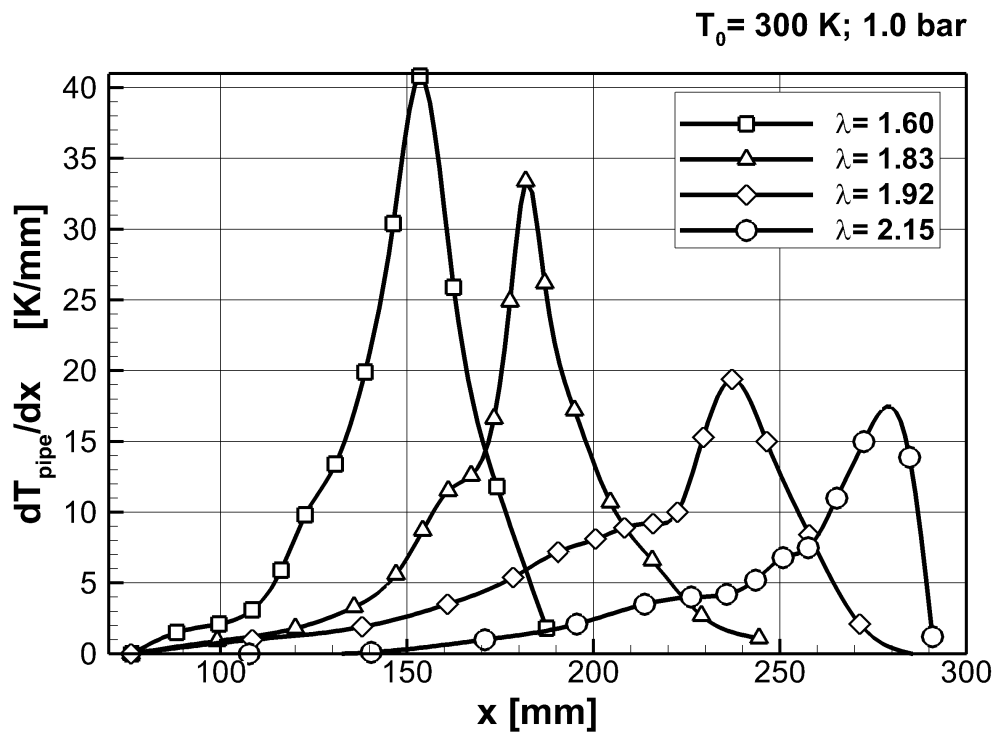
Figure 4.9: Axial gradients of pipe temperature along 10-PPI PIM at 1.0 bar and T_0= 300 K.

Fig.4.10 presents the effect of pressure on the maximum gradient of pipe temperature for two different air factors: λ= 1.6 and 1.8. At λ= 1.6, a considerable increase in the maximum pipe temperature gradient was observed with the increase of pressure from 5 to 8 bar. Consequently, the flame became considerably thinner in this pressure range. The flame position was also shifted downstream a significant distance with this increase

in pressure (see Fig.4.4), that is, the burning velocity value considerably decreased in this pressure range as well.
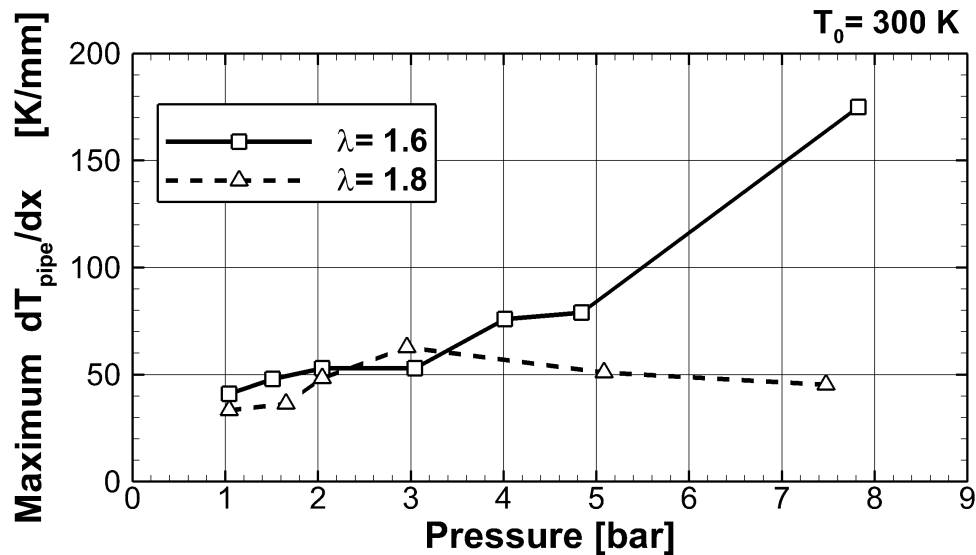
Figure 4.10: Axial gradients of pipe temperature along 10-PPI PIM at $\lambda=$ 1.6 and $\lambda=$ 1.8; $T_0=$ 300 K.

At $\lambda=$ 1.8, the maximum temperature gradient substantially increased with pressure in the pressure range between 1.5 and 3 bar (see Fig.4.10), where a substantial burning velocity decrease was also observed (see Fig.4.14).

From these measurements, it is concluded that the decrease of the flame thickness in flames stabilized within PIM was associated with a consequent decrease of the burning velocity, similarly to that in free laminar flames, with the difference that it occurred at higher pressure levels. The variation of the flow rate did not present any effect on the temperature gradient acquired in the central closed ceramic pipe.

4.3.2 Combustion instabilities

With the use of this temperature measurement technique in a central closed pipe, combustion instabilities could be detected for some operative conditions: elevated combustion temperature 1700 K ($T_0 = 300 K$ and $\lambda = 1.6$) and moderately elevated pressure 3-6 bar. The temperature signal in any of the measured locations inside the macroscopic reaction region, that is, when the sensor indicated an average temperature in the range of 700-1300 K, showed a sinusoidal curve with time, with an amplitude of approximately 50 K and a wave period of five seconds. In contrast, the measurements of temperature at fixed locations inside the PIM did not show any fluctuation with the used acquisition rate.

For the other experiments, namely, lower combustion temperature, no instabilities were detected.

In order to estimate the behavior of this combustion mode with instabilities, consider that for any reason there is a region of the cross sectional area A_{pim} where temperature increased. This condition has as consequence an increase of the flow resistance in this region. The flame front will displace upstream. In the upstream region will reach cold solid and gas phases and therefore will loose heat. For this reason, temperature of this region will drop and the flame front will be shifted back downstream. The downstream region is the burned zone wehre the flame front reaches hot surrounding solid phase. Heat will be transferred more intensively to the incoming fresh mixture, temperature of this region will increase again and the burning velocity increases as well, originating a cyclic operation mode.

An energy balance analysis of the solid phase in the combustion zone yields that the heat transfer rate is equal to the enthalpy change rate of the solid phase:

$$\lambda_s \cdot A_{pim} \cdot \frac{\Delta T_s}{\Delta x} = m_s \cdot c_{p,s} \cdot \frac{\Delta T_s}{\Delta t} \qquad (4.1)$$

Replace the mass of solid for its respective volume and density: $m_s = \rho_s \cdot \Delta x \cdot A_{pim}$, it yields for the time period of this process:

$$\Delta t = (\Delta x)^2 \cdot \frac{\rho_s \cdot c_{p,s}}{\lambda_s} \qquad (4.2)$$

Consider 1000 K as the mid temperature of the combustion region Δx for determining property values of the solid phase, $\frac{\lambda_s}{\rho_s \cdot c_{p,s}}(1000 K) = 0.12 \ cm^2/s$ [191] and as combustion region the thermal thickness value obtained from present experiments for an air factor of $\lambda = 1.6$ in Fig.4.6, $\Delta x = \delta = 0.8 \ cm$. Then, a value of time period of $\Delta t = 5,3 \ s$

is obtained, which is the same value of the time period of the observed phenomenon of instabilities.

4.4   Burning velocity

The used burner was constructed with a conical shape with the expectation that, with the acquisition of the location of a stable flame, the possibility of determining the burning velocity could be provided, since the burning velocity is one of the most important combustion parameters of premixed flames.

In the laminar free combustion mode, the laminar burning velocity S_l must be equal to the velocity of unburned gas that enters the flame in a direction normal to the flame front, to attain the flame in a stationary location $u_u = S_l$ [29].

This definition has been used in numerical studies of flame stabilization within PIM with a constant cross-sectional shape burner using a 1D model, and has been proven with experiments at the flame stability limit of lean blow-off in a two-layer burner at quasi-adiabatic condition around the reaction zone [15].

In the case of PIM combustion, there are two possibilities to define S as being equal to the superficial velocity u or the interstitial velocity u_g, where $u = u_g \cdot \varepsilon$. The superficial S comprises both solid and gas phase areas.

$$S = u_u \tag{4.3}$$

Although combustion takes place only in the gas phase, the superficial velocity is chosen in this study, in order to report burning velocity values that can easily be used for technical design purposes. These values are directly related to the superficial firing rate (see Eq.(1.1)).

The complication of obtaining the burning velocity for combustion within a conical PIM is the formulation of an approach that can yield comparable values to the ones obtained in a burner with constant cross-sectional area. Therefore, a unified definition of burning velocity is necessary to allow the comparison of results obtained from burners with different geometries.

In the conical burner, the mean velocity of gases decreases along the burner, as shown in Fig.4.11, where it is compared with that in a burner with constant cross-sectional area, named a cylindrical burner. Owing to the isobar expansion, the velocity of gases is increased at the flame front.

A possible definition comprises the mass flow rate, the cross-sectional area of the burner A_{pim} at the flame location x_f (must be defined as well) using continuity in Eq.(4.4), and the density of the unburned mixture ρ_0, according to the S_l definition of laminar planar free flames.

$$\dot{m} = \rho_0 \cdot u_0 \cdot A_{PIM}(x_0)$$
$$\dot{m} = \rho_0 \cdot u_u^{T_0}(x_f) \cdot A_{PIM}(x_f) \tag{4.4}$$
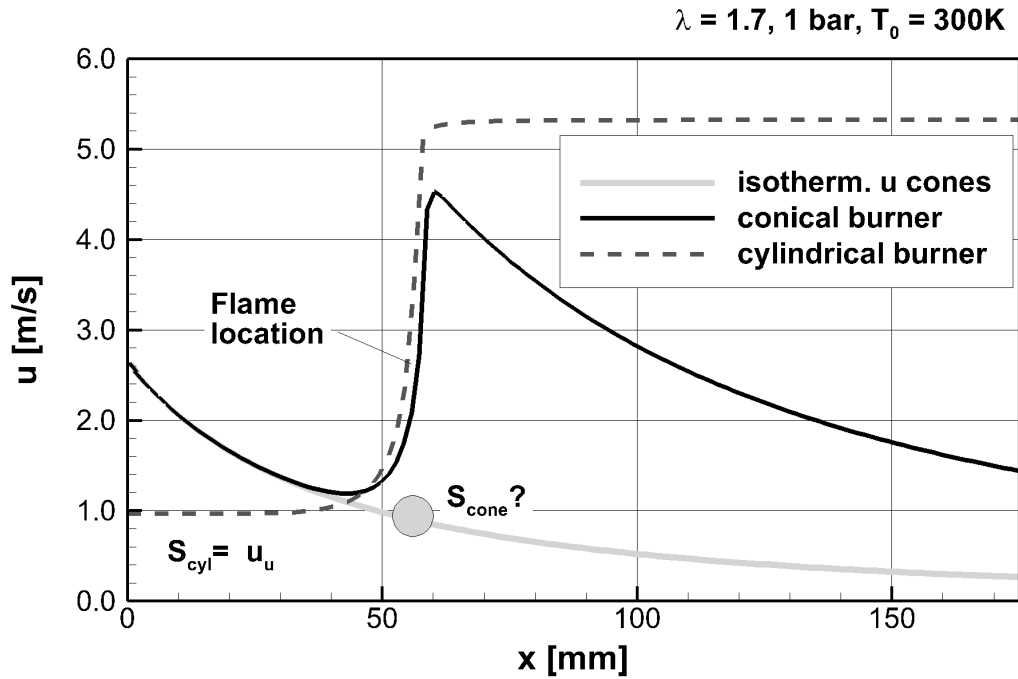
Figure 4.11: Isothermal profile of gas velocity along the conical burner compared with the velocity profiles in the conical and cylindrical burners: 10-PPI PIM, 1.0 bar, T_0= 300 K.

where u^{T_0} is the velocity at constant temperature T_0, which is also presented in Fig.4.11 and named the isothermal velocity. From the definition of flame stability:

$$S = u_u^{T_0}(x_f) \tag{4.5}$$

and using Eq.(4.4), the burning velocity is given as Eq.(4.6),

$$S = \dot{m}/(A_{pim}(x_f) \cdot \rho_0) \tag{4.6}$$

where x_f represents the flame position that has to be defined in the case of burners with

variable cross-sectional area, such as the conical burner used here. In the present work, the flame location was experimentally acquired using thermocouples; thus, the flame location is defined as the location where 50% of the total temperature rise occurs. Owing to the low resolution of temperature profile acquisition, the flame location definition is the cause of the highest error in the measurements, which yield a maximum error of 12% for the burning velocity.

The flow rate was determined by the measured fuel mass flow rate and the air-to-fuel ratio AFR obtained from the flue gas sample analysis. Although the air flow rate was also measured, higher accuracy was provide by the analysis of flue gases, while comparing the measured flame temperatures with the adiabatic combustion temperatures.

$$\dot{m} = \dot{m}_f \cdot (AFR + 1) \tag{4.7}$$

An important factor for the flame stabilization is the preheating effect of the premixed fuel/air mixture, which is positively influenced by heat recirculation through the solid porous matrix and the contribution of hydrodynamic dispersion in the gas flow. In contrast, if the reaction zone is being cooled by external heat sinks, the heat feedback from the reaction zone to the preheating zone decreases. Therefore, for determination of the burning velocity, the adiabatic condition around the reaction zone is mandatory, that is, the flame must be located far enough from the exit porous matrix surface to minimize the cooling effect on the reaction zone due to radiative heat transfer from the porous surface to the internal walls of the plenum housing, which is water-cooled. Thus, a minimum gap of 60 mm was kept between the flame location and the PIM exit surface in the present work.

Nevertheless, radial heat losses through the lateral high-temperature insulation are inevitable. They can be minimized with respect to the input power with the increase of the flow rate of unburned mixture. Consequently, the flame location should be displaced downstream from the conical burner inlet. That is, the studied flames were located at least 100 mm from the inlet. It should be borne in mind that the length of the tested porous burner was 300 mm in total.

The increase of the sensible enthalpy of the cooling fluid circulating through the double-walled lateral combustor housing was calculated from measured coolant temperatures and coolant flow rate. Although this quantity is related to the heat loss from the whole burner in the radial direction, it can be used as an indication of the heat loss from the reaction zone.

With adiabatic boundaries, numerical studies of combustion within homogeneous PIM

with constant cross-sectional area predict a unique condition, in which the flame is stabilized without the use of special stabilization techniques [15, 172]. Consequently, it is expected that the burning velocity does not vary with the change of flow rate in the used conical burner, that is, the flame location should vary.

Experiments of variation of the flow rate were performed at $T_0 = 300\ K$ and approximately 1.1 bar for different air-to-fuel ratios. The results of burning velocity S are presented in Fig.4.12 as a function of the burner inlet bulk velocity u_0 (the burner inlet had a diameter of 30 mm).

At the lowest tested air factor, namely, $\lambda = 1.45$, owing to the high burning velocity, the variation of flow rate was limited to a ratio of two because higher flow rates increased the combustor pressure above 15%. For leaner mixtures, the pressure did not increase as much.

The most important feature of Fig.4.12 that merits discussion is that, with the exception of the lowest tested air factor $\lambda = 1.45$, the burning velocity was not influenced by the flow rate, as predicted for the adiabatic condition [15, 172].

The reason for the increase of burning velocity at $\lambda = 1.45$ with the increase of inlet velocity is that the radial heat loss from the reaction zone is large relative to the input power. $\lambda = 1.45$ exhibits the highest tested combustion temperature and for the lowest tested input power, the relative radial heat loss from the burner was 35% with respect to the input power, and for the highest tested input power, it was 22%. In contrast, for the next highest air factor tested, $\lambda = 1.60$, the relative radial heat loss possesses a maximum of 20%.

Therefore, the adiabaticity of the used facility was proven for the determination of the burning velocity for combustion temperatures below 1750 K, which is the temperature too, above which the active oxidation of the used porous material SiSiC is presented.

Fig.4.13 shows the variation of S in the PIM with the air factor λ at atmospheric conditions $T_0 = 300$ K, 1.0 bar, obtained from experiments and compared with experiments in porous burners in the literature [15, 192] using the same PIM as used here. The laminar burning velocity of free premixed flames S_l is also shown as a reference. S_l was calculated with PREMIX [39] using GRI mech 3.0 [41].

These experiments were carried out at constant thermal load while varying the air flow rate. Djordjevic et al. [15] measured the burning velocity at the flame stability limit of lean blow-off using a cylindrical burner with two porous layers: flame trap (45-PPI partially stabilized zirconia) and combustion layer (10-PPI SiSiC).

Diezinger [192] reported temperature profiles in steady flames in a conical PIM with the
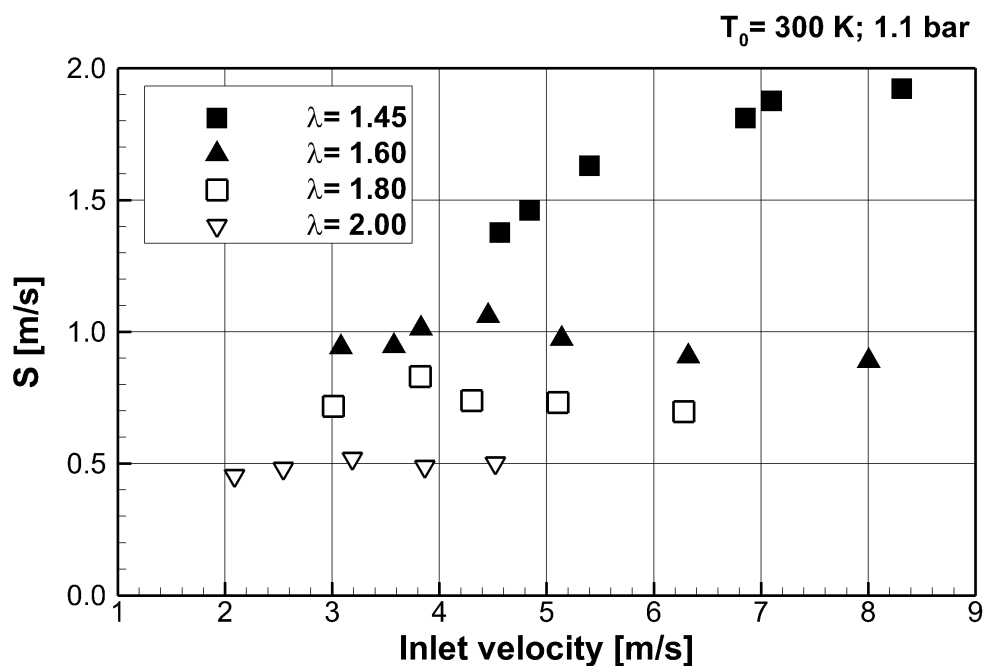
T₀= 300 K; 1.1 bar

Figure 4.12: Burning velocity at atmospheric conditions as a function of the velocity at the burner inlet, 10-PPI PIM, $T_0 = 300K$, 1.01.1 bar.
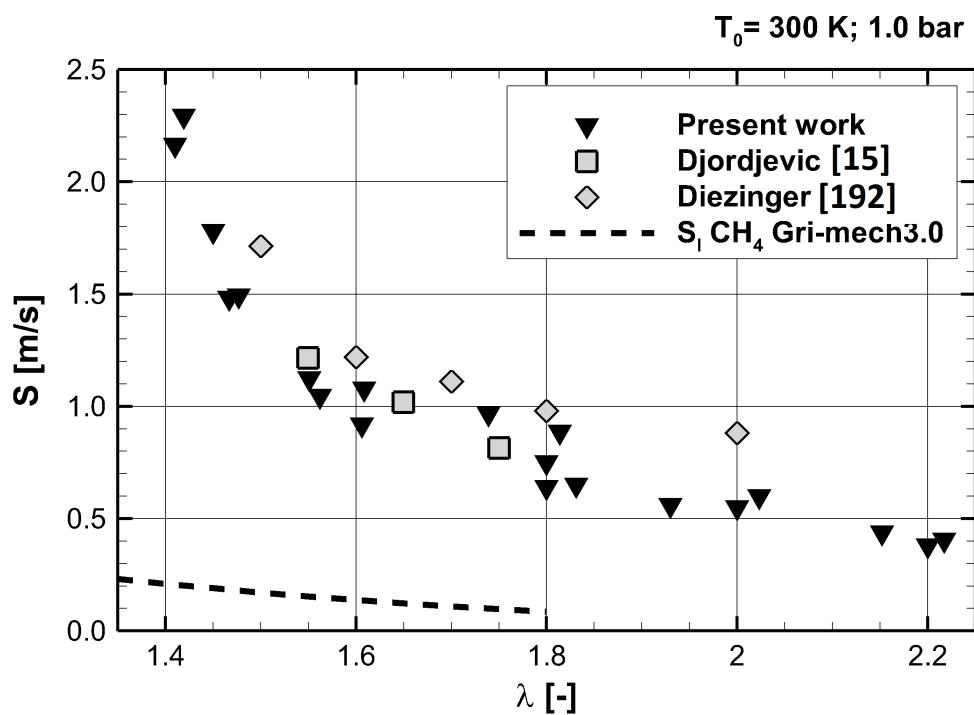
T₀= 300 K; 1.0 bar

Figure 4.13: Burning velocity at atmospheric conditions as a function of air factor, 10-PPI PIM, T_0= 300 K, 1.0 bar.

same structure and material as used in the present work. In order to compare these data with the present ones, the burning velocity was extracted from the published data by using the present evaluation procedure based on the temperature profiles.

It is important to note that, compared with S_l of free laminar flames, the measured burning velocity S in PIM is considerably greater (from 7 to 10 times) and that the experimental results satisfactory agree with each other even with different burner geometric configurations. Since the same definition of burning velocity was used and relative heat losses were low, the comparability of geometrically different burners is validated by this result.

Experimental study of the influence of pressure on the flame stabilization in PIM was carried out by keeping constant the other parameters, such as air-to-fuel ratio and unburned gas temperature T_0. Additionally, the inlet velocity u_0 was kept constant, which implies a proportional increase of the mass flow rate related to the pressure increase.
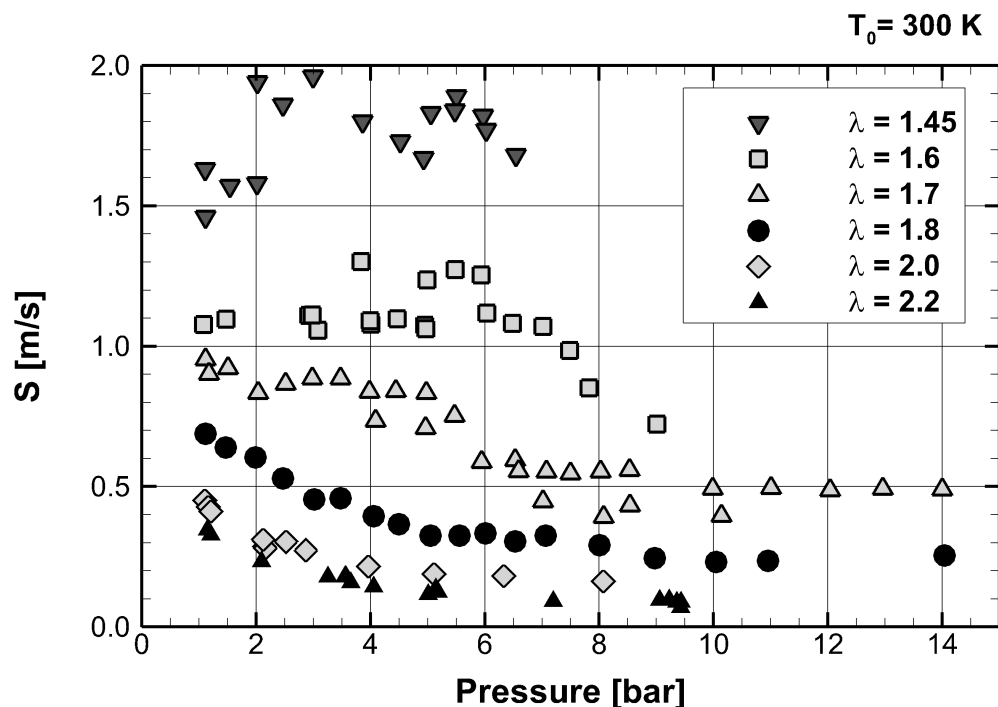
Figure 4.14: Burning velocity at elevated pressure 10-PPI PIM, $T_0 = 300$ K.

Fig.4.14 presents the burning velocity S as a function of pressure obtained from measurements in the 10-PPI burner at different air-to-fuel ratios. It is observed that pressure has a non-monotonic effect on the burning velocity. At a constant air-to-fuel ratio, for example, $\lambda = 1.6$, the burning velocity S increases with increasing pressure; it then reaches a

maximum and, with further increase of pressure, S decreases. For higher air factors, the increase in burning velocity is less considerable and the decrease in the burning velocity begins from lower pressure values.

The augmentation of S with pressure in PIM combustion is basically the most visible difference from the influence of pressure on the laminar burning velocity S_l in free laminar flames (shown in Fig.2.3 and Fig.2.4).

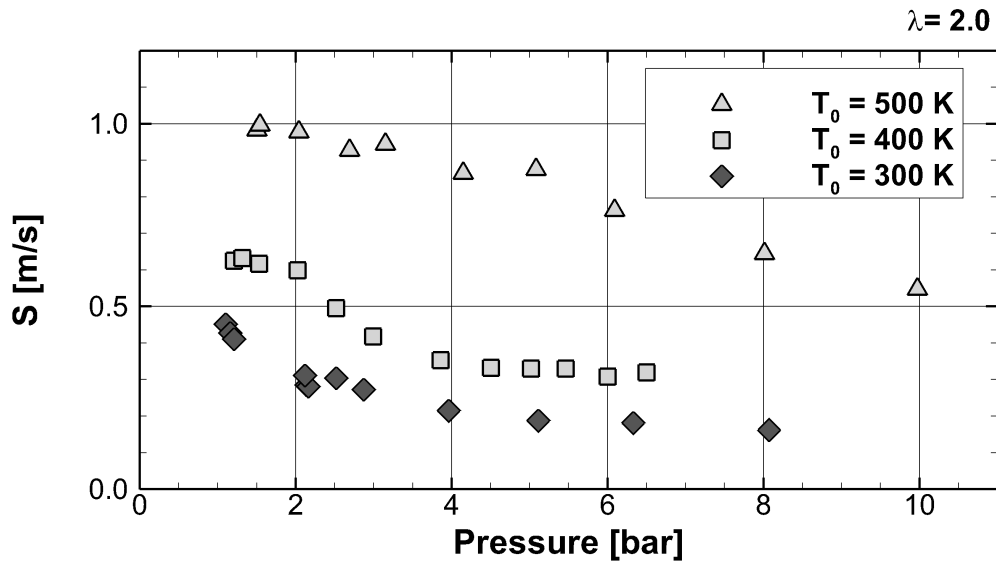
Figure 4.15: Burning velocity at elevated pressure and temperature 10-PPI PIM, λ= 2.0.

The influence of pressure on the burning velocity was tested at elevated initial temperatures of 400 and 500 K. Fig.4.15 presents a comparison of the obtained results for a mixture with air factor $\lambda = 2.0$ for different inlet temperatures. The increase of the inlet temperature has similar effects on the burning velocity as the decrease of the air factor. For a higher inlet temperature, the burning velocity increased. At $T_0 = 400\ K$, the burning velocity stayed nearly constant up to 2 bar; with further increase of pressure, it sharply decreased. In contrast, at $T_0 = 300\ K$, the burning velocity sharply decreased at 1 bar.

At $T_0 = 500\ K$, no such steep decrease of burning velocity with pressure was observed in the tested sponge compared with the other results at lower initial temperatures.

The understanding of the relevant phenomena occurring in the flame stabilization within PIM is presented in the following sections, where comparisons with free flames are made and numerical and theoretical approaches to the processes are employed.

4.5   Effect of PIM pore density

Experiments of flame stabilization within PIM were carried out in the same porous burner using a PIM with a higher pore density, 20 PPI, made of the same material, SiSiC, and with the same porosity, $\varepsilon = 0.87$. The results of burning velocity are compared with those in the 10-PPI sponge in Fig.4.16 and Fig.4.17.
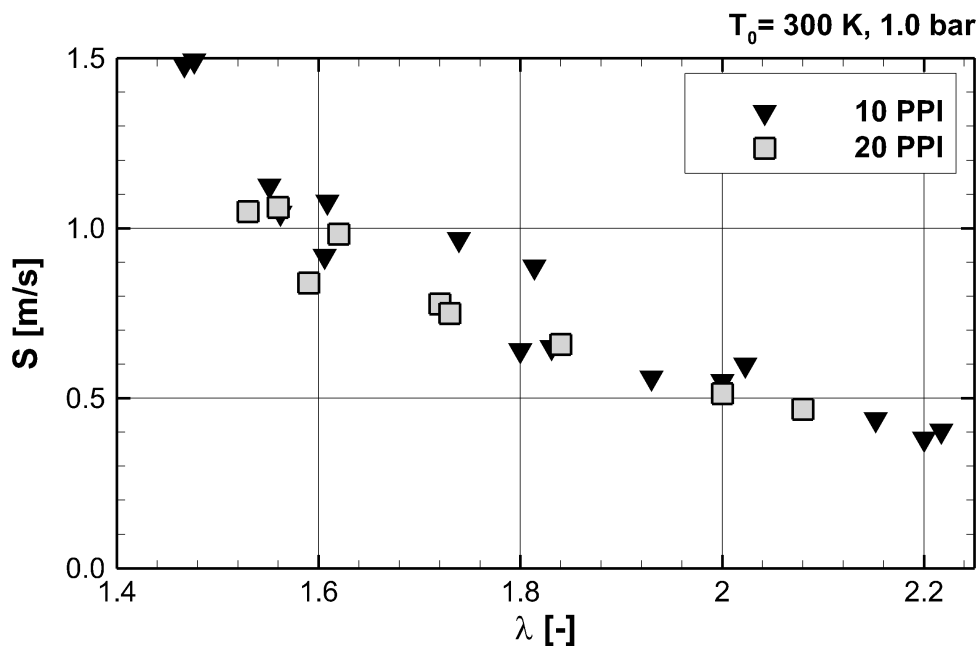
Figure 4.16: Burning velocity at atmospheric conditions as a function of air factor 20 PPI and 10 PPI, $T_0 = 300 \; K$, 1.0 bar.

Fig.4.16 shows the burning velocity as a function of the air factor at atmospheric conditions $T_0 = 300K$, 1.0 bar. The increase of pore density from 10 to 20 PPI had a slightly negative effect on the burning velocity at air factors lower than 1.8. For leaner mixtures, no differences were observed.

Fig.4.17 presents the burning velocity as a function of pressure for several air-to-fuel ratios. Empty symbols represent 20 PPI and filled symbols represent 10 PPI. At $\lambda = 2.0$, the observed absence of differences at atmospheric pressure was maintained at higher pressure levels.

In contrast, at $\lambda = 1.8$ and a pressure between 2 and 3 bar, the burning velocity of the 20-PPI burner was lower than that of the 10-PPI burner; that is, the decrease of the burning velocity became steeper with the increase of PPI. In spite of this, the burning velocities were nearly the same at higher pressures.

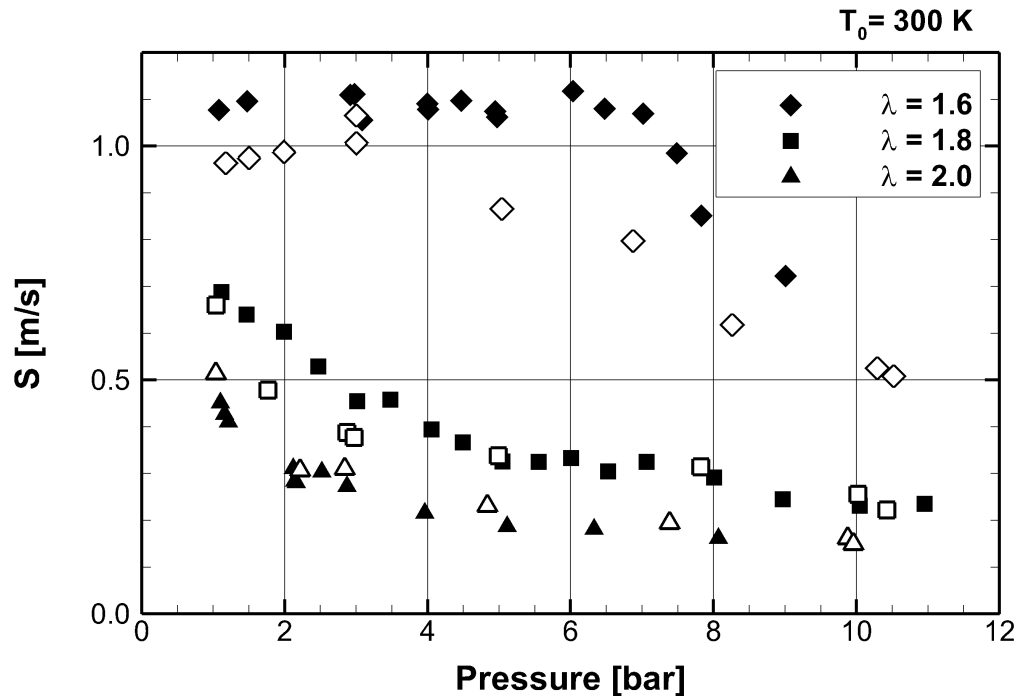Figure 4.17: Burning velocity at elevated pressure: empty symbols represent 20 PPI and filled symbols represent 10 PPI, $T_0 = 300\ K$.

At $\lambda = 1.6$, the burning velocity showed a maximum at 3 bar in the 20-PPI burner, while the maximum of the 10-PPI burner was exhibited at a considerably higher pressure.

4.6   Discussion

The obtained results of burning velocity of flames stabilized within PIM were in agreement with the results obtained at the flame stability limit of lean blow-off in the two-phase porous burner [15]. For a quasi-adiabatic condition around the flame region, the used technique for flame stabilization yielded burning velocity values independent of the burner power.

Considerable increases of the burning velocity and the mean flame thickness were observed with respect to the laminar free combustion mode.

Fig.4.18 shows a comparison of the observed burning velocity S within PIM with the burning velocity of turbulent flames as a function of the turbulence intensity at $\lambda = 1.43$ and 1.50, 1.0 bar and $T_0 = 300\ K$. Since the turbulent intensity was not measured within PIM, the value of burning velocity is depicted as a constant line along the axis.

The presented turbulent burning velocities were measured for methane air mixtures in

[193, 194]. Weiß[194] studied spherically expanding flames in an explosion vessel. S_t was measured at a radius of 60 mm using transient pressure signals and a thermodynamic model. The flame front displacement was optically detected. Shy et al. [193] investigated downward-propagating premixed flames through a nearly isotropic turbulent flow field in a large cylindrical vessel. A pair of ion probes located at 200 mm from the ignition source were used to measure S_t.
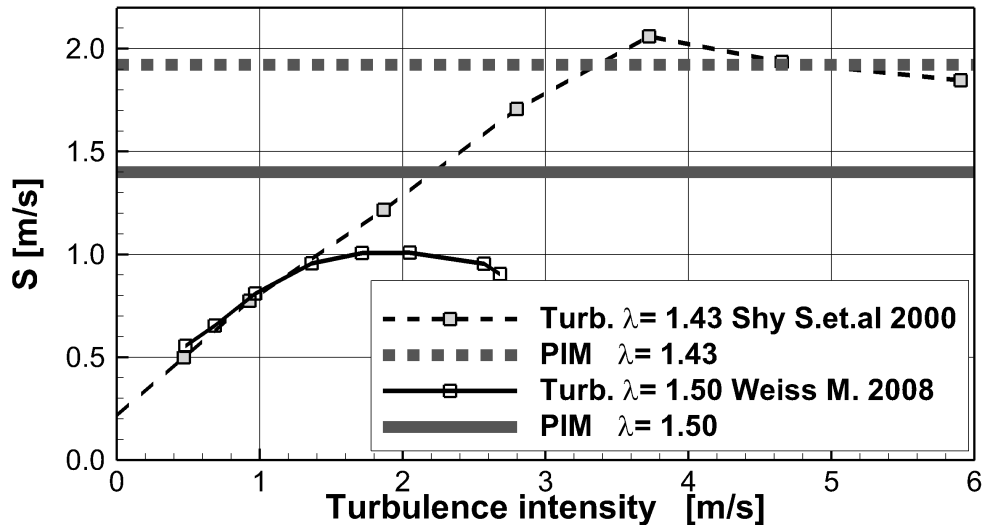
Figure 4.18: Burning velocity of turbulent free flames as a function of the turbulence intensity; Burning velocity in PIM (SiSiC 10 PPI) 1.0 bar, $T_0 = 300\ K$.

The burning velocity of flames stabilized within PIM appeared to be of the same order of magnitude as that of turbulent free flames, but with considerably lower emission of pollutant species and noise. Fig.4.18 shows that a porous burner can exhibit higher burning velocity than turbulent flames at leaner conditions. To the best of the author's knowledge, measurements of turbulent burning velocity are not available at leaner conditions such as those studied here.

A similar comparison was made in [68]. The specific power at the flame stability limit of a two-phase porous burner was compared against the power of a swirl flame at the stability limit divided by the combustion chamber cross-sectional area. This comparison also showed that the energy density in a porous burner is comparable to that of burners with aerodynamically stabilized flames.

An easy way to compare the contribution of the phenomena in PIM against the reaction kinetics is to use the burning velocity ratio (SR) between the flame stabilization within PIM and the laminar free flame:

$$SR = S/S_l \tag{4.8}$$

which is commonly called the acceleration factor. Fig.4.19 shows the SR in the 10-PPI burner at two different inlet temperatures: T_0= 300 and 500 K, and 1.0 bar. The burning velocity in PIM flame stabilization increased by a factor between 5 and 13 with respect to the laminar burning velocity.

The burning velocity ratio SR was calculated for the conditions that can also be stabilized in the laminar free mode. For example, at T_0= 300 K, the laminar free flames cannot be stabilized for air factors above $\lambda = 2.0$, while the flame stability within PIM was observed up to λ= 2.2. At those ultra-lean conditions, the calculated laminar burning velocity tends to zero. This is the reason for the increase of the burning velocity ratio with increasing air factor.
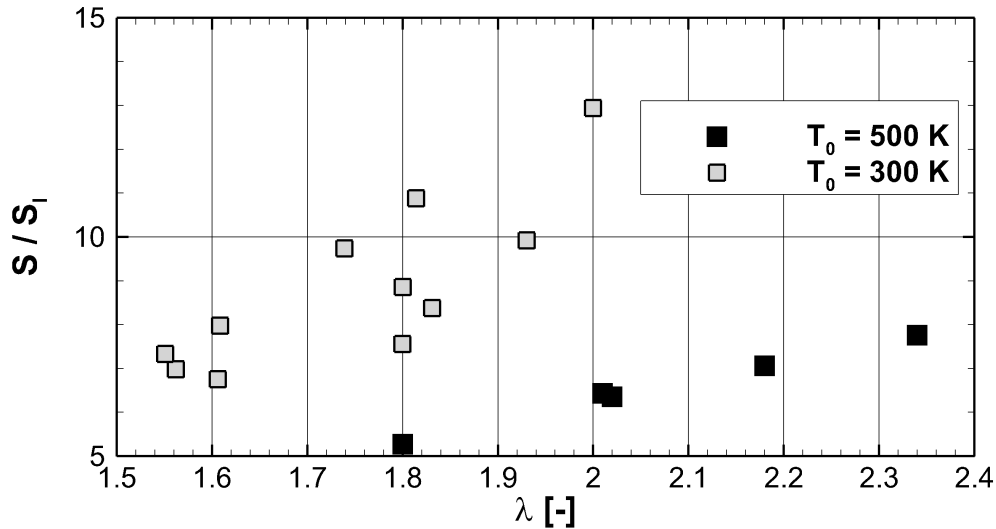
Figure 4.19: Burning velocity ratio SR, 10-PPI PIM, 1.0 bar.

The burning velocity ratio SR decreased with the increase in the initial temperature from 300 to 500 K. The reason for this can be found calculating the heat fluxes namely by dispersion, solid conduction, solid radiation and inter-phase convection.

The effective coefficient of dispersion and inter-phase depend on the gas velocity, since the observed burning velocity is higher for T_0= 500 K than for 300 K, the respective coefficients increased, which is favorable for improving the flame stabilization within PIM. The radiation conductivity λ_r depends on temperature to the third power. In contrast, the thermal conductivity of the solid phase is exponentially dependent on the inverse of temperature.

Thus, it could be inferred that the dominating mechanism at the presented ultra-lean conditions was the thermal conduction through the solid phase, which in turn could

be responsible for the extension of the flame stability limit. Nevertheless, it cannot be stated yet, without the numerical and theoretical studies presented in sections below.

Fig.4.20 shows that the burning velocity ratio SR can increase up to 25 at elevated pressure. The effect of pressure on the burning velocity in PIM differs substantially from that in the laminar free case. It is observed that S can increase with pressure and that the influence of pressure on S is considerably affected by the air-to-fuel ratio and initial temperature. The shape of the curves of burning velocity ratios SR show a peak. This peak is higher for conditions with higher laminar burning velocities (higher T_0, lower λ) and shifted towards higher pressure values. For example the peak of $\lambda = 1.6$, 300 K is located at 6 bar and has a value of 25, but for a leaner mixture $\lambda = 1.7$, 300 K it is located at 4.5 bar and is 20.

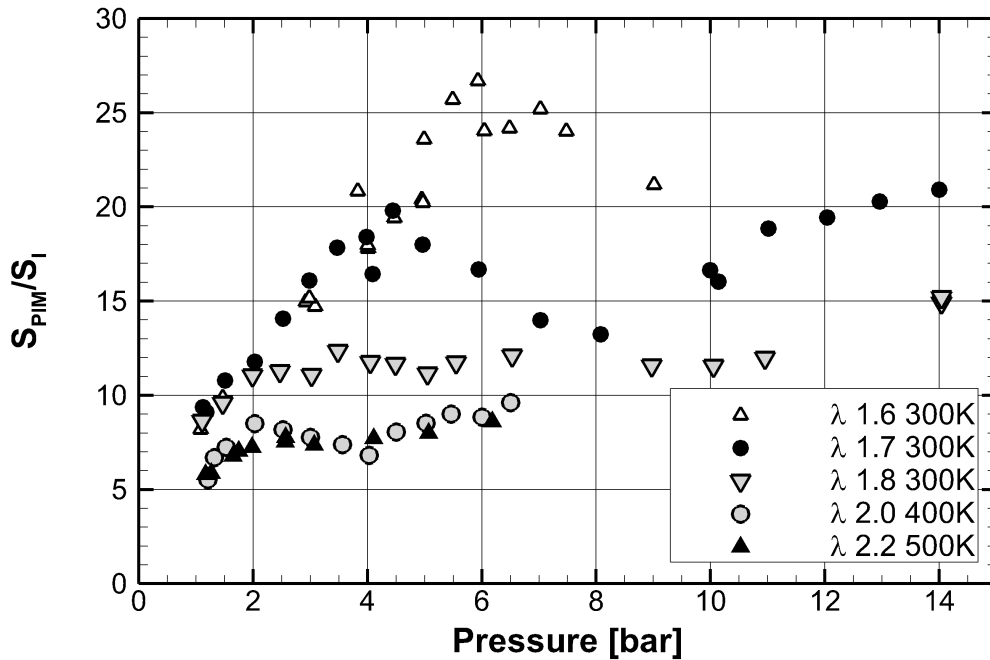Figure 4.20: Burning velocity ratio SR 10-PPI PIM at elevated pressure

The following analogy to free flames roughly explains these observations. According to the thermal theory of laminar flat premixed free flames, Eq.(2.11) and Eq.(2.12)

$$S_l \propto (a_m/\tau_c)^{0.5}$$

$$\delta_l \propto (a_m \cdot \tau_c)^{0.5}$$

express S_l and δ_l, respectively, as functions of the molecular thermal diffusivity a_m and

the heat release timescale τ_c.

Similarly, in the case of PIM combustion, assuming roughly that τ_c is not affected by the PIM, an effective thermal diffusivity a_{eff} can be introduced for PIM in Eq.(4.9),

$$a_{eff} = \varepsilon \cdot a_{dis} + (1 - \varepsilon)a_{hr} \qquad (4.9)$$

which considers the contribution of axial dispersion a_{dis} and the heat recirculation a_{hr} coupled in parallel, as shown in Fig.2.6. On one side, the dispersion coefficient a_{dis} from Eq.(2.34)

$$a_{dis} = 0.5 \cdot d_p \cdot u \qquad (4.10)$$

is directly proportional to velocity. For gas flowing at a velocity of 1 m/s (typical S value of combustion in solid sponges) through a 10-PPI sponge, the effective coefficient of dispersion is two orders of magnitude higher than the molecular diffusivity of the gas at atmospheric conditions of both species and heat. This substantially augments the species transport and the macroscopic heating rate of incoming unburned gas, in comparison to the case of flow through an empty straight pipe.

On the other side, the heat recirculation through the solid phase consists of three mechanisms: solid conduction, solid-to-solid radiation and interface convection. Since the thermal transport properties of solid matter are around two orders of magnitude higher than those of gas at atmospheric conditions, a considerable amount of heat from the hot burned gas is transferred upstream by conduction and solid-solid radiation through the PIM, preheating the incoming unburned gas. The local temperature in unburned gases increases and the combustion temperature achieved locally may reach higher values than without this kind of preheating.

The heat recirculation coefficient a_{hr} depends on the heat transfer by convection between gas and solid and the heat transfer through the solid (by conduction and radiation $(\lambda_s + \lambda_r)/(\rho_g \cdot c_{p,g})$), which are connected in series; thus, a rough approach based on a thermal resistance network is:

$$a_{hr}^{-1} = a_{conv}^{-1} + [(\lambda_s + \lambda_r)/(\rho_g \cdot c_{p,g})]^{-1} \qquad (4.11)$$

where $(\lambda_s + \lambda_r)/(\rho_g \cdot c_{p,g})$ at 800 K is two orders of magnitude higher than the molecular thermal diffusivity of the gas a_m, and a_{conv} is proportional to the heat transfer coefficient α, the amount of superficial area involved in the reaction region and the local temperature difference between phases. Therefore, it is complex to formulate an approach to introduce a theoretical value of a_{hr}. A simpler approach is presented in Section 6.

In a previous investigation of this kind of burner by Djordjevic [68], it was found that, due to the high surface area between phases in sponge-like structures, convection offers lower thermal resistance than that in the solid phase; thus, it is not a relevant mechanism. However, owing to the high thermal conductivity of SiSiC, this is not the case at ultra low gas velocities.

On the basis of the contribution of the dispersion and the heat transfer through the solid, the introduction of a_{eff} in the results of the thermal theory Eq.(2.11) and Eq.(2.12) simply explains the increase of the burning velocity and the macroscopic flame thicknesses with respect to the laminar free mode, which were observed in flames stabilized within PIM.

Since the hydrodynamic dispersion coefficient a_{dis} in porous media depends on the fluid velocity, the case of flame stability of highly turbulent flames is worthy to be compared with flame stabilization within PIM, because the effective transport coefficient a_t, which considers the turbulence effects, depends on velocity as well. In this case, highly turbulent flames, the thermal theory of Mallard and Lechatelier is applied in a direct analogy with the laminar case. The result is applied for determination of flame stability limits or scaling of burners as explained in the laminar case in Section 2.2.1 (Bunsen burner).

Here it is briefly explain a derivation of the relation of the stability model of highly turbulent flames, whose result is a relation of the with the S_l and the Peclet number.

The basis of the model is the result of the thermal theory in Eq.(2.11):

$$S_l \propto \left(\frac{a_m}{\tau_c} \right)^{0.5}$$

where the molecular thermal diffusivity a_m of gases (free flames) is directly proportional to the average speed of the molecules Ω and the mean free path Γ:

$$a_m \propto \Omega \cdot \Gamma \tag{4.12}$$

As well for the transport phenomena, the effect of turbulence are associated to the velocity fluctuation along time u' and the size of the vortex averaged along time l_t, thus for

$$a_t \propto u' \cdot L_t \tag{4.13}$$

The thermal theory applied to the turbulent effects on the burning velocity of a flame

brush (volume and time averaged approach) yields:

$$S_t \propto \left(\frac{a_t}{\tau_c}\right)^{0.5} \tag{4.14}$$

where τ_c is the time scale of heat release, assumed to have negligible effects of turbulence, since it depends predominatly on the reaction kinetics.

The effects of velocity fluctuation along time u' are proportional to the mean gas velocity u and the size of the vortex averaged along time l_t, on a characteristic length of the system l, for example the diameter of discharge port of a burner, therefore

$$a_t \propto u \cdot l \tag{4.15}$$

The ratio of burning velocities yields a direct relationship to the square root of the Peclet number:

$$S_t/S_l \propto (u \cdot l/a_m)^{0.5} \tag{4.16}$$

and using the definition of flame stability $u = S_t$, then

$$S_t \propto S_l^2 \cdot l/a_m \tag{4.17}$$

or

$$\frac{S_t \cdot l}{a_m} \propto \left(\frac{S_l \cdot l}{a_m}\right)^2 \tag{4.18}$$

where a modification of the Peclet number for the laminar flame based on the S_l was proposed Pe_l. This correlation was validated for highly turbulent free flames (Karlovitz number $>> 1$) in [195]. In the case of flame stabilization within PIM, a comparable model is obtained from present experimental results in Section 4.7.

From Eq.(4.17), the pressure influence on the turbulent burning velocity can be deduced using Eq.(2.16)

$$S_l \propto p^b$$

and $a_m \propto p^{-1}$, to yield:

$$S_t \propto p^{2 \cdot b + 1} \tag{4.19}$$

The fitted exponent b was calculated for lean air-methane mixtures using Eq.(2.16) in Section 2.2.1 (see Fig.2.4). b depends considerably on pressure and this dependence is significantly affected by the air-to-fuel ratio.

The influence of the exponent b on the turbulent burning velocity has been numerically studied. Eq.(4.19) can be written as:

$$S_t(p)/p^{2 \cdot b(p)+1} = constant \tag{4.20}$$

$$\frac{S_t(p_1)}{S_t(p_0)} = \frac{p_1^{2 \cdot b(p_1)+1}}{p_0^{2 \cdot b(p_0)+1}} \tag{4.21}$$
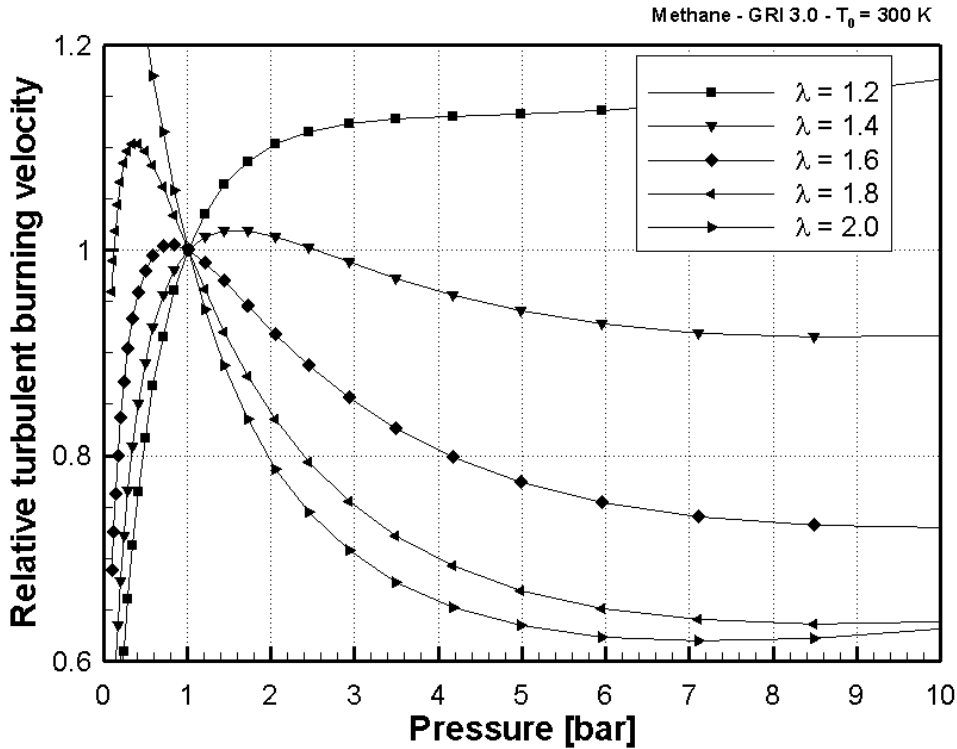
Figure 4.21: Relative turbulent burning velocity as a function of pressure for different λ, 1.0 bar and T_u= 300 K [49]

As a reference value, $S_t(1bar)$= 1 was used, and by Eq.(4.21), the relative turbulent burning velocity was defined as a function of pressure. The resulting values are presented in Fig.4.21 [49].

Fig.4.21 shows that the effect of pressure on the turbulent burning velocity is similar to that observed in flame stabilization within PIM (Fig.4.14). This similarity corresponds to the existence of considerable temporal fluctuations in the combustion behavior of highly turbulent free flames; while the combustion in PIM exhibits considerable spatial variations (observed in experiments), both yield substantial enhancement of the transport of mass and heat with respect to the laminar free flame case, which are proportional to the gas velocity. Since turbulent flames do not have recirculation of heat through

a solid phase like in PIM combustion, it is to infer that in PIM the dispersion effects dominate on those of the heat recirculation. To obtain absolute values also including the effect of heat recirculation through the solid phase, results of numerical simulations of the flame stabilization within PIM are presented in Chapter 5.

4.7   Peclet similarity model

Eq.(4.17) is a result of the thermal theory presented in Section 4.6, from which the turbulent burning velocity can be obtained for different conditions and different fuels at high turbulence intensities with only knowledge of the laminar burning velocity and the molecular thermal diffusivity:

$$\frac{S_t \cdot l}{a_m} \propto \left(\frac{S_l \cdot l}{a_m}\right)^2 \tag{4.22}$$

or

$$Pe_t \propto Pe_{lam}^2 \tag{4.23}$$

This correlation has also been proven in other types of flames to predict the stability limits with scaled geometrical size, operation with different fuels and at different conditions of mixture, temperature and pressure.

Examples are available for laminar premixed flames in a Bunsen burner (see Eq.(2.27)), as well as for highly turbulent flames stabilized by internal recirculation of flue gases, for example, swirling flames with geometrical similarity [196] and flames with flame holders for small blockage ratios [197].

In the present section, the use of this model for determination of the burning velocity of flames stabilized within PIM was tested. The theoretical derivation of an accurate model for flame stabilization within PIM is difficult due to the complexity of the relevant phenomena and the uncertainty of the PIM properties. Therefore, the use of a model with the form

$$Pe_{pim} = C_{Pe} \cdot Pe_{lam}^m \tag{4.24}$$

was proposed to correlate the experimental results of the present work obtained at different pressure levels. Where Pe_{pim} is the Peclet number based on the burning velocity within the quasi-adiabatic porous burner,

$$Pe_{pim} = S \cdot d_{dis}/a_{m,u} \tag{4.25}$$

d_{dis} is the dispersion length scale (e.g. d_{dis}= 0.324 mm for SiSiC 10 PPI) and $a_{m,u}$ is

the molecular thermal diffusivity of the unburned gas mixture $a_{m,u} = \lambda_u/(\rho_u \cdot c_{p,u})$ and Pe_{lam} is the Peclet number based on the laminar burning velocity:

$$Pe_{lam} = S_l \cdot d_{dis}/a_{m,u} \tag{4.26}$$

Since the model is based on the laminar burning velocity, it is limited to the stability range of laminar free flames, as given in [50]. The experimentally obtained results are presented in Fig.4.22 with logarithmic axes. These results correspond to the experiments performed with the PIM of 10 PPI for the tested pressure levels, initial temperatures and air-to-fuel ratios, excluding the leanest conditions that in the laminar free mode could not produce burning ($\lambda > 2.0$ at $T_u = 300$ K).

The laminar burning velocity values were calculated for planar laminar premixed flames of methane air mixtures with the PREMIX code of the CHEMKIN package [39] using GRI mech 3.0 [41].

The symbols discriminate the air factor and the initial temperature from each other and group all pressure levels tested. The plot legend also displays the calculated adiabatic combustion temperature. It is noteworthy that all results together can be well correlated with the Peclet similarity model proposed, even for different air factors up to the flame stability limit corresponding to the laminar free flame. However, the accuracy of the model was increased by grouping the results into certain ranges of adiabatic combustion temperature. Tab.4.1 presents the resulting correlating parameters.

Table 4.1: Semi empirical model Eq.(4.24) for flame stabilization within PIM SiSiC 87% porosity

PPI	d_{dis} [mm]	T_{ad} range [K]	C_{Pe}	m
10	3.24	1550 - 1825	1.101	1.753
10	3.24	1630 - 1825	0.771	1.857
10	3.24	1550 - 1600	1.838	1.586
20	3.02	1580 - 1710	1.485	1.638

It is notable that the exponent m tends to a value of two, as in the theory of free flames, for the highest tested combustion temperatures.

The present proposed model represents a useful easy-to-use tool for engineering dimensioning of porous burners in terms of prediction of the lean flame stability limit of submerged flames. On the basis of the values of laminar burning velocity, the porous burner can be scaled for different sizes, different conditions and to operate with other fuels by using this model.
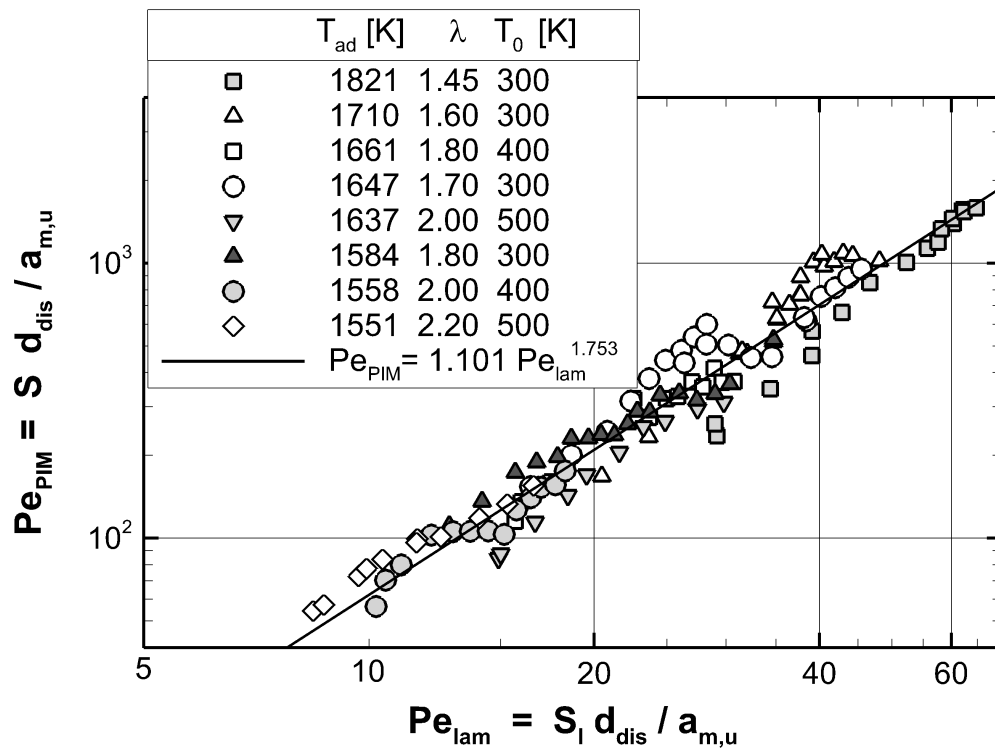
Figure 4.22: Peclet number of burning velocity in PIM S as a function of the Peclet number of laminar burning velocity S_l

Chapter 5

Numerical simulation of flame stabilization within PIM

The numerical investigation of combustion within PIM plays a crucial role in the development and optimization of porous burners and in the basic understanding of the overlap of relevant processes of transport and the chemical kinetics of reactions in the presence of PIM. In the present work, a well-known one-dimensional model was used based on the method of volume-averaging [15, 24, 161, 185, 189, 198–202] for simulation of the process at the macroscopic scale, containing effective medium coefficients that provide the connection with the processes occurring at the microscale. These coefficients were obtained from direct pore-level simulations (DPLS) on a reconstructed real PIM sample scanned by micro-tomography (see Appendix A).

The used model is described in Section 5.1.1 for the direct calculation of a detailed reaction mechanism of methane oxidation, named the direct chemistry model (DCM). It considers adiabatic boundaries and laminar flow. Relevant results of the burning velocity are presented in Section 5.1.2, which show the effect of the used stabilization technique, namely, the continuous increase of the cross-sectional area of the conical burner, as well as the effect of the air-to-fuel ratio, the initial temperature of unburned mixture, the pore density and especially the effect of pressure on the burning velocity. At the end of the section, the importance of the transport processes on the burning velocity at elevated pressure is analyzed from results of the systematic change of the transport coefficients of this model.

The temperature deviations along the cross section observed in the present experiments were not considered in the DCM. Therefore, the calculation of non-linearly dependent parameters such as the source terms may deviate considerably. A way of considering this is proposed in Section 5.3 by introducing probability density functions PDF of

gas temperature along the cross-sectional area. Since this measure markedly increased the computational demands and the stiffness to converge on an accurate solution, the chemical composition during the progress of combustion was looked up from tabulated results of the DCM. This technique for the reduction of computational demands has been commonly used in turbulent flames. Validation of its use in PIM combustion is presented in Section 5.2.

The studied burner geometries were cylindrical and conical. The PIM structure was made of SiSiC 87% porosity and mainly 10 PPI, although the effect of increasing the pore density from 10 to 20 PPI was also studied.

5.1   Direct chemistry calculations

5.1.1   Direct chemistry model (DCM)

Principal assumptions:

1. Effects of spatial deviations of the dependent variables were neglected

2. Gas radiation was not included

3. The porous matrix was considered optically thick

4. There is thermal non-equilibrium between phases (heat transfer between phases)

5. Air and fuel are perfectly premixed

6. Potential catalytic effects of the solid phase are negligible

7. The pressure drop through the porous burner is not high and its effect can be neglected

8. Dufour effects, namely, bulk viscosity and body forces, are negligible

9. The flow is one-dimensional and incompressible

10. Neither turbulence nor flame stretch is induced by the flow through the PIM

The theoretical derivation of the balance equations for porous media is beyond the scope of the present work, but is widely available from the use of different methods [17, 81, 82].

On the basis of the above assumptions, the flame can be assumed to be one-dimensional. Eqs.(5.1-5.4) are the balance equations of mass, energy in gas phase, energy in solid phase

and species, respectively, using volume-averaged quantities along the cross section of the respective phase. They account for detailed chemistry, species diffusion, gas and solid conduction, solid-to-solid radiation, convection heat transfer between the phases, the Soret effect and hydrodynamic dispersion.

$$0 = \partial(\rho_g u_g A_g)/\partial x \tag{5.1}$$

$$
\begin{aligned}
0 = u_g A_g \frac{\partial T_g}{\partial x} - \frac{\partial^2(a_{g,eff} A_g T_g)}{\partial x^2} + \frac{\alpha A_g}{\rho_g c_{p,g}} \frac{S_v}{\varepsilon}(T_g - T_s) \\
+ \frac{A_g}{c_{p,g}} \sum_i Y_i \upsilon_{D,i} c_{p,i} \frac{\partial T_g}{\partial x} + \frac{A_g}{\rho_g c_{p,g}} \sum_i \dot{\omega}_i h_i
\end{aligned}
\tag{5.2}
$$

$$0 = \frac{\alpha \cdot S_v}{1 - \varepsilon}(T_s - T_g) - (\lambda_{s,eff} + \lambda_r)\frac{\partial^2 T_s}{\partial x^2} \tag{5.3}$$

$$0 = A_g \rho_g u_g \frac{\partial Y_i}{\partial x} + \frac{\partial}{\partial x}\left[\rho_i \left(-D_{eff,im} \frac{A_g}{X_i} \frac{\partial(X_i)}{\partial x}\right) Y_i\right] - A_g \dot{\omega}_i M_i \; ; \; i = 1 \ldots N_i \tag{5.4}$$

The subscripts s and g stand for solid and gas phases, respectively; therefore, A_g is the area corresponding to the gas phase or interstitial area. Under the assumption that the surface porosity is the same as the porosity ε, A_g is related to the burner total area $A_g = A_{pim} \cdot \varepsilon$. Thus, the present model is capable of incorporating the axial mass flux variations due to change of A_g along the conical burner.

The transport properties in the gas phase are given by the mixture average formulation, where $\upsilon_{D,i}$ is the diffusion velocity included in the term of the Soret effect of the gas energy conservation equation

$$\upsilon_{D,i} = -D_{g,eff} \frac{1}{X_i} \frac{\partial X_i}{\partial x} \tag{5.5}$$

The effective mass diffusivity of the ith species Eq.(2.36)

$$D_{eff,i} = D_{m,i}/\tau + D_{dis}$$

considers the contribution of the hydrodynamic dispersion D_{dis}

$$D_{dis} = 0.5 \cdot d_{dis} \cdot u \tag{5.6}$$

upon the molecular diffusivity of the gas phase $D_{m,i}$.

$$D_{m,i} = (1 - Y_i)/\left(\sum_{ii \neq i}^{N_i} X_i i / D_{i-ii}\right) \tag{5.7}$$

In the same way, the effective thermal diffusivity of the gas phase

$$a_{g,eff} = a_{g,m}/\tau + a_{dis} \tag{5.8}$$

was increased by the cross-mixing effects of hydrodynamic dispersion a_{dis} with the assumption that the magnitude is the same as in the transport of mass

$$a_{dis} = D_{dis} \tag{5.9}$$

The code PREMIX [38, 39] was modified to solve the above conservation equations by the method of finite differences. For the numerical solution to the problem, the TWOPNT solver [203] was used.

The reaction source terms were calculated as the net production from the elementary reactions $k = 1$ to N_k. The general form of the calculation of the production rate of the ith species is given by the equation

$$\dot{\omega}_i = \sum_{k=1}^{N_k} (\nu'_{ik} - \nu''_{ik}) \cdot \dot{r}_k \tag{5.10}$$

where $\dot{r}_k$ is the specific reaction progress rate of the kth reaction, which is the reaction rate difference between the forward and backward directions of the reaction Eq.(2.5):

$$\dot{r}_k = k_{f,k} \prod_{i=1}^{N_i} [X_i]^{\nu'_{ik}} - k_{b,k} \prod_{i=1}^{N_i} [X_i]^{\nu''_{ik}}$$

The reaction rate coefficients k_k were calculated using a modified Arrhenius equation Eq.(2.6). The used reaction mechanism is given by Egolfopoulos, which is validated for laminar free flames up to 3 bar and involves $N_i = 17$ species and $N_k = 58$ reactions [43].

The thermodynamic properties for the gas mixture averaged over a cross-sectional plane were obtained from the database CHEMKIN II [39] as a function of the average gas temperature, pressure and concentration, as well as the molecular transport properties, which were determined using the TRANFIT subroutine [40].

The energy conservation equations of the two phases are connected by the source/sink term of convective heat transfer between phases, which consists of the local temperature difference between phases, the effective convection coefficient α and the volumetric surface area.

The effective thermal conductivity of the solid phase considers the contribution of solid-to-solid radiation by a radiation conductivity λ_r and the reduction of the thermal conductivity due to the tortuous paths imposed by the geometry of the solid matrix on the heat flow $\lambda_{s,eff} = \lambda_s/\tau$.

Boundary conditions, domain and computational grid

The values of molar fractions, temperature and pressure were specified at the cold boundary. At the outlet boundary, all gradients were set to zero, since the adiabatic case is the focus of the present work.

The domain length L was 300 mm and the flame location was specified by fixing a temperature value of 500 K. The flame location was selected as in experiments to be in the central region of PIM. The domain cross-sectional area was taken to be constant and equal to unity for a first domain called a cylindrical burner. A second domain called a conical burner was used for calculations of flame stabilization; in this case, the cross-sectional area was set as a quadratic function of the axial coordinate x, which conforms to the geometry of the burner used for the experimental study (see Fig.3.3).

An adaptive mesh refinement method [38] was used to enhance the convergence of partial solutions. The starting step was a coarse grid density of 1.8 nodes/mm of uniformly distributed nodes at the flame region. Then, adaptive nodes were added to ensure relative values of gradients and curvatures lower than 0.10. Finer grids did not considerably increase the accuracy of the results.

Effective coefficients of transport

The effective coefficients of dispersion of both heat a_{dis} and mass D_{dis} were defined using the asymptotic value of two for the modified Peclet number Eq.(2.34); it yields:

$$D_{dis} = a_{dis} = 0.5 \cdot u \cdot d_{dis}; \quad for \quad Pe_m = (u \cdot d_{dis})/a_m > 10$$

The effective thermal conductivity of the solid phase $\lambda_{s,eff}$ must be considerably lower than that in the material used due to enlargement of the heat flux paths at the pore level. The material was considered continuous, in contrast to discrete porous media such

as packed beds, where the contact resistance imposes a more considerable decrease in this effective property. Thus, Eq.(2.48)

$$\lambda_{s,eff} = \lambda_s/\tau_s$$

was used, where τ_s is the tortuosity of conductive heat flow through the solid phase.

The solid conductivity λ_s of sintered SiSiC was evaluated as a function of the solid temperature using a correlation given in Eq.(6.15) from [191]. Since the conductivity depends on the inverse of the exponential of the material temperature, this consideration should be included to improve the accuracy of the results.

Solid-to-solid radiation was accounted for by using the Rosseland equation, Eq.(2.53). The use of the Rosseland approximation is justified as the domain is optically thick $(L \cdot \beta = 49 >> 1)$ [151] due to a large extinction coefficient of the solid sponge and a large domain length.

The effective convection coefficient α was calculated with the correlation of the Nusselt number, Eq.(2.44):

$$Nu = \alpha \cdot d_h/\lambda_g = c_1 \cdot Re^{c2} \cdot Pr^{c3} \quad with \quad Re = \frac{u_g \cdot d_h}{\nu_g}$$

The property data of the PIM used in the 1D model for flame stability in SiSiC sponge are listed in Tab.5.1. They were obtained by DPLS performed on a real sample of the used PIM scanned using micro-tomography. Some details of the DPLS are presented in the Appendix A.

Table 5.1: Property data used for the SiSiC PIM with 87% porosity.

PPI	Tortuo-sity τ	disp.char. length d_{dis} [mm]	solid cond. tortuosity τ_s	ext. coef. β $[m^{-1}]$	volumetric surface S_v $[m^{-1}]$	Eq.(2.44) c_1	c_2	c_3
10	1.30	3.24	3.85	149	473	3.70	0.38	0.25
20	1.30	3.02	3.85	211	685	5.14	0.30	0.24
Source	[67]	[15, 27, 49]	[28]	[26]	[7, 28]	[28]		

5.1.2   Results

Fig.5.1 shows the profiles of average temperatures of the gas and solid phases and the production rates of some selected species along the cylindrical porous burner made of
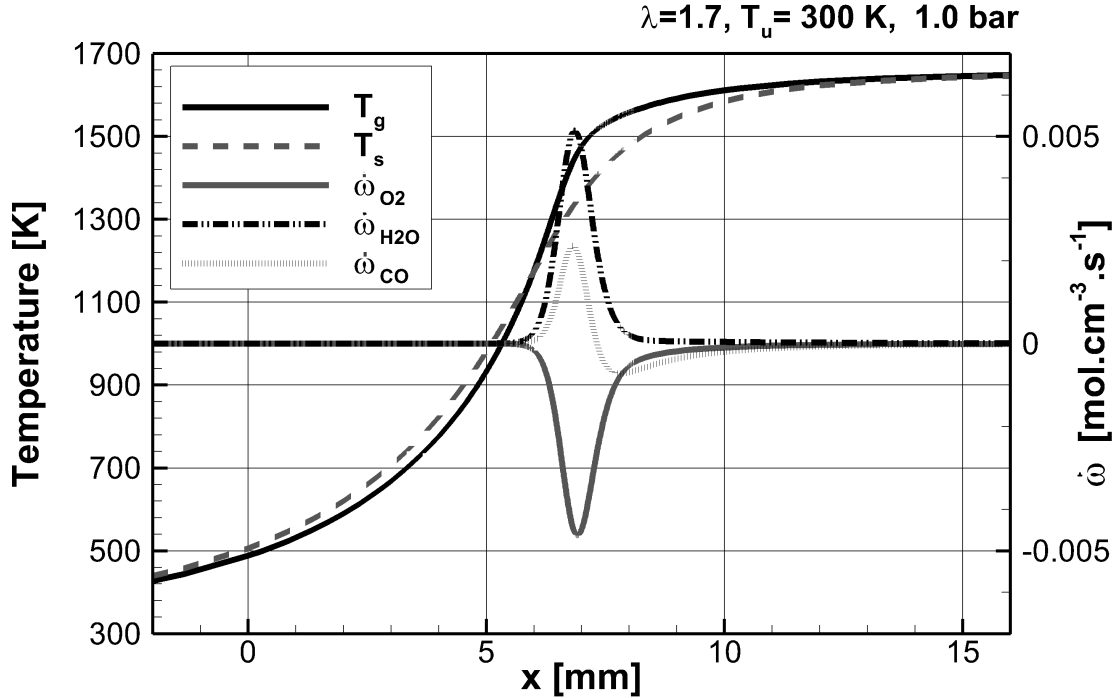
10-PPI SiSiC at λ= 1.7, T_u= 300 K, 1.0 bar.

Figure 5.1: Simulated profiles of average temperature and production rate of selected species, cylindrical 10-PPI burner λ=1.7, T_u= 300 K, 1.0 bar

It should be noted that the flame structure does not differ considerably from that of laminar free flames, while analyzing the ratio between the thicknesses of the reaction zone and the inert zone; that is, the reaction zone is considerably thinner than the inert zone. The predicted temperature profile did not show a considerable super-adiabatic temperature peak due to heat recirculation, in agreement with previous numerical results of the simulation of the same case [56]. The temperature difference between phases is less than 40 K.

Since the present experiments were carried out in a conical porous burner, 1D simulations were carried out for flame stabilization in such geometry in order to identify any possible effect of the diverging channel on combustion parameters like the burning velocity and the combustion temperature.

Flame stretch in the conical burner

1D calculations were performed using the DCM model in the conical geometry of the burner used for the present experiments with the 10-PPI sponge-like PIM made of SiSiC. The conical geometry may influence the flame stabilization due to the change in

cross-sectional area A_{pim}, since the reaction takes place in a region with larger cross-sectional areas than that where the unburned mixture is preheated, and this effect results in macroscopic flame stretch. The flame stretch obtained from the volume-averaged approach is therefore defined in macroscopic terms; that is, it is not related to the effect of the porous structure at the pore level.

In a diverging geometry, both heat flux and species flux from the reaction zone to the preheating zone (burned to unburned zone) are increased, see Fig.5.2. The increase of heat flux accelerates the wave flame. However, in lean premixed flames of air-methane mixtures, the increase of molecular flux makes the unburned mixture leaner; thus, the effect of the heat flux increase is compensated for and the overall result on the burning velocity depends on the Lewis number, the amount of flame stretch, the air-to-fuel ratio (AFR) and the thermodynamic conditions [204].
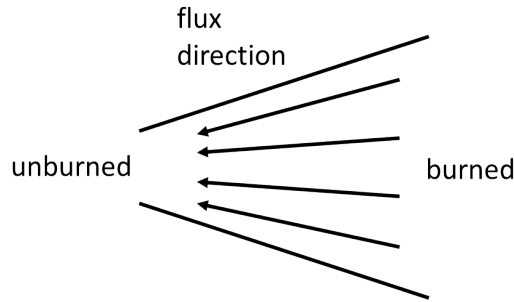

Figure 5.2: Sketch of upstream flux of heat and species in a diverging flow

The definition of the burning velocity in the conical burner was selected to be the same as that used in the experiments in order to validate the experimental results and to allow for comparability of the burning velocity results from numerical and experimental methods. The burning velocity is defined as the isothermal velocity at the flame location (see Fig.4.11 and Eq.(4.6)). The flame location is defined as the location where maximum oxygen consumption occurs.

$$x_f = max(-\dot{\omega}_{O2}) \tag{5.11}$$

This flame location definition allows for higher burning velocity accuracy over other definitions, like that used in the experiments, namely, the location of 50% temperature rise. This definition was selected in the experimental study because of the low resolution of measurements.

Fig.4.11 presents the velocity profile of numerical results obtained with the 1D DCM in the cylindrical and conical domains and the corresponding isothermal velocity u^{T_0} profile in the conical domain. The gas velocity at constant temperature does not vary along

the cylindrical burner; thus, $S = u_{g,u} \cdot \varepsilon$. For the conical burner, Fig.4.11 shows the velocity profile for a flame front located 59 mm away from the cone inlet ($x_f = 59\ mm$). The definition of stretch is:

$$\kappa(x) = \frac{1}{A_g(x)} \cdot \frac{dA_g(x)}{dt} = \frac{1}{A_g(x)} \left(\frac{\partial A_g(x)}{\partial t} + u(x) \cdot \frac{\partial A_g(x)}{\partial x} \right) \qquad (5.12)$$

The change of the area along time is neglected (steady state problem), thus in the present study, the macroscopic stretch κ is calculated using Eq.(5.12).

$$\kappa(x) = \frac{1}{A_g(x)} \cdot \frac{\partial A_g(x)}{\partial t} = \frac{u(x)}{A_g(x)} \cdot \frac{\partial A_g(x)}{\partial x} \qquad (5.13)$$

In the conical configuration, the following relationships along the burner axial coordinate apply:

$$A_g \propto x^2 \qquad (5.14)$$

$$u \propto A_g^{-1} \rho^{-1} \qquad (5.15)$$

Then, Eq.(5.12) yields

$$\kappa \propto x^{-3} \rho^{-1} \qquad (5.16)$$

Fig.5.3 presents the results of stretch profile κ along the conical PIM from the present 1D model for a flame stabilized at $x_f = 59\ mm$. The air factor was $\lambda = 1.7$ and the inlet thermodynamic conditions were 1.0 bar and 300 K. The figure shows that stretch is always positive for this geometry. It depends on the inverse of the axial coordinate at the power of three and, at the flame front, the stretch exhibits a maximum due to the isobar increase of temperature, which accelerates the gas velocity.

The macroscopic flame stretch is defined as the macroscopic stretch κ at the flame location x_f,

$$\kappa_f = \kappa(x_f) \qquad (5.17)$$

for which, in the exemplary case of Fig.5.3, where $x_f = 59$ mm, the macroscopic flame stretch was found to be $\kappa_f = 60\ s^{-1}$. This value of stretch is one order of magnitude lower than those in other kinds of stretched free flames, such as spherical outwards propagating flames.

Fig.5.4 presents the differences in the temperature distribution along the burner predicted for the cylindrical and conical burners. In the case of the conical burner, the flame location is $x_f = 59$ mm; in the case of the cylindrical burner, the flame location does not affect the flame stabilization. A difference in the temperature of burned gases
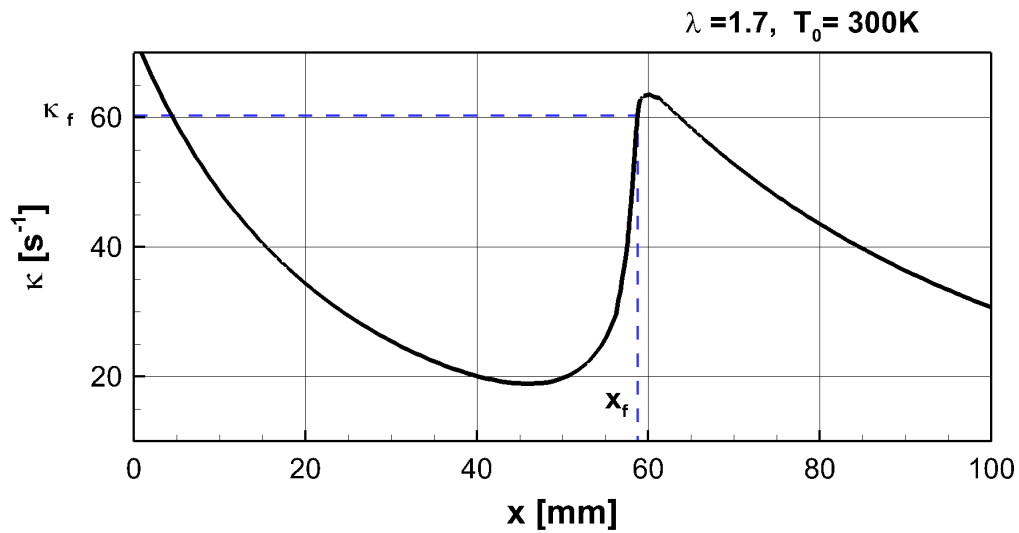
Figure 5.3: Stretch distribution along the conical 10-PPI PIM for a flame stabilized at x_f= 59 mm, λ= 1.7, T_u= 300 K, 1.0 bar
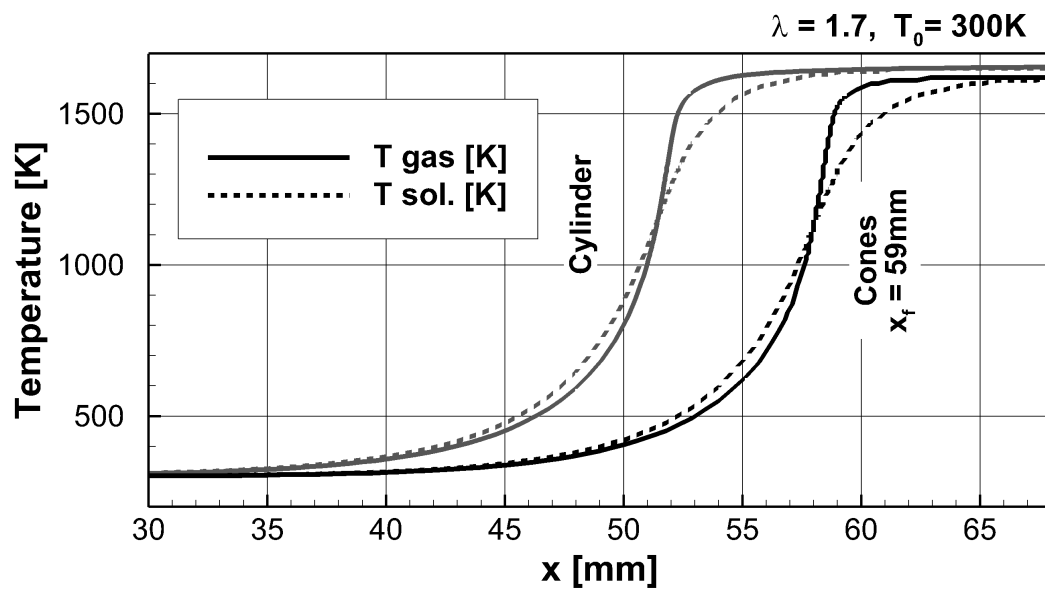

Figure 5.4: Temperature distribution calculated along the cylindrical and conical burners, 10 PPI, λ= 1.7, T_u= 300 K, 1.0 bar

between the predictions for the geometrically different domains was observed, namely, 17 K lower for the stretched flame.

This simulation was repeated at many other flame locations in the conical burner, ranging from 59 to 180 mm from the burner inlet; that is, higher inlet velocities were required in order to stabilize the flame in a downstream location. Results of the stretch at each corresponding flame location κ_f are presented in Fig.5.5 as a function of the location where the flame was stabilized x_f, at $\lambda = 1.7$ $T_0 = 300$ K 1.0 bar. It shows clearly that the flame stretch is lower if the flame location is further away from the cone's vertex, where the change of area with respect to the axial distance tends to zero (increasingly resembling a cylindrical geometry).

The flame stabilization in PIM was calculated for different air factors and pressures, keeping each of those parameters constant; the flame was stabilized at different axial locations along the conical burner inside the same range, namely, 59 to 180 mm.

Fig.5.6 shows the results of burning velocity S for the present calculations in the conical burner (empty symbols) with respect to the flame stretch κ_f at $T_u = 300$ K, $\lambda = 1.45$ and 1.7 and at pressures of 1 and 5 bar. It is observed that, in this case, the flame stretch has a negative effect on the burning velocity. The burning velocity values obtained from the simulation in the cylindrical burner are also shown in the figure with filled symbols at $\kappa_f = 0$, assuming that there is no flame stretch in this geometry. These flame conditions were selected because all of them exhibit different burning velocity, which, as shown in Eq.(5.13), together with the flame location, determines the flame stretch.

The results show that the stretched burning velocity S_s is linearly proportional to κ_f for combustion of methane premixed with air in PIM, similarly to the effect of flame stretch on the premixed combustion of the same mixtures in laminar free condition, where the negative of the slope Eq.(5.18) is known as the Markstein length L, which depends on the fuel type, the burning temperature and the pressure.

$$S_s = -L \cdot \kappa_f + S \qquad (5.18)$$

The non-stretched burning velocity S can be obtained by extrapolating the function to $\kappa_f = 0$. Actually, Fig.5.6 shows a good match between the burning velocities S obtained from calculations under the same conditions using the cylindrical burner and the extrapolation of the straight curve obtained using the conical burner at $\kappa_f = 0$.

The negative values of the obtained curve slopes L_{pim} are compared in Tab.5.2 with the Markstein lengths of laminar free flames L obtained from calculations of freely propagating laminar planar flames using GRI 3.0. Tab.5.2 also presents the non-stretched
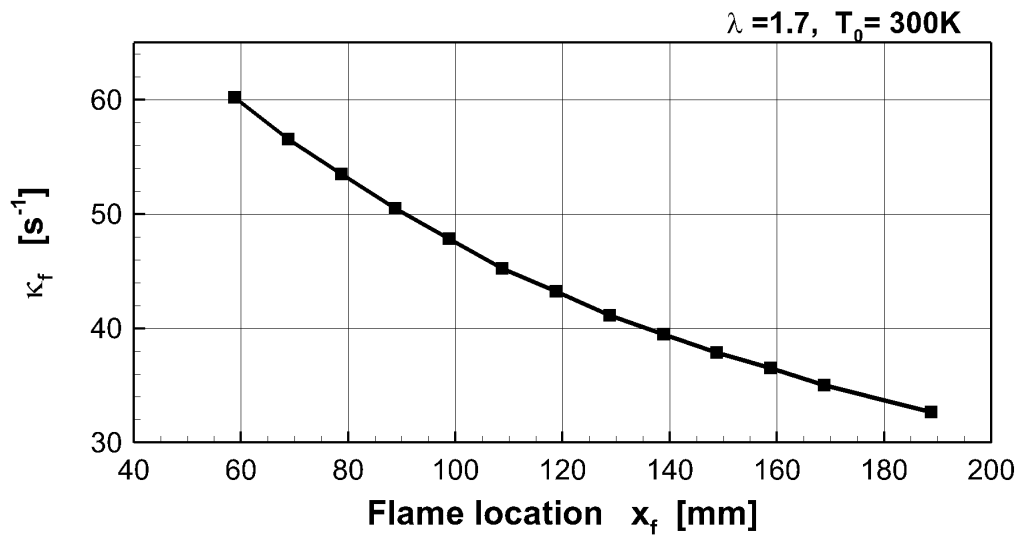
Figure 5.5: Flame stretch κ_f of different flames stabilized in the conical burner as a function of the flame location with respect to the burner inlet $\lambda = 1.7$ $T_0 = 300$ K 1.0 bar
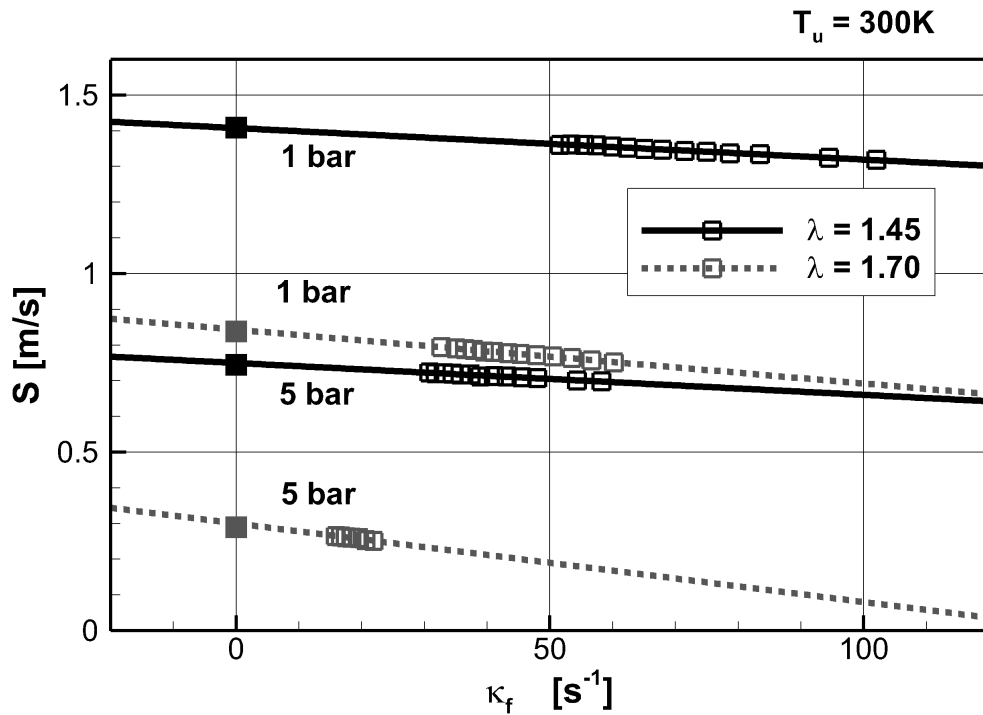

Figure 5.6: Burning velocity with respect to the flame stretch: Conical burner: Empty dots. Cylindrical burner: Filled dots. T_u= 300 K

burning velocity in PIM and in laminar free flames S_l. The results show that the air-to-fuel ratio dominates the PIM stretch length L_{pim} and, in contrast, pressure does not affect it considerably.

Table 5.2: Comparison of L and S between PIM combustion and free laminar flames $T_u=$ 300 K

$p\,[bar]$	λ	$L_{pim}\,[mm]$	$L\,[mm]$	L_{pim}/L	$S\,[m/s]$	$S_l\,[m/s]$	S/S_l
1	1.45	0.936	0.1130	8.3	1.409	0.195	7.23
5	1.45	0.852	0.0273	31.2	0.745	0.055	11.4
1	1.7	1.634	0.1314	12.4	0.837	0.102	8.21
5	1.7	1.892	0.0406	46.6	0.252	0.020	12.6

The present results show that the experimentally tested flames confined in the conical burner could exhibit macroscopic flame stretch, which could yield stretched burning velocity values of at most 7% below the burning velocity values without macroscopic flame stretch. In addition, the maximum achieved temperature could be around 20 K lower. The reason for this is the change of the cross-sectional area along the flow direction, which imposes stretch on the flame. The macroscopic flame stretch in the conical burner depends on the flame location and velocity. These predicted effects on the burning velocity are not as considerable to be experimentally observed since the error range of the measurements is higher and one should bear in mind that this model is an approximation based on average volumes and does not consider in detail the temperature distributions along the cross-sectional area; additionally, the PIM presents uncertainties in the structural parameters, from which errors of this magnitude arise [205].

Thus, in the present work, further numerical investigations of flame stabilization within PIM are performed using the cylindrical burner, where there are no macroscopic flame stretch effects.

Effects of air-to-fuel ratio, pressure and temperature on the flame stabilization in PIM

In the previous section, the effects of the change of the cross-sectional area along the conical burner on the 1D numerical results were analyzed using the DCM. The effect of other factors influencing the flame stabilization in PIM, such as air-to-fuel ratio, pressure and initial temperature, were numerically studied with the same 1D model using the cylindrical porous burner domain made of 10-PPI SiSiC.

Fig.5.7 presents the predicted burning velocity results of the 1D calculations under atmospheric conditions, compared with those of the present experiments and simulated planar laminar free flames of methane-air mixtures using the detailed chemistry mechanism

GRI 3.0 [41]. The burning velocity values and tendencies agree with the experimental ones, apart from small discrepancies. The burning velocity was underestimated for less lean mixtures ($\lambda < 1.45$). Nevertheless, the prediction of the slope was better than in previous works [15, 169], since the effective coefficients of transport were determined by DPLS on a reproduced sample of the used PIM.
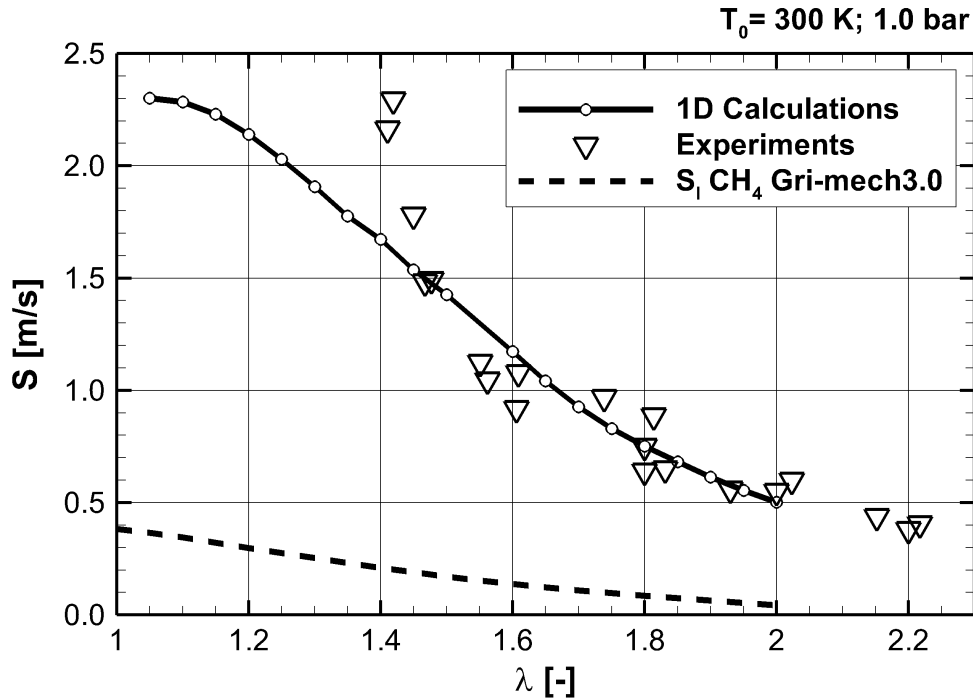

Figure 5.7: Burning velocity under atmospheric conditions as a function of air factor, 10-PPI PIM, $T_u = 300$ K, 1.0 bar.

The burning velocity results at elevated pressure are presented in Fig.5.8 for some of the air-to-fuel ratios experimentally investigated. As a result, it is stated that the 1D results yield the same pressure influence on the burning velocity as that observed in the measurements (see Fig.4.14).

At a constant air-to-fuel ratio, the burning velocity increases with increasing pressure until it reaches a maximum. With further increase in pressure, the burning velocity decreases. The slope of the decrease in the burning velocity is attenuated at higher pressures. Comparing one curve with another, that is, different air-to-fuel ratios, the augmentation of burning velocity with pressure decreases as the air-to-fuel ratio increases (larger λ) and the maximum of burning velocity is shifted towards lower pressure values.

The influence of pressure on the burning velocity at the same air factor $\lambda = 1.6$ is shown in Fig.5.9 at an elevated preheating temperature $T_u = 400$ K, in comparison to the
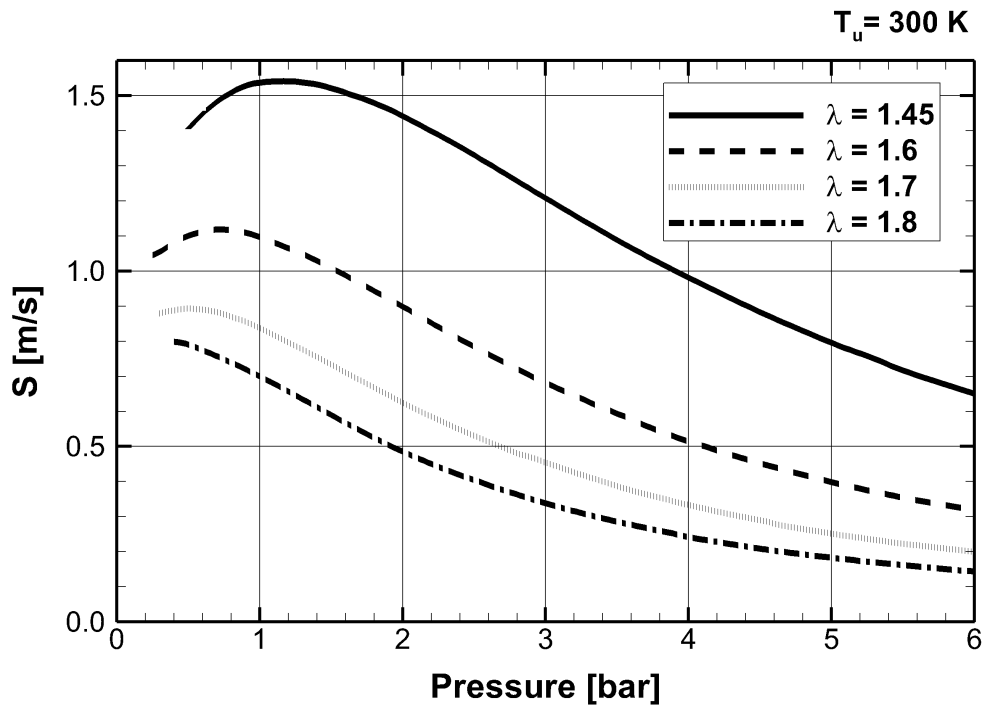
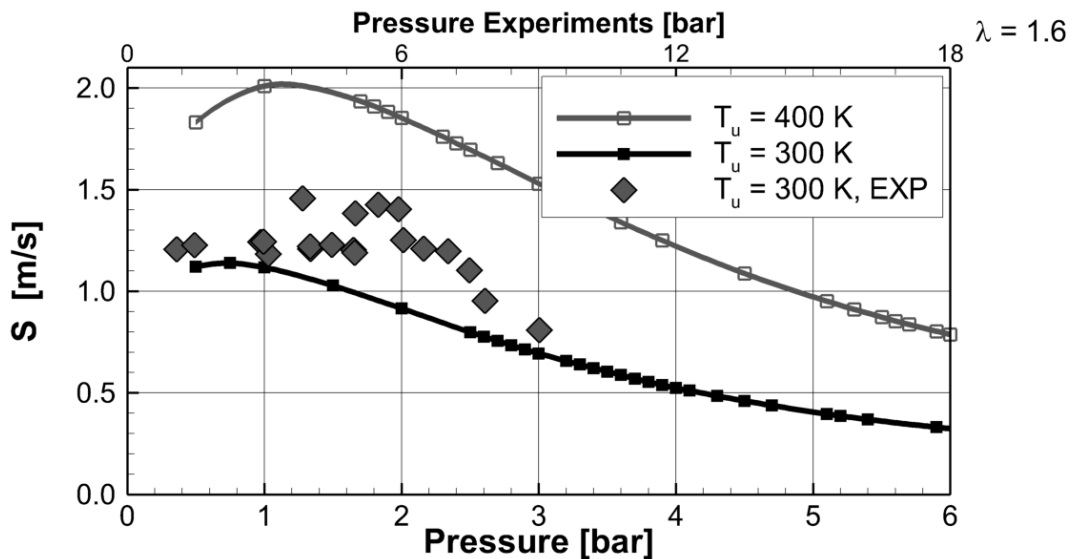Figure 5.8: 1D results of burning velocity at elevated pressure, 10 PPI, T_u= 300 K.

Figure 5.9: 1D and experimental results of burning velocity at elevated pressure and temperature, 10 PPI, λ= 1.60.

results at ambient unburned mixture temperature (300 K). The effect of increasing the temperature of the unburned mixture is similar to that of decreasing the air excess ratio; that is, the burning velocity is higher, the increase of the burning velocity with pressure is more considerable and the maximum of the burning velocity is shifted to a higher pressure value.

The obtained trends of effect of initial temperature on the pressure influence on the burning velocity are explained from results from present numerical simulations in Section 5.1.4 and theoretical analysis in Chapter 6. Modifications of parameters were performed with both models to quantify the effects of dispersion in comparison of heat recirculation through the solid phase. It was shown that pressure can have a positive effect on the burning velocities for conditions were the effects of dispersion dominate over heat recirculation, it implies conditions which exhibit a higher laminar burning velocity, namely, higher initial temperature, air to fuel ratios near the stoichiometry and pressure near 1 bar.

Although these numerical results of effects of pressure on the burning velocity qualitatively describe the experimental observations, the burning velocity values at elevated pressure appear to be underestimated, that is, the maximum S was exhibited at lower pressures and the decrease of S was considerably steeper. See a comparison between present experimental results and simulations in Fig.5.9.

Besides the burning velocity, the flame thickness is a very important combustion parameter to describe global characteristics of the flame, for example, to indicate the global volumetric reaction rate. The thermal definition of the flame thickness (see Eq.(2.18))

$$\delta = (T_{max} - T_u)/\max(\partial T/\partial x)$$

has been used in order to compare it with the experimental results obtained at atmospheric pressure.

In the case of simulation of combustion submerged in PIM, the temperature profiles of the solid and gas phases are available, while in the experiments, every temperature measurement is affected by both phases. Therefore, the thermal flame thickness obtained from measurements must be compared with the numerical results of both solid and gas temperatures, as presented in Fig.5.10. A better agreement with the thermal flame thickness based on the solid-phase temperature was obtained. Nevertheless, the predicted flame thicknesses are considerably underestimated by this model, as was also observed by Voss et al. [57] in the validation of the same model against experiments.

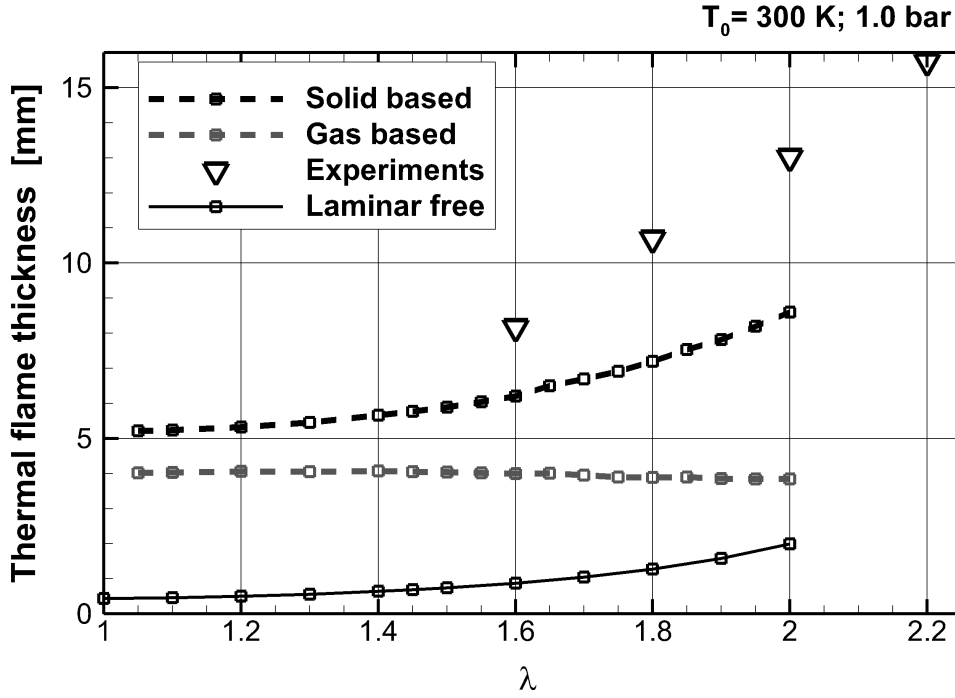Although the predicted thermal flame thickness is ≈ 5 times larger than that of the

Figure 5.10: Thermal flame thickness as function of air factor, 10-PPI PIM, T_u=300 K, 1.0 bar.

laminar free case, the 1D model fails while predicting the considerably larger macroscopic flame thickness observed in experiments. These conditions were presented for the two burner geometries, cylindrical and conical, calculated with the 1D model. The limitation observed in the results of the 1D calculations is attributed to the lack of consideration of temperature deviations along the cross-sectional area.

It seems reasonable to conjecture that the presence of the PIM itself imposes considerable spatial deviations of properties such as velocity, temperature and species concentrations, as observed in the present measurements and in [20, 67, 77, 165]. The calculation of non-linearly dependent terms such as the source terms differ considerably while formulating the model based on volumetric averages dismissing the deviations in space. As the most important example is the calculation of the averaged conversion rate of fuel, as expressed in the following inequality statement:

$$\dot{\omega}_f(X_f, X_a, T_g) \neq \int \int \int \dot{\omega}_f^*(X_f^*, X_a^*, T_g^*) \, dX_f^* \, dX_a^* \, dT_g^* \tag{5.19}$$

where the superscript * stays for local properties. Properties without this superscript represent volume averaged quantities. The calculation of the averaged conversion rate of species using the averaged molar fractions and averaged temperature (as performed

so far) is not equal to the weighted average of local conversion rates $\dot{\omega}_i^*$.

A new model is proposed in Section 5.3 as an approximation to consider the temperature deviations to calculate the average production rates. The temperature deviations were modeled using a suggested correlation based on the dispersion length scale and the gradient of average gas temperature.

Finally, Fig.5.11 shows that the effect of pressure on the predicted thermal flame thickness is, for both definitions, based on the solid-phase and gas-phase temperatures, comparable to that in the laminar free combustion mode: the flame thickness decreases with increasing pressure.
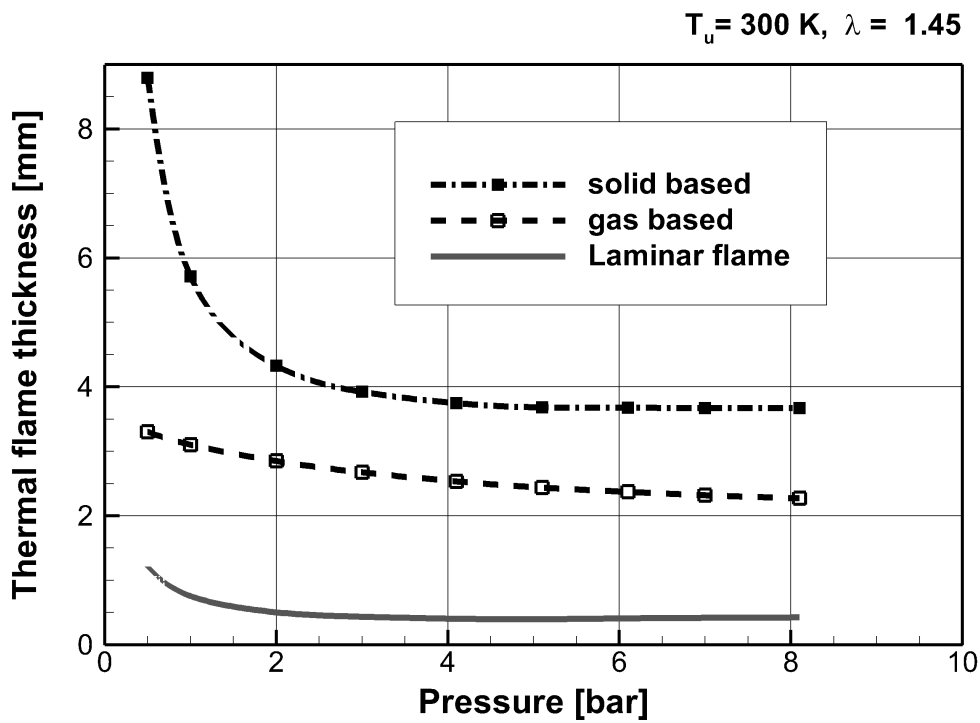
Figure 5.11: Thermal flame thickness as function of pressure, 10-PPI PIM, $T_u = 300\ K$, $\lambda = 1.45$.

5.1.3   Effect of the pore density

Simulations of the flame stabilization within a PIM with a higher pore density were performed. The pore density selected was 20 PPI, the same as that used in the experiments to study the effect of pore density.

The material and porosity were kept constant: SiSiC and 87%, respectively. The predictions of burning velocity are compared with that for the 10-PPI PIM in Fig.5.12 at

T_u= 300 K, 1.0 bar, where it can be observed that the increase of the pore density, that is, the decrease of the pore size, has a slightly negative effect on the burning velocity.

The reason for this is that the dispersion length scale d_{dis} and the inverse of the extinction coefficient β^{-1} of the 20-PPI PIM are slightly lower than those of the 10-PPI sponge, which has negative effects on the preheating of the unburned mixture. Since dispersion depends on velocity and the radiation conductivity depends on the temperature, it was to be expected that the effect of the increase of pore density from 10 to 20 PPI on the burning velocity was more evident for flames with high burning velocity and high combustion temperature (e.g. lower air-to-fuel ratio). This observations compare well with those from experimental results observed in Fig.4.16 and Fig.4.17.
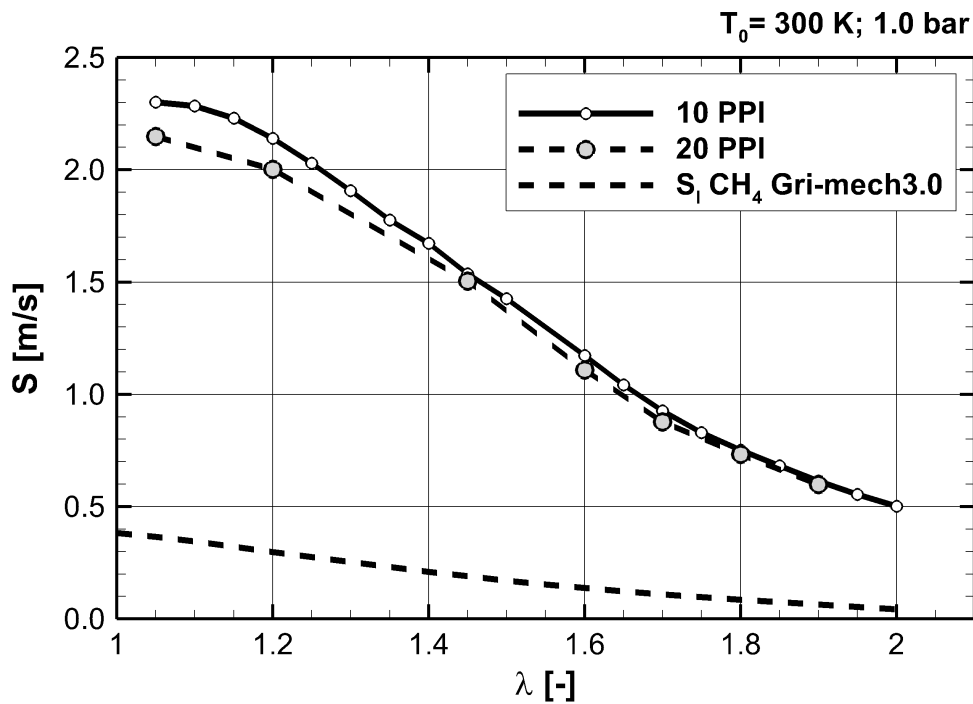
Figure 5.12: Predicted burning velocity as function of air factor, PIM at 20 PPI compared with 10 PPI, under atmospheric conditions T_u= 300 K, 1.0 bar.

The increase of pore density actually has a positive effect on the volumetric surface area of the PIM; hence, convection heat transfer could be higher. As no positive effect was observed, one could infer that the contribution of convection is not important under the conditions tested. This is supported by the parametric study described in the next section.

5.1.4   Parametric study of transport mechanisms

In order to acquire an understanding of the transport phenomena relevant to flame stabilization within PIM, parametric calculations were carried out using the 1D DCM. The transport parameters were separately varied at the same ratio (1/10) and the effect on the burning velocity was analyzed. The reference case is the 1D model presented in Section 5.1.1, namely, the PIM case, to be compared with the following cases: less dispersion, less heat recirculation, less conduction (of solid phase), less radiation and less convection. The respective variations of the transport coefficients are presented in Tab.5.3.

Table 5.3: Manipulation of transport coefficients respect the PIM reference case

Case	a_{dis}	D_{dis}	λ_s	λ_r	Nu
Less dispersion	$0.1 \cdot a_{dis}$	$0.1 \cdot D_{dis}$	λ_s	λ_r	Nu
Less heat recirculation	a_{dis}	D_{dis}	$0.1 \cdot \lambda_s$	$0.1 \cdot \lambda_r$	$0.1 \cdot Nu$
Less conduction	a_{dis}	D_{dis}	$0.1 \cdot \lambda_s$	λ_r	Nu
Less radiation	a_{dis}	D_{dis}	λ_s	$0.1 \cdot \lambda_r$	Nu
Less convection	a_{dis}	D_{dis}	λ_s	λ_r	$0.1 \cdot Nu$

The first two cases consisted separately of reduction of the transport parameters of the main two heat transport paths, as shown in Fig.2.6: 1) the contribution of hydrodynamic dispersion to transport heat and species through the gas phase and 2) the heat recirculation through the solid phase.

In the less dispersion case, the dispersion coefficients of diffusion of both heat and species were reduced down to 10% of that in the real case (PIM case), while the coefficients of the mechanisms involved in the heat recirculation through the solid phase stayed at full scale.

In the less heat recirculation case, all three coefficients of the mechanisms involved in the heat transfer though the solid phase were reduced, namely, conduction through the solid phase, solid-to-solid radiation and interface convection heat transfer. Dispersion was kept at full scale.

The other three cases consisted of the separate reduction of each of the coefficients of the processes involved in recirculating heat through the solid phase.

The burning velocities obtained at different pressure levels are used to compare the modified models with the reference case PIM in Fig.5.13 and Fig.5.14. Fig.5.13 shows that a reduction of one order of magnitude in each of the transport mechanisms has an

important effect on the value of burning velocity S at $T_u= 300$ K, 1.0 bar and different air-to-fuel ratios.

The first two cases, namely, less dispersion and less heat recirculation, show the most significant reductions of the burning velocity; thus, these two transport paths are the basic phenomena occurring in combustion within PIM.

Fig.5.13 shows that the contribution of dispersion appears to be the most important mechanism at $\lambda < 1.7$, that is, for the mixtures that exhibit the highest burning velocities, owing to the fact that the amount of cross-mixing directly depends on the bulk velocity.
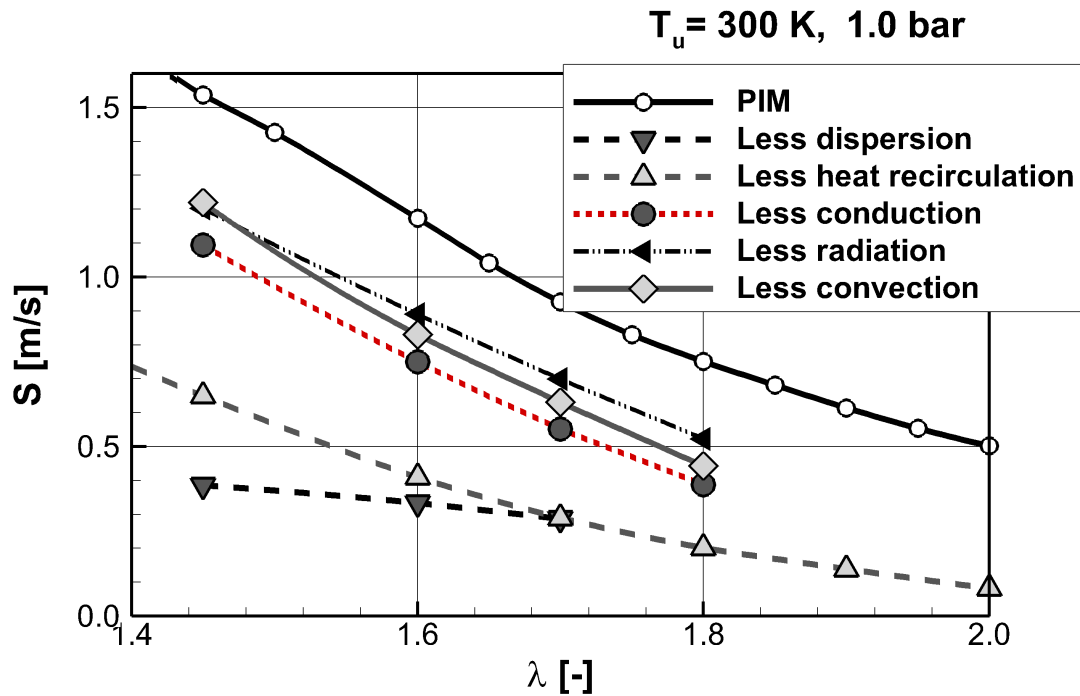

Figure 5.13: Effect of transport coefficients on S predicted with DCM model at $T_u= 300$ K and 1.0 bar

In the schematics of the coupling of heat transport (Fig.2.6), the sub-mechanisms involved in heat recirculation are connected in series, that is, the interface convection and the heat transport through the solid phase. Therefore, the dominating mechanism will be that which exhibits the highest thermal resistance from among these. In contrast, from the mechanisms involved in transport through the solid phase, namely, conduction and radiation, the dominating mechanism will be that with the smallest thermal resistance.

Fig.5.13 shows that the most important mechanism in the heat recirculation is solid

conduction, since the modeled material (SiSiC) exhibits high thermal conductivity that is one order of magnitude higher than those of other ceramic materials commonly used in porous burners. The interface convection is the least important transport process due to the large interface area between gas and solid that solid sponges exhibit, which results in lower transport resistance than those offered by the heat transport processes in the solid phase (radiation and conduction).

Nevertheless, at $\lambda > 1.5$, radiation appears to be less important than convection, since these mixtures exhibit lower combustion temperature and the radiation conductivity depends on the temperature at the power of three. Additionally, since the Nusselt number depends on velocity (see Eq.(A.8)), the trend is that convection gains in importance when the air factor increases.

Fig.5.14 shows the burning velocity S as a function of pressure for $\lambda = 1.45$ and $T_u = 300$ K calculated with the models described in Tab.5.3 in comparison with the PIM reference case and the laminar free flames. The following observations are made:

1. convection is the least important mechanism in the process at pressures higher than 1.0 bar because, with the increase of density due to pressure, the Reynolds number linearly increases and the thermal resistance decreases below that of the solid phase;

2. at elevated pressure, the contribution of dispersion is considerably more important than that of heat recirculation; and

3. dispersion represents the mechanism responsible for the increase of the burning velocity with pressure. That is, only the case of less dispersion did not show augmentation of the burning velocity, or at least the effect of pressure was not resolved sufficiently at very low pressures ($p < 0.5bar$) to observe the curve peak. However, at the studied pressure range, the influence of pressure on the burning velocity S seemed to be similar to that in laminar free flames; namely, S was not augmented with increasing pressure. The reason for this is that the only mechanism involved in heat recirculation that is affected by pressure is convection, the contribution of which is not important, as stated above. Therefore, the increase of the burning velocity in PIM with pressure is attributed to the contribution of dispersion.

The case of less heat recirculation exhibits a maximum burning velocity that is slightly shifted to a higher pressure value with respect to the reference case PIM. The simulations showed that the maximum burning velocity is presented at 1.7 bar and 1.2 bar for the less
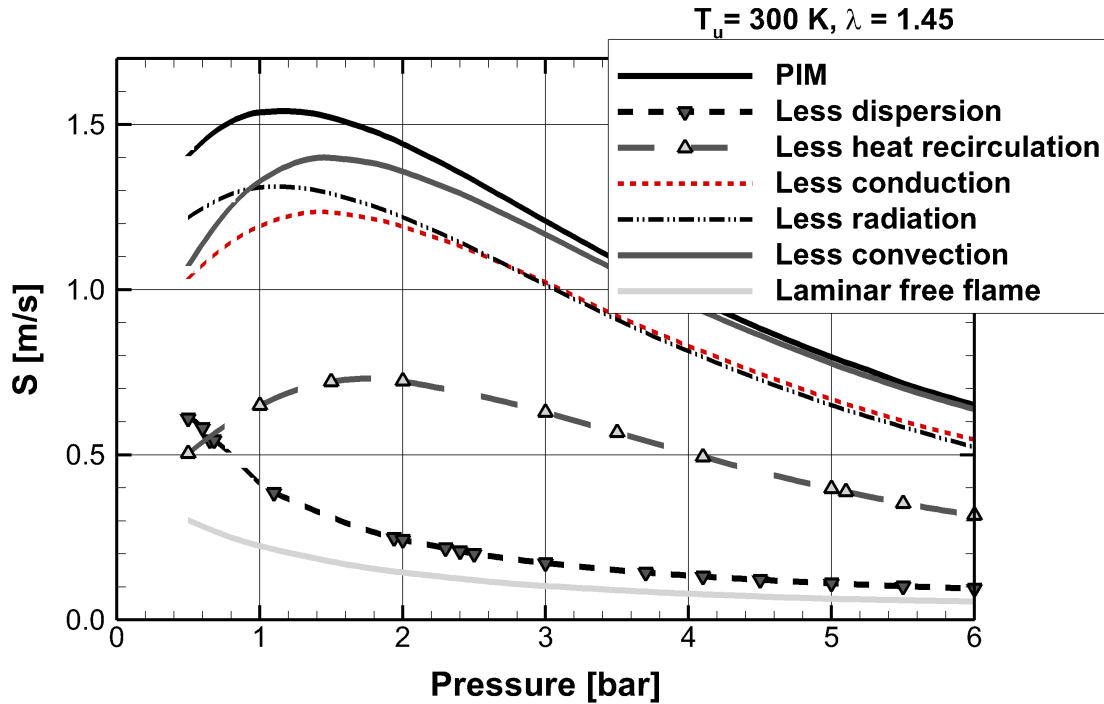
Figure 5.14: Effect of transport coefficients on S predicted with 1D model $\lambda = 1.45$ and $T_u = 300$ K

recirculation case and the PIM case, respectively. Consequently, the effect of pressure on the burning velocity depends not only on the contribution of dispersion, but on the interaction of dispersion with the heat recirculation through the solid phase.

From the sub-mechanisms involved in the heat recirculation through the solid phase, conduction appeared to be the most important, since the modeled material is highly conductive.

In conclusion, at elevated pressure, the contribution of dispersion to transport heat and species is the most relevant transport process in the flame stabilization within open cell sponges, and in turn, dispersion is responsible for the increase of the burning velocity with the increase of pressure.

In the present work, the dispersion coefficients were obtained from DPLS on a reproduced sample of the sponge used in experiments in order to minimize the uncertainty. The simulations were performed for tracer diffusion and a nearly constant Peclet number was observed. If better agreement with experiments is required, the performance of more detailed studies of the determination of mass and thermal dispersion coefficients is encouraged for combustion-like conditions, such as high temperature gradients, transport of highly diffusive species and combined effects of temperature and mass gradients.

5.2   Tabulated chemistry model (TCM)

This 1D model is proposed with the aim of providing considerably easier convergence than that of the detailed computation of direct chemistry, since the main objective is to include the consideration of temperature deviations along the burner cross-sectional area for the calculation of the average production rate of each species $\dot{\omega}_i$ in Section 5.3. Therefore, the scope of the present section is to demonstrate the validity of a new model with tabulated chemistry to predict the stabilization of premixed flames.

The tabulated chemistry model (TCM) is basically the same as the DCM but, instead of the solution of a conservation equation for each of the species considered, this model solves only a conservation equation of a reaction progress variable, which is related to the chemical composition from tabulated results of the same kind of flame obtained from a detailed pre-processor. In this case, the DCM was used to generate the chemistry table.

In this model (TCM), Eqs.(5.1-5.3) are also solved, for the balance of mass, the balance of energy in the gas phase and energy in the solid phase, respectively. The transport equation of a progress variable is

$$0 = A \cdot \rho_g \overline{u_g} \frac{\partial Y_\zeta}{\partial x} - A \cdot \dot{\omega}_\zeta M_{O2} + \frac{\partial}{\partial x} \left[\rho_\zeta \left(-D_{dis} \frac{A}{X_\zeta} \frac{\partial X_\zeta}{\partial x} \right) Y_\zeta \right] \qquad (5.20)$$

where the mass fraction of chemically bound oxygen Y_ζ has been selected as a progress variable defined as:

$$Y_\zeta = M_{O2} \cdot c_i \sum \frac{Y_i}{M_i} \qquad (5.21)$$

where M_i and Y_i are the molecular mass and the mass fraction of the ith species and c_i is the number of oxygen molecules chemically bound to the ith species, for example: $c_{CO} = 0.5$, $c_{CO2} = 1$ ...

The production rate of bound oxygen ζ is the negative value of that of oxygen:

$$\dot{\omega}_\zeta = -\dot{\omega}_{O2} \qquad (5.22)$$

For the use of this model, a look-up table of the chemical gas composition as a function of the progress variable is required. This chemistry table was generated previously from the solution of the DCM, for the same combustion case, namely, the same thermodynamic conditions, air-to-fuel ratio and environment (e.g. PIM-structural and thermo-physical properties). A general sketch of the TCM is presented in Fig.5.15.
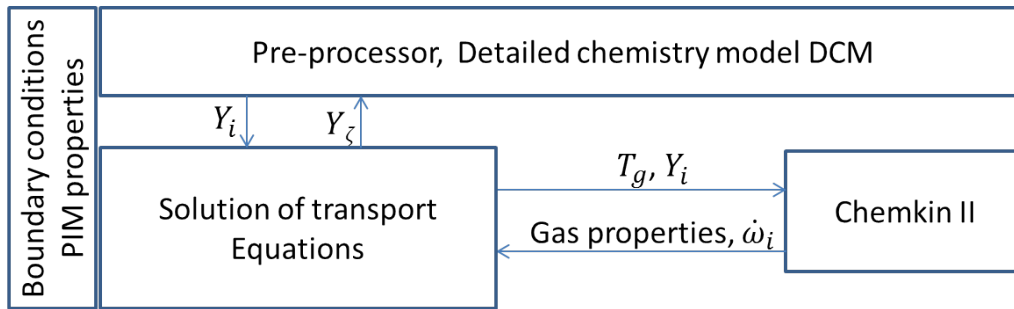
Figure 5.15: Block diagram of the tabulated chemistry model (TCM)

The chemistry table could be generated from a laminar free flame pre-processor or from the present DCM of combustion within PIM, but only the latter case makes sense for the prediction of combustion in PIM. Nevertheless, both cases were tested.

To validate the TCM, the predictions of temperature distribution, species production rates and burning velocity of reaction embedded in PIM were compared with those results from the detailed computation for combustion in the same PIM under the same conditions.

Actually, the TCM should also be able to simulate a steady planar laminar free flame with the use of the chemistry table of the corresponding flame case and the appropriate modification of the transport coefficients. In order to simulate a free laminar flame, the molecular species and thermal diffusion coefficients D_m and a_m must be included instead of the dispersion coefficients D_{dis} and a_{dis}. Additionally, the term of heat transfer with the solid phase in the energy balance of the gas phase must be set to zero.

The predicted temperature distributions, species production rates and burning velocities of laminar free flames were compared with those results from the detailed computations of laminar free flames.

Another kind of flame that was used for testing the tabulated chemistry model is the combustion in honeycombs. In this kind of porous burner, cross-mixing is avoided, that is, there is no hydrodynamic dispersion, but there is heat recirculation through the solid phase, mainly by conduction and slightly less by radiation, since the reflection angle between phases is perpendicular to the gas flow direction. Combustion in a hypothetical honeycomb burner was simulated in the present work using modified versions of the models DCM and TCM, where dispersion was not accounted for; that is, the molecular diffusion coefficients were used instead of those of dispersion.

The combinations of models used in this section are listed in Tab.5.4 by the kind of combustion and the method of access for the chemistry. Additionally, the TCM presents

other variables for which there is the possibility of using a chemistry table from other
kinds of flame. For example, combustion in PIM could be simulated with the TCM using
a table from a laminar free flame, from a honeycomb burner or from a PIM burner;
however, only the latter table makes physical sense. The results of the simulations
exploring the possibility of using tables from different kinds of flame demonstrated it.
Only the use of a table generated from the simulation of combustion within PIM allowed
reproduction of the DCM results of combustion within PIM; in contrast, the use of the
laminar free flame table yielded a burning velocity 50% lower than it should have been,
while the burning velocity using the table from the honeycomb burner was overestimated
by a factor of approximately 3.5, since the heat recirculation through the solid phase and
dispersion considerably influence the thermodynamic conditions at which the reaction
takes place.

Table 5.4: Models used

Kind of flame	Direct chemistry model DCM	Tabulated chemistry model TCM
Laminar free flame	$\star$	$\star$
Solid heat recirculation HR (Honey-comb burner)	$\star$	$\star$
PIM burner (10 PPI)	$\star$	$\star$

The three kinds of flame presented in Tab.5.4 were simulated with the DCM. The results
were used to generate the chemistry table for the corresponding kind of flame to be
simulated with the TCM.

A comparison between the two models, direct chemistry (solid lines) and tabulated
chemistry (dashed lines), for the three kinds of flame simulated is shown in Fig.5.16.
The predicted gas temperature profiles match the reference solution for all of the three
flame cases. Tab.5.5 also presents satisfactory agreement for the flame thickness based
on the maximum gas temperature gradient.

Table 5.5: Thermal flame thickness [mm] of simulated flames $T_u = 300$ K, $\lambda = 1.7$, 1.0
bar

Kind of flame	Detailed chemistry model DCM	Tabulated chemistry model TCM
Laminar free flame	1.00	1.00
Honey-comb burner	0.59	0.60
PIM burner	3.96	3.98

The simulated temperature profile of the honeycomb burner (heat recirculation) presents
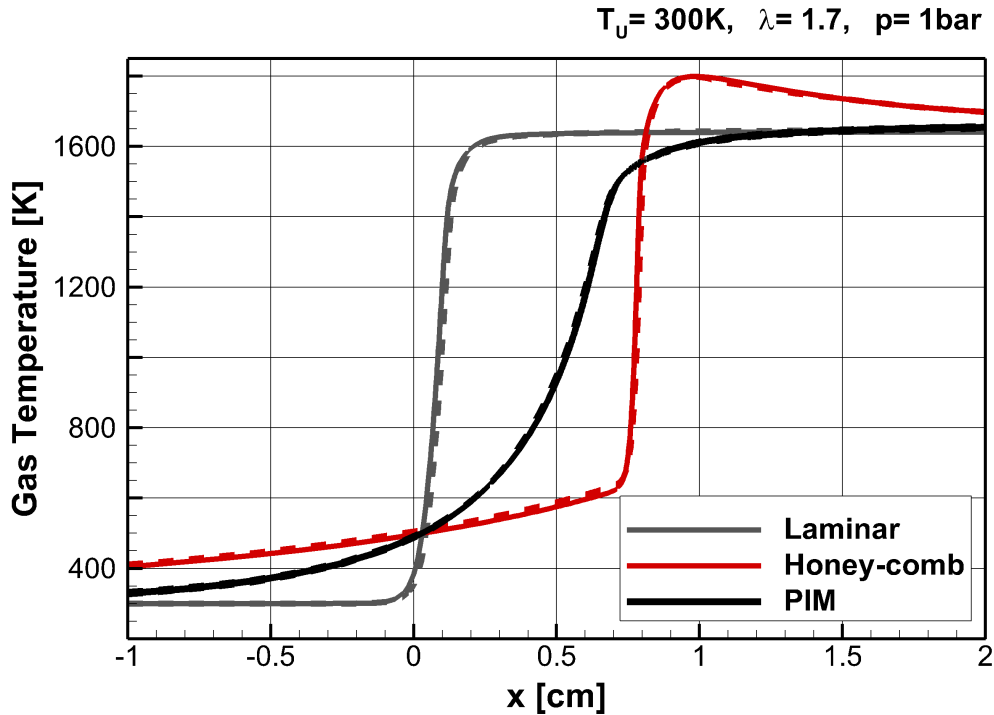
Figure 5.16: Temperature profile of gas phase of the three kinds of flame (see plot legend) from simulations using DCM and TCM: solid and dashed lines, respectively, λ=1.7, T_u=300 K, 1.0 bar.

a considerably larger preheating zone with respect to the laminar free flame. The preheating zone shows a nearly constant temperature gradient. Since the reactions take place at higher temperature, the temperature gradient in the reaction zone is considerably increased. A temperature peak is observed over the adiabatic combustion temperature. Downstream of the reaction zone, the temperature decreases down to the adiabatic combustion temperature due to the heat recirculation.

In the case of the flame stabilized within PIM, the preheating zone is also larger than in the laminar free flame, but not as large as in the honeycomb burner, that is, the flame with heat recirculation and without dispersion. The temperature gradient in the preheating zone predicted with the PIM model rises continuously due to the gradual increase of velocity, which the dispersion coefficients depend on. Since the PIM case has higher effective gas thermal conductivity and species diffusivity than in the honeycomb case, the heat and the species from the reaction zone are transported more rapidly to the preheating zone; thus, the resulting temperature gradient near the reaction zone is lower than that in the honeycomb burner and a considerable peak of average temperature is not observed; that is, there is no considerable super-adiabatic condition in the gas temperature.

Fig.5.17 presents good agreement of the burning velocity S as a function of the air factor λ for the three kinds of flame used in this validation procedure for the TCM (symbols), with respect to those results from the model with direct chemistry (DCM) (lines).
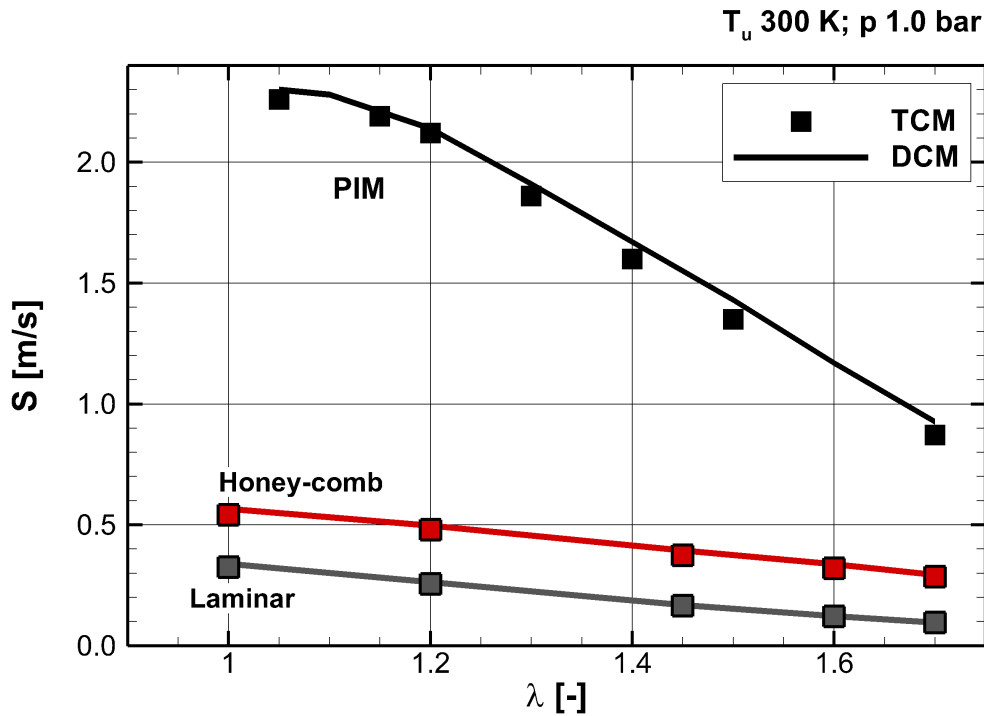

Figure 5.17: Burning velocity of different kinds of flame calculated with both models: tabulated chemistry (TCM) (symbols) and detailed chemistry models (DCM) (lines), $T_u = 300~K$, 1.0 *bar*.

The honeycomb burner exhibits a burning velocity approximately 0.23 m/s higher than the laminar burning velocity. This absolute increase is nearly constant for all the flames calculated with different air factors.

With the inclusion of the dispersion effect in the PIM flame, the burning velocity approaches an increase of 10 times the laminar burning velocity and the slope of the curve is also considerably affected.

Fig.5.18 shows the gas temperature and the volumetric oxygen production rate as functions of the reaction progress variable for the three selected kinds of flame simulated with the models DCM and TCM, shown with solid and dashed lines, respectively. Good prediction of the tabulated method with respect to the detailed computation was obtained.

The volumetric reaction rate in the honeycomb burner is considerably higher than that in the other kinds of flame, since the reaction takes place at higher temperature due to
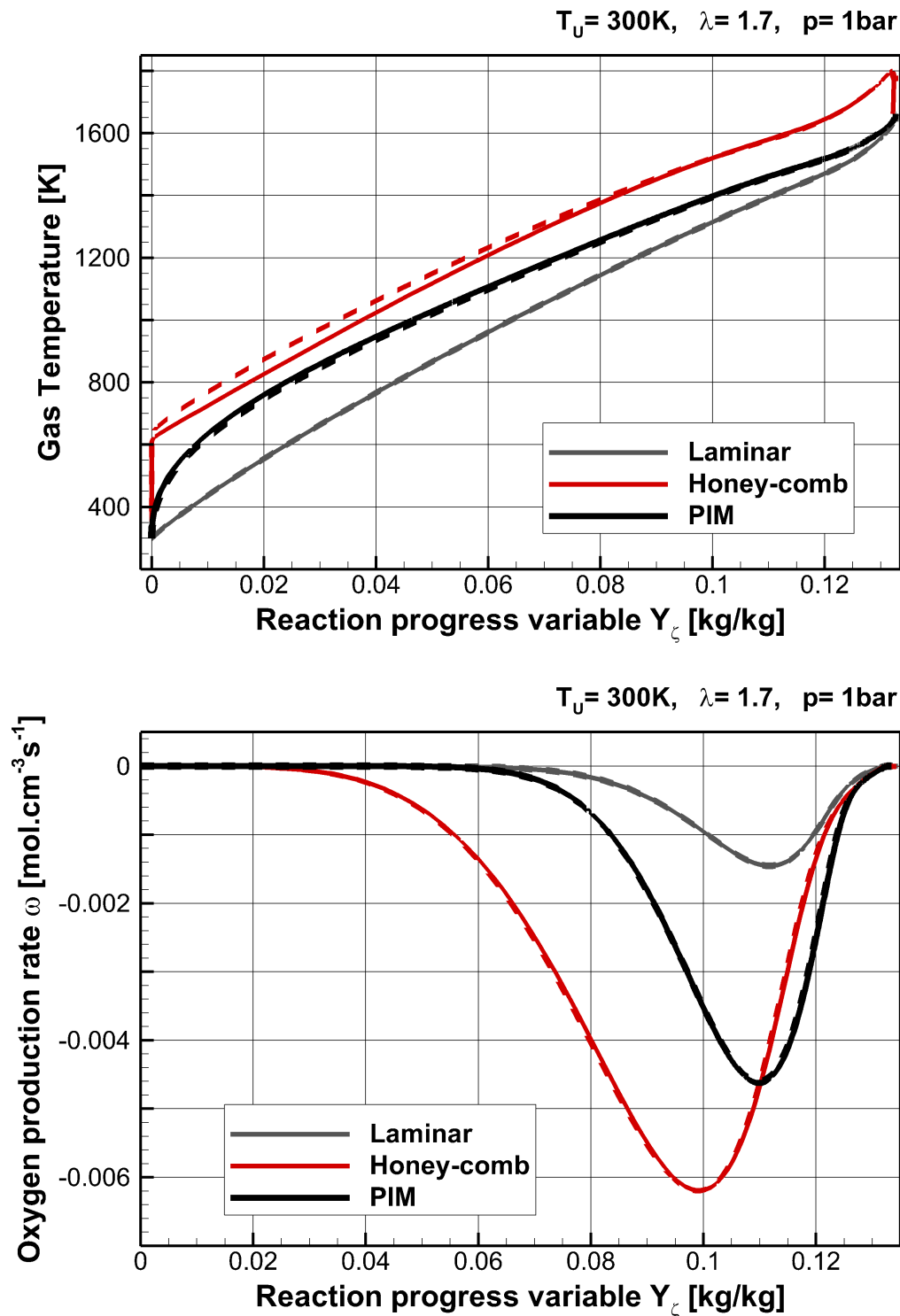
Figure 5.18: Gas temperature (top) and volumetric oxygen production rate $\dot{\omega}_{O2}$ (bottom) as functions of the mass fraction of bound oxygen of the three kinds of flame (see plot legend) from simulations using DCM and TCM: solid and dashed lines, respectively, λ=1.7, $T_u = 300\ K$, 1.0 *bar*.

heat recirculation through the solid phase. Meanwhile, in the model of combustion in PIM, higher amounts of bound species from the reaction zone are transported to the inert zone; thus, the reaction zone is considerably enlarged and the volumetric reaction rate is lower, although the resulting burning velocity is substantially higher than that without the consideration of dispersion effects.

As a conclusion of this sub-section, it is stated that the model with tabulated chemistry has been successfully validated to reproduce the results with direct computation of chemistry for laminar free flames, honeycomb burners and PIM modeled flames.

5.3 Model of temperature spatial deviations in PIM combustion

In the present measurements, it was shown that the structure of embedded flames within PIM is corrugated and discontinuous due to the random geometry of the PIM itself, as some authors have previously inferred [3, 20, 206]. The existence of spatial fluctuations of temperature along the cross-sectional area in the macroscopic region of the flame was evidenced in the present measurements. To the best of the author's knowledge, the spatial fluctuations of properties are not considered in any of the commonly used models based on the volume-averaged approach for the simulation of combustion within PIM.

The possible error from the lack of this consideration may become considerable when calculating terms that are non-linearly dependent, such as the reaction rates, the thermal conductivity of the solid phase and the solid-to-solid radiation.

In the present work, a 1D volume-averaged model of combustion within PIM called PIM PDF is formulated to consider statistical variations of the gas temperature along the burner cross-sectional area for the calculation of source terms, with the expectation of achieving better prediction of the widening of the flame brush thickness. Simulations in porous cones and cylinders at different air-to-fuel ratios were carried out for the 10-PPI burner.

5.3.1 Numerical set-up: PIM PDF model

Some examples of the consideration of statistical variation in the modeling of premixed flames are cited here for turbulent combustion [207, 208]. In the present model, the spatial distributions of temperature were modeled with probability density functions

(PDF) to calculate the source terms. The variations of species concentrations were coupled with those of temperature.

The present model uses tabulated chemistry in order to reduce the computational cost and to enhance the convergence, as a commonly used approach to address fluid/chemistry interactions in heterogeneous systems [209]. The chemistry tables were previously obtained using the DCM (see Section 5.1.1) under the same boundary conditions and for the same PIM properties. The spatial fluctuations of the local temperature T_g^* along the cross-sectional area (root mean square values RMS) were modeled using the gradient of averaged temperature T_g, which avoids the need to solve an additional differential equation to balance the fluctuations of temperature. With the variance of temperature, PDF functions were constructed. Their shape was selected as a clipped Gaussian distribution.

The local production rates $\dot{\omega}_i^*$ ($*$ stays for locally defined quantities) were weighted with the corresponding spatial probability density for the calculation of the average value of species production rates:

$$\dot{\omega}_i = \int_0^1 \dot{\omega}_i^*(\theta^*) \cdot p(\theta^*) \cdot d\theta^* \tag{5.23}$$

where θ^* is the normalized local gas temperature

$$\theta^* = (T_g^* - T_u)/(T_{g,max} - T_u) \tag{5.24}$$

and $p(\theta^*) \cdot d\theta^*$ is the probability of temperature being in the range between θ^* and $\theta^* + d\theta^*$.

Therefore, $\int_0^1 p(\theta^*)d\theta^* = 1.0$ must be fulfilled.

The local production rates $\dot{\omega}_i^*$ were calculated with the local temperature T^* and the local chemical composition $[Y_i^*]_{1-N_i}$ using the same approach as explained in Section 5.1.1.

The local mass fractions Y_i^* were coupled with the local gas temperature T_g^* under the assumption that

$$Y_i^*(T_g^*) = Y_i(T_g^*) \tag{5.25}$$

that is, Y_i^* were taken from the volume-averaged values at the domain position x, where $T_g = T_g^*$.

The presumed PDF can be constructed with the knowledge of at least the gas temperature average and its RMS values. The RMS values of gas temperature were calculated as a function of the gradient of the temperature average using a correlation obtained

from an assumption of analogy to the Boussinesq hypothesis:

$$T_{g,RMS} \cdot u_{RMS} \approx a_{dis} \cdot \frac{\partial T_g}{\partial x} \tag{5.26}$$

In the DPLS of flame stabilization in PIM [20], it was found that the spatial RMS value of the bulk velocity is 90% normalized with respect to the average bulk velocity value.

$$u_{RMS} = 0.9 \cdot u \tag{5.27}$$

then Eq.(5.26) becomes

$$T_{g,RMS} = \frac{a_{dis}}{0.9 \cdot u} \frac{\partial T_g}{\partial x} \tag{5.28}$$

This correlation offers the possibility of using an algebraic calculation of the RMS of the average gas temperature instead of the solution of an additional transport balance equation. The substitution of a_{dis} from Eq.(5.6) in Eq.(5.28) states in this case that the $T_{g,RMS}$ depends only on the axial gradient of the average gas temperature $\partial T_g/\partial x$. The results of DPLS of modeled combustion within PIM showed good agreement with this semi-theoretical correlation for all conditions simulated in the work of Bedoya et al. [20]; therefore, the generation of reality-nearer predictions with this model is expected.

An overview of the PIM PDF model is presented in Fig.5.19.

Probability density function (PDF): clipped Gaussian distribution

It is assumed that the probability density of gas temperature in a cross section in the reaction front exhibits a shape comparable to a Gaussian distribution [20]. For a considerably small width of the Gaussian distribution, this distribution turns into a Dirac delta function, which is used at the inlet (outlet) of the burner where the probability of having T_u (T_{max}) is one.

The physical limits T_u and T_{max} were used to restrict the distribution. All values of Gaussian distribution below T_u (above T_{max}) were accumulated on this point. The Dirac peak at T_u (T_{max}) represents the area below the Gaussian curve for all values between $-\infty$ and T_u (T_{max} and ∞). Fig.5.20 shows an example of the clipped Gaussian distribution corresponding to $\theta = 0.45$ and $\theta_{RMS} = 0.19$.

A database of clipped Gaussian distributions was generated by P. Habisreuther [49] varying the average μ and the standard deviation σ of the Gaussian distribution (not clipped). The values outside the physical range $0 < \theta^* < 1$ correspond to the factors α
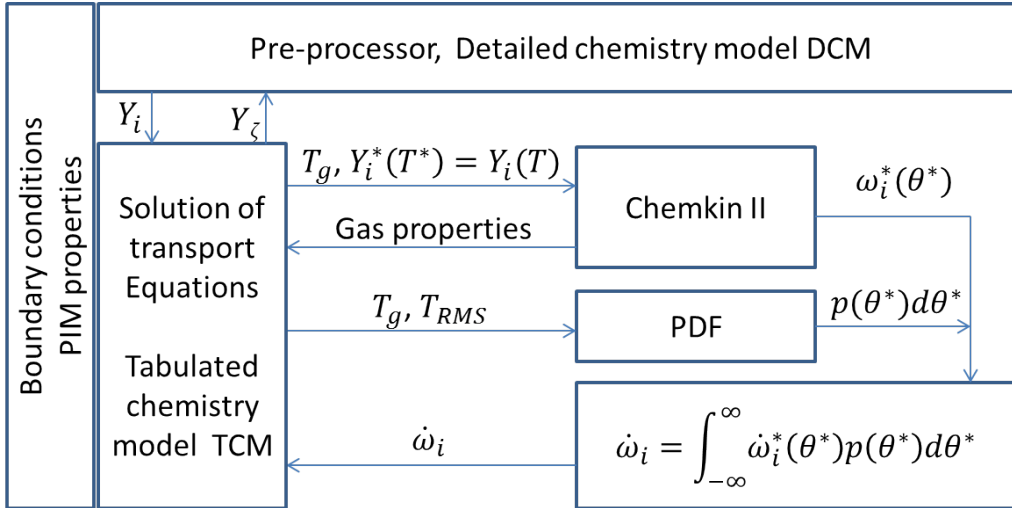
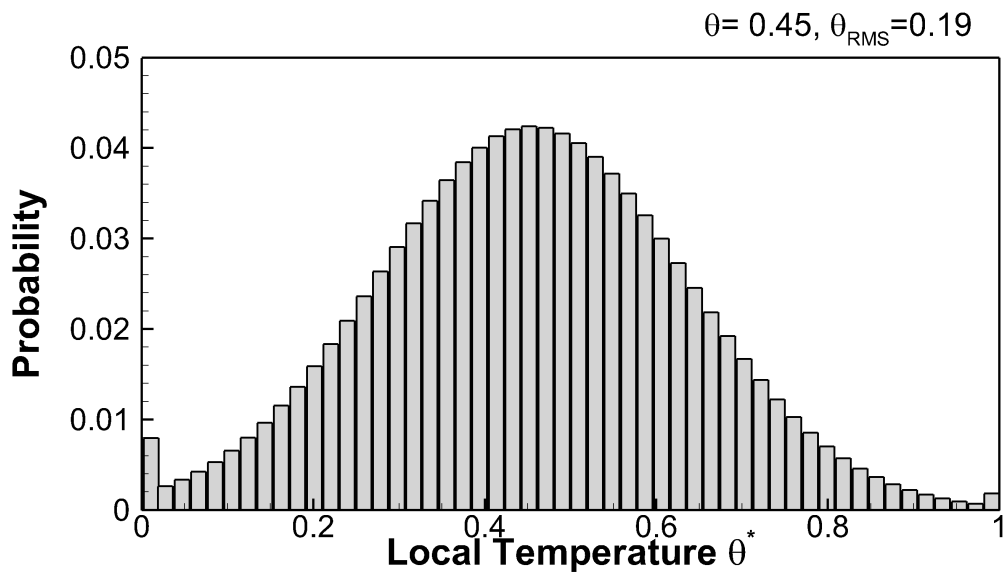Figure 5.19: Block diagram of model PIM PDF

Figure 5.20: Clipped Gaussian distribution with $\theta = 0.45$, $\theta_{RMS} = 0.19$

and β of the Dirac delta functions δ.

$$p(\theta^*) = \alpha\delta(\theta^*) + \beta\delta(1 - \theta^*) + \gamma e^{-\left((\theta^*-\mu)^2/(2\sigma^2)\right)} \tag{5.29}$$

where γ is the normalization factor:

$$\gamma = \frac{1 - \alpha - \beta}{\sigma\sqrt{\pi/2}\left[\text{erf}\left(\frac{1-\mu}{\sigma\sqrt{2}}\right) + \text{erf}\left(\frac{\mu}{\sigma\sqrt{2}}\right)\right]} \tag{5.30}$$

and erf is the error function:

$$\text{erf}(z) = \frac{2}{\sqrt{\pi}} \int_0^z e^{-t^2 dt} \tag{5.31}$$

5.3.2 Results

In order to appreciate the sensitivity of the present model to the inclusion of the temperature deviations, modification of this model was carried out:

$$\dot{\omega}_i = (1 - R) \cdot \dot{\omega}_i^*(\theta_g) + R \cdot \int_0^1 \dot{\omega}_i^*(\theta^*) \cdot p(\theta^*) \cdot d\theta^* \tag{5.32}$$

where R is called the PDF contribution coefficient, which was systematically varied from 0 to 1. For $R = 0$, the reaction rates are calculated with the average gas temperature and mass fractions; that is, the model is the same as that presented in Section 5.2, PIM without PDF. In contrast, for $R = 1$, the reaction rates are calculated with the proposed model PIM PDF, which considers the spatial deviations in temperature.

The results of burning velocity and thermal flame thickness in the cylindrical 10-PPI burner are presented in Fig.5.21 for different values of R at $\lambda=1.7$, $T_u = 300\ K$ and 1.0 *bar*. It is noted that the consideration of temperature deviations produced a considerable increase in the flame thickness; that is, the maximum temperature gradient decreased down to almost 50% at full inclusion of the PIM PDF model ($R = 1$).

For low values of R, the temperature gradient is the highest; then, the temperature variations are the highest due to the use of the correlation to obtain $T_{g,RMS}$ in Eq.(5.28). At elevated $T_{g,RMS}$, the probability density values of intermediate temperatures vanish and the PDFs all adopt the two-Dirac delta function shape, with peaks at the extremes of the temperature range of the process (T_u, T_{max}), where the reactions rates tend to be zero. Therefore, the second term on the right side of Eq.(5.32) yields so low values that the increase of R produces a decrease in the burning velocity.
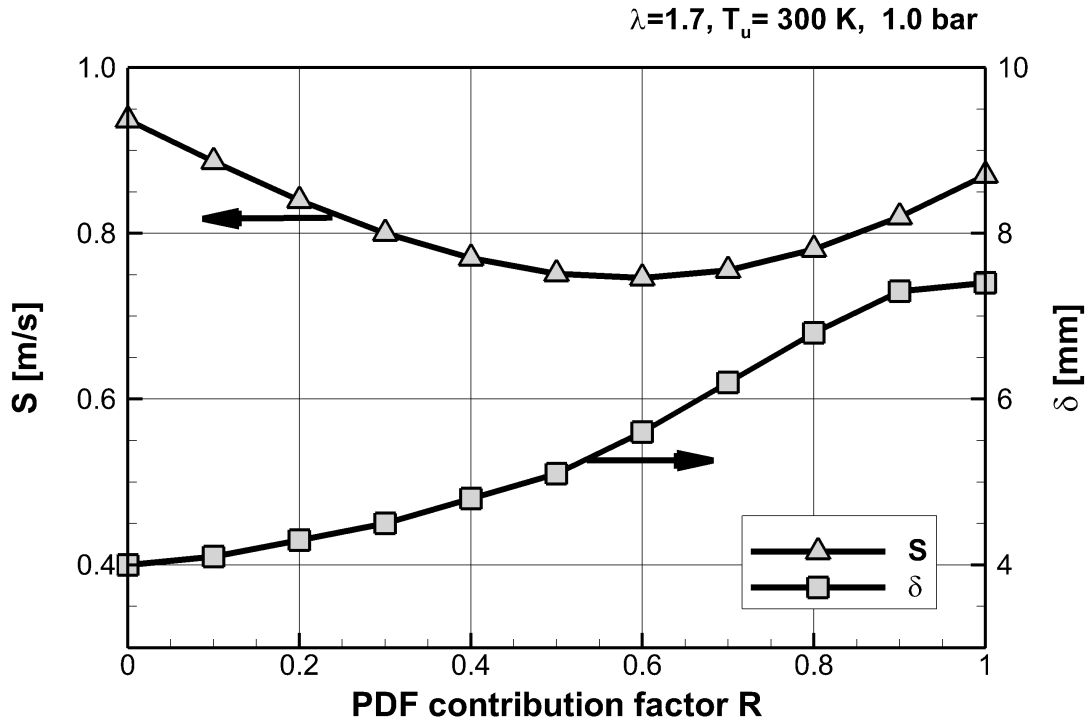
Figure 5.21: Effect of the consideration of temperature deviations on the burning velocity S and the thermal flame thickness δ at T_u= 300 K, λ= 1.7, 1.0 bar

For $R > 0.6$, the temperature gradient was low enough to allow for lower temperature variations, and then the increase of the PDF contribution R produces an increase in S.

For R=1, the burning velocity compared with that obtained without PDF under the same conditions is around 7% lower. Further results are presented and analyzed below for the model with R= 1, that is, for the proposed model PIM PDF.

In order to visualize the distribution of species conversion rates along the cross-sectional area, Fig.5.22 presents the local conversion rate ω^* of molecular oxygen weighted by its probability density $p \cdot d\theta^*$ as a function of the local normalized temperature θ^* at different selected locations x at λ=1.7, T_u=300 K and 1.0 bar. The corresponding average normalized temperature θ and its RMS are also displayed in the plot legend.

At the normalized average temperature of $\theta = 0.26$, there is no net conversion of oxygen, while at $\theta = 0.39$, namely, T_g= 836 K, considerable values are obtained. The maximum weighted local reaction rate does not occur at a local normalized temperature θ^* equal to the average one (0.39), but at a higher value of $\theta^* = 0.8$. The reason for this is that the used modified Arrhenius equation depends exponentially on temperature; that is, the local conversion rate tends to zero for $\theta^* < 0.5$.

In contrast, in a cross section near the burned side of the flame, that is, at a high θ of
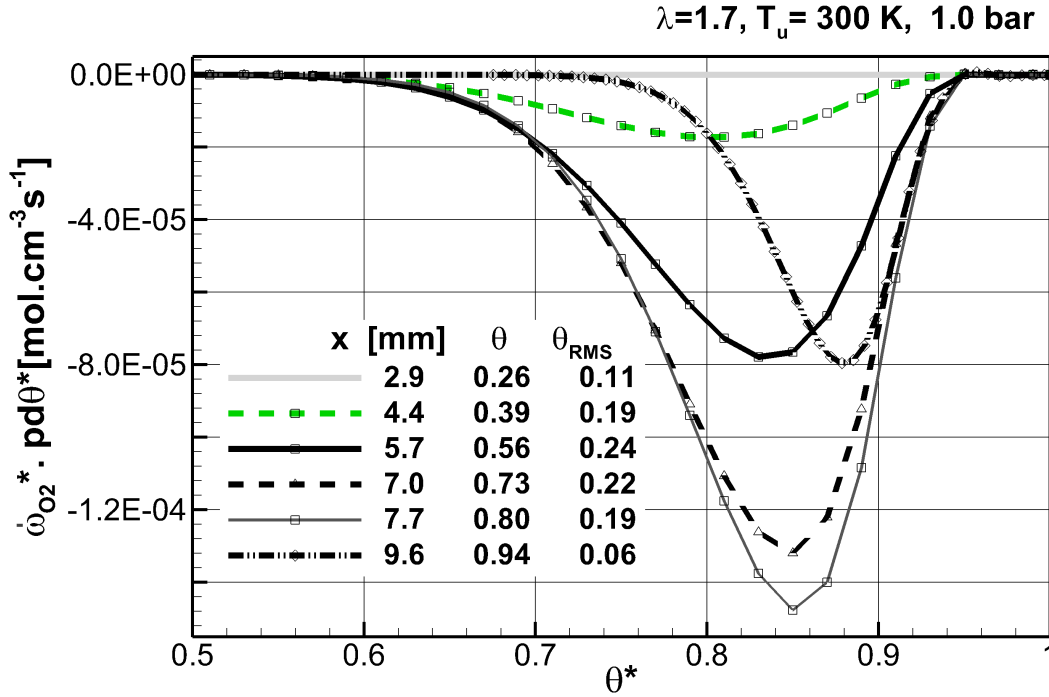
Figure 5.22: Weighted oxygen conversion rates along the cross-sectional area at different x locations as a function of the normalized local temperature θ^*, λ=1.7, T_u=300 K, 1.0 bar.

0.94, the maximum of the distribution of the weighted conversion rate is located at a lower θ^* of 0.88 because, at high θ^*, the educts possesses lower concentrations.

Fig.5.23 presents the axial profiles of average temperatures of the gas and solid phases, as well as the average production rates of some selected species: O_2, H_2O and CO at λ=1.7, T_u=300 K and 1.0 bar. The conversion of species was initiated at an average temperature of approximately 720 K, normalized to $\theta = 0.29$. The size of the region where the conversion of species takes place is clearly considerable with respect to the domain where temperature increases; that is, the reaction thickness ranges between 6 and 11 mm depending on the definition used: 5% of the maximum production rate of oxygen or that of water, respectively. In contrast, the whole thermal flame thickness (defined in Eq.(2.18) is 7.4 mm. The obtained preheating zone is also considerably thicker than that of a laminar free flame.

A comparison with the model without consideration of temperature deviations (PIM without PDF) and the laminar free flame is displayed in Fig.5.24 and Fig.5.25 for the same conditions λ=1.7, T_u= 300 K, 1.0 bar. The temperature profile obtained considering PDF is considerably smoother than in the other cases and there is neither a considerable gas temperature peak observed nor considerable super-adiabatic condition
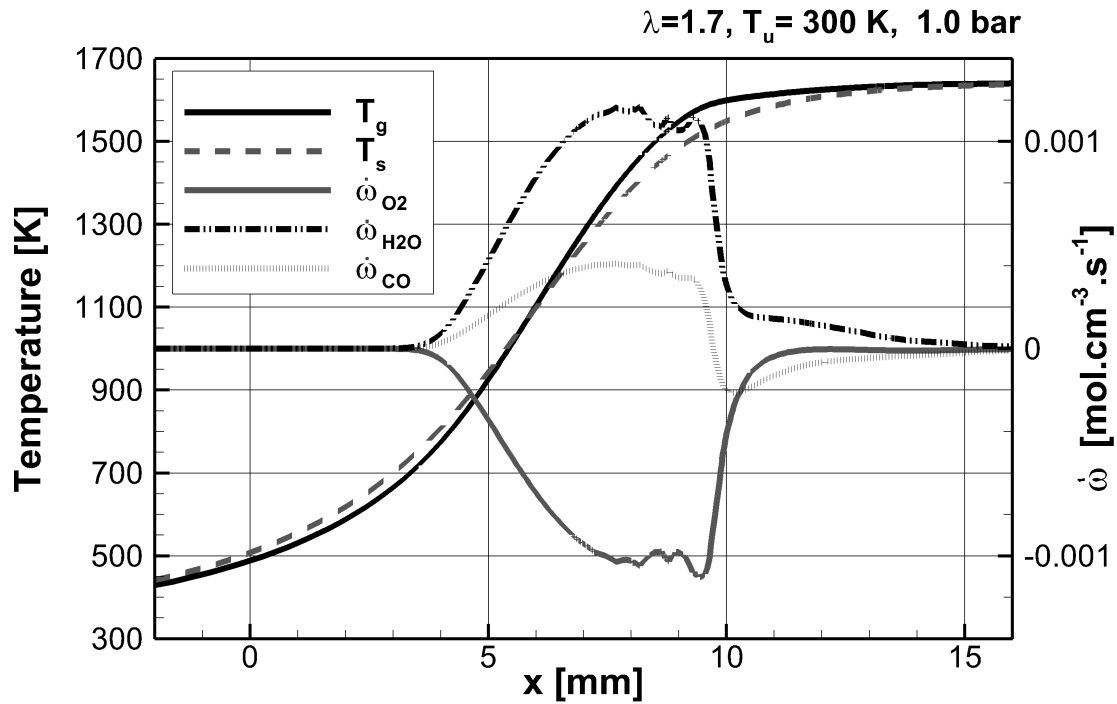
Figure 5.23: 1D model PIM PDF profiles of average temperature and production rate of selected species, λ=1.7, T_u= 300 K, 1.0 bar

(see Fig.5.24).

The average conversion rate of oxygen as a function of the average gas temperature presents a completely different shape than that calculated with merely the average temperature (see Fig.5.25); that is, the simulation of combustion within PIM without considering spatial deviations of temperature results in a reaction zone with similar dependence on temperature as that in a laminar free flame, which cannot predict the average flame brush thickness observed in experiments.

Simulations with this model (PIM PDF) were carried out in the conical porous burner, while also varying the flame stabilization location. The observed effect of the diverging geometry on the burning velocity and the temperature profiles did not differ from that observed with the detailed computations, which were carried out while neglecting temperature variations.

The flame stabilization within PIM was simulated for other air-to-fuel ratios under lean conditions with the model PIM PDF. Fig.5.26 shows the thermal flame thickness based on the maximum gradient of average temperature of both gas and solid phases for different air factors at 300 K and 1.0 bar, in comparison with experiments and the PIM model without PDF. It is notable that the predicted thermal flame thickness δ based
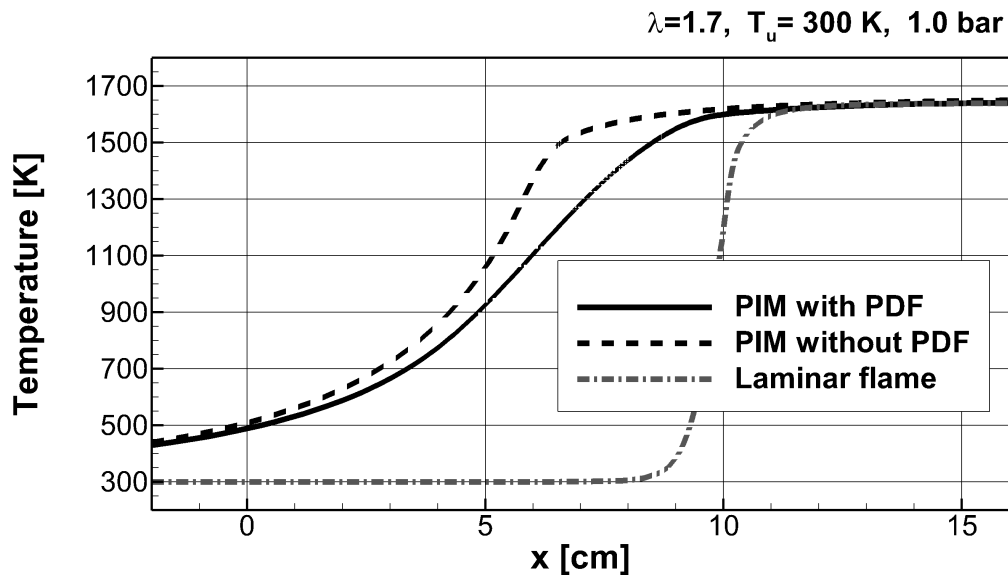
Figure 5.24: Comparison of the gas temperature profile obtained from the models with and without PDF, λ=1.7, T_0=300 K, 1 bar.
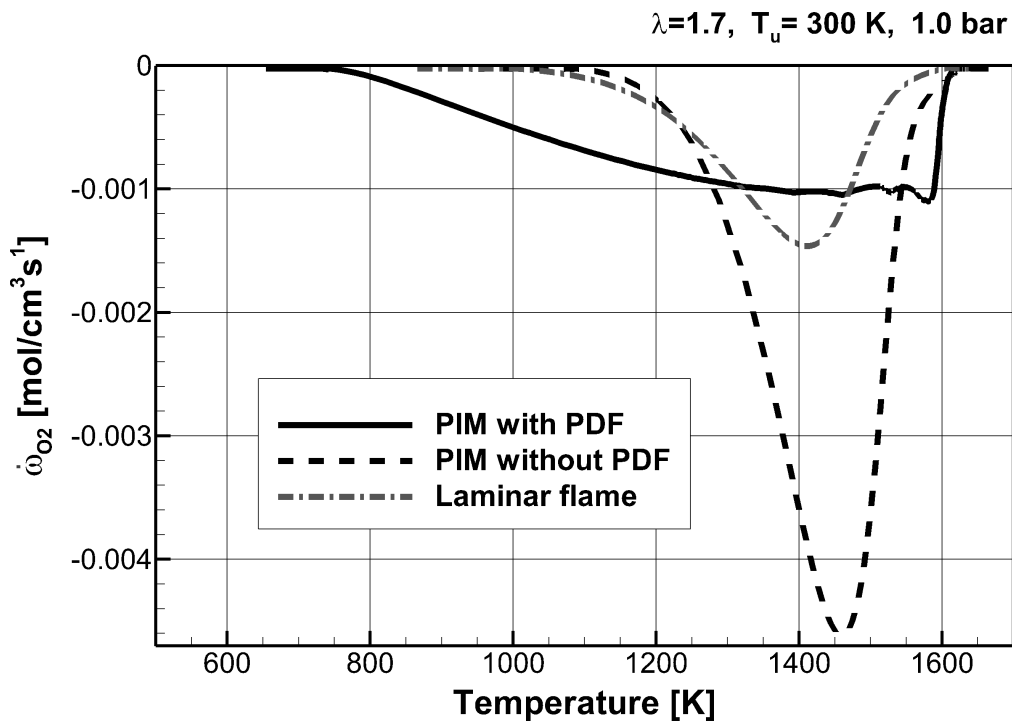

Figure 5.25: Average production rates of oxygen in a flame in PIM simulated with and without consideration of temperature deviations in comparison to that in the laminar free flame, λ=1.7, T_u= 300 K, 1.0 bar

on the solid temperature compares well with the experiments. δ_{gas} is almost twice that predicted by the model without PDF.

Fig.5.27 presents the results of burning velocity. It is observed that the good agreement with experiments predicted with the other model was maintained. The burning velocity obtained with the PIM PDF model shows a nearly constant difference with the other model of 7 cm/s

In summary, the model considering the effect of temperature variations on the species production rates yields substantially flattened temperature profiles at the reaction zone, which compare well with the experiments. Study of the effect of the temperature RMS is encouraged, with the possibility of considering statistical variations of other parameters by using joint PDF models, such as mass fractions and velocity, as well as the use of other PDF shapes such as the β distribution, in order to consider the locally super-adiabatic regions in the PDF. The species production rates show considerable values at very low average gas temperatures ($\approx 710\ K$) compared with those in the continuum models used so far ($\approx 1300\ K$). An average temperature of activation of reactions T^0 was defined as the gas temperature at which 5% of the maximum oxygen consumption occurs. Fig.5.28 shows that T^0 is a function of the air factor. Nevertheless, T^0 does not vary considerably, that is, $T^0 = 690\ K\ \pm 40\ K$.

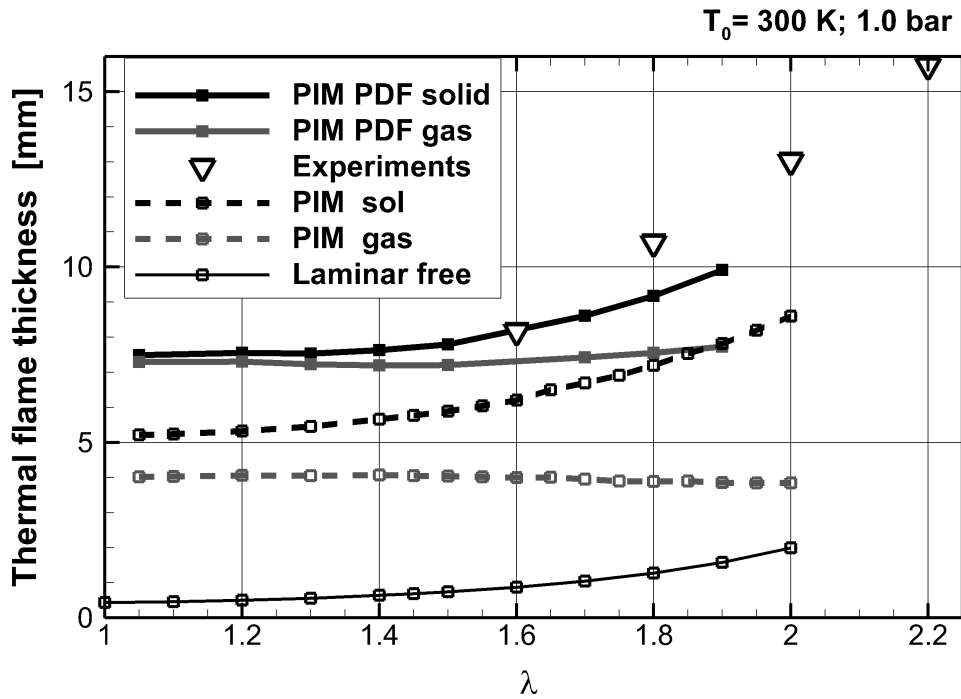Figure 5.26: Thermal flame thickness with the 1D model PIM PDF compared with experiments, PIM model without PDF and laminar free flames, $T_u = 300$ K, 1.0 bar
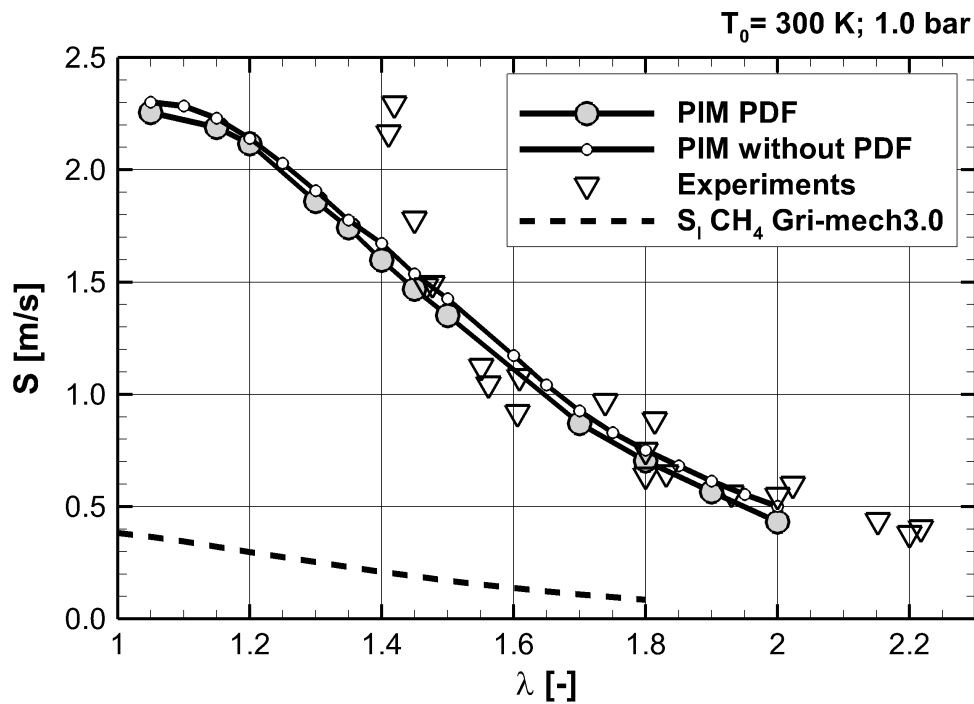

Figure 5.27: Comparison of burning velocity in PIM obtained from the 1D model with and without PDF; $T_u = 300K$, 1.0 bar
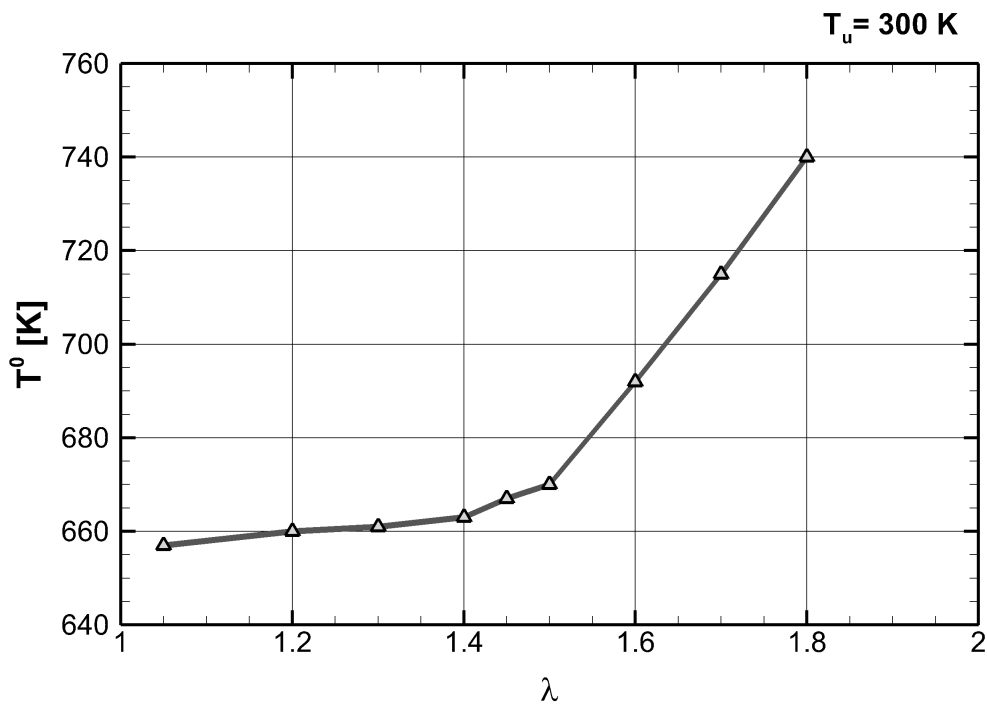
Figure 5.28: Temperature of reaction activation T^0 as a function of the air factor obtained with the PIM PDF model; $T_u = 300K$, 1.0 bar

Chapter 6

Theoretical study of flame stabilization within PIM

The classic thermal theory of Mallard and Le Chatelier [34] for laminar free flames is applied in the present section analogously to the case of premixed stationary combustion within PIM for the analytical and simple prediction of the burning velocity and flame thickness in porous burners as functions of the laminar burning velocity, with the objective of developing a simple model for practical use in the dimensioning of porous burners and to promote understanding of the physics behind the process.

6.1 Theoretical model

The following assumptions are made:

1. Local thermal equilibrium between phases

2. The heat release timescale τ_c is not affected by the presence of the PIM

The first assumption is the adoption of local thermal equilibrium between phases, namely, $T_g = T_s = T$. This assumption is justified for a rough approach because convection between phases in this kind of sponge-like structure exhibits considerably lower heat transfer resistance than the other involved mechanisms, that is, solid conduction and solid-to-solid radiation. Thus, in the present analytical model, it is assumed that heat conduction processes in the solid and gas phases take place in parallel, so there is no net heat transfer from one phase to the other.

Analogously to laminar free flames (see Section 2.2.1), the existence of two main layers was observed, an inert zone and a reaction zone. Thus, an enthalpy balance around the inert zone and the assumption of a linear temperature profile yield:

$$\dot{m} \cdot c_{p,g,u}(T^0 - T_u) = \lambda_{eff,2-ph} \cdot A_{pim}(T_b - T^0)/\delta \tag{6.1}$$

where $\lambda_{eff,2-ph}$ is the overall effective thermal diffusivity of the medium at temperature T^0, A_{pim} is the burner cross-sectional area taken to be a constant at unity and $c_{p,g,u}$ is the specific heat capacity of the unburned gas phase, which are assumed to be constant. The bulk flow can be considered as one-dimensional:

$$\dot{m} = \rho \cdot A_{pim} \cdot u = \rho_u \cdot A_{pim} \cdot u_u \tag{6.2}$$

where u is the bulk superficial velocity ($u = \varepsilon \cdot u_g$). For the flame stabilization in a stationary location:

$$S = u_u \tag{6.3}$$

Eq.(6.1) becomes

$$\rho_u \cdot S \cdot c_{p,g,u}(T^0 - T_u) = \lambda_{eff,2-ph}(T_b - T^0)/\delta \tag{6.4}$$

or

$$S = \frac{\lambda_{eff,2-ph}}{\rho_u \cdot c_{p,g,u}} \frac{(T_b - T^0)}{(T^0 - T_u)} \cdot \frac{1}{\delta} \tag{6.5}$$

The reaction zone thickness is related to the burning velocity

$$\delta = S \cdot \frac{T^0}{T_u} \cdot \tau_{c,pim} \tag{6.6}$$

by the heat release time in this kind of burner $\tau_{c,pim}$. The second basic assumption for this analytical model is that the timescale of heat release is not affected by the presence of the PIM,

$$\tau_{c,pim} = \tau_c \tag{6.7}$$

Therefore, the same result as in the classic theory is yielded as expected,

$$S^2 = \frac{\lambda_{eff,2-ph}}{\rho_u \cdot c_{p,g,u}} \frac{(T_b - T^0)}{(T^0 - T_u)} \cdot \frac{1}{\tau_c} \cdot \frac{T_u}{T^0} \tag{6.8}$$

where τ_c is related to the laminar burning velocity S_l from the approximation of the thermal theory of laminar freely propagating flames from Eq.(2.9) and Eq.(2.10):

$$S_l^2 = \frac{\lambda_{g,b}}{\rho_u \cdot c_{p,g,u}} \frac{(T_b - T^0)}{(T^0 - T_u)} \cdot \frac{1}{\tau_c} \cdot \frac{T_u}{T^0} \qquad (6.9)$$

Then, dividing Eq.(6.8) by Eq.(6.9) it yields

$$S = \left(\frac{\lambda_{eff,2-ph}}{\lambda_{g,b}} \right)^{1/2} \cdot S_l \qquad (6.10)$$

the expression for obtaining the burning velocity in PIM. After evaluating the S, the flame thickness is obtained from Eq.(6.5).

This adaptation of the thermal theory to the combustion within PIM could be evaluated as a very rough approximation. It was performed in this way because special care must be taken for calculation of the overall effective thermal conductivity of the medium $\lambda_{eff,2-ph}$, since the contribution of dispersion to heat transport depends on the gas velocity, namely, $\lambda_{eff,2-ph}$ also depends on the burning velocity.

6.2   Effective transport parameter

From the first assumption, that the heat conduction in the solid and gases phases occurs in parallel, then the overall conductivity is the weighted arithmetic mean of the effective conductivities, Eq.(2.49) becomes:

$$\lambda_{eff,2-ph} = \varepsilon \cdot (\lambda_g/\tau + \lambda_{dis}) + (1 - \varepsilon) \cdot (\lambda_s/\tau_s + \lambda_r) \qquad (6.11)$$

The effective conductivity of gas phase considers the contribution due to dispersion λ_{dis} and the reduction of the molecular conductivity λ_g due to flow tortuosity τ. $\lambda_{m,g}$ is negligible compared to λ_{dis}.

λ_{dis} from Eq.(2.51):

$$\lambda_{dis} = \rho_u \cdot c_{p,g,u} \cdot a_{dis}$$

With the substitution of the dispersion coefficient a_{dis} from Eq.(5.6)

$$\lambda_{dis} = \rho_u \cdot c_{p,g,u} \cdot 0.5 \cdot d_{dis} \cdot u(T^0) \qquad (6.12)$$

the superficial velocity at temperature T^0 can be related to the velocity of unburned

gas, that is, the burning velocity using Eq.(6.2) $[u(T^0)/T^0 = S/T_u]$; then,

$$\lambda_{dis} = \rho_u \cdot c_{p,g,u} \cdot 0.5 \cdot d_{dis} \cdot \frac{T^0}{T_u} \cdot S \tag{6.13}$$

In the case of the solid phase, the effective thermal conductivity of the solid phase considers the reduction due to the tortuous heat conduction paths through the sponge-like structure τ_s and the contribution of radiation $\lambda_r(T^0)$ (see Eq.(2.53)).

$$\lambda_r = (16 \cdot \sigma \cdot T_s^3)/(3 \cdot \beta)$$

Finally, the overall effective thermal conductivity of the medium can be substituted in Eq.(6.10),

$$\frac{\lambda_{g,b}}{S_l^2} \cdot S^2 - 0.5 \cdot \varepsilon \cdot \rho_u \cdot c_{p,g,u} \cdot d_{dis} \frac{T^0}{T_u} \cdot S - (1 - \varepsilon) \cdot (\lambda_s/\tau_s + \lambda_r) = 0 \tag{6.14}$$

This algebraic equation has the form: $a \cdot S^2 + b \cdot S + c = 0$, which can be analytically solved for S. The inclusion of the second term of the equation, namely, the dispersion term, involves the density, which is directly proportional to pressure. Since the laminar burning velocity of methane approximately decreases with the inverse of the square root of pressure, identification of the effect of pressure on the burning velocity in PIM is not trivial as shown by this model. Thus, an evaluation of the model was carried out for the PIM used in the present work. Since the increase of the pore density from 10 to 20 PPI is not associated with a representative decrease in either the dispersion coefficient or the effective thermal conductivity, these parameters were artificially varied in order to observe their importance in the flame stabilization mechanism.

6.3 Evaluation and discussion

The results of burning velocity from the evaluation of Eq.(6.14) are presented in Figures 6.1, 6.2, 6.3 and 6.4 for a sponge-like PIM with 10 PPI made of SiSiC. The gas properties and the laminar burning velocities were calculated with the CHEMKIN package using GRI mech 3.0. The used properties of the PIM are listed in Tab.5.1. The solid conductivity λ_s of sintered SiSiC was estimated at the temperature $T_s = T^0$ using a correlation from [191].

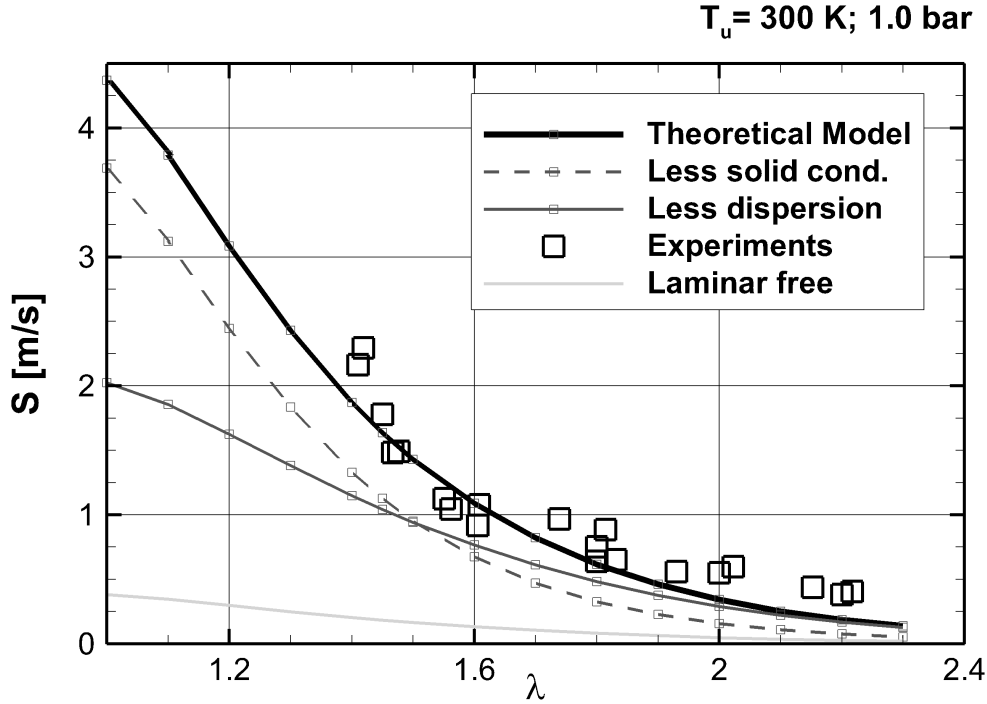$$\lambda_s = \left[(52000 \cdot \exp(-1.24 \cdot 10^5 (T_s - 273))) \right] / (T_s + 164) \tag{6.15}$$

Figure 6.1: Theoretical burning velocity calculated with different models in comparison to the experiments, PIM 10 PPI, T_u=300 K, 1.0 bar.

The temperature T^0 value used was 690 K. This value of average temperature of ignition was observed in the 1D numerical simulations, with consideration of temperature deviations (PIM-PDF model) to be in the range of 650 to 750 K. The arbitrary selection of this value is justified below.

The values of the effective solid conductivities at this temperature value are $(1 - \varepsilon)\lambda_s/\tau_s = 3.51\,W/mK$ and $(1 - \varepsilon)\lambda_r = 0.08\,W/mK$, while the value of dispersion conductivity at a bulk velocity of gases of $u = 1.42 \cdot (670\ K/300\ K)\ m/s$ is $(\varepsilon \cdot \lambda_{dis}) = 5.46\,W/mK$.

Fig.6.1 shows that the burning velocity results at 1.0 bar and 300 K obtained from the present theoretical model agree well with experimental values obtained at different air factors λ. It appears to provide good prediction of the burning velocity at air factors lower than 1.9.

In order to appreciate the influence of the involved parameters, the main terms in the present model Eq.(6.14) were separately reduced, as presented in Tab.6.1, to generate two hypothetical cases: less dispersion and less solid conduction. The resulting burning velocities from these model cases are also shown in Fig.6.1, which indicates that dispersion is more important than solid conduction for air factors lower than 1.5, while for leaner mixtures, the stabilization mechanism is dominated by the heat transfer through

the solid phase; since the burning velocity is lower, the dispersion contribution is not as important.

Table 6.1: Modification of transport coefficients respect the PIM reference case

Case	λ_{dis}	λ_s
Less dispersion	$0.1 \cdot \lambda_{dis}$	λ_s
Less solid conduction	λ_{dis}	$0.1 \cdot \lambda_s$

As mentioned above, the effect of pressure on the burning velocity in PIM was not clear from the model proposed in the present section, without a detailed evaluation of an example case. Fig.6.2 shows the resulting burning velocities from the reference PIM case as a function of pressure for different air-to-fuel ratios at T_u= 300 K. It is clear that the effect of pressure differs considerably from that in laminar free flames, where its effect is always negative. In contrast, in the PIM case, it was observed that pressure can have a positive effect for a stoichiometric mixture until the burning velocity reaches a maximum value and, upon a further increase of pressure, the burning velocity can decrease to achieve a nearly constant value.

The reason why the pressure can positively affect the burning velocity is based on the second term of Eq.(6.14), namely, the dispersion contribution, which is considerably more important at higher velocities, that is, in burnable mixtures that can exhibit higher laminar burning velocities (i.e. with air-to-fuel ratios near the stoichiometric proportion, higher initial temperatures and lower pressures).

Fig.6.3 presents the obtained results of burning velocity in the PIM reference case at $\lambda = 1.2$ as a function of pressure compared with the other two cases, low dispersion and low solid conduction. The results from the exemplary case of the present theoretical model show that the burning velocity seems to be nearly pressure-independent.

In the case in which dispersion is not reduced, that is, the less solid conduction case, the burning velocity increases considerably with pressure up to approximately 5 bar, but for further increases of pressure, it stays nearly constant.

For the other case, where dispersion is reduced (i.e. less dispersion), the influence of pressure on the burning velocity is like that of free laminar flames, where its effect is merely negative. Thus, the hydrodynamic dispersion is more important than the heat transfer through the solid phase in a wide pressure range starting at 0.5 bar.

Fig.6.4 presents the obtained results of burning velocity in the PIM reference case at $\lambda = 1.8$ as a function of pressure compared with the other two cases: less dispersion and less
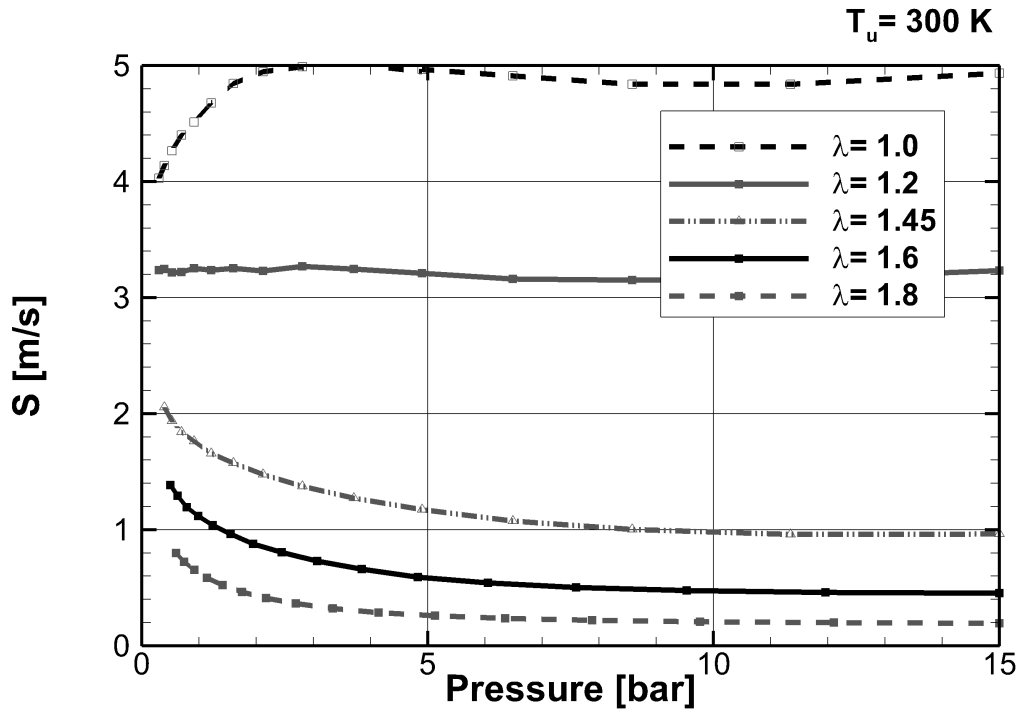
Figure 6.2: Theoretical burning velocity as a function of pressure, 10-PPI PIM, T_u=300 K.
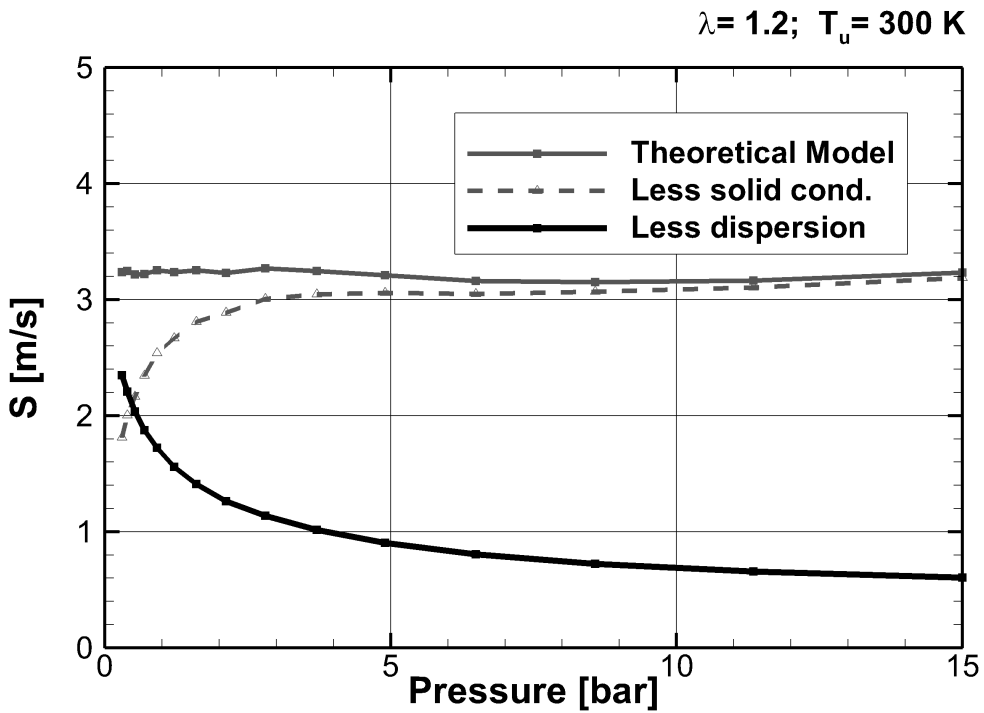

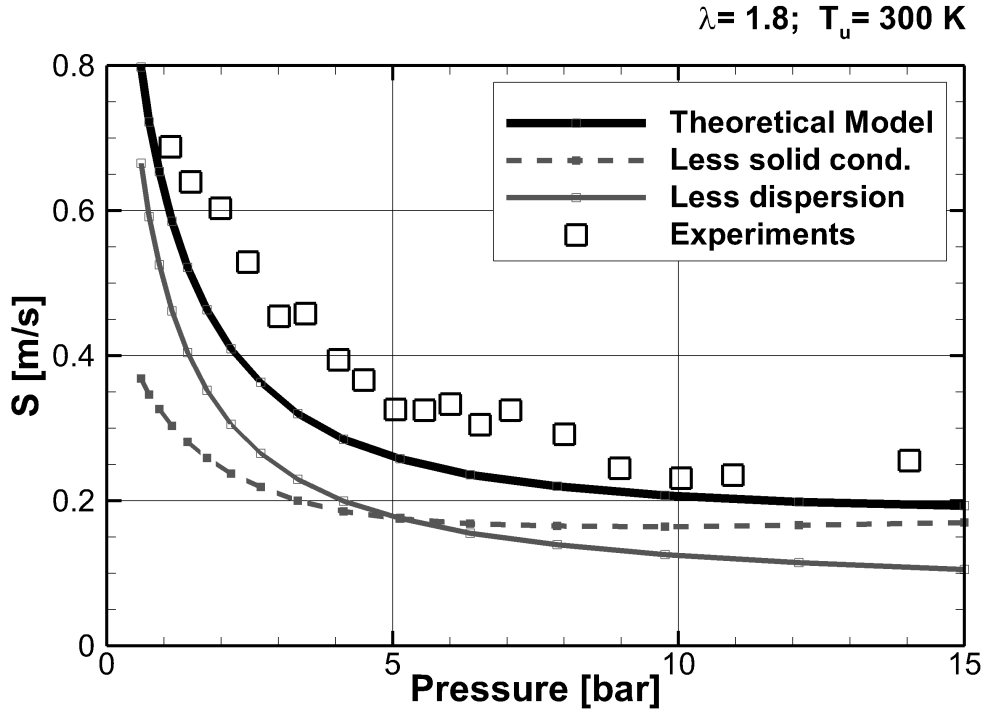Figure 6.3: Theoretical burning velocity calculated with different models, PIM 10 PPI, T_u=300 K, λ= 1.2.

Figure 6.4: Theoretical burning velocity calculated with different models in comparison to the experiments, PIM 10 PPI, T_u=300 K, λ= 1.8.

solid conduction, and compared with the present experimental results. It is observed that the burning velocity agrees well with the experiments, although the predicted values are lower and decrease more steeply with pressure than in the experiments.

From the other two manipulated case models, it can be observed in Fig.6.4 that dispersion is more important than solid heat transfer at pressures above 5 bar. The model case in which the solid conduction term was reduced, namely, less solid conduction, nearly exhibits independence from pressure in this pressure range. It is important to note that in none of the studied cases did pressure have a positive effect on the burning velocity for this air-to-fuel ratio.

Compare the shape of the $S(p)$ curves obtained with the model with reduced solid thermal conductivity for the air factor of $\lambda = 1.2$ with that of the air factor $\lambda = 1.8$, that is, the dashed curves of Less solid cond. in Fig.6.3 versus that in Fig.6.4. It is observed that, for a less lean mixture $\lambda = 1.2$ (Fig.6.3), this curve has a positive slope in the pressure range $p < 3\ bar$, but at higher pressure, the slope tends to zero; however, for the leaner mixture $\lambda = 1.8$ (Fig.6.4), the slope of the curve for this model is negative in the whole studied pressure range of $0.3\ bar - 15\ bar$.

From these exemplary cases, it is concluded that the pressure can have a positive effect
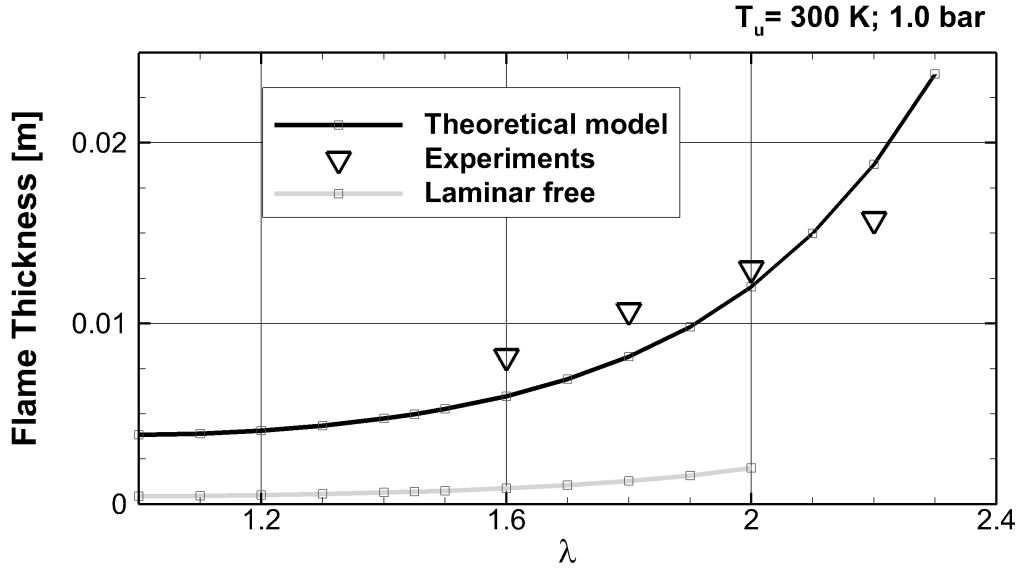
Figure 6.5: Theoretical flame thickness in comparison to experiments, PIM 10 PPI, T_u=300 K, 1.0 bar.

on the burning velocity for conditions in which the contribution of dispersion is more important than that of heat transfer through the solid phase, that is, for burnable mixtures with a high laminar burning velocity or for porous inert media with low effective heat transfer coefficients of conduction or radiation.

One of the assumptions of the present model is that the reaction zone thickness is the same as the inert zone thickness:

$$\delta = \frac{\lambda_{eff,2-ph}}{\rho_u \cdot c_{p,g,u}} \cdot \frac{1}{S} \qquad (6.16)$$

The resulting burning velocity S from the reference PIM example using the present theoretical model was used to evaluate the flame thickness δ in Eq.(6.16). The results are shown in Fig.6.5 at 1.0 bar as a function of the air factor in comparison with the thermal flame thickness obtained from experiments and the thermal flame thickness of laminar free flames. Good agreement of the prediction of burning velocity, as shown in Fig.6.1, is also observed with the predictions of the flame thickness using this simple model.

Eq.(6.16) was also used to analyze the effect of pressure on the flame thickness, as presented in Fig.6.6, where the results show that the flame thickness of the stoichiometric mixture decreases with the increase of pressure until an asymptotic value is reached (at approximately 1.5 bar). For leaner mixtures, the minimum value of thermal thickness is reached at higher pressures.
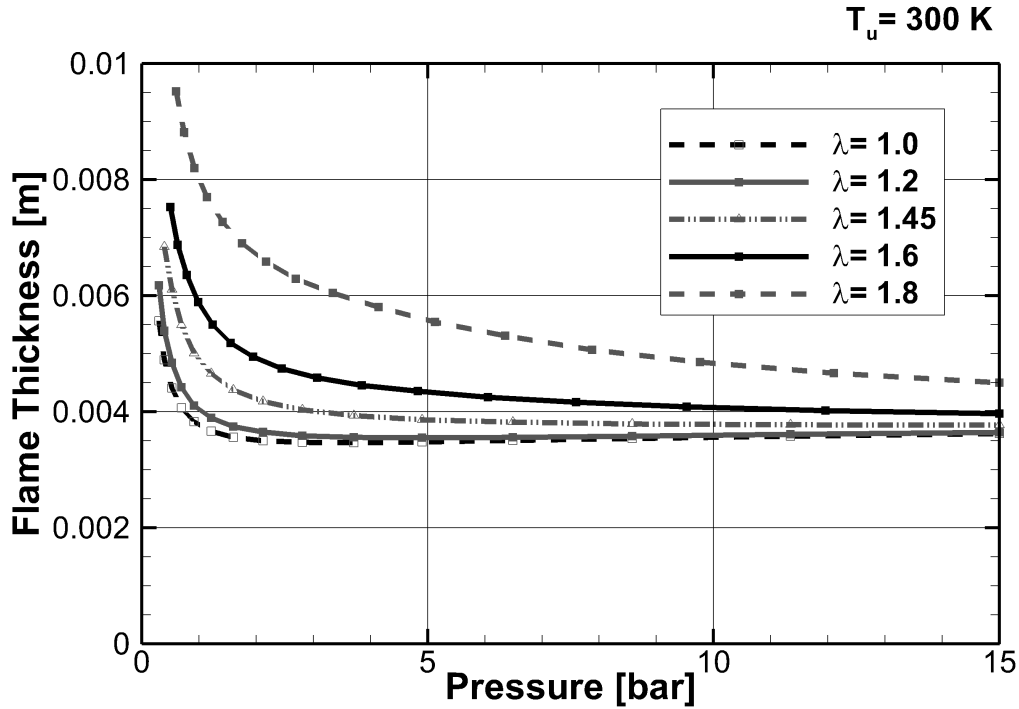
Figure 6.6: Theoretical flame thickness as a function of pressure, PIM 10 PPI, T_u=300 K.

The proposed model has yielded interesting results that do not differ considerably from the values and trends observed in experiments and simulations of flame stability within PIM. Therefore, it is recommended for engineering use during the dimensioning of porous burners when numerical tools are not available. The main inaccuracy of the model at elevated pressure is the uncertainty of the values of laminar burning velocities, which have yet to be validated at elevated pressure for lean mixtures, to the best of the author's knowledge.

The accuracy of the presented model fails for lean mixtures $\lambda > 1.9$, see Fig.6.1. The accuracy can be enhanced with the inclusion of results from numerical models such as the one presented in Section 5.3 with consideration of temperature fluctuations in space.

A heat release timescale τ_{pim} for the results of the model PIM-PDF was calculated with Eq.(2.15) using the gas temperature:

$$\tau_c = \min(T_g \cdot (\partial T_g / \partial x)^{-1} / u_g(x))$$

The results are compared with those of laminar free flames in Fig.6.7. The ratio between PIM PDF and the laminar case ranges between 0.6 and 2.5.

A correction factor as a function of the air factor taken from the results of Fig.6.7 is
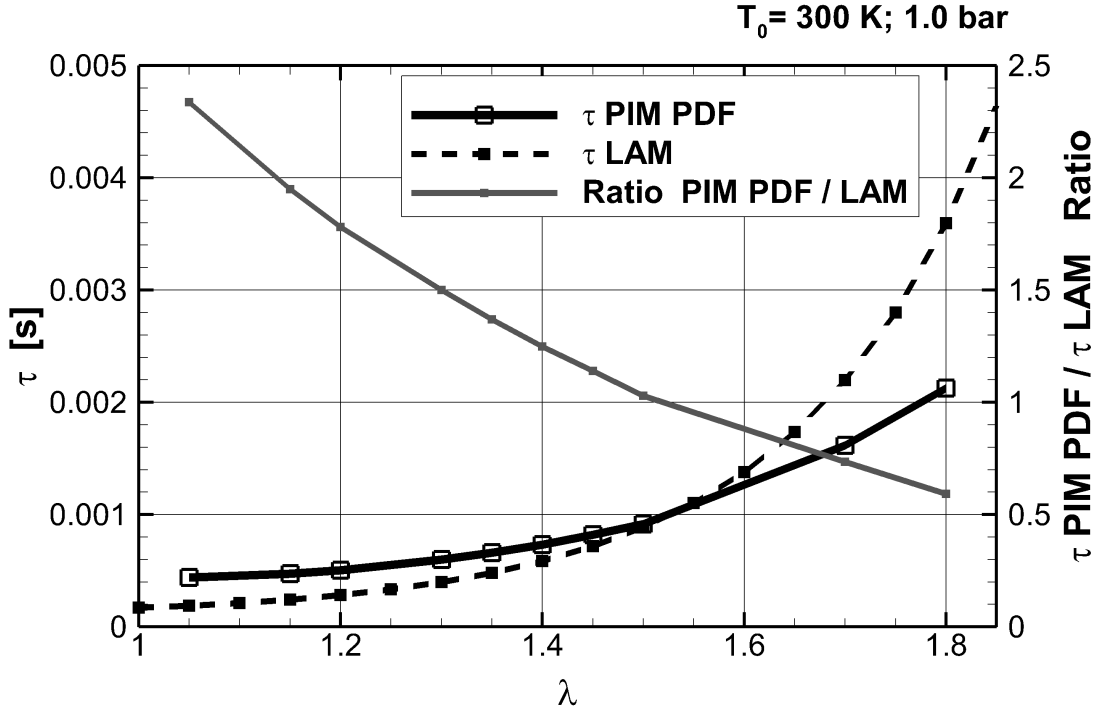
Figure 6.7: Heat release timescale τ_{pim} obtained from the 1D model PIM PDF compared with laminar free flames; $T_u = 300K$, 1.0 bar

introduced:

$$\frac{\tau_{pim}}{\tau_c} = 4.381 \cdot \lambda^2 - 14.669 \cdot \lambda + 13.108 \tag{6.17}$$

which can be used in the model proposed here:

$$\frac{\tau_{pim}}{\tau_c} \cdot \frac{\lambda_{g,b}}{S_l^2} \cdot S^2 - 0.5 \cdot \varepsilon \cdot \rho_u c_{p,g,u} d_{dis} \frac{T^0}{T_u} \cdot S - (1 - \varepsilon) \cdot \lambda_{s,eff}(T^0) = 0 \tag{6.18}$$

The results are presented in Fig.6.8. A clear better agreement with experiments for $\lambda > 1.9$. For lower air factors more experimental results are required for judging the presented correction.

The value of the ignition temperature T^0 was taken from the 1D numerical simulations under consideration of spatial fluctuations of temperature, as the temperature where the average production rate of oxygen achieved 0.5% of the maximum value observed. It was found to be in the range of 650 to 750 K from $\lambda= 1.05$ to $\lambda= 1.80$, respectively. In this range, the selection of this temperature has a considerable effect on the dispersion conductivity and solid conductivity, while the radiation conductivity is not markedly affected.

Nevertheless, the effects of temperature on the solid and dispersion conductivities are op-
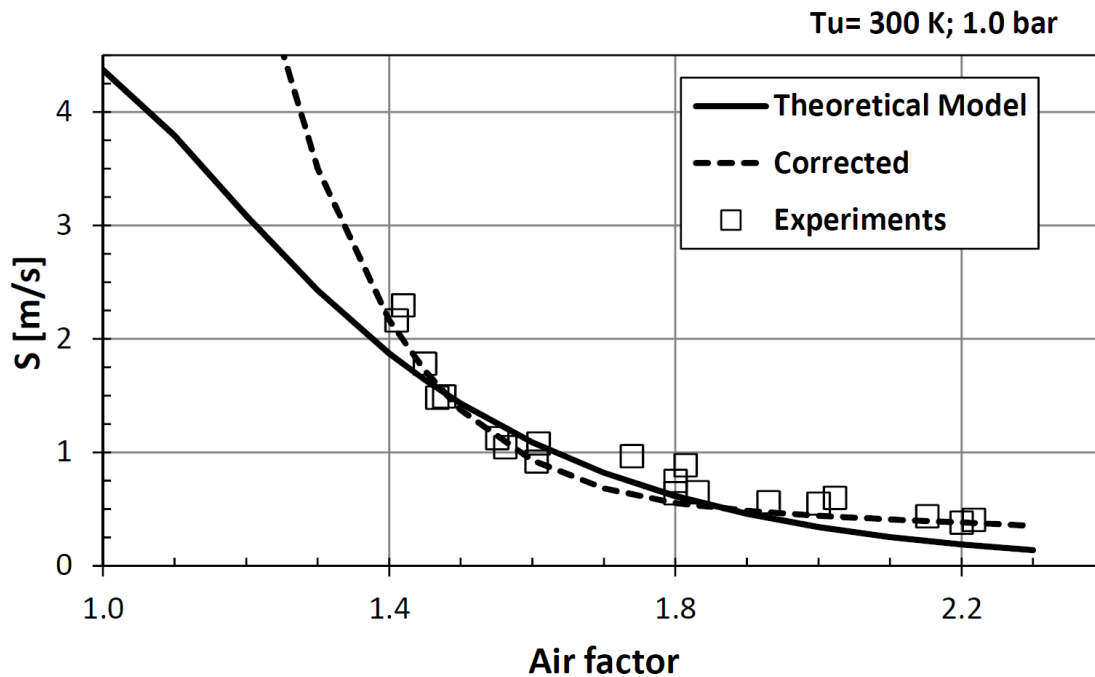
Figure 6.8: Corrected S by the τ_{pim} from simulations with PIM-PDF model; $T_u = 300K$, 1.0 bar

posite, since the solid conductivity depends exponentially on the inverse of temperature (see Eq.(6.15)), and the velocity increases linearly with temperature due to the isobar expansion in a straight pipe. This fact in addition to the small size of the temperature range of T^0 are the reasons why the exact selection of this temperature is not relevant to determine the effects of air-to-fuel ratio and pressure on the resulting burning velocities. However, the temperature T^0 was systematically varied in order to obtain better results, such as changing it to the initial temperature or to the combustion temperature for the separate definition of each of the involved conductivities; however, none of their combinations gave better results than the theoretical model presented here.

Chapter 7

Conclusions

Porous burners appear to be a feasible alternative to conventional burners (based on combustion in free spaces, such as laminar and turbulent flames). Commercially, porous burners, with recognized higher efficiency in terms of heat transfer by radiation to a charge, have been increasingly widely used due to the advantage exhibited by the solid porous surface to accommodate a high proportion of the infrared spectrum in comparison to gases. Some common applications of this kind of burner are industrial drying and household grills.

Combustion in porous inert media (PIM) can take place at the porous surface or within the porous media. When the flame is stabilized at the porous surface, some of the heat released by the combustion reactions is transferred to the solid phase. The temperature of solid may increase under determined conditions, so that the burner adopts a radiative mode. Heat from the solid phase is transferred in turn to the incoming gases, which accelerates the combustion wave so it can propagate within the PIM. Combustion within the PIM can occur as a propagating flame front along the PIM or as a stationary flame stabilized by an applied technique, such as the convective technique (where the flow velocity is higher at the unburned zone to avoid flashback) or the thermal quenching technique (where the porous layer with a pore size smaller than the thermal quenching distance is used in the unburned zone).

For the practical use of porous burners, the temperature at which active oxidation of the porous material takes place (e.g. for SiSiC, this corresponds to 1750 K for an atmosphere with 15% vol. oxygen) and the resistance to thermal shock during burner start-up and turn-down are parameters to be taken into account when designing the combustor housing and when setting process conditions.

The higher thermal emissivity and thermal conductivity of the solid material compared with those of gases yield higher heat feedback from burned gases to preheat the incoming

unburned gas mixture at a higher rate through radiation between solid surfaces and conduction through the solid phase. This phenomenon is known as heat recirculation or excess enthalpy, which leads to certain characteristics for this kind of combustion, with considerable differences compared with combustion in free mode. These characteristics include minimal emission of pollutant species, namely, NOx and CO, even at elevated combustion temperatures, and the achievement of superadiabatic temperatures in some locations. Another notorious characteristic is the enlargement of the flame stability range, which allows for special applications, such as partial oxidation of hydrocarbons to produce synthetic gas or the combustion of ultra-lean mixtures, which is of interest for utilization or inertization of fuels with low heating values or the production of hot gases at a sufficiently low temperature that can be withstood by materials in machinery downstream, as in the case of combustion in gas turbines. For example, in the present study, the lower stability limit of a stationary flame for mixtures at ambient temperature $T_0 = 300 \ K$ was observed at 4.5% vol. methane mixed in air (when the CO emissions were below 30 ppm vol.), which corresponds to an adiabatic combustion temperature of 1390 K. In contrast, the flammability limit of this fuel in air is 5% vol. Other studies have shown that, for stable flame front propagation through a PIM, where the flame front propagates in the same direction as the flow, the lower stability limit is extended to 1.5% vol. [24].

The acceleration of the combustion wave, namely, the increase of the burning velocity S, is another important characteristic that allows for the increase of the installed power specific to the burner cross-sectional area. It represents the possibility of constructing firing rooms with smaller sizes with the same installed power. This phenomenon of increased burning velocity is not only a result of the heat recirculation through the solid phase, but also a result of cross-mixing of the gas stream due to the tortuous flow paths imposed by the PIM. It macroscopically leads to intensified transport of mass and heat in the gas phase. This phenomenon is known as hydrodynamic dispersion, which in PIM combustion yields flattened profiles of average temperature and average concentration along the bulk flow direction. The hydrodynamic dispersion coefficients of a PIM with fixed geometry depend merely on the fluid velocity (for $Pe > 10$, i.e. for the typical conditions of PIM combustion). The importance of these two phenomena, heat recirculation and dispersion, in the modeling of stationary flames in PIM has been discussed in the present work.

One of the motivations of the present study was the possibility of applying this technology to combustion in stationary gas turbines and the fact that burning velocity values were not available at elevated pressure, which is an inherent condition in this kind of engine. In addition, the lack of a complete understanding of the processes relevant to

combustion processes in PIM prompted this work. The study of combustion within PIM faces some challenges, such as the access of optical and mechanical probes due to the presence of the PIM itself and the stiffness of the PIM structure.

The present study focused exclusively on the flame stabilization in a stationary location within the PIM of lean premixed methane-air mixtures under adiabatic conditions and at elevated pressure. Experimental, numerical and theoretical investigations were carried out, with the main objective of producing a substantial database of burning velocity values and acquiring a basic understanding of the physics behind the processes relevant to combustion within PIM and of the flame structure itself. The PIM studied in this work was a sponge-like structure made of SiSiC with 87% porosity and 10 (and 20) PPI. This material was selected, since it appears to have the best ratio between temperature shock resistance and the highest operable temperature, in addition to the very high thermal conductivity in comparison to other ceramic materials. The main obtained results were on the burning velocity and the macroscopic thickness region, as well as the identification of temperature deviations in space.

One of the most important results of the present study is a definition of the burning velocity that can be validated by reproducibility in burners with different geometric shapes and different flame stabilization techniques. A massive database of burning velocity values was generated at different pressure levels. The effects of the air factor and pressure on the burning velocity were studied and tendencies were clearly identified. The experimental results of burning velocities were well correlated with a model of modified Peclet numbers based on the burning velocity in PIM S and the burning velocity of laminar free flames S_l:

$$Pe_{pim} = C_{Pe} \cdot Pe_{lam}^{m}$$

which represents an easy-to-use tool for engineering while dimensioning or scaling burners with different geometries, using different fuels or operating at different conditions of temperature, pressure and air-to-fuel ratio.

The obtained results were satisfactorily predicted with the 1D numerical model used here, as well as with the theoretical model proposed in the present study. The numerical model is based on finite differences of volume-averaged quantities with the use of effective coefficients that provide information about the processes occurring at the microscopic scale. The observed temperature fluctuations in the experiments were considered to calculate the average of non-linearly dependent terms such as the species production rates $\dot{\omega}_i$, with the use of presumed statistical distributions along the cross-sectional area of the burner.

In a parallel study by Parthasarathy et al. [26–28], the effective coefficients of transport

in the used PIM were determined by direct pore-level simulations (DPLS) on a reproduced sample of PIM scanned by micro-computer tomography. The velocity fluctuations in space were also identified. In another parallel work by Dinkov et al. [210] and Bedoya et al. [20], DPLS of combustion in the reproduced sample of PIM were carried out, in which a heterogeneous shape of the flame was observed and the temperature fluctuations were correlated with the gradient of the average temperature.

With the measurements of the present study, it was possible to demonstrate the existence of temperature fluctuations in space during combustion within PIM; this confirms that the flame structure in a porous burner is corrugated and discontinuous, as Dinkov et al. [210] predicted in their DPLS.

In this study, the burning velocity in PIM was compared with that in free flames, namely, laminar and turbulent. At low air excess ratios, the burning velocity in PIM combustion exceeds the laminar burning velocity by a factor of seven, which is lower than the turbulent burning velocity. In contrast, under leaner conditions, this factor increases up to 13, which is considerably higher than that of turbulent flames (without recirculation of hot gases). This effect of the air factor on the burning velocity was fairly well predicted by the numerical and theoretical models. Additionally, the effective parameters of transport in these models were systematically varied in order to quantify the relative importance of the transport mechanisms involved in PIM combustion. It was found that the heat recirculation through the solid phase becomes dominant over the hydrodynamic dispersion for a very lean mixture, that is, where lower burning velocities are exhibited. In contrast, at lower air excess ratios, the contribution of dispersion to transport mass and heat becomes dominant in the combustion processes in stationary flames within PIM.

Owing to the high volumetric surface area, which is typical of solid sponges, interfacial convection was identified as a non-limiting process in the combustion within this kind of PIM, since the heat transfer through the solid phase offers higher thermal resistance (which is in series connected with the convective thermal resistance).

This is the first study reporting burning velocity values at elevated pressure. The identified behavior of the burning velocity against pressure variation is considerably non-monotonic, which substantially differs from that in laminar free flames. It was observed that, under conditions that exhibit a high laminar burning velocity, namely, low air excess and/or high initial temperature, the burning velocity in PIM increases with the increase of pressure until it reaches a maximum. For further increase of pressure, the burning velocity decreases. In contrast, for mixtures that have a low laminar burning velocity, the positive effect of the pressure increase on the burning velocity in PIM was

not observed or it was less considerable and occurred in a shorter pressure range. This behavior was well predicted by both models used here, and the reason for the increase of the burning velocity in PIM with pressure was identified as the contribution of dispersion, since the dispersion coefficients depend on the gas velocity. This statement was confirmed upon the systematic variation of the model parameters in the numerical and theoretical models.

Some representative results of the macroscopic thermal flame thickness in PIM (based on the maximum temperature gradient) were produced by the repetition of experiments varying the thermal power, namely, the flow rate. It was found that the thermal flame thickness in PIM exceeds that of laminar free flames by a factor of approximately seven. The effect of the air factor was found to be similar to that in laminar free flames: that is, the flame thickness increases with the increase of the air factor.

The flame thickness in PIM was not predicted to be as large by the 1D model when neglecting the temperature fluctuations in space while calculating the source terms, as was the case in state-of-the-art studies using the same model [15, 57]. In the present study, a model to consider the temperature variations was proposed and validated, which consisted of the use of presumed probability functions (PDF) of local temperature to obtain the average of the species production rates:

$$\dot{\omega}_i = \int_0^1 \dot{\omega}_i^*(\theta^*) \cdot p(\theta^*) \cdot d\theta^*$$

The local gas chemical composition was coupled with the local temperature θ^*. The PDF shape was a clipped Gaussian distribution, which was constructed with the average gas temperature and the temperature variance. The temperature variance was determined using an algebraic equation function of the gradient of average temperature. This correlation was produced analogously to the Boussinesq hypothesis. With this model, namely, the PIM-PDF model, it was possible to compare the measurements well. It was found that the macroscopic reaction zone is considerably large and constitutes a representative part of the complete (macroscopic) flame region.

The activation of reactions was observed at a very low average temperature (670 K) in comparison to that for laminar free flames ($\approx 1300K$). The identification of this temperature value was crucial for the accuracy of the theoretical model proposed here, which is based on the division of the flame into two layers: inert and reaction zones, as carried out by Mallard and Lechatellier for laminar free flames. This theoretical model is based on the assumption of local thermal equilibrium of the two phases, that is, the thermal resistance imposed by interfacial convection tends to zero. Theoretical results

compared well with the experiments, that is, the burning velocity and thermal flame thickness values were well predicted, as well as the effect of pressure on the burning velocity. Thus, this theoretical model is presented as a simple tool for understanding and rough dimensioning of burners:

$$S = \left(\frac{\lambda_{eff,2-ph}}{\lambda_{g,b}} \right)^{1/2} \cdot S_l$$

where $\lambda_{eff,2-ph}(T^0) = \varepsilon \cdot \lambda_{dis} + (1 - \varepsilon) \cdot (\lambda_s/\tau_s + \lambda_r)$,

and $\lambda_{dis} = \rho_u \cdot c_{p,g,u} \cdot 0.5 \cdot d_{dis} \cdot u_u \cdot (T^0/T_u)$

Another relevant observation from the present experiments and model results is the relationship between the burning velocity and the flame thickness as it occurs in laminar free flames; for example, when pressure increases and has a considerable effect on the burning velocity, it also affects the flame thickness considerably:

$$\delta = \frac{\lambda_{eff,2-ph}}{\rho_u \cdot c_{p,g,u}} \cdot \frac{1}{S}$$

After this intensive study of the flame stabilization within PIM, there are still further fields of research to be undertaken. In particular, the experimental detailed determination of temperature deviations in space requires the development of new measuring techniques, such as detailed pore-level measurements. The modeling of these temperature fluctuations in the method presented here for the volume-averaged model was limited by the tabulated chemistry, which was generated with a model that neglects those fluctuations. In fact the reaction path varies as well, there are locations in the PIM where the cross-mixing is not as considerable and considerable superadiabatic temperatures are achieved, while there are locations with cosiderably higher cross mixing, as the case modeled in the present work.

In addition to the modification of chemistry modeling, the use of other PDF shapes, such as the β-distribution, has not been evaluated. The stiffness of the used model avoided the convergence of accurate solutions at numerous pressure levels; thus, the results obtained were insufficient to draw conclusions on the effect of pressure by the use of the PIM-PDF model.

Combustion instabilities were observed in a certain pressure range under conditions with high combustion temperature. Further work needs to be carried out to establish physical models in order to explain and predict this operation mode, as well as the development and use of a more detailed measurement technique to describe it better.

In a near future, it is expected that substantial results of DPLS of combustion within PIM can be identified from the work of Dinkov et al., which is the first work in this field using reproduced solid sponge samples. The exploration of this research area is encouraged in order to acquire a better understanding of the processes taking place at the microscopic scale and to find possible approaches to enhance simplified models, such as those presented here.

Appendix A

Determination of effective transport properties in PIM

The effective parameters of transport in the PIM used in the present work in the volume averaged model were obtained by different kind of direct pore level simulations DPLS in our institute by Pandy Parthasarathy for his Dissertation. Since some of the results were not jet elsewhere published than in [28], the procedures are roughly described and some results are presented in this section with his permission.

For the generation of the computational grid comprising two domains representing the solid part of the sponge and the fluid domain the 3D images of the sponges were acquired by micro-computer-tomography consisting of gray values for the 3072 x 1024 x 1024 voxels of the investigated SiSiC sponge sample. Details of the PIM structure and of the technique for acquiring this data are given in [7]. Using the 3D volume data of the sponge, a model of the interface from solid to fluid could be extracted with digital filter routines for noise reduction and a threshold value to separate solid from void.

The whole procedure yields the discretized interface comprising 5 million connected triangles. In order to construct the 3D computational grid from this surface a standard meshing tool (ANSYS ICEM CFD) was used. The specific sponge sample of 10 PPI applied in the current work span a straight geometry with 43 mm length and cross section of 9x9 mm^2. The resulting numerical grid was locally refined near the solid phase walls. It comprised approx. 20 Mio. elements for the fluid part (4 Mio. nodes) and 9 Mio. elements for the solid part (2 Mio. nodes). Fig.A.1 shows the solid part of the computational grid.

The determination of the extinction coefficient β was evaluated using an in house ray tracing code. The results are well documented in [26] with other relevant radiative pa-
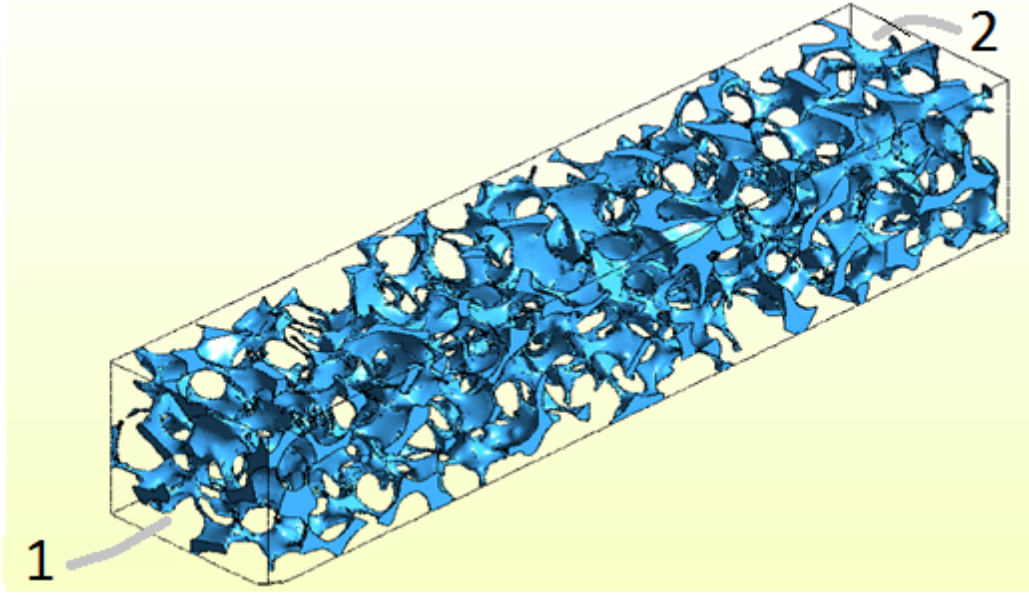
Figure A.1: Computational domain/Surface of the solid domain for DPLS, 10 PPI

rameters such as absorption coefficient and scattering phase function for a large number of samples with different materials and structural specifications.

As well the longitudinal dispersion was numerically examined in [15, 27] with tracer molecules. Parthasarathy et al.[27] presents a larger data basis than Djordjevic et al. [15]. The earlier also analyzed the radial gradients of velocity, i.e. the spacial deviations of velocity and the effects on the dispersion coefficient by introducing a mixing length scale. Some of their results for the sponges used in the present work are presented in this section.

A.1 Axial dispersion coefficients

The coefficients of axial dispersion of mass and heat were numerically obtained by transient CFD at DPLS by the method of moments [15, 27]. Basically, the fluid composition of the one dimensional bulk flow was suddenly changed from 100% air to 100% NO (trying to avoid considerable changes in the molecular weight). The starting point was the steady state solution of flow of air through the sponge calculated with the Navier-Stockes equations. Then the transient simulation of the flow of the tracer was conducted, whose results of concentration of the tracer were used to determine D_{eff} in the following way: NO concentration was mass-flow averaged along the cross sectional area of the fluid at every position x and time t, that is $Y(x,t)$. Since the axial gradient of any instantaneous curve can fit as a Gauss distribution $(\partial Y(x,t)/\partial x)$, Eq.(A.1) can be used to determine

D_{eff}.

$$D_{eff}(t) = 0.5 \cdot (\sigma^2(t_1) - \sigma^2(t_2))/(t_1 - t_2) \tag{A.1}$$

Where $\sigma^2(t)$ is the variance of the gradient of averaged concentration along x. The resulting $D_{eff}(t)$ was plot along time, concluding from there, that $D_{eff}(t)$ reaches a constant value after some delay time, i.e. 1 ms or 3 pores approximately. This value was taken as D_{eff}.

The asymptotic value of the modified dispersion Peclet number equal two obtained for packed beds [211] in Eq.(2.34)

$$Pe_{dis} = (u \cdot d_{dis})/D_{dis} = 2; \ Pe_m = (u \cdot d_{dis})/D_m > 10$$

was used to determine the value of a characteristic length of dispersion d_{dis}.

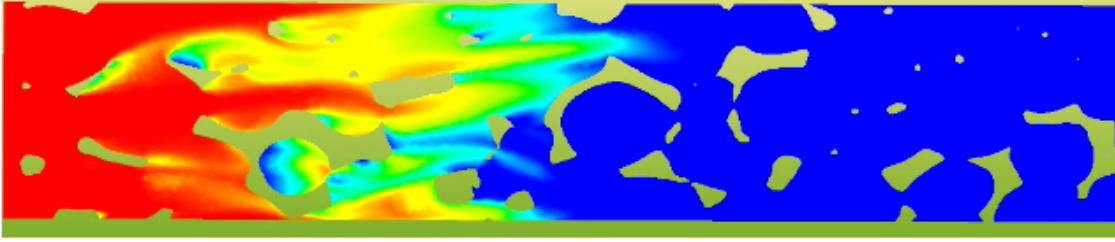where the subscripts dis and m refer to axial dispersion and molecular, respectively.

Figure A.2: An instantaneous contour of tracer mass fraction in a 10 PPI SiSiC open cell matrix, at $Re_p = 1000$, red: 100% Y_{NO}, blue: 0% Y_{NO}.

Djordjevic et al. [15] performed the simulation for flow through the 10 PPI sponge with a bulk velocity of $u = 4.0$ m/s and 1.0 bar. An instantaneous contour of tracer mass fraction along the mid plane parallel to flow is shown in Fig.A.2. The procedure described above was conducted. The obtained D_{dis} was $4.68 \cdot 10^{-3}$, which is two orders of magnitude larger than the molecular diffusion coefficient D_m as well as the molecular thermal diffusivity of the gas phase $a_{g,m}$. By using Eq.(5.6) the dispersion length scale was obtained as $d_{dis} = 3.24$ mm. DPLS were carried out for other reticulated structures and materials, it was found that d_{dis} is not related to neither geometrical, nor structural nor hydraulic parameters, reasons were discussed in [7].

In further simulations performed by Parthasarathy et al. [27] varying velocity and pressure as desired conditions for the present work of combustion within PIM. It was observed that the value of the Peclet number based on dispersion stayed constant around two as in Eq.(5.6) using that value of d_{dis}. The results are presented in Fig.A.3 with comparison to the empirical results of [108, 113, 211–214].
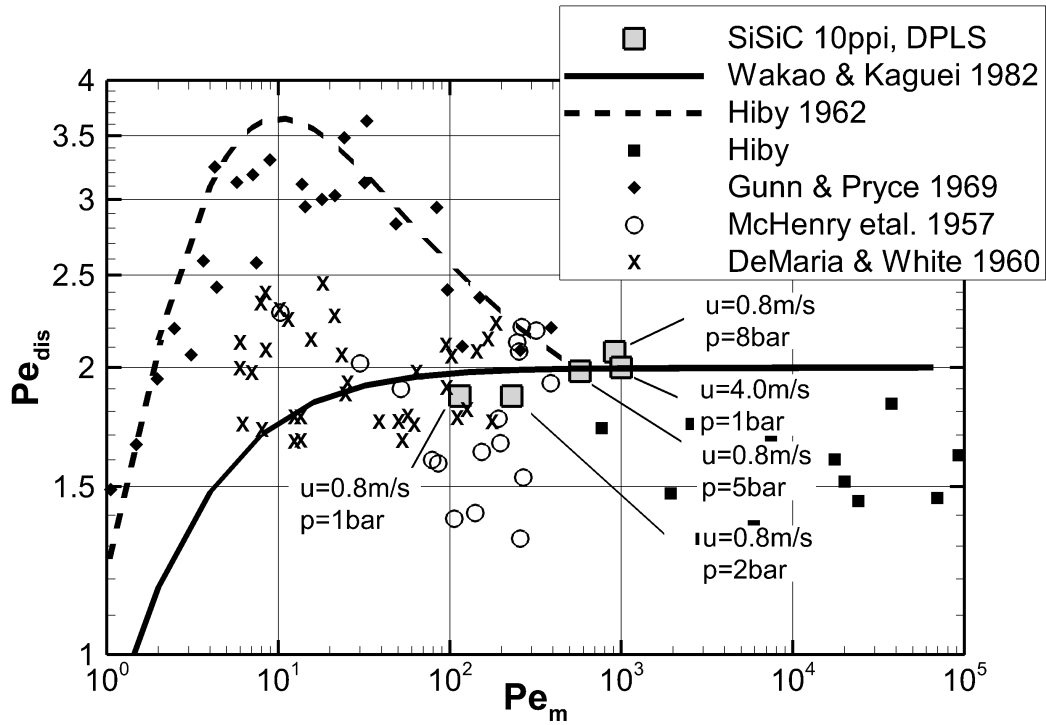
Figure A.3: Peclet numbers based on dispersion as function of molecular Peclet, correlation $Pe_{dis} = 2$

A.2   Effective thermal conductivity of the sponge

The steady-state one dimensional heat flux due to conduction in any media can be calculated using Fourier's law of heat conduction:

$$\dot{q} = -\lambda_s \cdot dT/dx \tag{A.2}$$

where λ_s is the material thermal conductivity. For a constant thermal conductivity λ_s and for a temperature difference of ΔT, the Fourier's heat equation can be written in terms of resistance to heat flow:

$$\dot{q} = -\Delta T/R \tag{A.3}$$

where $R = \Delta x/\lambda_s$ is the thermal resistance. The thermal resistance is proportional to the length parallel to the path taken by the heat flow and is inversely proportional to the thermal conductivity of the material.

In case of porous structures the effective conductivity of the solid structure is less than that of the material conductivity due to the increase in the path taken by the heat to flow for a given distance. The increase in the path taken by the heat to flow from plane 1 to plane 2 (lets in Fig.A.1) can be accounted into the resistance by use of the term

conduction tortuosity τ_s:

$$\tau_s = \frac{\text{actual distance taken by heat to flow}}{\text{distance between plane 1 and plane 2}} \tag{A.4}$$

The heat resistance R can be expressed in terms of tortuosity τ_s, distance Δx and thermal conductivity λ_s as:

$$R = \tau_s \cdot \Delta x / \lambda_s \tag{A.5}$$

With the use of Eq.(A.5), the effective conductivity $\lambda_{s,eff}$ of the sponge in Fig.A.1.a can now be used in Eq.(A.2):

$$\dot{q} = -\lambda_{s,eff} \cdot \Delta T / \Delta x \tag{A.6}$$

where the effective conductivity $\lambda_{s,eff} = \lambda_s / \tau_s$ depends on the material conductivity and the structural profile of the sponge.

DPLS were performed to determine the effective conductivity of solid phase of the SiSiC sponge as shown in Fig.A.1. Details of the computational grid are given in a section below. The temperature at plane 1 and 2 were fixed and adiabatic boundary condition is imposed on all other Cartesian planes, the average heat flux value was obtained from the simulation. For a fixed conductivity λ_s, the effective conductivity was obtained using Eq.(A.6).

A.3   Convection heat transfer coefficient

DPLS of non reacting and steady flow within the porous matrix were carried out. The boundary conditions at the inlet and outlet, i.e. plane 1 and plane two in Fig.A.1 respectively, were specified using constant velocity and temperature at the inlet and static pressure together with zero gradient condition for the velocity at the outlet. The domain surfaces parallel to the flow direction were given with translational periodic boundary conditions. The structure surfaces were modeled as wall with fixed temperature (1000 K) and no slip boundary conditions. Viscous dissipation was neglected.

The simulations were carried out at Reynolds numbers 10, 100 and 500, and for Prandtl numbers 0.7, 2 and 6. The Reynolds numbers were calculated using the hydraulic diameter $d_h = 4\varepsilon / S_v$ as the characteristic length. The local heat transfer coefficient between the axial locations x and $x + \Delta x$ is given as:

$$\alpha(x) = \frac{\int_x^{x+\Delta x} \dot{q} \cdot dA_{sg}}{A_{sg} \cdot \Delta T_{lm}} \tag{A.7}$$

where $\Delta T_{lm} = \frac{\Delta T_x - \Delta T_{x+\Delta x}}{ln(\Delta T_x / \Delta T_{x+\Delta x})}$ is the log mean temperature difference. The local Nusselt number $Nu(x) = \alpha(x) \cdot d_h / \lambda_g$ values were nearly constant along the axial direction, the arithmetic average of the Nusselt numbers along axial locations was taken as the average Nusselt number Nu of the porous media. The convection heat transfer coefficients were reported in terms of the correlation obtained by lest square fit method:

$$Nu = c_1 \cdot Re^{c_2} \cdot Pr^{c_3} \tag{A.8}$$

Appendix B

Direct pore level simulations of combustion within PIM

The same technique of generation of computational grids based on reproduced solid sponge samples was used by Bedoya et al. [20] and Dinkov et al. [210] to generate computational domains and directly simulate combustion of premixed Methane-air within PIM at the microscopic scale. Different reaction mechanisms were used the global reaction scheme and that given by Egolfopoulos et al. [43].

In this section some results of the simulations carried out with the global reaction with finite rate chemistry modeled with a modified Arrhenius equation given by Westbrook and Dryer [32].

The flow was assumed as laminar. The thermal conductivity of the solid domain was defined as function of temperature Eq.(6.15). It is to be beard in mind, that since the simulation is carried out directly at the microscopic scale, coefficients of transport should not be altered as it is required in volume averaged methods. Radiation effects were not considered.

The complete domain consist on an idealized piece of a burner with radial flow. This burner configuration bases the stabilization of the flame on the convective concept, since the flow is being decelerated downstream due to the proportional increase of the cross sectional area with the radius. The simulated domain is shown in Fig.B.1 with the respective boundary conditions.

Since velocity varies along the radius, the same definition of burning velocity used in the present study was used, where the flame location was defined as it was done in the present numerical investigation. Fig.B.2 presents the results of burning velocity at atmospheric conditions as function of the air to fuel ratio in comparison with the present
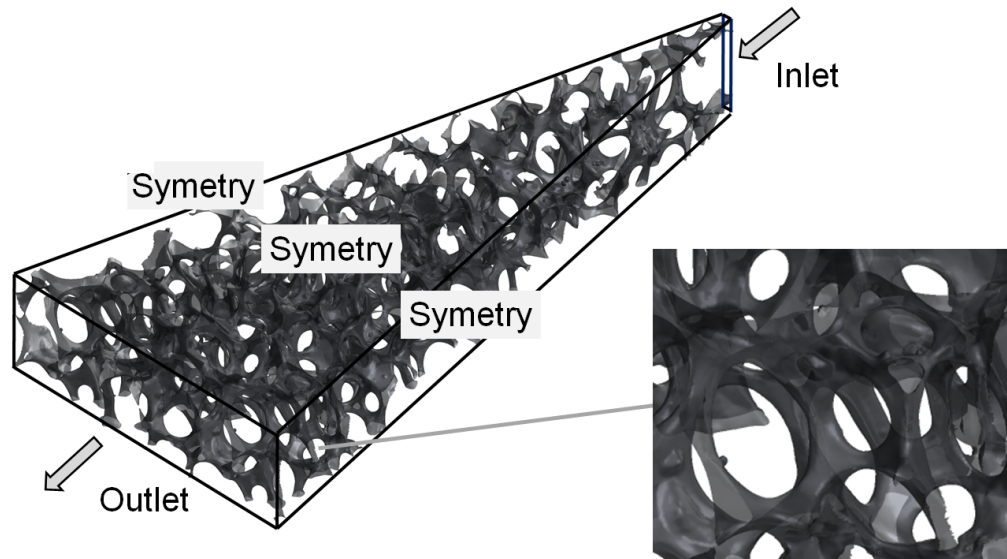
Figure B.1: Computational domain/Surface of the solid domain for DPLS, 10 PPI

results (experiments and 1D calculations). A well agreement with the experiments is observed.

Fig.B.3 presents a distribution of local temperature along a middle plane of the domain, where a section of the flame structure can be appreciated. It is to be remarked that the obtained flame structure is corrugated and considerably discontinuous. Fig.B.4 presents the local gas temperature along 80 streamlines. The root mean square values of average temperature of the gas phase was calculated weighted by the area of the cell. The results of T_{RMS} from DPLS and those calculated with the correlation of the gradient of averaged temperature are shown in Fig.B.5 where a good comparison is observed.

DPLS of combustion have been also preformed at elevated pressure. The resulting burning velocities are shown in Fig.B.6 compared with the present experiments. These results are better presented and deeply discussed in [20].
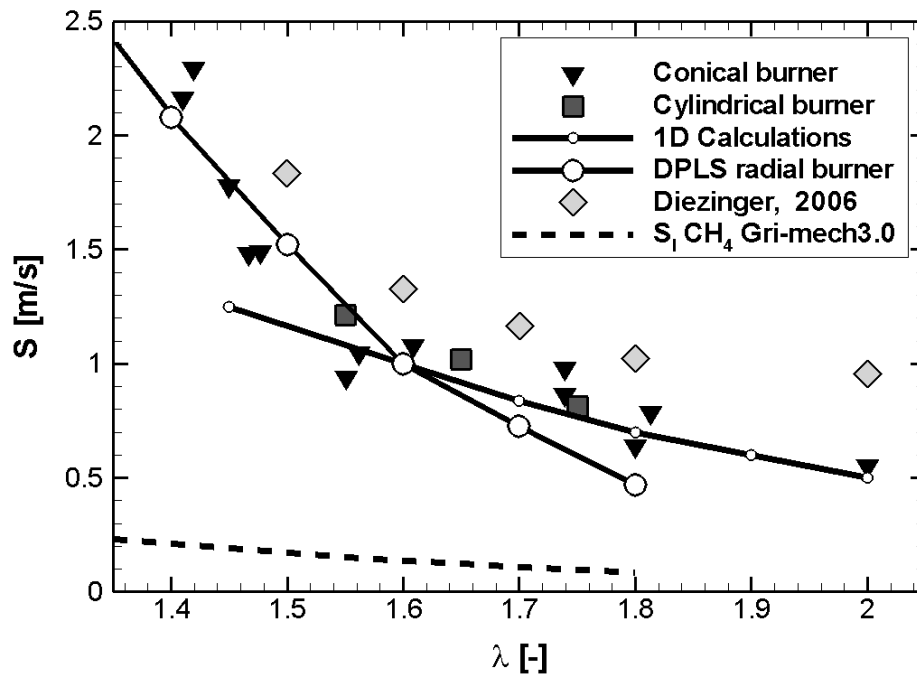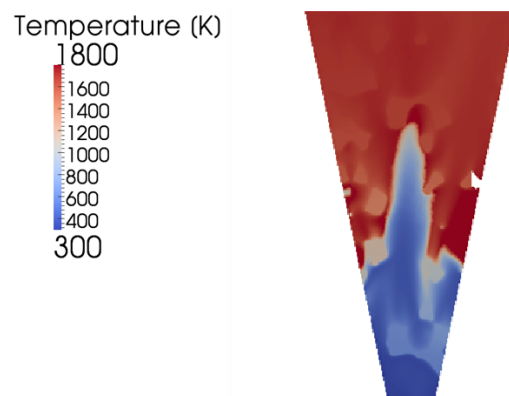
Figure B.2: Burning velocity versus air factor

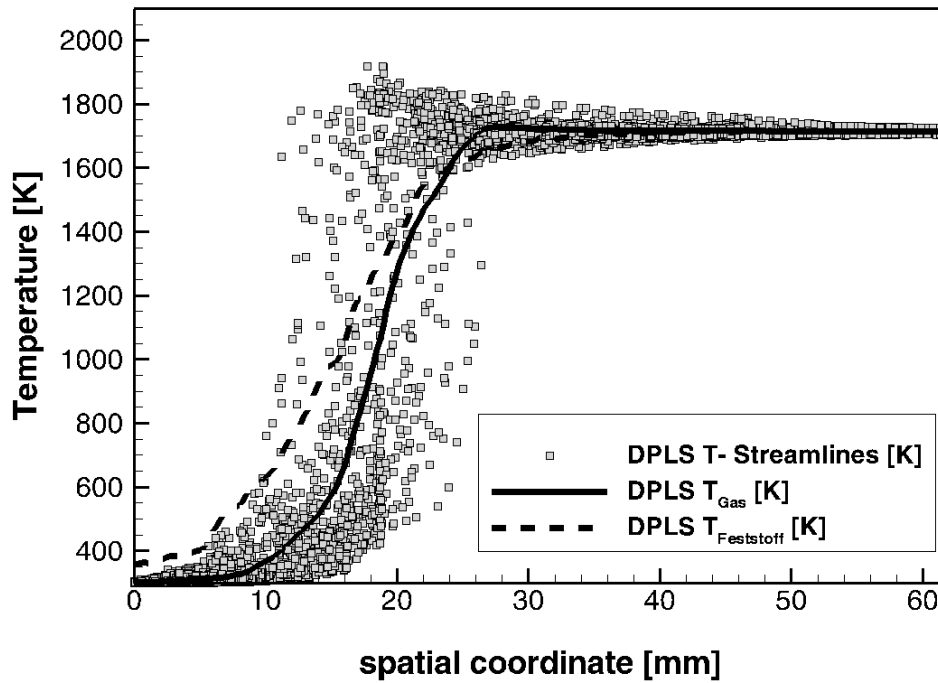Figure B.3: Local temperature distribution

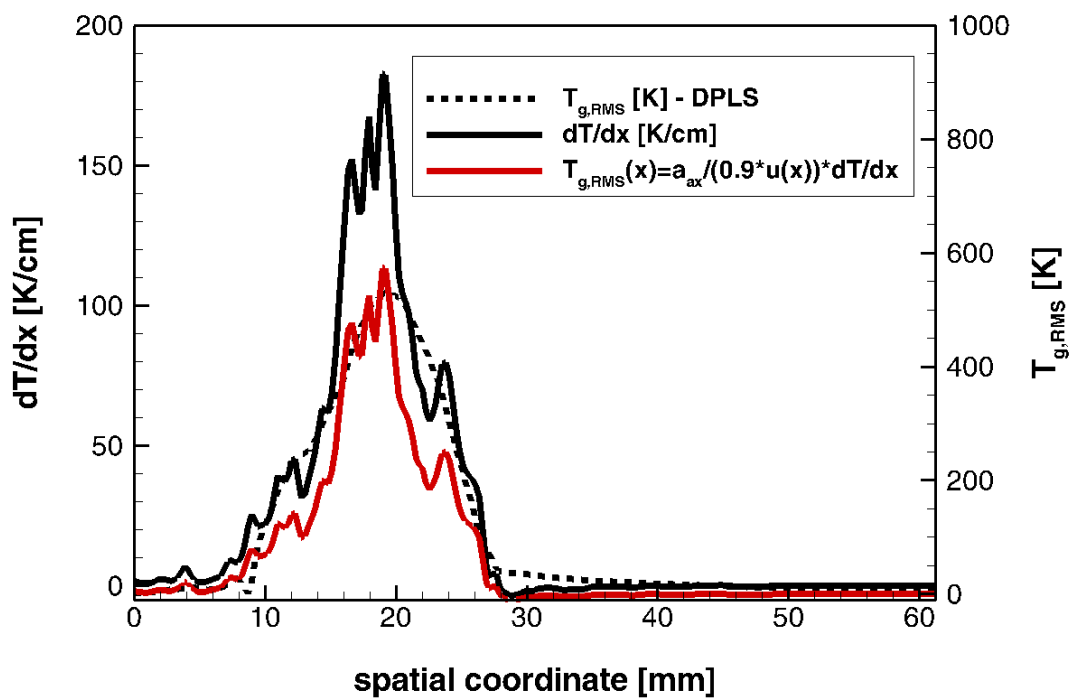Figure B.4: Local temperature along 80 streamlines

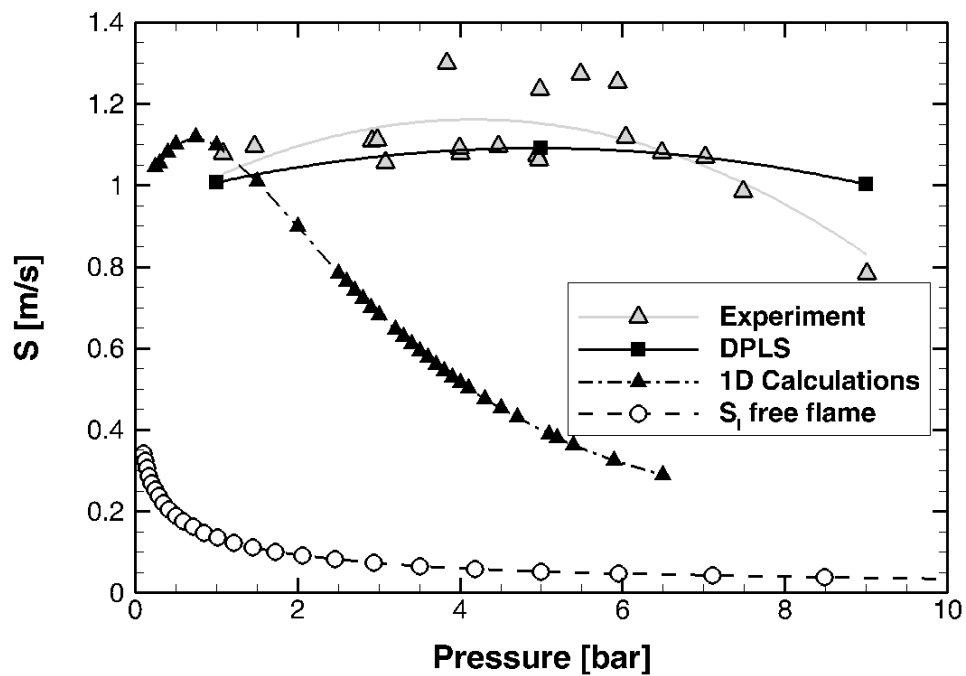
Figure B.5: Local temperature distribution

Figure B.6: Burning velocity as function of pressure

Bibliography

[1] IPCC. Climate change, synthesis report. *IPCC Plenary XXVII (Valencia, Spain, 12-17 November 2007)*, 2007.

[2] M. M. Kamal and A. A. Mohamad. Combustion in porous media. *Proceedings of the Institution of Mechanical Engineers, Part A: Journal of Power and Energy*, 220(5):487–508, 2006.

[3] R. Viskanta. Combustion and heat transfer in inert porous media. *Handbook of Porous Media*, Second Edition:607–644, 2005.

[4] R. Viskanta. Modeling of combustion in porous inert media. *Special Topics & Reviews in Porous Media - An International Journal*, 2(3):181–204, 2011.

[5] A.A.M Oliveira and M Kaviany. Nonequilibrium in the transport of heat and reactants in combustion in porous media. *Progress in Energy and Combustion Science*, 27(5):523 – 545, 2001.

[6] M. Scheffler and P. Colombo. *Cellular Ceramics: Structure, Manufacturing, Properties and Applications*. Weinheim, Wiley-VCH, 2005.

[7] J. Grosse, B. Dietrich, Gerardo Incera Garrido, P. Habisreuther, N. Zarzalis, H. Martin, M. Kind, and B. Kraushaar-Czarnetzki. Morphological characterization of ceramic sponges for applications in chemical engineering. *Industrial & Engineering Chemistry Research*, 48:10395–10401, 2009.

[8] www.keramikblech.com, www.made-in-china.com, www.dialnsearch.com.

[9] D. Trimis and F. Durst. Combustion in a porous medium-advances and applications. *Combust Sci Technol*, 121(1-6):153–168, 1996.

[10] M. A. Mujeebu, M.Z. Abdullah, M.Z. A. Bakar, A.A. Mohamad, and M.K. Abdullah. Applications of porous media combustion technology a review. *Applied Energy*, 86(9):1365 – 1375, 2009.

[11] M. A. Mujeebu, M.Z. Abdullah, M.Z. A. Bakar, A.A. Mohamad, R.M.N. Muhad, and M.K. Abdullah. Combustion in porous media and its applications a comprehensive survey. *Journal of Environmental Management*, 90(8):2287 – 2312, 2009.

[12] J.R. Howell, M.J. Hall, and J.L. Ellzey. Combustion of hydrocarbon fuels within porous inert media. *Prog Energ Combust*, 22(2):121 – 145, 1996.

[13] F. J. Weinberg. Combustion temperatures: The future? *Nature*, 233:239–241, 1971.

[14] S. Wood and A. T. Harris. Porous burners for lean-burn applications. *Prog Energ Combust*, 34(5):667 – 684, 2008.

[15] N. Djordjevic, P. Habisreuther, and N. Zarzalis. A numerical investigation of the flame stability in porous burners employing various ceramic sponge-like structures. *Chem Eng Sci*, 66 (4)(4):682 – 688, 2011.

[16] M. A. Mujeebu, M. Z. Abdullah, A.A. Mohamad, and M.Z. A. Bakar. Trends in modeling of porous media combustion. *Prog Energ Combust*, 36(6):627 – 650, 2010.

[17] W. G. Gray, C. T. Miller, and B. A. Schrefler. Averaging theory for description of environmental problems: What have we learned? *Advances in Water Resources*, 51(0):123 – 138, 2013. ¡ce:title¿35th Year Anniversary Issue¡/ce:title¿.

[18] X. Fu, R. Viskanta, and J. P. Gore. Combustion and heat transfer interaction in a pore-scale refractory tube burner. *Journal of Thermophysics and Heat Transfer*, 12:164–171, 1998.

[19] N. S. Kaisare and D. G. Vlachos. A review on microcombustion: Fundamentals, devices and applications. *Progress in Energy and Combustion Science*, 38(3):321 – 359, 2012.

[20] C. Bedoya, I. Dinkov, P. Habisreuther, N. Zarzalis, H. Bockhorn, and P. Parthasarathy. Experimental study, 1D volume-averaged calculations and 3D direct pore level simulations of the flame stabilization in porous inert media at elevated pressure. *Combust Flame*, 162(10):3740 – 3754, 2015.

[21] K. Yamamoto, N. Takada, and M. Misawa. Combustion simulation with Lattice Boltzmann method in a three-dimensional porous structure. *Proc. Combust. Inst.*, 30:1509–1515, 2005.

[22] D. Trimis, O. Pickenaecker, and K. Wawrzinek. *Porous Burners, Chapter 5.5 in Cellular Ceramics: Structure, Manufacturing, Properties and Applications*. Wiley-VCH Verlag GmbH, 2005.

[23] Y. Kotani, H.F. Behbahani, and T. Takeno. An excess enthalpy flame combustor for extended flow ranges. *Symposium (International) on Combustion*, 20(1):2025 – 2033, 1985. ¡ce:title¿Twentieth Symposium (International) on Combustion¡/ce:title¿.

[24] M. R Henneke and J. L Ellzey. Modeling of filtration combustion in a packed bed. *Combustion and Flame*, 117(4):832 – 840, 1999.

[25] D. Trimis. Stablized combustion is porous media-applications of the porous burner technology in energy-and heat engineering. *AIAA Paper No. 20002298*, 2000.

[26] P. Parthasarathy, P. Habisreuther, and N. Zarzalis. Identification of radiative properties of reticulated ceramic porous inert media using ray tracing technique. *J. Quant. Spectrosc. Radiat. Transfer*, 113:1961 – 1969, 2012.

[27] P. Parthasarathy, P. Habisreuther, and N. Zarzalis. Evaluation of longitudinal dispersion coefficient in open-cell foams using transient direct pore level simulation. *Chemical Engineering Science*, 90(0):242 – 249, 2013.

[28] N. Zarzalis, P. Habisreuther, and P. Parthasarathy. Flow field and heat transfer simulation inside porous inert media. Final report of project FOR-583-T2 for the German Research Foundation DFG, Engler-Bunte-Institute division of combustion technology EBI-VBT, Karlsruhe Institute of Technology KIT, 2013.

[29] S.R. Turns. *An Introduction to Combustion*. McGraw-Hill Book Co. Singapore, 2000.

[30] I. Glassman. In *Combustion*. Academic Press, Burlington, fourth edition, 2008.

[31] T. Poinsot and D. Veyante. *Theoretical and numerical combustion*. R.T. Edwards, Inc., 2005.

[32] C. Westbrook and D. Frederick. Simplified reaction mechanisms for the oxidation of hydrocarbon fuels in flames. *Combustion Science and Technology*, 27(1-2):31–43, 1981.

[33] J. Goettgens, F. Mauss, and N. Peters. Analytic approximations of burning velocities and flame thicknesses of lean hydrogen, methane, ethylene, ethane, acetylene,

and propane flames. *Symposium (International) on Combustion*, 24(1):129 – 135, 1992.

[34] I. Mallard and A. LeChatelier. Recherches exprimentales et thoriques sur la combustion des mlanges gazeux explosifs. *Annales des Mines, 8*, 4:274–568, 1883.

[35] N. Semenov. Thermal theory of combustion and explosion. *NACA Technical Memorandum*, 1024:56, 1942.

[36] B. Lewis and G. von Elbe. *Combustion, Flames and Explosion of Gases.* third ed., Academic Press, Inc. Ney York, London, 1987.

[37] N. Peters and F.A. Williams. The asymptotic structure of stoichiometric methane-air flames. *Combustion and Flame*, 68(2):185 – 207, 1987.

[38] R. J. Kee, J. F. Grcar, M. D. Smooke, and J. A. Miller. PREMIX. A fortran program for modeling steady laminar one-dimensional premixed flames. *Sandia National Laboratories: Livermore.*, 1985.

[39] J. Kee, F. Rupley, and J. Miller. Chemkin-II: A Fortran chemical kinetics package for the analysis of gas-phase chemical kinetics. Technical report, Report No. SAND89-8009B, Sandia National Laboratories, 1989.

[40] J. Kee. A fortran computer code package for the evaluation of gas-phase, multicomponent transport properties. *Snadia National Lab.*, pages SAND86–8246, 1986.

[41] G.P. Smith, D.M. Golden, M. Frenklach, N.W. Moriarty, M. Goldenberg B. Eiteneer, C.T. Bowman, R.K. Hanson, S. Song, V. Lissianski W.C. Gardiner, and Z. Qin. GRI-MECH 3.0. 1999.

[42] H. Schmid. *Ein Verbrennungsmodell zur Beschreibung der Waermefreisetzung von vorgemischten turbulenten Flammen.* PhD thesis, University of Karlsruhe, Germany, 1995.

[43] F.N. Egolfopoulos, P. Cho, and C.K. Law. Laminar flame speeds of methane-air mixtures under reduced and elevated pressures. *Combust Flame*, 76(3–4):375 – 391, 1989.

[44] T. Iijima and T. Takeno. Effects of temperature and pressure on burning velocity. *Combust Flame*, 65 (1)(1):35 – 43, 1986.

[45] Y. Ogami and H. Kobayashi. Laminar burning velocity of stoichiometric CH4/air premixed flames at high-pressure and high-temperature. *JSME International Journal*, 48:603–609, 2005.

[46] C. Bedoya, P. Habisreuther, N. Zarzalis, C. Prathap, and H. Ebrahimi. Study on the influence of pressure on the flame stabilization in porous inert media (PIM). *Proceedings of ASME Turbo Expo 2012: Power for Land, Sea and Air*, Copenhagen, Denmark,:GT2012–68234, 2012.

[47] G. Rozenchan, D.L. Zhu, C.K. Law, and S.D. Tse. Outward propagation, burning velocities, and chemical effects of methane flames up to 60 atm. *Proceedings of the Combustion Institute*, 29(2):1461 – 1470, 2002.

[48] X.J. Gu, M.Z. Haq, M. Lawes, and R. Woolley. Laminar burning velocity and markstein lengths of methane-air mixtures. *Combustion and Flame*, 121(12):41 – 58, 2000.

[49] P. Habisreuther. Professional assitance, colaboration and discussion. 2011-2012.

[50] M. Zabetakis. *Flammability chacharacteristics of combustible gases and vapors.* US Bureau of Mines, 1965.

[51] N. Zarzalis. Applied combustion technology. *Lecture notes in process engineering, Karlruhe Institut of Technology*, 2009.

[52] H. Davy. Some researches on flame. *Philosophical Transactions of the Royal Society London*, 107:45–76, 1817.

[53] D.B. Spalding. A theory of inflammability limits and flame-quenching. *Proceedings of the Royal Society of London A*, 240:83–100, 1957.

[54] S Raimondeau, D Norton, D Vlachos, and R. Masel. Modeling of high temperature microburners. *Proceedings of the Combustion Institute*, 29:901–907, 2003.

[55] C.M. Miesse, R.I. Masel, C.D. Jensen, M.A. Shannon, and M. Short. Submillimeter-scale combustion. *AIChE Journal*, 50(12):3206–3214, 2004.

[56] N. Djordjevic. *Flammenstabilisierung durch Verbrennung in festen Schwaemen.* PhD thesis, Karlsruhe Institute of Technology, Karlsruhe, Germany, 2011.

[57] S. Voss, M.A.A. Mendes, J.M.C. Pereira, S. Ray, J.C.F. Pereira, and D. Trimis. Investigation on the thermal flame thickness for lean premixed combustion of low calorific H2/CO mixtures within porous inert media. *Proceedings of the Combustion Institute*, 34:3335 – 3342, 2013.

[58] F.A. Lammers and L.P.H. de Goey. A numerical study of flash back of laminar pre-mixed flames in ceramic-foam surface burners. *Combustion and Flame*, 133(12):47 – 61, 2003.

[59] R. L. Curl. Dispersed phase mixing effects on second moments in dominantly first-order, backmix reactors. *Chemical Enineering Science*, 22:353–358, 1967.

[60] H. Gao, Z. Qu, X. Feng, and W. Tao. Combustion of methane/air mixtures in a two-layer porous burner: A comparison of alumina foams, beads, and honeycombs. *Experimental Thermal and Fluid Science*, 52:215–220, 2014.

[61] M.V. Twigg and J.T. Richardson. Fundamentals and applications of structured ce-ramic foam catalysts. *Industrial & Engineering Chemistry Research*, 46(12):4166–4177, 2007.

[62] J. Banhart. Manufacture, characterisation and application of cellular metals and metal foams. *Progress in Materials Science*, 46(6):559 – 632, 2001.

[63] A. Fuessel, D. Boettge, J. Adler, F. Marschallek, and A. Michaelis. Cellular ceram-ics in combustion environments. *Advanced Engineering Materials*, 13(11):1008–1014, 2011.

[64] H.B. Gao, Z.G. Qu, X.B. Feng, and W.Q. Tao. Methane/air premixed combustion in a two-layer porous burner with different foam materials. *Fuel*, 115(0):154 – 161, 2014.

[65] R.C. Robinson and J.L. Smialek. SiC recession caused by SiO2 scale volatility under combustion conditions: I, experimental results and empirical model. *Journal of the American Ceramic Society*, 82(7):1817–1825, 1999.

[66] A Ortona, S Pusterla, P Fino, F R A Mach, A Delgado, and S Biamino. Aging of reticulated Si-SiC foams in porous burners. *Adv Appl Ceram*, 109 (4)(4):246–251, 2010.

[67] P. Habisreuther, N. Djordjevic, and N. Zarzalis. Statistical distribution of res-idence time and tortuosity of flow through open-cell foams. *Chem Eng Sci*, 64 (23)(23):4943 – 4954, 2009.

[68] N. Djordjevic, P. Habisreuther, and N. Zarzalis. Experimental study on the basic phenomena of flame stabilization mechanism in a porous burner for premixed combustion application. *Energy & Fuels*, 26(11):6705–6719, 2012.

[69] R. Phelan, D. Weaire, and K. Brakke. Computation of equilibrium foam structures using the surface evolver. *Experimental Mathematics*, 4(3):181–192, 1995.

[70] T.J. Lu, H.A. Stone, and M.F. Ashby. Heat transfer in open-cell metal foams. *Acta Materialia*, 46(10):3619 – 3635, 1998.

[71] K. Boomsma and D. Poulikakos. On the effective thermal conductivity of a three-dimensionally structured fluid-saturated metal foam. *Int J Heat Mass Tran*, 44(4):827 – 836, 2001.

[72] K. Boomsma, D. Poulikakos, and Y. Ventikos. Simulations of flow through open cell metal foams using an idealized periodic cell structure. *International Journal of Heat and Fluid Flow*, 24(6):825 – 834, 2003.

[73] S.R. Annapragada, J.Y. Murthy, and S.V. Garimella. Permeability and thermal transport in compressed open-celled foams. *Numerical Heat Transfer, Part B: Fundamentals*, 54(1):1–22, 2008.

[74] S. Krishnan, J. Murthy, and S. Garimella. Direct simulation of transport in open-cell metal foam. *ASME J. Heat Transfer*, 128:793–799, 2006.

[75] C. Hutter, A. Zenklusen, R. Lang, and Ph. R. von Rohr. Axial dispersion in metal foams and streamwise-periodic porous media. *Chemical Engineering Science*, 66(6):1132 – 1141, 2011.

[76] C. Hutter, A. Zenklusen, S. Kuhn, and Ph. R. von Rohr. Large eddy simulation of flow through a streamwise-periodic structure. *Chem Eng Sci*, 66(3):519 – 529, 2011.

[77] D. Butscher, C. Hutter, S. Kuhn, and P. Rudolf von Rohr. Particle image velocimetry in a foam-like porous structure using refractive index matching: a method to characterize the hydrodynamic performance of porous structures. *Exp Fluids*, 53:1123–1132, 2012.

[78] C. Hutter. *Laser sintered meso scale reactor by design: Characterization of heat and mass transfer*. PhD thesis, ETH Zurich, 2010.

[79] J. Petrasch, P. Wyss, and A. Steinfeld. Tomography-based monte carlo determination of radiative properties of reticulate porous ceramics. *Journal of Quantitative Spectroscopy and Radiative Transfer*, 105(2):180 – 197, 2007.

[80] E. Bianchi, T. Heidig, C. Visconti, G. Groppi, H. Freund, and E. Tronconi. Heat transfer properties of metal foam supports for structured catalysts: Wall heat transfer coefficient. *Catalysis Today*, 216(0):121 – 134, 2013.

[81] W. G. Gray. A derivation of the equations for multi-phase transport. *Chemical Engineering Science*, 30(2):229 – 233, 1975.

[82] S. Whitaker. *The Method of Volume Averaging*. Kluwer academic publishers, 1999.

[83] A. Onstad, E. Christopher, F. Medina, W. Ryan, and J.K. Eaton. Full-field measurements of flow through a scaled metal foam replica. *Experiments in Fluids*, 50(6):1571–1585, 2011.

[84] M. J. Hall and J. P. Hiatt. Exit flows from highly porous media. *Physics of Fluids (1994-present)*, 6(2):469–479, 1994.

[85] D. Butscher, C. Hutter, S. Kuhn, and R. von Rohr. Particle image velocimetry in a foam-like porous structure using refractive index matching: a method to characterize the hydrodynamic performance of porous structures. *Experiments in Fluids*, 53(4):1123–1132, 2012.

[86] G. Incera Garrido and B. Kraushaar-Czarnetzki. A general correlation for mass transfer in isotropic and anisotropic solid foams. *Chemical Engineering Science*, 65(6):2255 – 2257, 2010.

[87] M. Kaviany. *Principles of Heat Transfer in Porous Media*. Springer, 2nd edition, 1999.

[88] S. Ferrouillat, P. Tochon, and H. Peerhossaini. Micromixing enhancement by turbulence: Application to multifunctional heat exchangers. *Chemical Engineering and Processing: Process Intensification*, 45(8):633 – 640, 2006.

[89] M.A.A. Mendes. *Modeling and Simulation of Hydrocarbon Oxidation Processes within Porous Inert Media*. PhD thesis, Universidad tecnica de Lisboa, Instituto superior tecnico, 2010.

[90] C. Hutter, C. Allemann, S. Kuhn, and Ph. R. von Rohr. Scalar transport in a milli-scale metal foam reactor. *Chemical Engineering Science*, 65(10):3169 – 3178, 2010.

[91] D Seguin, A Montillet, and J Comiti. Experimental characterisation of flow regimes in various porous mediai: Limit of laminar flow regime. *Chemical Engineering Science*, 53(21):3751 – 3761, 1998.

[92] M. de Lemos. *Turbulence in Porous Media: Modeling and Applications.* Elsevier, 2006.

[93] M. de Lemos and M. Saito. Computation of turbulent heat transfer in a moving porous bed using a macroscopic two-energy equation model. *International Communications in Heat and Mass Transfer*, 35(10):1262 – 1266, 2008.

[94] M. Saito and M. de Lemos. A macroscopic two-energy equation model for turbulent flow and heat transfer in highly porous media. *International Journal of Heat and Mass Transfer*, 53(1112):2424 – 2433, 2010.

[95] G. Brenner, T. Zeiser, and F. Durst. Simulation komplexer fluider transportvorgaenge in der verfahrenstechnik. *Chemie Ingenieur Technik*, 74(11):1533–1542, 2002.

[96] T.R. Brosten, S.L. Codd, R.S. Maier, and J.D. Seymour. Dynamic length-scale characterization and nonequilibrium statistical mechanics of transport in open-cell foams. *Phys. Rev. Lett.*, 103:218001, Nov 2009.

[97] D. Beugre, S. Calvo, G. Dethier, M. Crine, D. Toye, and P. Marchot. Lattice Boltzmann 3D flow simulations on a metallic foam. *Journal of Computational and Applied Mathematics*, 234(7):2128 – 2134, 2010.

[98] H. Darcy. *Les fontaines publiques de la ville de Dijon.* Paris, 1856.

[99] P. Forchheimer. Wasserbewegung durch boden. *Z. Ver. Deutsch. Ing.*, 45:1782–1788, 1901.

[100] B. Dietrich. Pressure drop correlation for ceramic and metal sponges. *Chemical Engineering Science*, 74(0):192 – 199, 2012.

[101] C. P. Lowe and D. Frenkel. Do hydrodynamic dispersion coefficients exist? *Phys. Rev. Lett.*, 77:4552–4555, Nov 1996.

[102] D. L. Koch and J. F. Brady. Dispersion in fixed beds. journal of fluid mechanics. 154:399–427, 1985.

[103] J. Bear. *Dynamics of Fluids in Porous Media.* elsevier Pub., New York, 1972.

[104] V. Alvarado, H.T. Davis, and L.E. Scriven. Effects of pore-level reaction on dispersion in porous media. *Chemical Engineering Science*, 52(17):2865 – 2881, 1997.

[105] R.G. Carbonell and S. Whitaker. Dispersion in pulsed systemsii: Theoretical developments for passive dispersion in porous media. *Chemical Engineering Science*, 38(11):1795 – 1802, 1983.

[106] J. P. Boon, E. Vanden Eijnden, and D. Hanon. A lattice gas automaton approach to turbulent diffusion. *Chaos, Solitons & Fractals*, 11(13):187 – 192, 2000.

[107] J.M.P.Q. Delgado. Longitudinal and transverse dispersion in porous media. *Chemical Engineering Research and Design*, 85(9):1245 – 1252, 2007.

[108] N. Wakao and S. Kaguei. *Heat and mass transfer in packed beds*. Gordon and Breach, New York, 1982.

[109] P. Benz, P. Huetter, and A. Schlegel. Radiale stoffdispersionskoeffizienten in durchstroemten keramischen schaeumen. *Waerme - und Stoffuebertragung*, 29(2):125–127, 1993.

[110] C. L. Hackert, J. L. Ellzey, O. A. Ezekoye, and M. J. Hall. Transverse dispersion at high peclet numbers in short porous media. *Exp Fluids*, 21:286–290, 1996. 10.1007/BF00190679.

[111] J.C.F. Pereira, I. Malico, T.C. Hayashi, and J. Raposo. Experimental and numerical characterization of the transverse dispersion at the exit of a short ceramic foam inside a pipe. *Int J Heat Mass Tran*, 48(1):1 – 14, 2005.

[112] J. Prausnitz. Longitudinal dispersion packed bed. *AIChEJ.*, 4:14M22M, 1958.

[113] R. S. Maier. Enhanced dispersion in cylindrical packed beds. *Philosophical Transactions of the Royal Society of London. Series A:Mathematical, Physical and Engineering Sciences*, 360(1792):497–506, 2002.

[114] T. Fend, R. Pitz-Paal, B. Hoffschmidt, and O. Reutter. *Solar Radiation Conversion, Chapter 5.6 in Cellular Ceramics: Structure, Manufacturing, Properties and Applications*. Wiley-VCH Verlag GmbH, 2005.

[115] R. Pitz-Paal, B. Hoffschmidt, M. Boehmer, and M. Becker. Experimental and numerical evaluation of the performance and flow stability of different types of open volumetric absorbers under non-homogeneous irradiation. *Solar Energy*, 60(34):135 – 150, 1997.

[116] W. Vroemen, V. Kornilov, and L. de Goey. Thermo-acoustic transfer function of flames embedded in porous media. *Proceedings of the European Combustion Meeting 2013, Lund, Sweden*.

[117] C.Y. Zhao. Review on thermal transport in high porosity cellular metal foams with open cells. *International Journal of Heat and Mass Transfer*, 55(1314):3618 – 3632, 2012.

[118] K. Kamiuto. *Modeling of Composite Heat Transfer in Open-Cellular Porous Materials at High Temperatures*, pages 165–198. Wiley-VCH Verlag GmbH & Co. KGaA, 2008.

[119] A. Bhattacharya, V.V. Calmidi, and R.L. Mahajan. Thermophysical properties of high porosity metal foams. *International Journal of Heat and Mass Transfer*, 45(5):1017 – 1031, 2002.

[120] E. Bianchi, T. Heidig, C. Giorgio V., G. Groppi, H. Freund, and E. Tronconi. An appraisal of the heat transfer properties of metallic open-cell foams for strongly exo-/endo-thermic catalytic processes in tubular reactors. *Chemical Engineering journal*, 198-199:512–528, 2012.

[121] B. Dietrich. Heat transfer coefficients for solid ceramic sponges experimental results and correlation. *International Journal of Heat and Mass Transfer*, 61(0):627 – 637, 2013.

[122] R. Bird, W. Stewart, and E. Lightfoot. *Transport Phenomena, second edition.* John Wiley and Sons, Inc., New York,, 2007.

[123] H. Martin. The generalized lvque equation and its practical use for the prediction of heat and mass transfer rates from pressure drop. *Chemical Engineering Science*, 57(16):3217 – 3223, 2002.

[124] A. Schlegel, P. Benz, and S. Buser. Waermeuebertragung und druckabfall in keramischen schaumstrukturen bei erzwungener stroemung. *Waerme - und Stoffuebertragung*, 28(5):259–266, 1993.

[125] V. V. Calmidi and R. L. Mahajan. Forced convection in high porosity metal foams. *Journal of Heat Transfer*, 122:557–565, 2000.

[126] L. Giani, G. Groppi, and E. Tronconi. Heat transfer characterization of metallic foams. *Industrial & Engineering Chemistry Research*, 44(24):9078–9085, 2005.

[127] S. Mancin, C. Zilio, A. C., and L. Rossetto. Heat transfer during air flow in aluminum foams. *International Journal of Heat and Mass Transfer*, 53(2122):4976 – 4984, 2010.

[128] S. Mancin, C. Zilio, L. Rossetto, and A. Cavallini. Foam height effects on heat transfer performance of 20 ppi aluminum foams. *Applied Thermal Engineering*, 49(0):55 – 60, 2012.

[129] S. Decker, F. Durst, D. Trimis, S. Nemoda, V. Stamatov, M. Steven, M. Becker, T. Fend, and B. Hoffschmidt. Thermisch beaufschlagte porenkoerper und deren durchstroemungs- und waermeuebertragungseigenschaften. Technical report, DFG Projekt DU101/55-1, 2002.

[130] L. B. Younis and R. Viskanta. Experimental determination of the volumetric heat transfer coefficient between stream of air and ceramic foam. *Int J Heat Mass Tran*, 36(6):1425 – 1434, 1993.

[131] X.Fu R., R. Viskanta, and J.P. Gore. Measurement and correlation of volumetric heat transfer coefficients of cellular ceramics. *Experimental Thermal and Fluid Science*, 17(4):285 – 293, 1998.

[132] K. Kamiuto and S. S. Yee. Heat transfer correlations for open-cellular porous materials. *International Communications in Heat and Mass Transfer*, 32(7):947 – 953, 2005.

[133] J. Hwang, G. Hwang, R. Yeh, and C. Chao. Measurement of interstitial convective heat transfer and frictional drag for flow across metal foams. *Journal of heat transfer*, 124:120–129, 2002.

[134] T. Fend, B. Hoffschmidt, R. Pitz-Paal, O. Reutter, and P. Rietbrock. Porous materials as open volumetric solar receivers: Experimental determination of thermophysical and heat transfer properties. *Energy*, 29(56):823 – 833, 2004.

[135] A. Nakayama, K. Ando, C. Yang, Y. Sano, F. Kuwahara, and J. Liu. A study on interstitial heat transfer in consolidated and unconsolidated porous media. *Heat and Mass Transfer*, 45(11):1365–1372, 2009.

[136] R. Lemlich. A theory for the limiting conductivity of polyhedral foam at low density. *Journal of Colloid and Interface Science*, 64(1):107 – 110, 1978.

[137] V. Calmidi and R. Mahajan. The effective thermal conductivity of high porosity fibrous metal foams. *ASME J. Heat Transfer*, 121:466–471, 1999.

[138] P. Hsu and J. Howell. Measurements of thermal conductivity and optical properties of porous partially stabilized zirconia. *Experimental Heat Transfer*, 5(4):293–313, 1992.

[139] X. Fu, R. Viskanta, and J.P. Gore. Prediction of effective thermal conductivity of cellular ceramics. *International Communications in Heat and Mass Transfer*, 25(2):151 – 160, 1998.

[140] S. Krishnan, J. Murthy, and S. Garimella. Direct simulation of transport in open-cell metal foam. *ASME J. Heat Transfer*, 128:793–799, 2006.

[141] D. Edouard, T. Huu, C. Huu, F. Luck, and D. Schweich. The effective thermal properties of solid foam beds: Experimental and estimated temperature profiles. *International Journal of Heat and Mass Transfer*, 53(1920):3807 – 3816, 2010.

[142] B. Dietrich, M. Kind, and H. Martin. Axial two-phase thermal conductivity of ceramic sponges experimental results and correlation. *International Journal of Heat and Mass Transfer*, 54(1112):2276 – 2282, 2011.

[143] M.L. Hunt and C.L. Tien. Effects of thermal dispersion on forced convection in fibrous media. *International Journal of Heat and Mass Transfer*, 31(2):301 – 309, 1988.

[144] Moran Wang and Ning Pan. Modeling and prediction of the effective thermal conductivity of random open-cell porous foams. *International Journal of Heat and Mass Transfer*, 51(56):1325 – 1331, 2008.

[145] R. Viskanta and J. Gore. Overview of cellular ceramics based porous radiant burners for supporting combustion. *Env. Combust. Technol.*, 1:167–203, 2000.

[146] L. Dombrovsky and D. Baillis. *Thermal Radiation in Disperse Systems: An Engineering Approach*. Begell House Inc., 2010.

[147] T.C. Hayashi. *Multidimensional modelling and calculation of combustion in porous MEDIA*. PhD thesis, Universidad Tecnica de Lisboa, Instituto superior tecnico, 2005.

[148] L. Glicksman, M. Schuetz, and M. Sinofsky. Radiation heat transfer in foam insulation. *International Journal of Heat and Mass Transfer*, 30(1):187 – 197, 1987.

[149] C.L. Hackert, J.L. Ellzey, and O.A. Ezekoye. Combustion and heat transfer in model two-dimensional porous burners. *Combust Flame*, 116(1–2):177 – 191, 1999.

[150] D J Diamantis, E Mastorakos, and D A Goussis. Simulations of premixed combustion in porous media. *Combustion Theory and Modelling*, 6(3):383–411, 2002.

[151] M.F. Modest. *Radiative Heat Transfer*. Elsevier Science, 2003.

[152] Howell J. R. *Handbook of Porous Media*, volume Radiative Transfer in Porous Media. Marcel Dekker, New York,, 2000.

[153] T. J. Hendricks and J. R. Howell. Absorption/scattering coefficients and scattering phase functions in reticulated porous ceramics. *ASME J. Heat Transfer*, 118:79–87, 1996.

[154] W. Tao, H. Hsu, C. Chang, C. Hsu, and Y. Lin. Measurement and prediction of thermal conductivity of open cell rigid polyurethane foam. *Journal of Cellular Plastics*, 37(4):310–332, 2001.

[155] M. Loretz, E. Maire, and D. Baillis. Analytical modelling of the radiative properties of metallic foams: Contribution of x-ray tomography. *Advanced Engineering Materials*, 10(4):352–360, 2008.

[156] W. Bone. Surface combustion. *J. Franklin Inst. State Penn.*, 173(2):101131, 1912.

[157] W. Bone, J. Wilson, and C. Mccourt. Process for producing heat., April 17 1917. US Patent 1,223,249.

[158] Y. Shaulov. Flame propagation through porous media. *Izd. Akad. Nauk Azerb. SSR*, 1954.

[159] G. de Soete. Stability and propagation of combustion waves in inert porous media. *Symposium (International) on Combustion*, 11(1):959 – 966, 1967.

[160] A. Weil, W. Staats, and R. Rosenberg. An analysis of porous plate combustion systems. *Am. chem. Soc., Div. Fuel Chem.*, 10(3):84–90, 1966.

[161] T. Takeno and K. Sato. An excess enthalpy flame theory. *Combust Sci Technol*, 20(1-2):73–84, 1979.

[162] R. Viskanta. Interaction of combustion and heat transfer in porous inert media. *S.H. Chand, ed. Transport phenomena in Combustion*, Taylor and Francis:64–87, 1996.

[163] E. Noordally, J.M. Przybylski, and J.J. Witton. Porous media combustors for clean gas turbine engines. *Final report, Cranfield University, United Kingdom*, Accession Number: ADA429816:pp. 1–45, 2004.

[164] A. Bakry, A. Al-Salaymeh, A. H. Al-Muhtaseb, A. Abu-Jrai, and D. Trimis. Adiabatic premixed combustion in a gaseous fuel porous inert media under high pressure and temperature: Novel flame stabilization technique. *Fuel*, 90 (2)(2):647 – 658, 2011.

[165] J. Kiefer, MC Weikl, T. Seeger, F. von Issendorff, F. Beyrau, and et al. Nonintrusive gas-phase temperature measurements inside a porous burner using dualpump CARS. *Proc Combust Inst*, 32:3123–3129, 2009.

[166] Q. Chen and S. Liu. Flame imaging in meso-scale porous media burner using electrical capacitance tomography. *chinese journal of chemical engineering*, 20(2):329–336, 2012.

[167] K. Yamamoto and N. Takada. LB simulation on soot combustion in porous media. *Physica A: Statistical Mechanics and its Applications*, 362:111 117, 2006.

[168] M. Liou and H. Kim. Pore scale simulation of combustion in porous media. In Haecheon Choi, Hyong Gwon Choi, and Jung Yul Yoo, editors, *Computational Fluid Dynamics 2008*, pages 363–374. Springer Berlin Heidelberg, 2009.

[169] A. Barra, G. Diepvens, J. Ellzey, and M. Henneke. Numerical study of the effects of material properties on flame stabilization in a porous burner. *Combust Flame*, 134 (4):369 – 379, 2003.

[170] M. R. Kulkarni and R. E. Peck. Analysis of a bilayered porous radiant burner. *Numer Heat Trans Appl: Int J Comput Method*, 30(3):219–232, 1996.

[171] X. Y. Zhou and J. C. F. Pereira. Comparison of four combustion models for simulating the premixed combustion in inert porous media. *Fire Mater.*, 22:187–197, 1998.

[172] P. Hsu and R. Matthews. The necessity of using detailed kinetics in models for premixed combustion within porous media. *Combustion and Flame*, 93(4):457 – 466, 1993.

[173] Z. Al-Hamamrea, S. Voss, and D. Trimis. Hydrogen production by thermal partial oxidation of hydrocarbon fuels in porous media based reformer. *International Journal Hydrogen Energy*, 34:827–832, 2009.

[174] M. Steven, A. Mach, F. von Issendorff, M. Altendorfner, and A. Delgado. Numerical simulation of combustion of a low calorific gas mixture in a porous inert

medium taking anisotropic dispersion into account. *Proceedings of the Third European Combustion Meeting, Chania, Crete*, 2007.

[175] I. Malico and J. C. F. Pereira. Numerical predictions of porous burners with integrated heat exchanger for household applications. *J Porous Media*, 2(2):153–162, 1999.

[176] I. Malico and J. C. F. Pereira. Numerical study on the influence of radiative properties in porous media combustion. *J Heat Transf*, 123:951–957, 2001.

[177] J-R Shi, M-Z Xie, G. Li, H. Liu, J-T Liu, and H-T Li. Approximate solutions of lean premixed combustion in porous media with reciprocating flow. *Int J Heat Mass Tran*, 52:702–708, 2009.

[178] M-Z Xie, J-R Shi, Y-B Deng, H. Liu, L. Zhou, and Y-N Xu. Experimental and numerical investigation on performance of a porous medium burner with reciprocating flow. *Fuel*, 88(1):206–213, 2009.

[179] M. Sahraoui and M. Kaviany. Direct simulation vs volume-averaged treatment of adiabatic, premixed flame in a porous medium. *International Journal of Heat and Mass Transfer*, 37(18):2817 – 2834, 1994.

[180] J.A. van Oijen, F.A. Lammers, and L.P.H. de Goey. Modeling of premixed laminar flames using flamelet-generated manifolds. *Combust Sci Technol*, 161:113–137, 2000.

[181] J.A. van Oijen, F.A. Lammers, and L.P.H. de Goey. Modeling of complex premixed burner systems by using flamelet-generated manifolds. *Combust Flame*, 127:124–134, 2001.

[182] T. Zeiser, M. Steven, H. Freund, P. Lammers, G. Brenner, F. Durst, and J. Bernsdorf. Analysis of the flow field and pressure drop in fixed-bed reactors with the help of lattice Boltzmann simulations. *Phil. Trans. R. Soc. Lond. A*, 360:507–520, 2002.

[183] Y-K. Chen, R.D. Matthews, and J.R. Howell. The effect of radiation on the structure of premixed flames within a highly porous inert medium. *Radiation, Phase Change, Heat Transfer, And Thermal Systems*, 81:35–41, 1987.

[184] Y. Yoshizawa, K. Sasaki, and R. Echigo. Analytical study on the structure of radiation controlled flame. *Int. J. Heat Mass Transfer*, 31 (2):311–319, 1988.

[185] V.S. Babkin and Y.M. Laevskii. Seepage gas combustion. *Combustion, Explosion, and Shock Waves*, 23 (5):531–547, 1987.

[186] S.B. Sathe, R.E. Peck, and T.W. Tong. Flame stabilization and multimode heat transfer in inert porous media: a numerical study. *Combust. Sci. Technol.*, 70 (4-6):93–109, 1990.

[187] P. Hsu, J. Howell, and R. Matthews. A numerical investigation of premixed combustion within porous inert media. *J Heat Transf*, 115 (3)(3):744–750, 1993.

[188] I. Malico, X.Y. Zhou, and J.C.F. Pereira. Two-dimensional numerical study of combustion and pollutants formation in porous burners. *Combust Sci Technol*, 152:57–79, 2000.

[189] A. Barra and J. Ellzey. Heat recirculation and heat transfer in porous burners. *Combust Flame*, 137 (1-2):230 – 241, 2004.

[190] F. Galeazzo, R. Valdes, W. Krebs, G. Donnert, P. Habisreuther, and N. Zarzalis. Measurement and simulation of turbulent mixing in a jet in crossflow. *J. Eng. Gas Turbines Power*, 133(6), 2011.

[191] R.G. Munro. Material properties of a sintered alpha-SiC. *J. Phys. Chem. Ref. Data*, 26:1195–1203, 1997.

[192] S. Diezinger. *Mehrstofffähige Brenner auf Basis der Porenbrennertechnik für den Einsatz in Brennstoffzellensystemen*. PhD thesis, University Erlangen-Nürnberg, Germany, 2006.

[193] S. Shy, W. Lin, and J. Wei. An experimental correlation of turbulent burning velocities for premixed turbulent methane-air combustion. *Proceedings of the Royal Society of London. Series A: Mathematical, Physical and Engineering Sciences*, 456(2000):1997–2019, 2000.

[194] M. Weiss. *Untersuchung von Flammenfrontstreckungseffekten auf die sphaerische Flammenausbreitung lamilaminar und turbulenter Brennstoff/Luft-Gemische*. PhD thesis, Karlsruhe Institute of Technology, Karlsruhe, Germany, 2008.

[195] R. Guenter. *Verbrennung und Feuerung*. Springer Berlin / Heidelberg, 1984.

[196] S. Hoffmann, P. Habisreuther, and B. Lenze. Development and assessment of correlations for predicting stability limits of swirling flames. *Chemical Engineering and Processing: Process Intensification*, 33(5):393 – 400, 1994.

[197] K. Loeblich. Semitheoretical consideration on scaling laws in flame stabilization. *Symposium (International) on Combustion*, 9(1):949 – 957, 1963.

[198] M. Steven. *Modellierung und numerische Simulation von Verbrennungsprozessen in Porenbrennern und Russfiltern*. PhD thesis, Karlruhe Universitaet, 2008.

[199] P. F. Hsu, J. R. Howell, and R. D. Matthews. A numerical investigation of premixed combustion within porous inert media. *Transactions of the ASME*, 115:744–750, 1993.

[200] A.A. Mohamad, S. Ramadhyani, and R. Viskanta. Modelling of combustion and heat transfer in a packed bed with embedded coolant tubes. *Int J Heat Mass Tran*, 37(8):1181 – 1191, 1994.

[201] J. Coutinho and M. de Lemos. Laminar flow with combustion in inert porous media. *Int Commun Heat Mass*, 39(7):896 – 903, 2012.

[202] P. Hsu, W. Evans, and J. Howell. Experimental and numerical study of premixed combustion within nonhomogeneous porous ceramics. *Combustion Science and Technology*, 90(1-4):149–172, 1993.

[203] J. Grcar. The Twopnt program for boundary value problems. *Sandia National Lab.*, pages SAND91–8230, 1992.

[204] V. Vukadinovic, P. Habisreuther, and N. Zarzalis. Influence of pressure and temperature on laminar burning velocity and markstein number of kerosene jet a-1: Experimental and numerical study. *Fuel*, 111(0):401 – 410, 2013.

[205] M.A.A. Mendes, J.M.C. Pereira, and J.C.F. Pereira. Calculation of premixed combustion within inert porous media with model parametric uncertainty quantification. *Combustion and Flame*, 158(3):466 – 476, 2011.

[206] M. de Lemos. Analysis of turbulent combustion in inert porous media. *Int Commun Heat Mass*, 37(4):331 – 336, 2010.

[207] K. Bray, N. Libby, and J. Moss. Unified modeling approach fror premixed turbulent combustion-part i: general formulation. *Combust Flame*, 61:87–102, 1985.

[208] N. Peters. *Turbulent Combustion*. Cambridge University Press, 2004.

[209] M. Anand and S. Pope. Calculation of premixed turbulent flames by PDF methods. *Combust Flame*, 67:127–142, 1987.

[210] I. Dinkov, P. Habisreuther, and H. Bockhorn. Numerical prediction of burning velocity and flame thickness in a radial-flow porous burner. *Proceedings of the European Combustion Meeting 2013, Lund, Sweden*, pages P5–78.

[211] F. Demaria and R. White. Transient response study of gas flowing through irrigated packing. *Aiche J*, 6(3):473–481, 1960.

[212] D. J. Gunn and C. Pryce. Dispersion in packed beds. *Trans. Inst. Chem. Eng.*, 47:T341–T350, 1969.

[213] J. W. Hiby. *Longitudinal and transverse mixing during single-phase flow through granular beds*. Inst. Chem. Engrg. London, 1962. Syrup. Interaction between Fluids and Particles.

[214] J. McHenry and R. Wilhelm. Axial mixing of binary gas mixtures flowing in a random bed of spheres. *American Institute of Chemical Engineers*, 3:83–91, 1957.

Curriculum Vitae

Family name:	Bedoya Ossa
Name:	César Andrés
Birthday:	22. 03. 1982
Birthplace:	Medellín, Colombia

1988 - 1998:	School at the Universidad Pontificia Bolivariana, Colombia
1999 - 2006:	Mechanical Engineering, Bachelor studies, Universidad de Antioquia, Colombia
2006 - 2008:	Project Engineer, Indisa S.A., Colombia
2008 - 2010:	Process Engineering, Master studies, Karlsruhe Institute of Technology KIT, Germany
2010 - 2013:	Promotion at Engler-Bunte-Institute, Division of Combustion Technology, Karlsruhe Institute of Technology KIT, Germany
2014 -	Project Engineer, Envirotherm GmbH, Germany